Title
Perfluorocarbon nanomaterials as theranostic delivery vehicles

Author
Day, Rachael Anne

Publication Date
2021

Peer reviewed|Thesis/dissertation

UNIVERSITY OF CALIFORNIA

Los Angeles

Perfluorocarbon nanomaterials as theranostic delivery vehicles

A dissertation submitted in partial satisfaction of the

requirements for the degree Doctor of Philosophy

in Chemistry

by

Rachael Anne Day

2021

ABSTRACT OF THE DISSERTATION

Perfluorocarbon nanomaterials as theranostic delivery vehicles

By

Rachael Anne Day

Doctor of Philosophy in Chemistry

University of California, Los Angeles, 2021

Professor Ellen May Sletten, Chair

Nanomaterials have been used in the treatment of cancer to increase the solubility of insoluble payloads, increase the plasma half-lives of payloads, avoiding rapid renal clearance, and diminish off-target effects by controlling the biodistribution and the non-specific uptake of the nanocarrier. Perfluorocarbon (PFC) nanoemulsions, droplets of fluorous solvent, stabilized by a surfactant dispersed in water, can solubilize and protect payloads, release payloads upon introduction of stimuli, and deliver oxygen simultaneously with the payload. Perfluorocarbons are biocompatible, with several garnering FDA approval for use in ^{19}F-MRI, and the inherent hydrophobicity of PFCs provide orthogonality from both hydrophilic and hydrophobic environments found within the body. By solubilizing payloads in the perfluorocarbon phase, we

form orthogonal droplets that do not significantly leach payload, increasing the utility of these nanoemulsions for drug delivery.

Chapter One is a perspective on cancer nanomedicine and the role of PFC nanoemulsions within this vast field. Chapter Two describes a systematic study of the polymer surfactant necessary for PFC nanoemulsion stabilization. Through this systematic study we put forward a series of design principles for PFC nanoemulsions.

Chapters Three and Four describe various payloads that can be solubilized within and delivered by PFC nanoemulsions. Chapter Three focuses on photodynamic therapy (PDT), a treatment modality that uses light, oxygen, and a photosensitizer to produce cytotoxic reactive oxygen species. PFC nanoemulsions were perfect for this application as photosensitizer and oxygen could be delivered simultaneously, increasing the photodynamic efficacy compared to other nanomaterial systems. This chapter also contains a perspective on the current state of fluorinated nanomaterials for PDT focusing on three architectures: lipid stabilized PFC nanoemulsions, macromolecule stabilized PFC nanoemulsions, and micelles. Chapter Four describes the design of a fluorous soluble, redox responsive, small molecule fluorophore as well as the first report of plasmid DNA (pDNA) solubilization within perfluorocarbon solvents. Upon delivery of redox responsive nanomaterials containing pDNA to the cytosol, the plasmid was released and transcribed into the fluorescent protein eGFP.

Chapter Five details two methods to visualize endosomal rupture: lysosome size and genetically engineered cells. Hopefully, these assays can be used to further understand the endosomal uptake of PFC nanoemulsions, with the goal of designing materials that can efficiently escape the endosomal / lysosomal pathway, avoiding degradation.

Chapter Six describes efforts toward targeting PFC nanoemulsions to diseased tissues using the well characterized RGD peptide. Through cyclization of the RGD peptide with bromomaleimide chemistry, we were able to cyclize and functionalize the peptide simultaneously. Unfortunately, the first iteration of this project was unsuccessful, and is currently being modified to increase avidity by appending the cyclic peptides directly to the PFC nanoemulsion.

The dissertation of Rachael Anne Day is approved.

Heather D. Maynard

Margot E. Quinlan

Keriann M. Backus

Ellen May Sletten, Committee Chair

University of California, Los Angeles

2021

This dissertation is dedicated to everyone who has supported me throughout this journey.

TABLE OF CONTENTS

LIST OF FIGURES

CHAPTER ONE

CHAPTER TWO

CHAPTER THREE

CHAPTER FOUR

CHAPTER FIVE

CHAPTER SIX

LIST OF SCHEMES

CHAPTER TWO

CHAPTER THREE

CHAPTER SIX

LIST OF TABLES

CHAPTER SIX

LIST OF EQUATIONS

CHAPTER TWO

CHAPTER THREE

CHAPTER FIVE

ACKNOWLEDGEMENTS

As I reflect on my time in graduate school, I am very thankful for all the people that were there to support me through the years. Entering graduate school, I was prepared for the long hours and the hard work, although I definitely did not fully understand what it meant to be one of the first students in a lab.

I owe my greatest of thanks to my advisor, Ellen Sletten. Throughout the years, Ellen has encouraged me to challenge myself to learn synthesis, nanotechnology skills, and push myself in learning more about the biology of nanotechnology. I am very grateful to have done my Ph.D. studies in a lab where I had the ability to learn such a vast array of skills and topics due to the breadth of research done in the Sletten lab. She has helped to make Los Angeles feel like home, by having us over to her apartment for many meals, including our first Thanksgiving when many of us were unable to go home.

In addition to lab work, Ellen pushed me to develop my teaching skills, mentorship skills, and leadership skills that proved crucial in my job search. I loved serving as a Teaching Assistant for the graduate / undergraduate Chemical Biology course for three years. In this time, Ellen let us as teaching assistants help write problem sets and exams, a skill that I was able to hone under her leadership. It was really that experience that confirmed my love for teaching and pushed me to search for other places that I could teach, ultimately leading to me designing and teaching my own course. It was an amazing experience to design my own course, although it was strange to not teach Chemical Biology my last year here at UCLA. Ellen was constantly pushing me to take undergraduate students in the research lab. I enjoy mentoring, and had the ability to mentor many students, ultimately culminating in the summer that I led three undergraduate students to publication within a few months. That experience taught me that mentoring multiple students is

difficult due to the interpersonal relationships that often need to be managed in addition to the experiments and schedules. This was another experience that I am eternally thankful for as I enter the next stage of my career where I will be mentoring many undergraduate students. Lastly, Ellen let me pursue my passion for outreach by encouraging me to put together the Sletten groups PhotoNBooth. After two iterations, I think we have found one that is much easier to put together (and a little less sketchy) than the original P.V.C. pipe iteration.

I am also very thankful to my Ph.D. committee for the support throughout the years, and the advice to enter the job market instead of pursuing a postdoctoral position. It was this advice that led to my next position at a university close to family, with a large chemistry department, and lots of students that are excited to pursue research. I also am extremely thankful to Prof. Margot Quinlan who has consistently written letters of recommendation for me since my first year of graduate school. Without her letters of support, I would not have received nearly the number of awards or fellowships that I did during my time at UCLA.

Within the lab, we really banded together as a support system, specifically my cohort of seven students. The countless hours we spent together helped us make friendships that wouldn't have been formed in other situations. Joe and I immediately bonded over our Midwest homes and cultures. We often joked we would present the poster at recruitment with heavy Midwest accents, although we never did, it is probably for the best. We might have deterred many students from the lab by dragging out our "ooo's." Gina and Monica planned many group outings, mostly to get food, that really helped the group band together. Anna was an amazing friend in the lab, and outside the lab, with many weekends spent together. In lab, she was always willing to stop and talk through a new difficult experiment with me, as we were really the only people working with cells. Margeaux's friendship has been invaluable to me over the years as we were always there to laugh

and commiserate over experiments that were unsuccessful. The months that I didn't see her in lab due to the pandemic felt very lonely, and I was always happy to see her again in lab so I could walk up to her and ask "can I complain to you for a second." I have valued my conversations with Irene, and the joint project we have begun working on. It was very nice to work along someone, and be able to bounce experiments off her from the beginning of the project. Anthony and Cesar are some of my favorite people, and I have loved watching them grow as scientists and hanging out with them outside of lab. Anthony and I have had a long-standing bet, that due to COVID, I believe I have won. I am still waiting on the drink he owes me!

My first day of graduate school, I sat next to Sydnee Green at orientation, by the end of the day we were proclaiming we would be best of friends. Five years later, we still live together, with Dan Estabrook and Edris Rivera. My friendship with the three of them, is going to be one of the things I miss the most from my time here in Los Angeles. Not only did Dan take the desk next to mine in the Sletten lab, but agreed to live with me very early on, showing how strong the friendship truly is as we spend 18+ hours together on most days. Edris has been my partner both in graduate school, and in life from the beginning. Without his support and encouragement, graduate school would have been so much more difficult. Not to mention, his culinary skills literally keeping me alive, and his wiliness to share his love of food and music with me. My relationship with Edris has truly helped me become a better person, and I am eternally grateful. I cannot wait to see the amazing science each of them continues to perform, and the way our friendships evolve as we disperse across the country.

Jessica Logan and Andrea Swanson have been invaluable friends both at and outside of graduate school. I have missed them both dearly and look forward to seeing them both. As scientists they were both always there to support me throughout my time here in graduate school.

I met Andrea in college, and we have been best of friends since. I met Jessica here at UCLA, our countless coffee dates, wine nights, and girls nights were necessary to keep us both sane. Jessica is another person whose friendship has made me a better person, and I am so thankful for her.

Last, but certainly not least, I need to acknowledge my family. My parents never questioned this crazy decision of mine to move across the country in search of a Ph.D. Instead, they listened to me as I talked about my failed experiments, my stress over classes, candidacy exams, paper writing and so on. They have cheered me on, every step of the way, even if they could not relate to what was happening in my life, and I am so thankful to that support. It has been incredibly difficult to be so far from home, and I am very thankful to be moving back to a day's drive away rather than a full day of flying.

There are so many amazing people in my life, and people that I will miss dearly as we enter the next stages academic freedom, and I truly look forward to taking everything I have learned with me as I begin a career of teaching and research.

Chapter one is an unpublished perspective on nanomedicine and perfluorocarbon nanoemulsions written by Day.

Chapter Two is a version of Rachael A. Day, Daniel A. Estabrook, Carolyn Wu, John O. Chapman, Alyssa J. Togle, and Ellen M. Sletten.* Systematic study of perfluorocarbon nanoemulsions stabilized by polymer amphiphiles. *ACS Appl. Mat. Interfaces* **2020**, *12*, 38887-38898. Day, Estabrook, Wu, Chapman, and Togle contributed to experimental work. Day and Sletten contributed to writing.

Chapter Three is a version of Rachael A. Day, Daniel A. Estabrook, Jessica K. Logan and Ellen M. Sletten.* Fluorous photosensitizers enhance photodynamic therapy with perfluorocarbon nanoemulsions. *Chem. Commun.* **2017**, *53*, 13043-13046. Day, Estabrook, and Logan contributed to experiments. Day and Sletten contributed to writing. Chapter Three also includes a version of Rachael A. Day, and Ellen M. Sletten.* Perfluorocarbon nanomaterials for photodynamic therapy. *Curr. Opin. Colloid Interface Sci.* **2021**, *54*, 101454. Day and Sletten contributed to writing.

Chapter Four is a version of Margeaux A. Miller,[±] Rachael A. Day,[±] Daniel A. Estabrook[±] and Ellen M. Sletten.* A reduction-sensitive fluorous fluorogenic coumarin. *Synlett*, **2020**, *31*, 450-454. And Daniel A. Estabrook, Rachael A. Day, and Ellen M. Sletten.* Redox-responsive gene delivery from perfluorocarbon nanoemulsions through cleavable poly(2-oxazoline) surfactants. *Angew. Chem. Int. Ed.* **2021**, *Accepted.* DOI: 10.1002/anie.202102413. Miller, Day and Estabrook contributed equally for the *Synlett* paper and Sletten contributed to writing. Day and Estabrook contributed to experiments for the *Angew. Chem*. Paper. Estabrook and Sletten contributed to writing.

Chapter Five is a version of submitted manuscript Rachael A. Day and Ellen M. Sletten.* Experimental perspectives on direct visualization of endosomal rupture. **2021**, *Submitted.* Day contributed to experiments. Day and Sletten contributed to writing.

Chapter Six is unpublished studies by Day. Day is responsible for writing.

Throughout these studies, I was supported by the Saul Winstein Fellowship and the Collegium of University Teaching Fellows. Additional funding sources for the work described herein include UCLA, Sloan Foundation, Hellman Foundation, NIH NIGMS, UC CRCC, American Chemical Society Petroleum Research, and instrumentation grants from the NSF and the NIH.

BIOGRAPHICAL SKETCH

Education:
University of California, Los Angeles, Los Angeles, CA
MS in Chemistry, 2018

Dordt University, Sioux Center, Iowa
BSc in Chemistry, 2016
Thesis advisor: Darren Stoub

Professional and Academic Experience:
Graduate Research Assistant
University of California, Los Angeles, Department of Chemistry and Biochemistry
Advisor: Prof. Ellen M. Sletten

- Design of PFC nanoemulsions
- Study of biological interactions of PFC nanoemulsions

Undergraduate Research Assistant
Rush Medical School
Advisor: Prof. Vineet Gupta

- Effect of small molecule agonists on the TLR4 mediated pathway
- Visualization of transcription factors with confocal microscopy

Undergraduate Research Assistant
Dordt University
Advisor: Darren Stoub

- Co-crystallization of small molecule agonists and protein targets
- Site directed mutagenesis to study protein-protein interactions

Honors and Awards:
Graduate
Dr. Myung Ki Hong Dissertation Award, 2021
CUTF Teaching Fellow, 2020-2021
Ralph and Charlene Bauer Award, 2020
Michael E. Jung Excellence in Teaching Award, 2020
Alumni Fellowship, 2019 – 2020
Saul Winstein Fellowship, Winter 2020
NSF GRFP Honorable Mention, 2018

Undergraduate
DC Presidential Scholarship, 2013 – 2016
Women's Volleyball Athletic Scholarship, 2013 – 2016
Kuyper Scholarship, 2013 – 2015
Van Klavern Achievement, 2013 – 2015
Chemistry Faculty Honors Scholarship, 2014 – 2015
Dordt College Undergraduate Summer Research Program, Summer 2014 & 2015

Publications:

Day, R.A.; Sletten, E.M.* "Experimental perspectives on direct visualization of endosomal rupture" **2021**, *Submitted.*

Estabrook, D. A.; **Day, R.A**.; Sletten, E.M.* "Redox-responsive gene delivery from perfluorocarbon nanoemulsions through cleavable poly(2-oxazoline) surfactants." *Angew. Chem. Int. Ed.* **2021**, DOI: 10.1002/ange.202102413.

Day, R.A.; Sletten, E.M.* "Perfluorocarbon nanomaterials for photodynamic therapy" *Curr. Opin. Colloid Interface Sci.* **2021**, *54*, 101454. DOI: 10.1016/j.cocis.2021.101454

Lim, I.; Vian, A.; van de Wouw, H.; **Day, R.A.**; Gomez, C.; Liu, Y.; Rheingold, A.; Campas, O.; Sletten, E. M. "Fluorous soluble cyanine dyes for visualizing perfluorocarbons in living systems." *J. Am. Chem. Soc.* **2020**, *142*, 16072-16081. DOI: 10.1021/jacs.0c07761.

Day, R.A.; Estabrook, D.A.; Wu, C.; Togle, A.; Chapman, J.A.; Sletten, E.M.* "Structure property relationships of poly(2-oxazoline) surfactants and perfluorocarbon nanoemulsions." *ACS Appl. Mat. Int*. **2020**, *12*, 38887-38898. DOI: 10.1021/acsami.0c07206

Miller, M.A.[‡]; **Day, R.A**.[‡]; Estabrook, D.A.[‡]; Sletten, E.M.* "A reduction-sensitive fluorous fluorogenic coumarin." *Synlett* **2020**, *30*, 450-454. DOI: 10.1055/s-0039-1690770.
[‡] denotes equal contribution

Estabrook, D.A.; Ennis, A.F.; **Day, R.A**.; Sletten, E.M.* "Controlling nanoemulsion surface chemistry with poly(2-oxazoline) amphiphiles." *Chem. Sci.* **2019**, *10*, 3994-4003. DOI: 10.1039/C8SC05735D

Day, R.A.; Estabrook. D.A.; Logan, J.K.; Sletten, E.M. "Fluorous photosensitizers enhance photodynamic therapy with perfluorocarbon nanoemulsions." *Chem. Commun.* **2017**, *53*, 13043–13046. DOI: 10.1039/C7CC07038A

Cosco, E.D.; Caram J.R.; Bruns, O.T.; **Day, R.A**.; Franke, D.; Farr, E.P.; Bawendi M.G.; Sletten E.M. "Flavylium polymethine fluorophores are bright near- and shortwave infrared emitters." *Angew. Chem. Int. Ed*. **2017**, *56*, 13126–13129. DOI: 10.1002/anie.201706974.

Faridi, M.H *et. al.* "Pharmacologic activation of CD11b suppresses TLR-dependent inflammatory injury and autoimmunity via AKT-FOX03-IRF7 axis." *J.Clin. Invest*. **2017**, *127*, 1271-1283. DOI: 10.1172/JCI88442

CHAPTER ONE

A perspective on perfluorocarbon nanoemulsions as a delivery platform for both therapeutic and diagnostic agents

1.1 Perspective

Nanomaterials, particles less than 1 μm in diameter, have been hailed as the next advance in cancer medicine (Figure 1.1A). These materials have been employed for drug delivery, diagnosis and imaging, synthetic vaccine development and miniature medical devices.[1–3] Several nanoparticle platforms, such as liposomes, albumin nanoparticles, and polymeric micelles, have been approved for cancer treatment with several others currently undergoing clinical trials.[4,5] Although nanomaterials provide longer serum half-lives, can solubilize insoluble cargoes and drugs, and can be designed to be stimuli responsive (Figure 1.1B), there are several limitations.[4] These include the protein corona that forms when nanomaterials are introduced to biological environments,[6–8] the control of biodistribution and non-specific uptake,[9] and the failure to escape the endosomal pathway that often results in complete degradation (Figure 1.1C).[10–12]

Often, the enhanced permeability and retention (EPR) effect is credited for the accumulation of nanoparticles within the tumor microenvironment.[13] Most nanoparticles are administered systemically, circulate through the vascular system, and accumulate within the tumor due to the leaky vasculature and poor lymphatic drainage that surrounds the solid tumor.[14] The EPR effect works well in mice as most mouse models for cancer use xenograft tumors, but does not translate well to human tumors. This along with the fact that most nanoparticles are not fully investigated

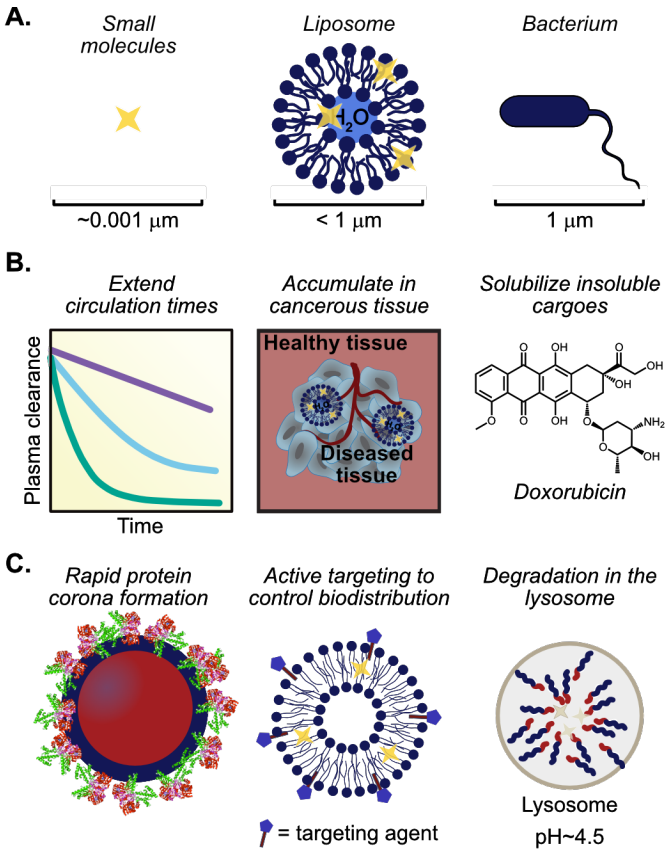

Figure 1.1 Nanomaterial benefits and limitations. (A) Size comparison of small molecules, nanomaterials, and bacteria. (B) Advantages of nanomaterials. (C) Disadvantages of nanomaterials.

in human patients prior to clinical trials, has resulted in the success of relatively few nanoparticles.[15]

When designing new nanoparticles for cancer nanomedicine, it is necessary to optimize all parts of the nanoparticle. These include physical properties like size,[16,17] surface charge,[18] and surface properties,[19–21] along with the chemical composition of the material.[22–24] These vary between liposomes, polymeric nanoparticles, micelles, dendrimers, protein, or viral nanoparticles and so on.[16–18,24–26] The addition of targeting ligands such as small molecules, aptamers, antibodies and antibody fragments, can be used to bias the biodistribution and uptake of the nanoparticle.[27] The physical properties and the chemical composition can be used to predict the amount of serum

proteins that will adhere to the surface of the nanoparticle,[19,28,29] the plasma half-lives,[30–32] and the payload release.[33]

This thesis focuses on nanoemulsions, a class of soft nanomaterials, in which an immiscible phase is stabilized in water with surfactants.[34,35] The surfactant or emulsifier plays a critical role in decreasing the interfacial tension, creating small droplets, and stabilizing the droplets through repulsive electrostatic interactions and steric hindrance.[36] Polymer amphiphiles, proteins, and lipids have all been used as surfactants to stabilize nanoemulsions. Nanoemulsions are kinetically stable, meaning they will not disassemble in dilute conditions.[37,38] The primary mechanism of destabilization for nanomaterials is Ostwald ripening,[39] with other mechanisms including flocculation, coalescence, and creaming/sedimentation.[40,41] Ostwald ripening occurs via mass transfer from the smaller to the larger droplets in a sample with a range of sizes, until the sample reaches a uniform size distribution.

Nanoemulsions can be prepared via either high or low energy methods.[38] High energy methods involve mixing oil, water and surfactant in a batch stirrer or ultrasonicating system for a sufficient period of time. Low energy methods often used homogenizers to push the macroemulsions through a narrow gap in which the droplets are exposed to extreme elongation and shear stress. The low energy methods typically form small nanoemulsions of more uniform sizes than can be reached via high energy ultrasonication.[42]

Traditional oil-in-water nanoemulsions have been used in drug delivery,[43] the food industry,[44] and in the cosmetic industry.[45] In drug delivery, nanoemulsions have been used for topical, ocular, intravenous, internasal, and oral delivery.[46,47] The inner lipophilic phase is used to solubilize water-insoluble drugs that can be easily delivered to patients. Similar to drug delivery, in the food

industry, nanoemulsions are used to create "smart foods" that incorporate low-water solubility molecules such a β-carotene or curcumin.[48,49]

A limitation of traditional oil-in-water nanoemulsions is the undesired leaching of payload into surrounding biological media.[50,51] As such, we are interested in using bioorthogonal, perfluorocarbon-in-water nanoemulsions. Perfluorocarbons (PFCs) are molecules in which all C—H bonds have been replaced with C—F bonds (Figure 1.2A). PFCs form a separate, extremely hydrophobic and lipophobic phase termed the "fluorous phase," attributed to the high electronegativity of fluorine atoms preventing van der Waals interactions with neighboring molecules.[52–54] It is important to note that the fluorous phase does not arise from enthalpically favorable fluorine-fluorine interactions, instead it is from the disinclination for perfluorinated molecules to interact with all other species.[55]

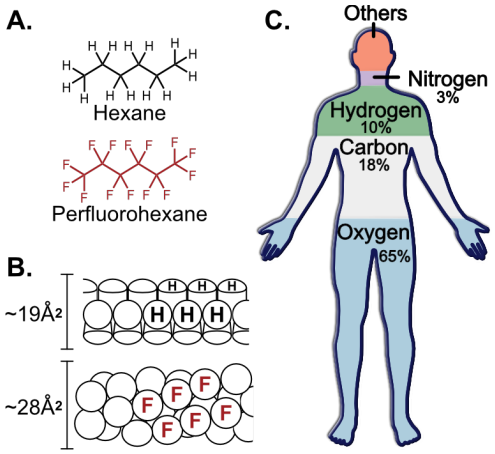

Figure 1.2 Properties of fluorine. (A) Comparison of hydrocarbon (hexane) and perfluorocarbon (perfluorohexanes). (B) The larger radii of fluorine makes molecules more rigid and increases the surface area of perfluorocarbons contributing to the extreme hydrophilicity. (C) Natural distribution of elements within the body (wt%), with minimal naturally occurring fluorine.

Perfluorocarbon nanoemulsions were first FDA approved for the use as a blood substitute[56,57] due to 20-fold higher dissolved gas concentrations compared to aqueous phases. The high gas solubility is attributed to the weak van der Waals interactions between perfluorocarbon chains, and the increased rigidity of perfluorocarbon chains, forming "pockets" that are readily able to solubilize gasses (Figure 1.2B).[53,56,58–60] This first formulation for oxygen delivery, termed Fluosol-DA,[61,62] was soon followed by PFC nanoemulsions used for ^{19}F-MRI,[63–65] as ultrasound contrast agents,[66,67] and as intracellular sensors.[68]

Fluorine is rarely found in living systems (Figure 1.2C),[69,70] thus making PFCs perfect as a contrast agent for ^{19}F-MRI.[63] The "perfect" PFC tracer for 19F-MRI should have high fluorine content, facile synthesis, biological stability, low toxicity and simple ^{19}F NMR spectrum.[63,64] As such PFCs such as perfluorodecalin, perfluoro-15-crown-5-ether, and perfluorooctyl bromide[71–74] have been employed as contrast agents. PFOB gained prominence in the early 199f0s and was ultimately FDA approved under the name Perflubron.[52] Perfluoro-15-crown-5-ether has become the stand-out fluorinated liquid ^{19}F-MRI agent due to the 20 equivalent fluorine atoms.[63,75]

PFCs have been found to be biologically inert, nontoxic *in vivo*, stable at physiological pH, generally not metabolized by enzymes, cleared via the reticuloendothelial system and excreted through the lungs by exhalation.[57] The half-lives of PFC nanoemulsions within the bloodstream, can be predicted by the size of the material, with larger nanoemulsions rapidly clearing via phagocytosis, and nanoemulsions smaller than 100 nm clearing in about four days.[76] As such, we strive to formulate nanoemulsions between 100-300 nm in size, with good stability over two months. To do this, we utilize a high energy method to form nanoemulsions, simply mixing fluorous solvent, buffer containing solubilized surfactant, and add energy (90 s, 35% amp, 0 °C, Figure 1.3A). [77–79] Common fluorous solvents used to form PFC nanoemulsions are seen in

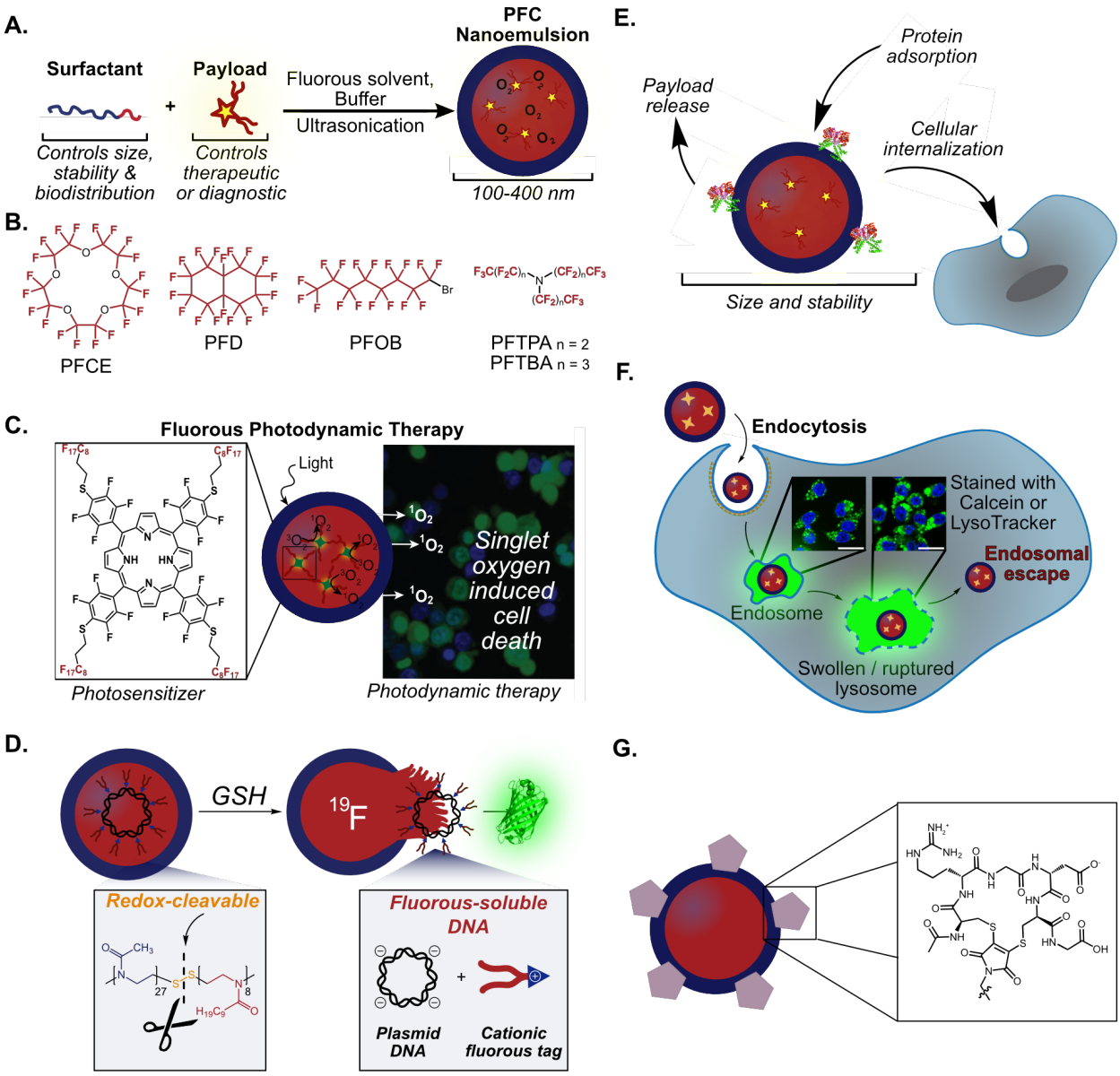

Figure 1.3 PFC nanoemulsions in biology. (A) Schematic of PFC nanoemulsion formation. (B) Commonly used perfluorocarbons in PFC nanoemulsions for ^{19}F-MRI and in the Sletten lab. (C) Incorporation of a photosensitizer in PFC nanoemulsions for therapeutic purposes (Chapter 3). (D) Incorporation of pDNA in PFC nanoemulsions for diagnostic purposes (Chapter 4). (E) Systematic study of the polymer surfactant stabilizing PFC nanoemulsions (Chapter 2). (F) Methods to visualize endosomal rupture (Chapter 5). G) Efforts to target PFC nanoemulsions with cyclic peptides (Chapter 6).

Figure 1.3B, these are FDA approved as ^{19}F-MRI contrast agents or were previously FDA approved in the Fluosol-DA formulation.

We have found that PFC nanoemulsions can be used to deliver oxygen and photosensitizers simultaneously for enhanced photodynamic therapy (Figure 1.3C; Chapter 3),[77,80] small molecule fluorophores,[81–83] and biomacromolecules such as plasmid DNA (Figure 1.3D; Chapter 4),[84] by first solubilizing the payload in the PFC through covalent and non-covalent fluorous tags. We can control the surface chemistry through custom poly(2-oxazoline) surfactants,[78] and can predict the bulk properties of nanoemulsions based on the hydrophilic block length, block identity, and hydrophilic : lipophilic balance of the amphiphilic surfactant (Figure 1.3E; Chapter 2).[79] It is known that PFC nanoemulsions are endocytosed via a clathrin mediated pathway,[68,79] and thus developed methods to directly visualize endosomal rupture (Figure 1.3F; Chapter 5) in the hope that it will lead to useful tools to study the endosomal escape of PFC nanoemulsions. In addition, work is ongoing to add targeting agents to the surface of PFC nanoemulsions (Figure 1.3G; Chapter 6) to better control the biodistribution and uptake of the nanomaterial *in vivo*.

1.2 References and Notes

(1) Ferrari, M. Cancer Nanotechnology: Opportunities and Challenges. *Nat. Rev. Cancer* **2005**, *5*, 161–171.

(2) Shi, J.; Votruba, A. R.; Farokhzad, O. C.; Langer, R. Nanotechnology in Drug Delivery and Tissue Engineering: From Discovery to Applications. *Nano Lett.* **2010**, *10*, 3223–3230.

(3) Kearney, C. J.; Mooney, D. J. Macroscale Delivery Systems for Molecular and Cellular Payloads. *Nat. Mater.* **2013**, *12*, 1004–1017.

(4) Shi, J.; Kantoff, P. W.; Wooster, R.; Farokhzad, O. C. Cancer Nanomedicine: Progress, Challenges and Opportunities. *Nat. Rev. Cancer* **2017**, *17*, 20–37.

(5) Bobo, D.; Robinson, K. J.; Islam, J.; Thurecht, K. J.; Corrie, S. R. Nanoparticle-Based Medicines: A Review of FDA-Approved Materials and Clinical Trials to Date. *Pharm. Res.* **2016**, *33*, 2373–2387.

(6) Biology, C.; Zanganeh, S.; Spitler, R.; Erfanzadeh, M.; Alkilany, A. M.; Mahmoudi, M. Protein Corona : Opportunities and Challenges. *Int. J. Biochem. Cell Biol.* **2016**, *75*, 143–147.

(7) Mahmoudi, M.; Bertrand, N.; Zope, H.; Farokhzad, O. C. Emerging Understanding of the Protein Corona at the Nano-Bio Interfaces. *Nano Today* **2016**, *11*, 817–832.

(8) Tenzer, S.; Docter, D.; Kuharev, J.; Musyanovych, A.; Fetz, V.; Hecht, R.; Schlenk, F.; Fischer, D.; Kiouptsi, K.; Reinhardt, C.; Landfester, K.; Schild, H.; Maskos, M.; Knauer,

S. K.; Stauber, R. H. Rapid Formation of Plasma Protein Corona Critically Affects Nanoparticle Pathophysiology. *Nat. Nanotechnol.* **2013**, *8*, 772–781.

(9) Owens, D. E.; Peppas, N. A. Opsonization, Biodistribution, and Pharmacokinetics of Polymeric Nanoparticles. *Int. J. Pharm.* **2006**, *307*, 93–102.

(10) Pei, D.; Buyanova, M. Overcoming Endosomal Entrapment in Drug Delivery. *Bioconjug. Chem.* **2018**, *30*, 273–283.

(11) Smith, S. A.; Selby, L. I.; Johnston, A. P. R.; Such, G. K. The Endosomal Escape of Nanoparticles: Toward More Efficient Cellular Delivery. *Bioconjug. Chem.* **2019**, *30*, 263–272.

(12) Selby, L. I.; Cortez-Jugo, C. M.; Such, G. K.; Johnston, A. P. R. Nanoescapology: Progress toward Understanding the Endosomal Escape of Polymeric Nanoparticles. *Wiley Interdiscip. Rev. Nanomedicine Nanobiotechnology* **2017**, *9*, e1452.

(13) Nel, A.; Ruoslahti, E.; Meng, H. New Insights into "Permeability" as in the Enhanced Permeability and Retention Effect of Cancer Nanotherapeutics. *ACS Nano* **2017**, *11*, 9567–9569.

(14) Wang, A.; Langer, R. S.; Farokhzad, O. Nanoparticle Delivery of Cancer Drugs. *Annu. Rev. Med.* **2011**, *63*, 85–98.

(15) Stefan Wilhelm, Anthony J. Tavares, Qin Dai, Seiichi Ohta, Julie Audet, H. F. D. and W. C. W. C. Analysis of Nanoparticle Delivery to Tumours. *Nat. Rev. Mater.* **2016**, *1*, 16073.

(16) Chithrani, B. D.; Ghazani, A. A.; Chan, W. C. W. Determining the Size and Shape

Dependence of Gold Nanoparticle Uptake into Mammalian Cells. *Nano Lett.* **2006**, *6*, 662–668.

(17) Albanese, A.; Tang, P. S.; Chan, W. C. W. The Effect of Nanoparticle Size, Shape, and Surface Chemistry on Biological Systems. *Annu. Rev. Biomed. Eng.* **2012**, *14*, 1–16.

(18) Su, G.; Zhou, H.; Mu, Q.; Zhang, Y.; Li, L.; Jiao, P.; Jiang, G.; Yan, B. Effective Surface Charge Density Determines the Electrostatic Attraction between Nanoparticles and Cells. *J. Phys. Chem. C* **2012**, *116*, 4993–4998.

(19) Walkey, C. D.; Olsen, J. B.; Guo, H.; Emili, A.; Chan, W. C. W. Nanoparticle Size and Surface Chemistry Determine Serum Protein Adsorption and Macrophage Uptake. *J. Am. Chem. Soc.* **2012**, *134*, 2139–2147.

(20) Lundqvist, M.; Stigler, J.; Elia, G.; Lynch, I.; Cedervall, T.; Dawson, K. A. Nanoparticle Size and Surface Properties Determine the Protein Corona with Possible Implications for Biological Impacts. *Proc. Natl. Acad. Sci. U. S. A.* **2008**, *105*, 14265–14270.

(21) Wan, J.; Wang, J. H.; Liu, T.; Xie, Z.; Yu, X. F.; Li, W. Surface Chemistry but Not Aspect Ratio Mediates the Biological Toxicity of Gold Nanorods in Vitro and in Vivo. *Sci. Rep.* **2015**, *5*, 11398.

(22) Epa, V. C.; Burden, F. R.; Tassa, C.; Weissleder, R.; Shaw, S.; Winkler, D. A. Modeling Biological Activities of Nanoparticles. *Nano Lett.* **2012**, *12*, 5808–5812.

(23) Rennick, J. J.; Johnston, A. P. R.; Parton, R. G. Key Principles and Methods for Studying the Endocytosis of Biological and Nanoparticle Therapeutics. *Nat. Nanotechnol.* **2021**, *16*,

266–276.

(24) Bai, X.; Liu, F.; Liu, Y.; Li, C.; Wang, S.; Zhou, H.; Wang, W.; Zhu, H.; Winkler, D. A.; Yan, B. Toward a Systematic Exploration of Nano-Bio Interactions. *Toxicol. Appl. Pharmacol.* **2017**, *323*, 66–73.

(25) Beduneau, A.; Ma, Z.; Grotepas, C. B.; Kabanov, A.; Rabinow, B. E.; Gong, N.; Mosley, R. L.; Dou, H.; Boska, M. D.; Gendelman, H. E. Facilitated Monocyte-Macrophage Uptake and Tissue Distribution of Superparmagnetic Iron-Oxide Nanoparticles. *PLoS One* **2009**, *4*, e4343.

(26) Hauck, T. S.; Ghazani, A. A.; Chan, W. C. W. Assessing the Effect of Surface Chemistry on Gold Nanorod Uptake, Toxicity, and Gene Expression in Mammalian Cells. *Small* **2008**, *4*, 153–159.

(27) Bazak, R.; Houri, M.; El Achy, S.; Kamel, S.; Refaat, T. Cancer Active Targeting by Nanoparticles: A Comprehensive Review of Literature. *J. Cancer Res. Clin. Oncol.* **2015**, *141*, 769.

(28) Haute, D. Van; Liu, A. T.; Berlin, J. M. Coating Metal Nanoparticle Surfaces with Small Organic Molecules Can Reduce Nonspecific Cell Uptake. *ACS Nano* **2018**, *12*, 117–127.

(29) Durán, N.; Silveira, C. P.; Durán, M.; Martinez, D. S. T. Silver Nanoparticle Protein Corona and Toxicity: A Mini-Review. *J. Nanobiotechnology* **2015**, *13*, 55–72.

(30) Malik, N.; Wiwattanapatapee, R.; Klopsch, R.; Lorenz, K.; Frey, H.; Weener, J. W.; Meijer, E. W.; Paulus, W.; Duncan, R. Dendrimers: Relationship between Structure and

Biocompatibility in Vitro, and Preliminary Studies on the Biodistribution Of125I-Labelled Polyamidoamine Dendrimers in Vivo. *J. Control. Release* **2000**, *65*, 133–148.

(31) Gustafson, H. H.; Holt-Casper, D.; Grainger, D. W.; Ghandehari, H.; Grainger, D. Nanoparticle Uptake: The Phagocyte Problem. *Nano Today* **2015**, *10*, 487.

(32) Jesse V Jokerst, Tatsiana Lobovkina, Richard N Zare, and S. S. G. Nanoparticle PEGylation for Imaging and Therapy. *Nanomedicine* **2011**, *6*, 715–728.

(33) Xing, H.; Hwang, K.; Lu, Y. Recent Developments of Liposomes as Nanocarriers for Theranostic Applications. *Theranostics* **2016**, *6*, 1336–1352.

(34) Tadros, T. F. *Emulsion Formation and Stability*; 2013.

(35) Jaiswal, M.; Dudhe, R.; Sharma, P. K. Nanoemulsion : An Advanced Mode of Drug Delivery System. *Biotech* **2015**, *5*, 123–127.

(36) Mason, T. G.; Wilking, J. N.; Meleson, K.; Chang, C. B.; Graves, S. M. Nanoemulsions: Formation, Structure, and Physical Properties. *J. Phys. Condens. Matter* **2006**, *18*, R635–R666.

(37) Tadros, T.; Izquierdo, P.; Esquena, J.; Solans, C. Formation and Stability of Nano-Emulsions. *Adv. Colloid Interface Sci.* **2004**, *108–109*, 303–318.

(38) Gupta, A.; Eral, H. B.; Hatton, T. A.; Doyle, P. S. Nanoemulsions: Formation, Properties and Applications. *Soft Matter* **2016**, *12*, 2826–2841.

(39) Levin, Aviad; Mason, Thomas O.; Adler-Abramovich, Lihi; Buell, Alexander K.; Meisl, George; Galvagnion, Celine; Bram, Yaron; Stratford, Samuel A.; Dobson, Christopher M.;

Knowles, Tuomas P. J.; Gazit, E. Ostwald's Rule of Stages Governs Structural Transitions and Morphology of Dipeptide Supramolecular Polymers. *Nat. Commun.* **2014**, *5*, 5219.

(40) Singh, Y.; Meher, J. G.; Raval, K.; Khan, F. A.; Chaurasia, M.; Jain, N. K.; Chourasia, M. K. Nanoemulsion: Concepts, Development and Applications in Drug Delivery. *J. Control. Release* **2017**, *252*, 28–49.

(41) Rahn-Chique, K.; Puertas, A. M.; Romero-Cano, M. S.; Rojas, C.; Urbina-Villalba, G. Nanoemulsion Stability: Experimental Evaluation of the Flocculation Rate from Turbidity Measurements. *Adv. Colloid Interface Sci.* **2012**, *178*, 1–20.

(42) Delmas, T.; Piraux, H.; Couffin, A. C.; Texier, I.; Vinet, F.; Poulin, P.; Cates, M. E.; Bibette, J. How to Prepare and Stabilize Very Small Nanoemulsions. *Langmuir* **2011**, *27*, 1683–1692.

(43) Ganta, S.; Talekar, M.; Singh, A.; Coleman, T. P.; Amiji, M. M. Nanoemulsions in Translational Research - Opportunities and Challenges in Targeted Cancer Therapy. *AAPS PharmSciTech* **2014**, *15*, 694–708.

(44) Silva, H. D.; Cerqueira, M. Â.; Vicente, A. A. Nanoemulsions for Food Applications: Development and Characterization. *Food Bioprocess Technol.* **2012**, *5*, 854–867.

(45) Sonneville-Aubron, O.; Simonnet, J.-T.; L'Alloret, F. Nanoemulsions: A New Vehicle for Skincare Products. *Adv. Colloid Interface Sci.* **2004**, *108–109*, 145–149.

(46) Aboalnaja, K. O.; Yaghmoor, S.; Kumosani, T. A.; McClements, D. J. Utilization of Nanoemulsions to Enhance Bioactivity of Pharmaceuticals, Supplements, and

Nutraceuticals: Nanoemulsion Delivery Systems and Nanoemulsion Excipient Systems. *Expert Opin. Drug Deliv.* **2016**, *13*, 1327–1336.

(47) Pathak, K.; Pattnaik, S.; Swain, K. Application of Nanoemulsions in Drug Delivery. In *Nanoemulsions: Formulation, Applications, and Characterization*; 2018; pp 415–433.

(48) Ahmed, K.; Li, Y.; McClements, D. J.; Xiao, H. Nanoemulsion- and Emulsion-Based Delivery Systems for Curcumin: Encapsulation and Release Properties. *Food Chem.* **2012**, *132*, 799–807.

(49) Qian, C.; Decker, E. A.; Xiao, H.; McClements, D. J. Nanoemulsion Delivery Systems: Influence of Carrier Oil on β-Carotene Bioaccessibility. *Food Chem.* **2012**, *135*, 1440–1447.

(50) Hörmann, K.; Zimmer, A. Drug Delivery and Drug Targeting with Parenteral Lipid Nanoemulsions - A Review. *J. Control. Release* **2016**, *223*, 85–98.

(51) Takino, T.; Konishi, K.; Takakura, Y.; Hashida, M. Long Circulating Emulsion Carrier Systems for Highly Lipophilic Drugs. *Biol. Pharm. Bull.* **1994**, *17*, 121–125.

(52) Riess, J. G. Understanding the Fundamentals of Perfluorocarbons and Perfluorocarbon Emulsions Relevant to in Vivo Oxygen Delivery. *Artif. Cells. Blood Substit. Immobil. Biotechnol.* **2005**, *33*, 47–63.

(53) Krafft, M. P.; Riess, J. G. Selected Physicochemical Aspects of Poly- and Perfluoroalkylated Substances Relevant to Performance, Environment and Sustainability-Part One. *Chemosphere* **2015**, *129*, 4–19.

(54) Gladysz, J. A.; Jurisch, M. *Structural, Physical, and Chemical Properties of Fluorous Compounds*; 2012; Vol. 308.

(55) Marsh, E. N. G. Fluorinated Proteins: From Design and Synthesis to Structure and Stability. *Acc. Chem. Res.* **2014**, *47*, 2878–2886.

(56) Riess, J. G.; Riess, J. G. Oxygen Carriers ("blood Substitutes") - Raison d'etre, Chemistry, and Some Physiology. *Chem. Rev.* **2001**, *101*, 2797–2919.

(57) Krafft, M; Riess, J. Perfluorocarbons: Life Sciences and Biomedical Uses. *J. Polym. Sci. Part A Polym. Chem.* **2007**, *45*, 1185–1198.

(58) Fraker, C. A.; Mendez, A. J.; Stabler, C. L. Complementary Methods for the Determination of Dissolved Oxygen Content in Perfluorocarbon Emulsions and Other Solutions. *J. Phys. Chem. B* **2011**, *115*, 10547–10552.

(59) Krafft, M. P. Alleviating Tumor Hypoxia with Perfluorocarbon-Based Oxygen Carriers. *Curr. Opin. Pharmacol.* **2020**, *53*, 117–125.

(60) Krafft, M. P. *The Curious World of Fluorinated Molecules*; 2020.

(61) Gould, S. A.; Rosen, A. L.; Sehgal, L. R.; Sehgal, H. L.; Langdale, L. A.; Krause, L. M.; Rice, C. L.; Chamberlin, W. H.; Moss, G. S. Fluosol-DA as a Red-Cell Substitute in Acute Anemia. *N. Engl. J. Med.* **1986**, *314*, 1653–1656.

(62) Spence, R K; Norcross, E D; Costabile, Joseph; Mccoy, Sue; Cernaianu, Aurel C; Alexander, James B; Pello, Mark J; Atabek, Umur; Camishion, Rudolph C; Norcross, E D; Costabile, Joseph; Mccoy, S.; Aurel, C. Perfluorocarbons as Blood Substitutes : The

Early Years : Experience with Fluosol DA-20 % in The. *Artif. Cells, Blood Substitutes, Biotechnol.* **1994**, *22*, 955–963.

(63) Tirotta, I.; Dichiarante, V.; Pigliacelli, C.; Cavallo, G.; Terraneo, G.; Bombelli, F. B.; Metrangolo, P.; Resnati, G. 19F Magnetic Resonance Imaging (MRI): From Design of Materials to Clinical Applications. *Chem. Rev.* **2015**, *115*, 1106–1129.

(64) Janjic, J.; Ahrens, E. Fluorine Containing Nanoemulsions for MRI Cell Tracking. *Wiley Interdiscip. Rev. Nanomedicine Nanobiotechnology* **2009**, *1*, 492–501.

(65) Tirotta, I.; Mastropietro, A.; Cordiglieri, C.; Gazzera, L.; Baggi, F.; Baselli, G.; Grazia Bruzzone, M.; Zucca, I.; Cavallo, G.; Terraneo, G.; Baldelli Bombelli, F.; Metrangolo, P.; Resnati, G. A Superfluorinated Molecular Probe for Highly Sensitive in Vivo 19F-MRI. *J. Am. Chem. Soc.* **2014**, *136*, 8524–8527.

(66) Tran, T. D.; Caruthers, S. D.; Hughes, M.; Marsh, J. N.; Cyrus, T.; Winter, P. M.; Neubauer, A. M.; Wickline, S. A.; Lanza, G. M. Clinical Applications of Perfluorocarbon Nanoparticles for Molecular Imaging and Targeted Therapeutics. *Int. J. Nanomedicine* **2007**, *2*, 515–526.

(67) Rapoport, N.; Nam, K. H.; Gupta, R.; Gao, Z.; Mohan, P.; Payne, A.; Todd, N.; Liu, X.; Kim, T.; Shea, J.; Scaife, C.; Parker, D. L.; Jeong, E. K.; Kennedy, A. M. Ultrasound-Mediated Tumor Imaging and Nanotherapy Using Drug Loaded, Block Copolymer Stabilized Perfluorocarbon Nanoemulsions. *J. Control. Release* **2011**, *153*, 4–15.

(68) Patrick, M. J.; Janjic, J. M.; Teng, H.; Hear, M. R. O.; Brown, C. W.; Stokum, J. A.; Schmidt, B. F.; Ahrens, E. T.; Waggoner, A. S. Intracellular PH Measurements Using

Perfluorocarbon Nanoemulsions. *J. Am. Chem. Soc.* **2013**, *135*, 18445–18457.

(69) O'Hagan, D.; Harper, D. B. Fluorine-Containing Natural Products. *J. Fluor. Chem.* **1999**, *100*, 127–133.

(70) Carvalho, M. F.; Oliveira, R. S. Natural Production of Fluorinated Compounds and Biotechnological Prospects of the Fluorinase Enzyme. *Crit. Rev. Biotechnol.* **2017**, *37*, 880–897.

(71) Laukemper-Ostendorf, S.; Scholz, A.; Buandrger, K.; Heussel, C. P.; Schmittner, M.; Weiler, N.; Markstaller, K.; Eberle, B.; Kauczor, H. U.; Quintel, M.; Thelen, M.; Schreiber, W. G. 19F-MRI of Perflubron for Measurement of Oxygen Partial Pressure in Porcine Lungs during Partial Liquid Ventilation. *Magn. Reson. Med.* **2002**, *47*, 82–89.

(72) Shukla, H. P.; Mason, R. P.; Bansal, N.; Antich, P. P. Regional Myocardial Oxygen Tension: 19F MRI of Sequestered Perfluorocarbon. *Magn. Reson. Med.* **1996**, *35*, 827–833.

(73) Ratner, A. V.; Muller, H. H.; Bradley-Simpson, B.; Hirst, D.; Pitts, W.; Young, S. W. Detection of Acute Radiation Damage to the Spleen in Mice by Using Fluorine-19 MR Imaging. *Am. J. Roentgenol.* **1988**, *151*, 477–480.

(74) Morawski, A. M.; Winter, P. M.; Yu, X.; Fuhrhop, R. W.; Scott, M. J.; Hockett, F.; Robertson, J. D.; Gaffney, P. J.; Lanza, G. M.; Wickline, S. A. Quantitative "Magnetic Resonance Immunohistochemistry" with Ligand-Targeted 19F Nanoparticles. *Magn. Reson. Med.* **2004**, *52*, 1255–1262.

(75) Ahrens, E. T.; Flores, R.; Xu, H.; Morel, P. A. In Vivo Imaging Platform for Tracking Immunotherapeutic Cells. *Nat. Biotechnol.* **2005**, *23*, 983–987.

(76) Maiti; Bidinger. Solubility and Transport Phenomena in Perfluorochemicals Relevant to Blood Substitution and Other Biomedical Applications. *Pure Appl. Chem.* **1982**, *54*, 2383–2406.

(77) Day, R. A.; Estabrook, D. A.; Logan, J. K.; Sletten, E. M. Fluorous Photosensitizers Enhance Photodynamic Therapy with Perfluorocarbon Nanoemulsions. *Chem. Commun.* **2017**, *53*, 13043–13046.

(78) Estabrook, D. A.; Ennis, A. F.; Day, R. A.; Sletten, E. M. Controlling Nanoemulsion Surface Chemistry with Poly(2-Oxazoline) Amphiphiles. *Chem. Sci.* **2019**, *10*, 3994–4003.

(79) Day, R. A.; Estabrook, D.; Wu, C.; Chapman, J. O.; Togle, A. J.; Sletten, E. M. Systematic Study of Perfluorocarbon Nanoemulsions Stabilized by Polymer Amphiphiles. *ACS Appl. Mater. Interfaces* **2020**, *12*, 38887–38898.

(80) Miller, M. A.; Sletten, E. M. A General Approach to Biocompatible Branched Fluorous Tags for Increased Solubility in Perfluorocarbon Solvents. *Org. Lett.* **2018**, *20*, 6850–6854.

(81) Sletten, E. M.; Swager, T. M. Fluorofluorophores: Fluorescent Fluorous Chemical Tools Spanning the Visible Spectrum. *J. Am. Chem. Soc.* **2014**, *136*, 13574–13577.

(82) Miller, M. A.; Day, R. A.; Estabrook, D. A.; Sletten, E. M. A Reduction-Sensitive

Fluorous Fluorogenic Coumarin. *Synlett* **2020**, *31*, 450–454.

(83) Lim, I.; Vian, A.; van de Wouw, H.; Day, R. A.; Gomez, C.; Liu, Y.; Rheingold, A. L.; Campas, O.; Sletten, E. M. Fluorous Soluble Cyanine Dyes for Visualizing Perfluorocarbons in Living Systems. *J. Am. Chem. Soc.* **2020**, *142*, 16072–16081.

(84) Estabrook, A. D. A.; Day, R. A.; Sletten, E. M. Redox-Responsive Gene Delivery from Perfluorocarbon Nanoemulsions through Cleavable Poly(2-Oxazoline) Surfactants. *Angew. Chemie Int. Ed.* **2021**. DOI: 10.1002/ange.202102413

CHAPTER TWO

Systematic study of perfluorocarbon nanoemulsions stabilized by polymer amphiphiles

Adapted from: Rachael A. Day, Daniel A. Estabrook, Carolyn Wu, John O. Chapman, Alyssa J. Togle, and Ellen M. Sletten.* Systematic study of perfluorocarbon nanoemulsions stabilized by polymer amphiphiles. *ACS Appl. Mat. Interfaces* **2020**, *12*, 38887-38898.

DOI: 10.1021/acsami.0c07206

2.1 Abstract

Perfluorocarbon (PFC) nanoemulsions, droplets of fluorous solvent stabilized by surfactants dispersed in water, are simple yet versatile nanomaterials. The orthogonal nature of the fluorous phase promotes the formation of nanoemulsions through a simple, self-assembly process while simultaneously encapsulating fluorous-tagged payloads for various applications. The size, stability, and surface chemistry of PFC nanoemulsions are controlled by the surfactant. Here, we systematically study the effect of the hydrophilic portion of polymer surfactants on PFC nanoemulsions. We find that the hydrophilic block length and identity, the overall polymer hydrophilic/lipophilic balance, and the polymer architecture are all important factors. The ability to modulate these parameters enables control over initial size, stability, payload retention, cellular internalization, and protein adsorption of PFC nanoemulsions. With the insight obtained from this systematic study of polymer amphiphiles stabilizing PFC nanoemulsions, design features required for the optimal material are obtained.

2.2 Introduction

Nanomaterials have been extensively studied for use as drug delivery vehicles due to their ability to transport insoluble cargoes, protect sensitive therapeutics, increase circulation times and allow for targeted delivery and release.[1,2] Numerous nanomaterial scaffolds have been developed, ranging from hard inorganic particles to soft materials.[3] Despite decades of work on nano delivery vehicles, several challenges remain in this field including 1) protein corona formation impeding targeted molecular recognition, 2) difficulties regulating cellular internalization, and 3) imprecise payload delivery.[4–6] Systematic studies of sub-classes of nanomaterials have provided insight into these challenges[7–12] and have revealed that the core nanomaterial structure significantly influences the interactions of the nanomaterials with biomolecules.[7,13–15] Thus, for each new class of nanomaterial a thorough investigation of structure—property relationships is required.

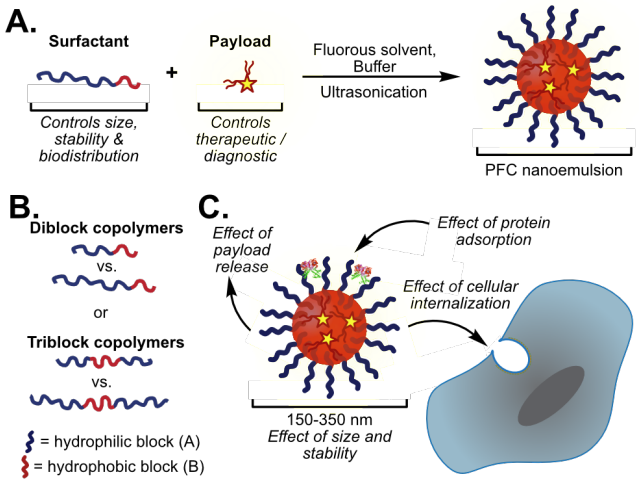

Figure 2.1 (A) One step formulation of PFC nanoemulsions stabilized by polymer surfactants containing fluorous soluble payloads. (B) Polymer amphiphile block length and architecture dictate properties. (C) Surfactants dictate the size, stability, protein adsorption and route of cellular endocytosis of PFC nanoemulsions.

To date, soft nanomaterials such as liposomes, polymer micelles and emulsions have had the most success regarding clinical translation.[16,17] These nanomaterials all rely on self-assembly of amphiphiles, with liposomes and polymer micelles being solely composed of the amphiphiles, while emulsions contain an oil phase that is stabilized by the amphiphiles (*i.e.* surfactants) in water. Nanoemulsions are kinetically stable and large amounts of cargo can be loaded into them, giving nanoemulsions advantages over liposomes and micelles that are prone to disassembly at low concentrations.[18,19] However, applications of emulsions in controlled drug delivery have been hindered by leakage of therapeutics from the emulsion core to surrounding hydrophobic environments.[20,21] We aim to overcome this limitation of nanoemulsions by employing an oil phase composed of bioorthogonal perfluorocarbons rather than traditional hydrocarbon oils. Using this approach, payloads can be localized in perfluorocarbon (PFC) nanoemulsions through the use of fluorous tags (Figure 2.1A). The matched solubility of fluorous solubilized payloads in PFC nanoemulsions decreases the leaching of the payloads significantly when compared to traditional hydrophobic analogs,[22] allowing the advantageous stability and high cargo loadings characteristic of emulsions to be capitalized upon.

Perfluorocarbons, molecules in which all C—H bonds have been replaced with C—F bonds, have unique properties. They phase separate from aqueous and organic solutions to form a dense fluorous phase.[23] The fluorous phase has high gas solubility which led to the first biomedical application of PFC nanoemulsions as blood substitutes, where Pluronic polymer amphiphiles were employed as surfactants to stabilize the perfluorocarbon in water.[24,25] In the decades since, PFC nanoemulsions have been used for ^{19}F-MRI,[26–28] as ultrasound contrast agents,[29,30] and intracellular sensors,[31] with both small molecule and polymeric surfactants stabilizing the droplets. Research has shown that PFC nanoemulsions are endocytosed by cells,[32,33] and the surfactant can dictate the

mechanism of endocytosis.[34] However, a systematic study of the effect of the amphiphile on PFC nanoemulsion stability, payload retention, protein corona formation and cellular internalization has yet to be performed. This knowledge is essential to advance the utility of PFC nanoemulsions as therapeutic and diagnostic nanocarriers.

Previously, we have investigated poly(2-oxazoline) (POx) amphiphiles as surfactants for PFC nanoemulsions rather than the Pluronic surfactants that were originally employed for oxygen delivery.[35] Our interest in poly(2-oxazoline)s stems from their controlled ring opening polymerization, ease of functionalization through incorporation of co-monomers or end-capping, and commercially available monomer starting materials. POx polymers have been utilized in protein polymer conjugates, grafted onto liposomal bilayers, formulated into micelles, applied to surfaces and are validated alternatives to poly(ethylene glycol) (PEG).[36,37] PEGylation has been widely successful at lengthening serum half-lives and minimizing protein coronas; however, its extensive use has led to immunogenicity concerns. Thus, in the next iteration of nanomaterials, alternatives to PEG (and Pluronics) are desireable.[36] In our initial work exploring poly(2-oxazoline) surfactants for nanoemulsions, we focused on variations in the hydrophobic portion of POx amphiphiles and found that poly(2-nonyl-2-oxazoline) outperformed either poly(2-propyl-2-oxazoline) or a fluorous-containing oxazoline.[38] Here, we systematically look at the role of the hydrophilic block in custom polymeric amphiphiles and readily available commercial PEG-containing surfactants for their ability to stabilize PFC nanoemulsions over time (Figure 2.1B). Subsequently, we analyze their effect on payload retention, protein corona formation, and cellular internalization (Figure 2.1C).

2.3 Results and Discussion

2.3.1 Synthesis and PFC nanoemulsion formulation

We synthesized a library of di-block and tri-block amphiphiles inspired by commercial Pluronic and Zonyl surfactants (**2.1-2.4**; Figure 2.2A). Both diblock and triblock copolymers stabilize the water-PFC interface; however, their mechanisms differ with the diblock surfactants having the hydrophobic block extended into the oil phase whereas the triblock surfactants create a U shape with the majority of the hydrophobic block positioned at the interface.[38–40] In both cases, the hydrophilic block extends out into the aqueous media, thus dictating the surface properties and ultimately contributing to the biodistribution of the PFC nanoemulsions. Notably, in previous works, we found distinct differences in nanoemulsion stability when the repeating unit of the polymer was altered or when the architecture of the surfactants was changed from diblock to triblock.[38] These results prompted the inclusion of different amphiphile structures and architectures in this study.

POx polymers were synthesized via microwave-assisted cationic ring-opening polymerizations[41] employing methyl triflate as the initiator and quenching with water (Scheme 2.1A). Due to the living nature of the polymerization, the block lengths can be finely tuned by adjusting the initiator to monomer ratio.[42] The block lengths have been rounded for simplicity, with exact block lengths in the NMRs reported in the original publication.[43] The polymer amphiphiles were synthesized in either an AB (**2.5**–**2.8**, **2.11**–**2.13**) or ABA (**2.9**–**2.10**) fashion, where A was either poly(2-methyl-2-oxazoline) (P(MeOx)) (**2.5**–**2.10**) or poly(2-ethyl-2-oxazoline) (P(EtOx)) (**2.11**–**2.13**), as both these polymers have been utilized as PEG replacements. The B block is the hydrophobic poly(2-nonyl-2-oxazoline) (P(NonOx)) (Figure 2.2B), which was chosen based on our previous studies.[38]

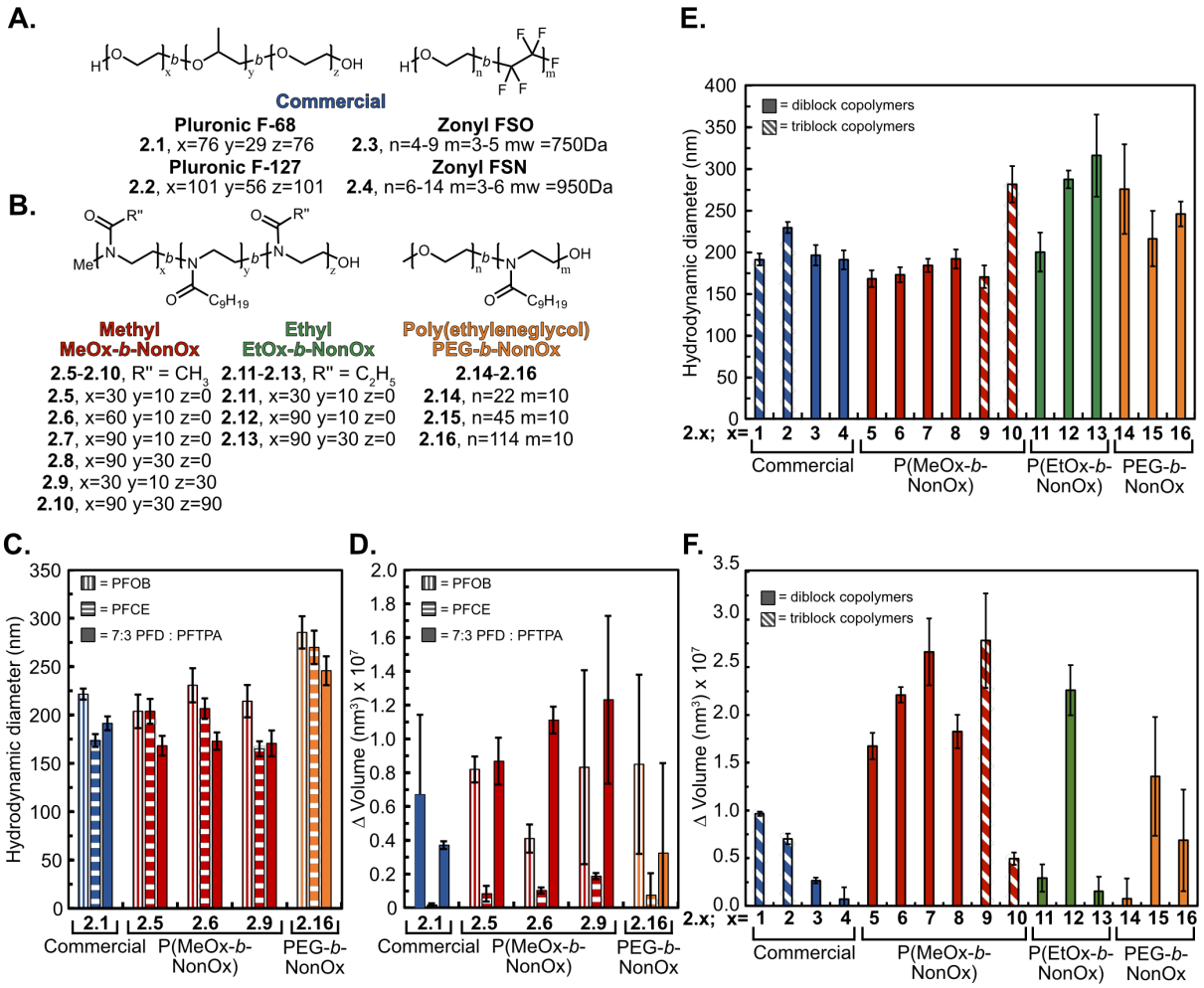

Figure 2.2 (A/B) Library of amphiphilic di- and triblock copolymers. Commercial (blue), P(MeOx) (red), P(EtOx) (green) and PEG-NonOx (orange) (**2.1**–**2.16**). (C) Initial size distribution of PFC nanoemulsions containing differing fluorous solvents (perfluorooctyl bromide (PFOB), vertical stripes; perfluoro-15-crown-5-ether (PFCE), horizontal stripes; 7:3 perfluorodecalin:perfluorotripropylamine, (PFD:PFTPA), solid) stabilized by **2.1** (PF68), **2.5** ($P(MeOx_{30}$-*b*-$NonOx_{10})$), **2.6** ($P(MeOx_{60}$-*b*-$NonOx_{10})$), **2.9** ($P(MeOx_{30}$-*b*-$NonOx_{10}$-*b*-$MeOx_{30})$), **2.16** (PEG_{5K}-*b*-$NonOx_{10}$). (D) Change in volume over 14 days of PFC nanoemulsions shown in C. (E) Initial size distributions of amphiphile stabilized 7:3 PFD:PFTPA PFC nanoemulsions. Nanoemulsions were prepared by sonication of a solution of 2.8 wt% surfactant with 10 vol% 7:3 PFD:PFTPA in phosphate buffered saline (PBS). Emulsions were diluted 1:1000 in deionized water prior to measurements by dynamic light scattering (DLS). Data represents the average of three independent samples, error bars represent the product of the dispersity and the z-average. (F) Change in volume over 30 days of emulsions shown in E. Data represents the average of three independent samples, error bars represent the standard deviation of three independent samples.

Scheme 2.1. Synthetic scheme for POx containing amphiphiles.
Polymers were synthesized by Daniel Estabrook. Detailed polymer synthesis and characterization can be found in *ACS Appl. Mat. Interfaces* **2020**, *12*, 38887-38898.

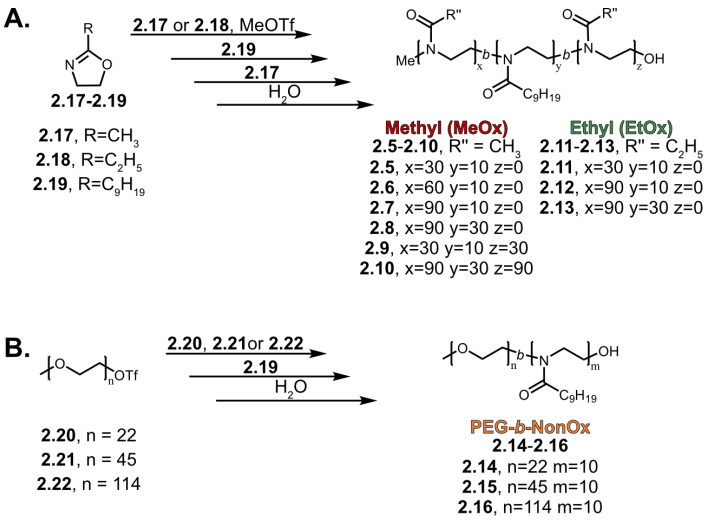

Hybrid amphiphiles **2.14–2.16** were also prepared with PEG as the hydrophilic block and P(NonOx) as the hydrophobic block by initiating P(NonOx) synthesis directly from the PEG chain (Scheme 2.1B).

Polymers **2.14**–**2.16** were prepared to aid in comparisons between the synthetic POx polymers (12 total) and four commercial polymers containing PEG A blocks: Pluronic F-68, Pluronic F-127, Zonyl FSO and Zonyl FSN (**2.1**–**2.4**). The Pluronics were chosen due to their previous success as FDA approved surfactants for PFC nanoemulsions.[44] The Zonyl surfactants were investigated as an alternative commercial PEG-containing block copolymers that have previously been employed for PFC formation. [45,46] It should be noted that the Zonyl surfactants have a fluorous B block and significantly shorter PEG A blocks than other amphiphiles in this study.

2.3.2 Size and Stability

To study the size and stability of perfluorocarbon nanoemulsions stabilized by the synthetic and commercial amphiphiles, the optimal concentration of polymer was investigated for select surfactants. Polymer surfactant, ranging from 28 mg/mL (2.8 wt%) to 3.5 mg/mL (0.35 wt%) were dissolved in water, added to fluorous solvent (7:3 perfluorodecalin (PFD) : perfluorotripropylamine (PFTPA)) (20 μL, 10 vol%) and sonicated (90s, 35% amp) to form nanoemulsions (Figure 2.3). The size and polydispersity (PDI) were analyzed via dynamic light scattering (DLS). In most cases, emulsions containing 28 mg/mL polymer were smaller and had lower dispersities, showing that more uniform droplets were obtained.

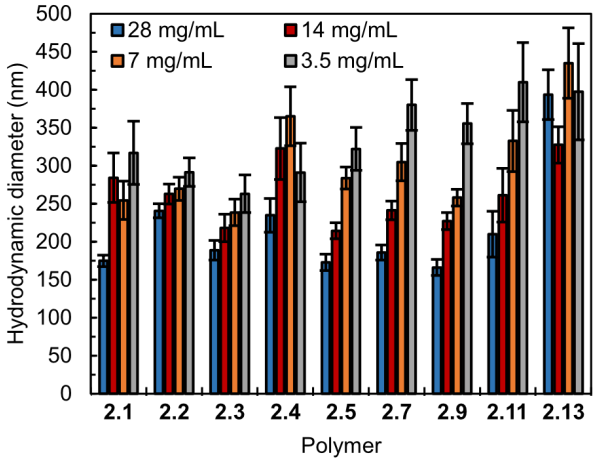

Figure 2.3. Size and dispersity of PFC nanoemulsions formed with various concentrations (blue, 28 mg/mL; red, 14 mg/mL; orange, 7 mg/mL; gray, 3.5 mg/mL) of polymer surfactants **2.1** (PF68)**, 2.2** (PF127), **2.3** (Zonyl FSO), **2.4** (Zonyl FSN), **2.5** [P(MeOx$_{30}$-*b*-NonOx$_{10}$)], **2.7** [P(MeOx$_{90}$-*b*-NonOx$_{10}$)], **2.9** [P(MeOx$_{30}$-*b*-NonOx$_{10}$-*b*-MeOx$_{30}$)], **2.11** [P(EtOx$_{30}$-*b*-NonOx$_{10}$)], **2.13** [P(EtOx$_{90}$-*b*-NonOx$_{10}$)]. Bars represent the average of three samples. Error bars represent the product of the Z-average and the PDI.

With this knowledge in hand, emulsions stabilized by select surfactants were prepared utilizing perfluorooctyl bromide (PFOB), perfluoro-15-crown-5-ether (PFCE) or 7:3 PFD: PFTPA as the fluorous phase (Figure 2.2C/D). PFOB and PFCE are commonly employed for ^{19}F MRI,[26,27] while 7:3 PFD:PFTPA represents the mixture that was FDA approved for oxygen delivery.[47] The size and stability data are grouped by surfactant type: commercial (blue), P(MeOx) (red), P(EtOx) (green), PEG$_n$-*b*-NonOx$_{10}$ (orange). From the data in Figure 2.2C/D, it is clear that the initial size and stability of PFC nanoemulsions are dependent on both the polymer amphiphiles and molecular structure of the perfluorocarbon. These results are consistent with those recently published by Mecozzi and coworkers[48] demonstrating that the use of PFCE as the oil phase results in more stable emulsions than those formed from PFD, and emulsions composed of PFOB experience similar levels of Ostwald ripening across all polymer amphiphiles. To study the effect of the polymer amphiphiles, we employed 7:3 perfluorodecalin (PFD): perfluorotripropylamine (PFTPA) as this mixture displayed the largest differences between each surfactant in both the size and stability.

Nanoemulsions were then formulated with the panel of surfactants (**2.1**–**2.16**) at a concentration of 28 mg/mL (2.8 wt%). The hydrodynamic diameter was monitored immediately after formation (Figure 2.2E), and subsequently, for 30 days (Figure 2.2F). To minimize micelle formation, all P(MeOx) and P(EtOx) containing polymers (**2.5**–**2.13**) were first dissolved in dimethylformamide (DMF) before dilution with water and addition of fluorous solvent. The PEG$_n$-*b*-NonOx$_{10}$ (**2.14**–**2.16**) were first dissolved in DMF, tetrahydrofuran (THF) and methanol (MeOH) respectively to fully solubilize the polymer.

The size and stability data are grouped by surfactant type, in addition, the diblock copolymers (solid) are differentiated from the triblock copolymers (diagonal stripes). The stability data in Figure 2.2F is represented by change in volume of the droplets over 30 days and raw data can be

found in Figure 2.4. The main pathway for destabilization of PFC nanoemulsions is Ostwald ripening, defined as a gradual increase in size over time as the solvent in the smallest droplets migrates to the larger droplets.[18] Factors that affect Ostwald ripening are sample polydispersity, concentration, presence of micelles, and identity of the perfluorocarbon.[48,49]

A universal trend observed in all polymers tested was the longer the hydrophilic block, the larger the droplets were on day zero. Looking at the commercial PEG containing polymers, we found that they all stabilize emulsions of similar size yet have varied stability over 30 days. Pluronic F-68 (**2.1**), which was employed in the original FDA-approved blood substitute formulation, has the worst stability of the four commercial amphiphiles tested, with the diblock fluorosurfactant Zonyl FSN (**2.4**) displaying the best stability. This could be due to the relative lipophilicities of the B block within the Pluronic and Zonyl surfactants. The B block of the Pluronic series is poly(propylene oxide) which is insoluble in water, with limited solubility in perfluorocarbon oils resulting in rejection anchoring to the fluorous solvent in contrast to the Zonyl surfactants containing a fluorous B block.[50] The Pluronic F-68 (**2.1**) nanoemulsions represent a good stability metric, as one of the reasons the FDA-approved formulation was removed from the market was inconsistencies in the formulation due to low stability.[44,51] Over 30 days, the Pluronic F-68 (**2.1**) emulsions increased in volume $1x10^7$ nm^3, with the other commercial surfactants (**2.2**–**2.4**), the P(MeOx) tri-block (**2.10)**, P(EtOx) (**2.11**, **2.13**) and PEG-*b*-NonOx (**2.14**, **2.16**) displaying similar or superior stability.

For the P(MeOx) series (**2.5**–**2.7**), as the hydrophilic block increased, there was an apparent decrease in stability over 30 days when the P(NonOx) block was kept constant at approximately 10 repeat units (volume increase of $1.7x10^7$, $2.2x10^7$, $2.7x10^7$ nm^3). When the P(NonOx) block

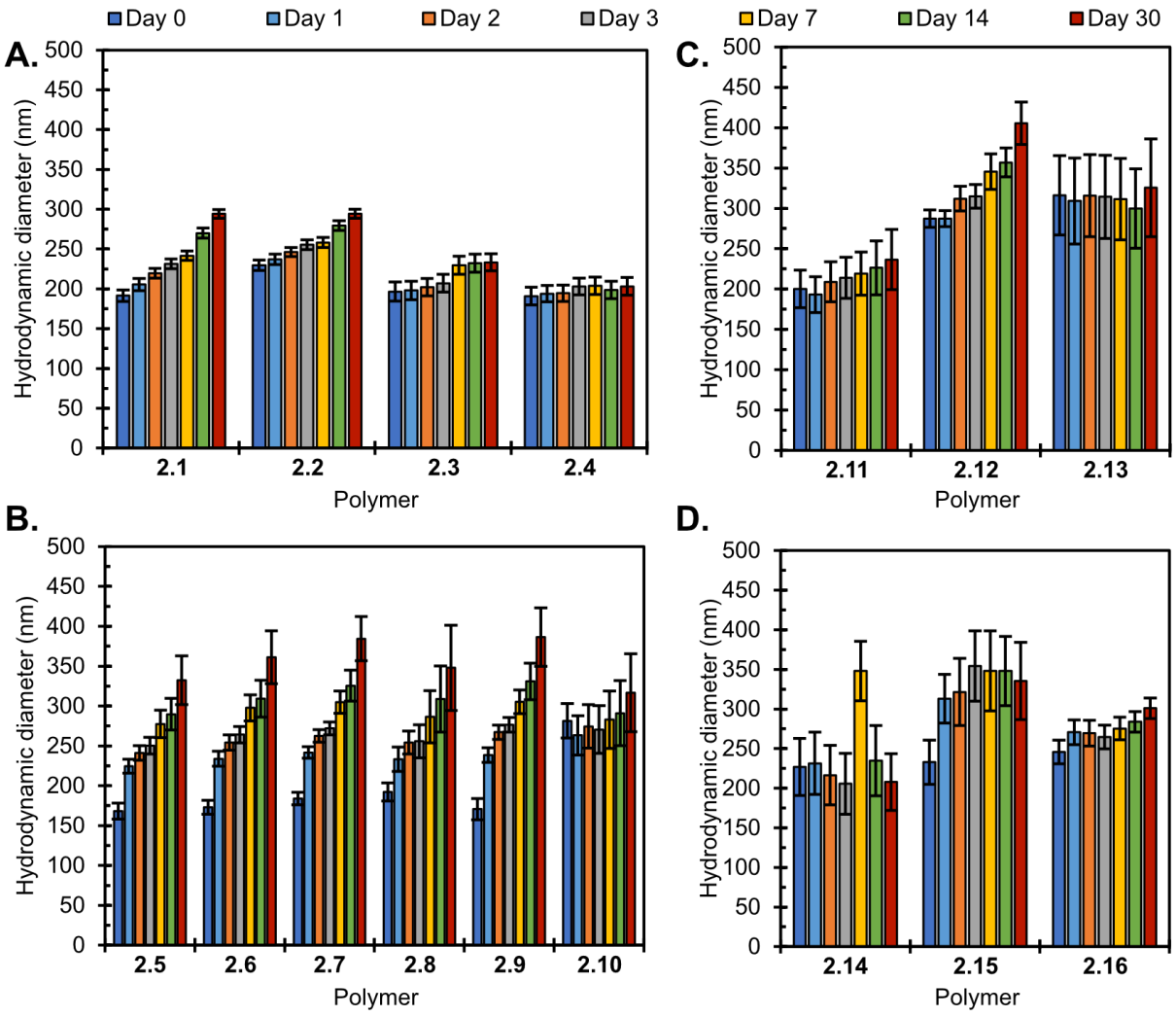

Figure 2.4. Stability of PFC nanoemulsions stabilized by polymer surfactants **2.1–2.16** over 30 days. Size was measured on day 0 (dark blue), day 1 (light blue), day 2 (orange), day 3 (gray), day 7 (yellow), day 14 (green), and day 30 (red). Bars represent the average of three samples and error bars represent the product of the Z-average and the PDI.

was lengthened to approximately 30 repeat units, we found that P(MeOx$_{90}$-*b*-NonOx$_{30}$) (**2.8**) has similar stability to P(MeOx$_{30}$-*b*-NonOx$_{10}$) (**2.5**), suggesting that for diblock surfactants the overall hydrophilic: lipophilic balance (HLB) is a critical metric (Figure 2.5). Notably, the triblock ABA surfactants: P(MeOx$_{30}$-*b*-NonOx$_{10}$-*b*-MeOx$_{30}$) (**2.9**) and P(MeOx$_{90}$-*b*-NonOx$_{30}$-*b*-MeOx$_{90}$) (**2.10**) which have the same HLB do not behave similarly, with **2.9** giving a smaller initial size but showing significant Ostwald ripening over 30 days ($2.8x10^7$ nm^3 increase), while **2.10** displays excellent stability ($0.5x10^7$ nm^3 increase). We attribute the 30 day stability difference between **2.9** and **2.10** to the larger A blocks favoring the steric stabilization method of triblock copolymers.[40,50] Of the P(MeOx) polymers, P(MeOx$_{30}$-*b*-NonOx$_{10}$) (**2.5**) diblock and the P(MeOx$_{90}$-*b*-NonOx$_{30}$-*b*-MeOx$_{90}$) (**2.10**) triblock amphiphiles are the most promising if stability is desired.

The P(EtOx) series displays similar trends of initial size increasing as the A block is lengthened. The P(MeOx) stability trends can be applied to the P(EtOx) series in which P(EtOx$_{30}$-*b*-NonOx$_{10}$) (**2.11**) and P(EtOx$_{90}$-*b*-NonOx$_{30}$) (**2.13**) diblock copolymers have equivalent HLB, and similar stabilities ($0.3x10^7$ vs $0.15x10^7$ nm^3 change in volume). These two P(EtOx) amphiphiles displayed superior overall stability to the P(MeOx) amphiphiles, showing that both P(MeOx) and P(EtOx) are viable monomers for amphiphiles to stabilize PFC nanoemulsions. Both HLB and overall amphiphile structure are important parameters.

Finally, looking at the use of PEG as the hydrophilic block and P(NonOx) as the hydrophobic block (**2.14**–**2.16**), we observe similar sized nanoemulsions with variable stability. The shortest PEG chain with 22 repeat units as the A block (**2.14**) led to the most stable emulsions over time, with all PEG$_x$-*b*-NonOx$_{10}$ stabilized emulsions (**2.14**–**2.16**) displaying superior or equivalent stability compared to the commercial PEG-containing surfactants.

A.

Polymer	Hydrophilic lipophilic balance (HLB)	Δ Volume (30 day)	Leaching % (14 day)
2.1	16.0	9.7	6.1
2.2	14.1	7.0	3.1
2.3	3.4	2.7	59.3
2.4	2.1	0.7	43.3
2.5	11.3	16.8	14.1
2.6	14.4	21.9	11.9
2.7	15.9	26.6	15.4
2.8	11.3	18.4	14.5
2.9	14.4	27.8	12.4
2.10	14.4	4.9	20.8
2.11	12.0	1.6	71.9
2.12	15.0	2.7	56.1
2.13	12.0	1.5	67.2
2.14	6.7	0.8	78.0
2.15	10.1	13.6	67.4
2.16	14.3	6.9	35.0

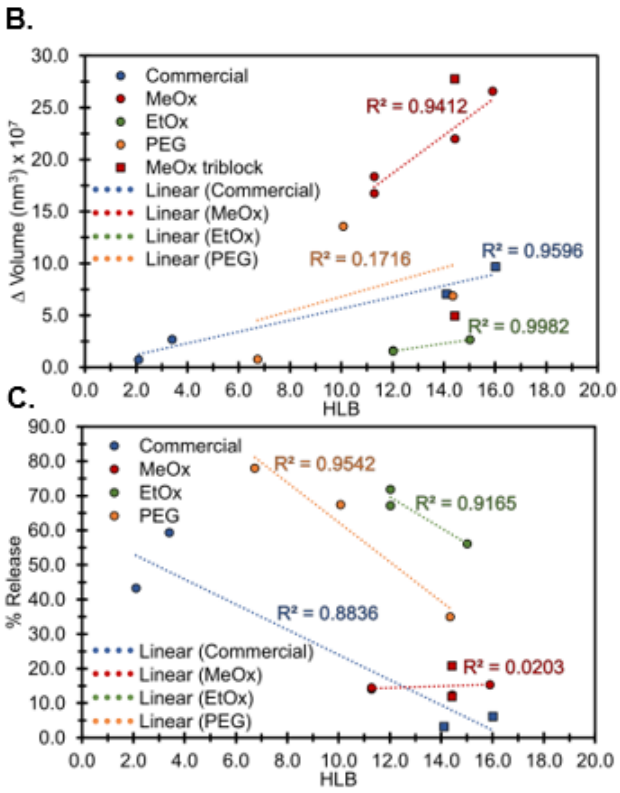

Figure 2.5. Hydrophilic-lipophilic balance (HLB) ratio of polymers **2.1**–**2.16** in relation to the change in volume of PFC emulsions over 30 days and leaching after 14 days.

A. HLB calculations determined by Griffin's non-ionic method:[52,53]
HLB is defined as

$$\mathrm{HLB} = \frac{\mathrm{E}}{5} \qquad (2.1)$$

for poly(oxyethylene)ester containing polymers where E is defined as the mass (or weight) percent of oxyethylene that can be more precisely calculated by

$$\mathrm{E} = \frac{\mathrm{M_{PEG}}}{\mathrm{M_{Total}}} \mathrm{x}\, 100. \qquad (2.2)$$

The same calculations were performed for the POx containing polymers.[54,55]
Zonyl FSO and Zonyl FSN HLB were taken from patent "Dry cleaning system with low HLB surfactant" (US6461387B1).

B. HLB ratios plotted against the change in volume of PFC nanoemulsions over 30 days. Raw data are seen in Figure 2.2 and Figure 2.3. Squares represent tri-block copolymers and circles represent diblock copolymers. Commercial polymers and respective trendline are found in Blue, P(MeOx) and trendline in red, P(EtOx) and trendline in green, and PEG-NonOx and trendline in orange. Note: P(MeOx) triblocks (**2.9**, **2.10**) are not included in the P(MeOx) trendline.

C. HLB ratios plotted against the % release of fluorous coumarin **2.24**. Raw data are found in Figure 2.6. Squares represent tri-block copolymers and circles represent diblock copolymers. Commercial polymers and respective trendline are found in Blue, P(MeOx) and trendline in red, P(EtOx) and trendline in green, and PEG-NonOx and trendline in orange.

Collectively, from these size and stability data we conclude that the HLB (Figure 2.5) is a good metric for predicting if diblock copolymer amphiphiles will lead to stable perfluorocarbon nanoemulsions ($<1x10^7$ nm^3 increase in volume). For triblock copolymers, sterics (*i.e.* length of the A block) of the hydrophilic block is a better predictor of stability than HLB.

2.3.3 Payload Retention

The ideal nanomaterial allows for control of payload release. The advantage of PFC nanoemulsions over traditional oil emulsions is that the orthogonal nature of the fluorous phase gives a chemical handle to control the loading of different payloads inside the droplets through the use of fluorous tags.[56] Previously, we have established a relationship between the fluorous tag on the payload and retention in the droplets.[57,58] Here, we assayed the role of the surfactant in payload release by analyzing emulsions containing a consistent payload, fluorous tagged coumarin **2.24**. Ultimately, multiple methods to control the release profiles of payloads are desirable. Our goal is to develop PFC nanoemulsions that can be applied to a wide array of diseases and patients. In some instances, slow release will be essential, while in others, complete payload delivery over a few days may be desirable.

To test the retention of the payload in the PFC nanoemulsions, diluted aqueous solutions of droplets stabilized by surfactants **2.1**–**2.16** containing coumarin were rocked against 1-octanol, a known cell membrane mimic[59] (Figure 2.6A). The fluorescence of the 1-octanol, which corresponded to coumarin leached from the nanoemulsions, was monitored to determine the percent release of the dye. It is immediately apparent looking at the payload release data in Figure 2.6B that the surfactant plays a significant role in payload retention. When comparing the three

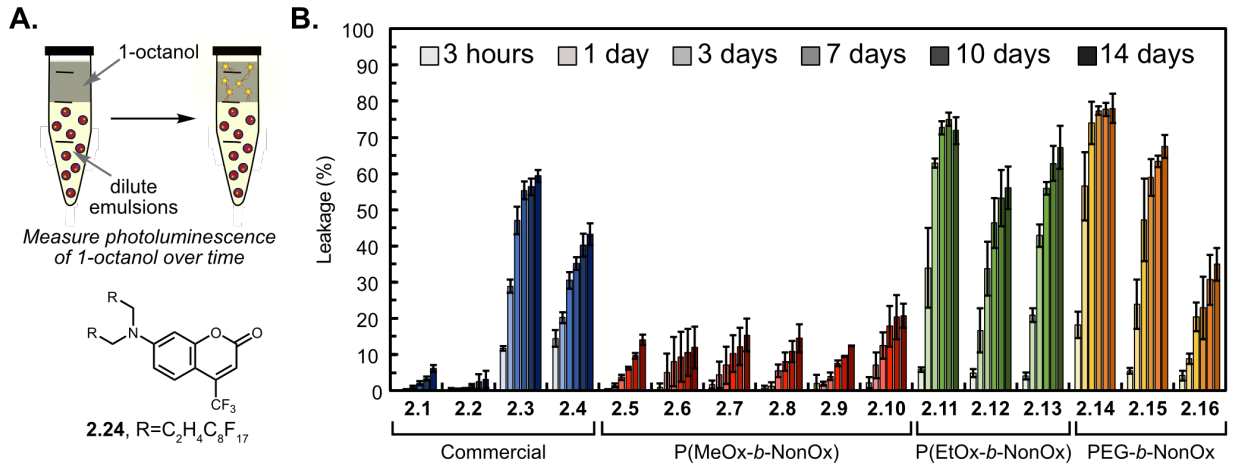

Figure 2.6 (A) Schematic of the partition experiment to determine the degree of coumarin (**2.24**) leaching in the presence of 1-octanol, a cell-membrane mimic. (B) Normalized fluorescence at 500 nm of 1-octanol layer representing the percentage of leached **2.24**. Fluorescence was normalized to a free control of **2.24** dissolved in 1-octanol. Bars represent the average of three independent samples and error bars represent the standard deviation of three independent samples.

hydrophilic blocks (P(MeOx), P(EtOx), and PEG), the P(MeOx) block (polymers **2.5**–**2.10,** red) display superior payload retention. We hypothesize this is due to the increased hydrophilicity of P(MeOx), over PEG and P(EtOx)[36] which minimizes the interaction of the nanoemulsions with the 1-octanol layer, retarding the leakage of the coumarin. The largest variability in release is observed with the PEG polymers where a clear trend with molecular weight is observed. The Pluronics (**2.1**, **2.2**, blue) have the largest PEG content and retain over 90% of their cargo over 14 days while the Zonyls (**2.3**, **2.4**, blue) which have short PEG blocks of 4–12 repeat units, release 30% of their cargo within 3 days. Looking at the hybrid PEG-*b*-NonOx amphiphiles (**2.14**–**2.16**), it is evident that the larger PEG chain is advantageous for cargo retention as PEG_{1K}-*b*-$NonOx_{10}$ (**2.14**) displays the worst retention of all polymers tested (74% coumarin loss after 3 days), while the PEG_{5K}-*b*-$NonOx_{10}$ (**2.16**) only loses 20% of the payload after 3 days. We attribute this molecular weight trend to the increased hydrophilicity and steric protection of the longer hydrophilic blocks at the interface, minimizing interactions of the droplets with the 1-octanol layer.[60,61]

From these data, it appears that leaching of payload from PFC nanoemulsions can be attributed to the hydrophilicity and sterics of the studied amphiphiles (Figure 2.5). The increased hydrophilicity, either by tuning innate hydrophilicity (PEG and P(EtOx) vs. P(MeOx)) or by increasing block length (PEG_{1K} vs. PEG_{5K}) decreases the overall leakage of fluorous payloads. If a nanomaterial is desired that will not release its payload, the P(MeOx) series is far superior. If slow release of payload over time is necessary, the Zonyl, P(EtOx) or PEG_{5K}-*b*-NonOx would be appropriate choices.

2.3.4 Cellular uptake

Next, we analyzed the effect of the surfactant on the cellular uptake of the PFC nanoemulsions. It is well established that nanomaterials, including PFC nanoemulsions, are most often internalized via endocytosis.[31,33] Previously, we have shown that nanoemulsions stabilized by Pluronic F-68 (**2.1**) and P($MeOx_{30}$-*b*-$NonOx_{10}$) (**2.5**) loaded with a fluorous soluble rhodamine[57] displayed colocalization with LysoTracker in phagocytic and non-phagocytic cell lines when analyzed by confocal microscopy.[38] We performed analogous experiments with surfactants **2.1**, **2.5**–**2.6**, **2.11**, and **2.16**, which all displayed robust colocalization with LysoTracker (Figure 2.7), showing the molecular structure of the hydrophilic block does not affect the cellular localization of the PFC nanoemulsions.

Despite all PFC nanoemulsions being internalized by endocytosis, we hypothesized that the varying surface chemistry may cause differences in the dominant pathway of endocytosis. To test this, we further explored the mechanism of endocytosis through treatment with common inhibitors for clathrin-mediated (chlorpromazine), caveolin-mediated (methyl-β-cyclodextrin), macropinocytosis (wortmannin), micropinocytosis (sodium azide) and energy dependent pathways (sodium azide, temperature) (Figure 2.8A).[4,5,62–64] We used the macrophage cell line RAW264.7 for these studies as it is the most well-characterized cell line with the chosen panel of inhibitors. To explore the different endocytosis pathways, RAW cells were incubated in basal media for one hour with each respective inhibitor. PFC nanoemulsions containing a fluorous soluble rhodamine label[57] were added and incubated for an additional three hours at 37 ˚C. For cells at 4 ˚C, emulsions were added and incubated for one hour, to minimize cell death (Figure 2.9). Following incubation, the cells were washed to remove excess emulsions. The cells were then imaged (Figure 2.10,

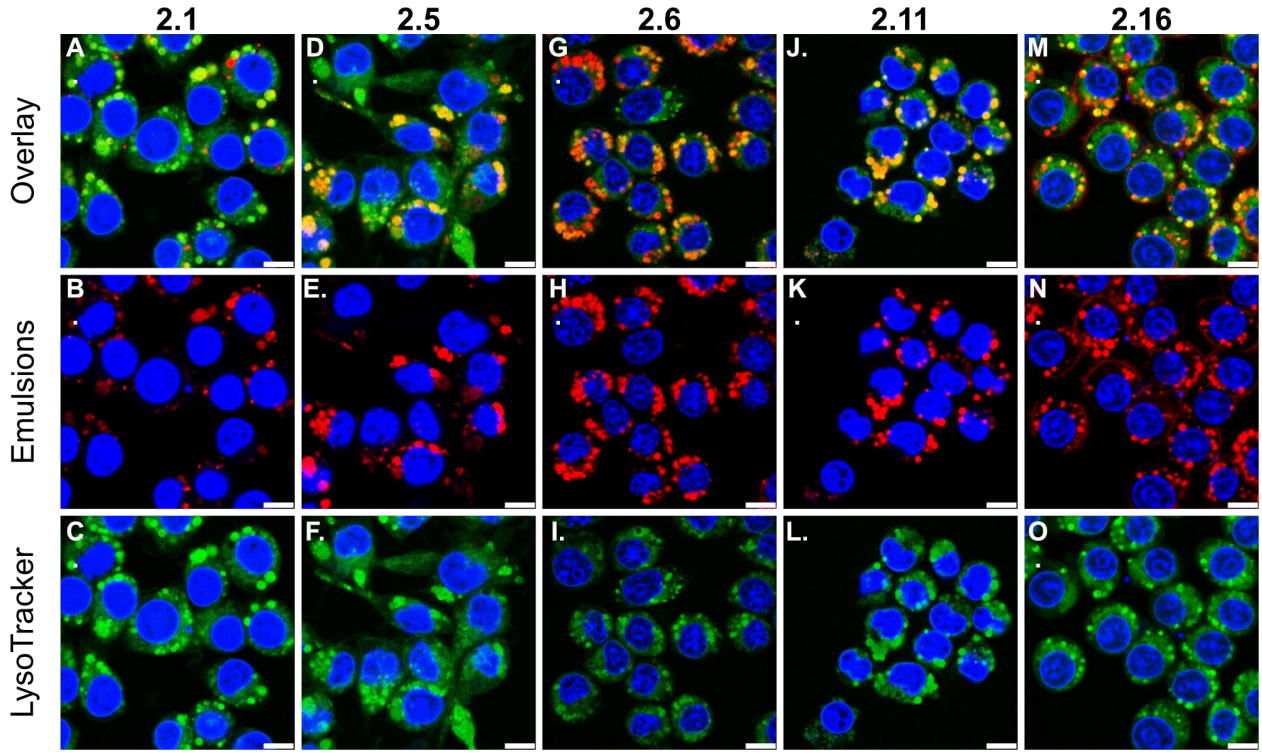

Figure 2.7. Colocalization of PFC nanoemulsions stabilized by polymer surfactants (**2.1** (PF68), **2.5** [P(MeOx$_{30}$-*b*-NonOx$_{10}$)], **2.6** [P(MeOx$_{60}$-*b*-NonOx$_{10}$)], **2.11** [P(EtOx$_{30}$-*b*-NonOx$_{10}$)], **2.16** PEG$_{5K}$-*b*-NonOx$_{10}$) and lysosomes imaged via LysoTracker. Emulsions were loaded with fluorous rhodamine (red – B, E, H, K, N) for visualization. Cells were stained with Hoescht (blue) and LysoTracker (green – C, F, I, L, O). Cells were imaged via excitation at 405 nm to visualize Hoescht, 488 nm to visualize the LysoTracker green (C, F, I, L, O), 532 nm to visualize the rhodamine (B, E, H, K, N), and merged to show colocalization (A, D, G, J, M). Black and white images can be found in section 2.7.2. Scale bars represent 7.5 μm.

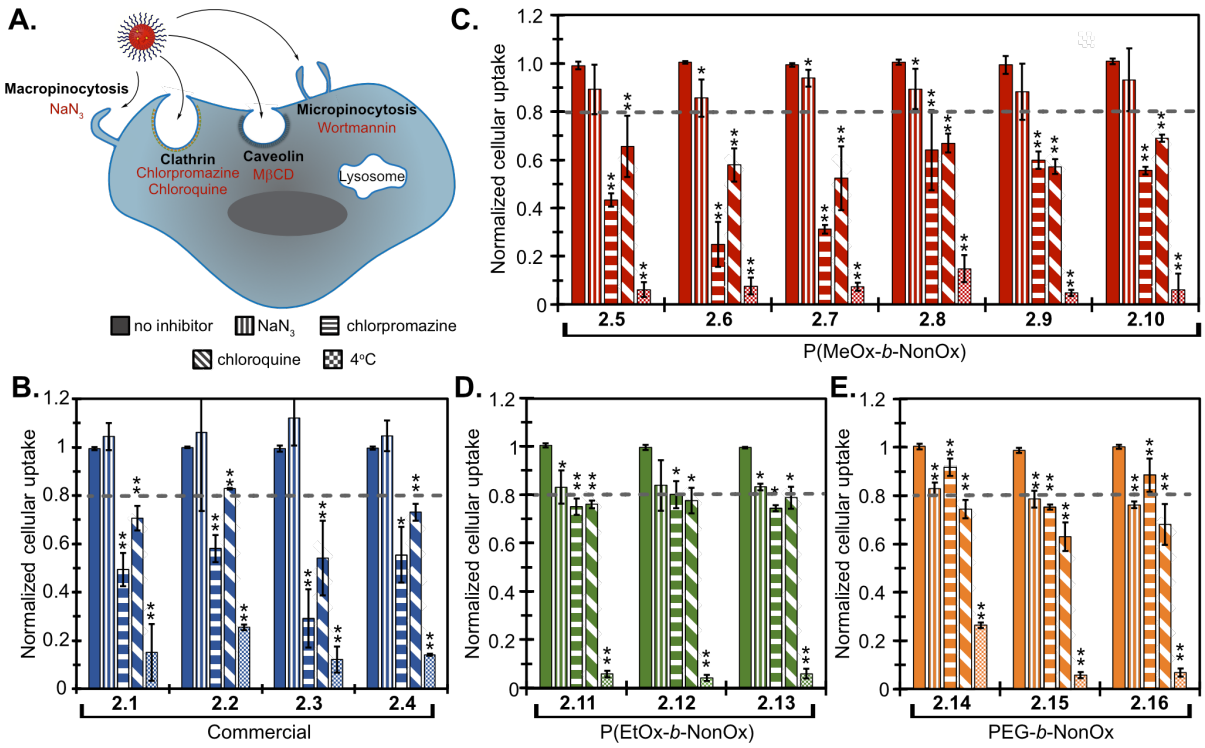

Figure 2.8 (A) Schematic of cellular uptake and the inhibitors used to inhibit each mechanism of endocytosis. (B-E) FACS analysis of the uptake of PFC nanoemulsions containing fluorous rhodamine. RAW264.7 cells were treated with inhibitors (NaN_3 (10 mM), Chlorpromazine (60 μM), Chloroquine (100 μM)) in basal media (DMEM, 0% FBS, 0% PenStrep) for 1 hour at 37 ˚C before addition of nanoemulsions and treatment for a further 3 hours. Cells were washed and analyzed for fluorous rhodamine fluorescence. Data are the average of three replicate experiments performed in triplicate and normalized to cells treated with emulsions but no inhibitor (vertical stripes). Error bars represent the standard deviation. Significance is determined by one tailed Student T's test of unequal variance as compared to the no inhibitor samples. $p \leq 0.05$ * $p \leq 0.005$ **

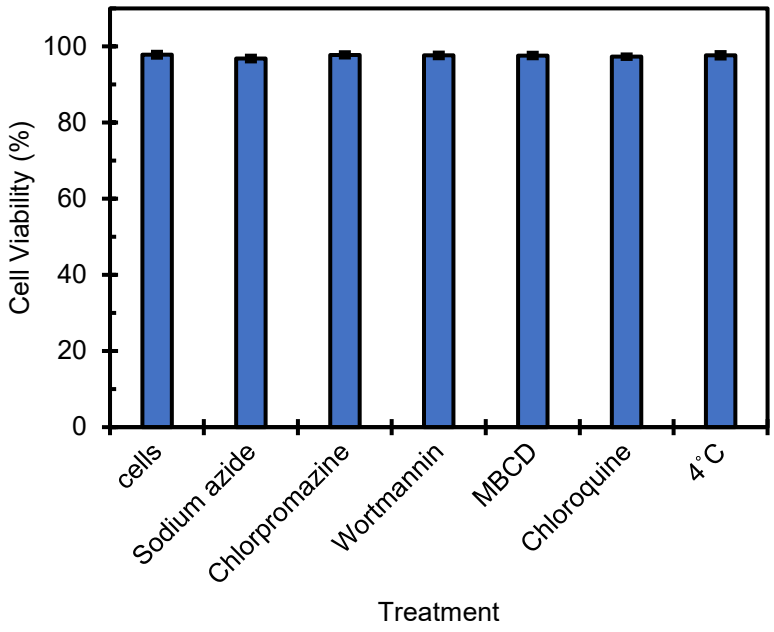

Figure 2.9. RAW264.7 cell viability after treatment with inhibitors NaN_3 (10 mM), Chlorpromazine (60 μM), Wortmannin (0.4 μM), MβCD (20 μM), Chloroquine (100 μM). Bars represent the average of three independent samples and error bars represent the standard deviation of three independent samples.

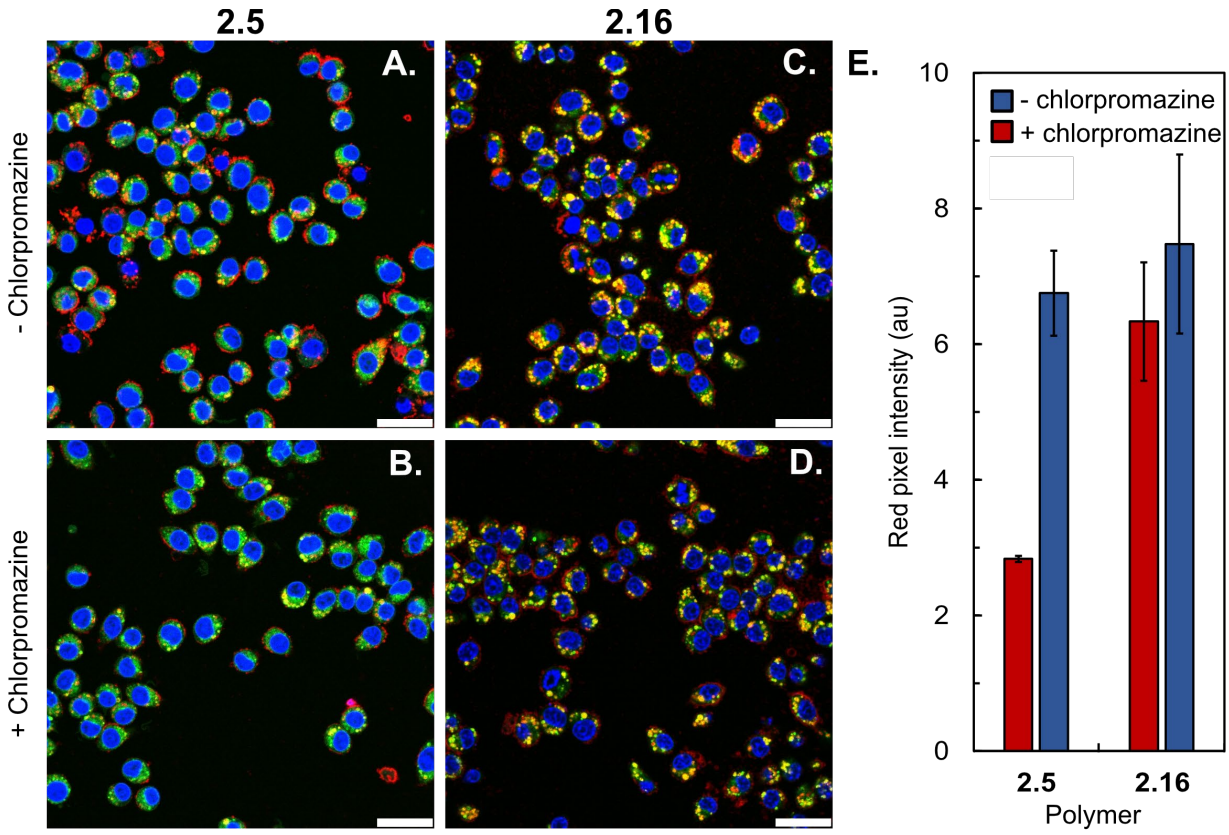

Figure 2.10. Uptake of PFC nanoemulsions stabilized by **2.5** [P(Me$_{30}$-*b*-Non$_{10}$)] and **2.16** (PEG$_{5K}$-*b*-NonOx$_{10}$) in RAW264.7 cells in the presence or absence of chlorpromazine. (A–D) Uptake visualized by confocal microscopy and (E) quantification of fluorous rhodamine pixel intensity. Bars represent the average of three independent images. Error bars represent the standard deviation of three independent images.

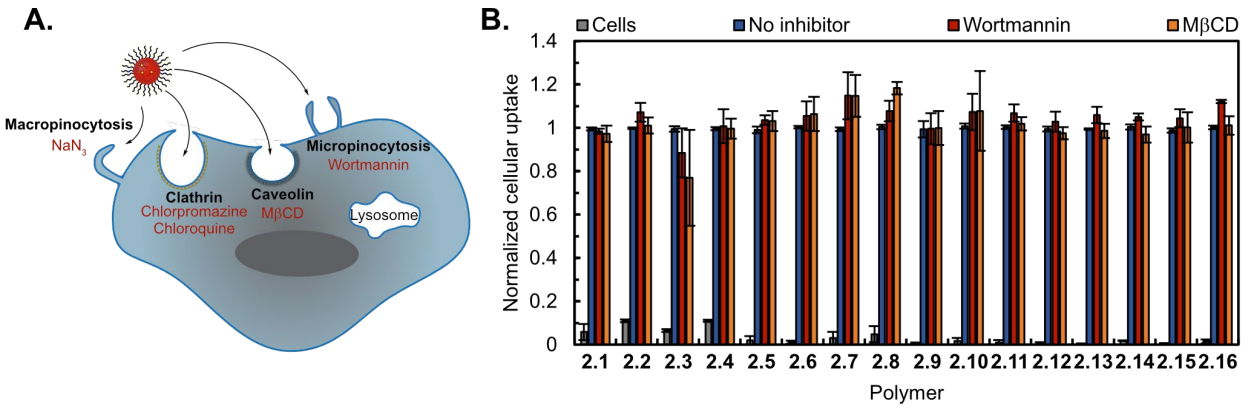

Figure 2.11. RAW264.7 cell uptake of PFC nanoemulsions stabilized by amphiphiles **2.1**–**2.16** after treatment with buffer (gray), emulsions but not inhibitors (blue), inhibitors Wortmannin (0.4 μM, purple) and MβCD (20 μM, black). Bars represent the average of three independent samples and error bars represent the standard deviation.

Supplemental figures 2.7.2) or analyzed via flow cytometry (Figure 2.8 B-E, Supplemental figures 2.7.1). The data suggest all commercial (**2.1**–**2.4**, blue) and P(MeOx) (**2.5**–**2.10**, red) emulsions are internalized through a clathrin-mediated process as shown by the 30–70% decrease in cellular uptake in the presence of chlorpromazine (Figure 2.8 B/C, horizontal stripes). For the more hydrophobic polymers P(EtOx) (**2.11**-**2.13**, green) and PEG_n-*b*-$NonOx_{10}$ (**2.14**-**2.16**, orange) chlorpromazine had much less of an effect, causing only a 20% decrease in uptake (Figure 2.8 D/E). Wortmannin, and methyl-β-cyclodextrin (MβCD) (Figure 2.11) had minimal effect on the uptake of all PFC nanoemulsions indicating that they are not internalized via caveolin or micropinocytosis pathways. Sodium azide (NaN_3, vertical stripes) did not affect the commercial (**2.1**–**2.4**), or P(MeOx) (**2.5**–**2.10**) but caused a 20% decrease in the uptake of P(EtOx) (**2.11**–**2.13**), and PEG_n-*b*-$NonOx_{10}$ (**2.14**–**2.16**) emulsions. Chloroquine (diagonal stripes), most commonly used as an endosomal escape agent,[65] has also been shown to inhibit clathrin-mediated endocytosis[66] and decreased uptake of all nanoemulsions by 20–30%. For all polymers, lowering the temperature drastically affected the uptake, leading to a decrease of 80–90%, indicating that internalization is an energy dependent process for all the PFC nanoemulsions assayed. For the commercial (**2.1**–**2.4**) and the P(MeOx) (**2.5**–**2.10**) polymers, clathrin-dependent endocytosis is the prominent route as shown by the >40% decrease in uptake when chlorpromazine is present. However, the P(EtOx) and the PEG_n-*b*-$NonOx_{10}$ polymers appear to be endocytosed by a combination of pathways allowing for uptake of PFC nanoemulsions in the presence of both chlorpromazine and NaN_3 (Figure 2.8 B-E).

To support that the differences in uptake observed for emulsions stabilized by different surfactants is due to the surfactant identity and not differences in the emulsion sizes, nanoemulsions of consistent surfactant yet different sizes were prepared by altering the weight

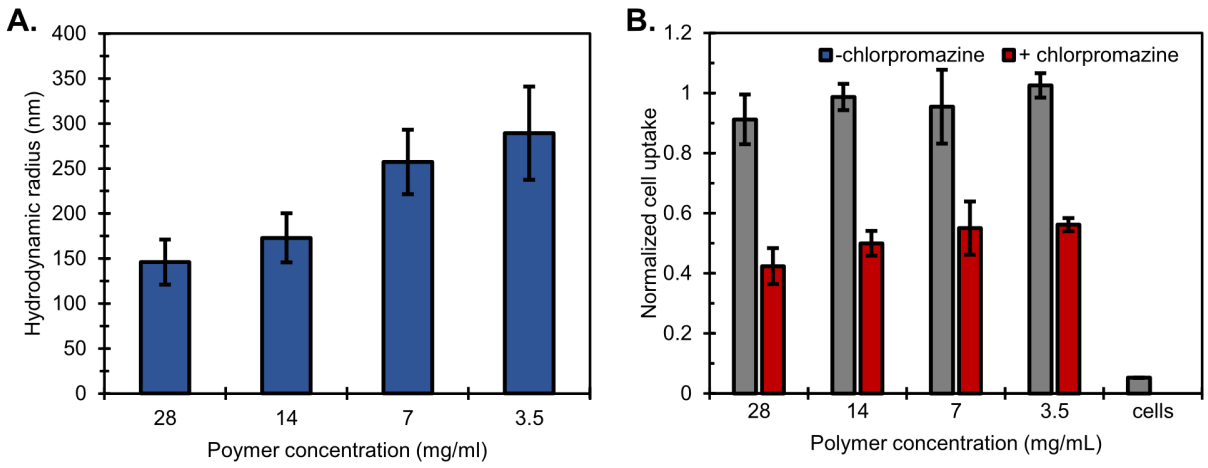

Figure 2.12. Cellular uptake of nanoemulsions ranging from 150–300 nm emulsions. (A) Hydrodynamic diameter of PFC nanoemulsions stabilized by different concentrations of P(MeOx$_{30}$-*b*-NonOx$_{10}$) (**5**). Bars represent the average of three independent samples, error bars represent the Z-average multiplied by the PDI of three independent samples. (B) RAW264.7 cell uptake of nanoemulsions in A in the presence (red) or absence (gray) of chlorpromazine (60 μM). Bars represent the average of three independent samples, and error bars represent the standard deviation of three samples.

percent of amphiphile employed during emulsion formation. Using this approach, emulsions of 150–300 nm in diameter were prepared from P(MeOx$_{30}$-*b*-NonOx$_{10}$) (**2.5**) (Figures 2.12). RAW cells were treated with or without chlorpromazine followed by emulsions of different sizes and the degree of uptake was assayed by flow cytometry. We found that uptake was universally reduced by 50% upon treatment with chlorpromazine, suggesting that any size differences between the emulsions did not significantly affect cellular uptake (Figure 2.12).

2.3.5 Protein adsorption

POx polymers have been used to replace PEG as a non-immunogenic, anti-biofouling alternative for surfaces,[67,68] protein conjugates,[36,69] and nanomaterials.[70,71] When nanomaterials come into contact with biological material, protein adsorbs to the surface forming a protein corona that masks the molecular identity of the material.[6] This corona alters the interaction of the nanomaterials and cells, which has been reported to influence routes of endocytosis.[4–6]

POx polymers have been reported to repel protein more effectively than PEG when conjugated to nanomaterials.[72,73] We looked to investigate if this trend was consistent for nanoemulsions stabilized by POx and PEG amphiphiles. To assay the relative protein adsorption on PFC nanoemulsions stabilized by surfactants (**2.1**–**2.16,** Figure 2.13A), emulsions were prepared and treated with bovine serum albumin (BSA, Figure 2.13, 2.14), cell culture media containing fetal bovine serum (FBS, Figure 2.13C), or 10% human serum in phosphate buffered saline (PBS, Figure 2.15). First, emulsions were rocked against a BSA solution for two hours, washed and any isolated protein was precipitated and quantified via Bradford assay (Figure 2.13B). The results of the Bradford assay indicate there is little difference in total protein adsorption between nanoemulsions stabilized by polymer surfactants containing PEG, P(MeOx), and P(EtOx)

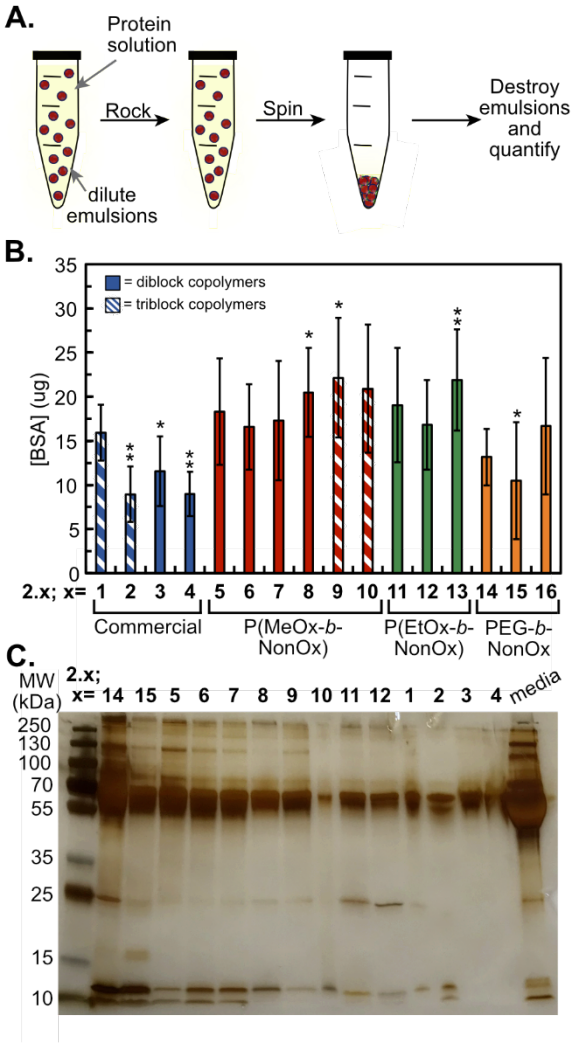

Figure 2.13. (A) Schematic of protein adsorption analysis in which emulsions are rocked against a protein solution, washed, and quantified. (B) Bradford analysis of PFC nanoemulsions treated with 60 mg/mL BSA for two hours at room temperature. Bars represent the average of three experiments, each done in triplicate. Error bars represent standard deviation. Significance is determined by one tailed Student T's test of unequal variance as compared to Pluronic F-68 (**2.1**) $p < 0.05$ *, $p < 0.005$ ** (C) SDS-PAGE of PFC nanoemulsions treated with complete media (DMEM, 10% FBS, 1% PenStrep), for two hours at room temperature. Protein was denatured, run on a 12% gel, and visualized with silver stain.

hydrophilic blocks. We further analyzed the protein adsorption by SDS-PAGE analysis. For these experiments, surfactants (**2.1**–**2.4**, **2.5**–**2.12**, **2.14**–**2.15**) were treated with media containing fetal bovine serum (FBS) and subjected to the same procedure as described above. SDS-PAGE analysis indicates that all nanoemulsions adsorb BSA present in media (65 kDa protein); however, differences are observed in the minor proteins present in FBS. Nanoemulsions stabilized by amphiphiles **2.11** and **2.12** containing P(EtOx) hydrophilic blocks displayed significant adsorption of the IgG light chain (25 kDa protein). Alternatively, emulsions stabilized by PEG or P(MeOx) containing diblock amphiphiles showed more adsorption of low molecular weight proteins Insulin (10 kDa) and Cytochrome C (12 kDa). Thus, the SDS-PAGE analysis suggests that the identity of the hydrophilic block is able to alter the proteins within the corona, even if the overall magnitude of protein adsorbed is similar. The identity of proteins adsorbed to the nanomaterial surface has been implicated in promoting the stealth effect through the avoidance of the mononuclear phagocyte system (MPS) *in vivo*.[74,75]

After studying the protein corona formed on PFC nanoemulsions *in vitro*, we were interested in the effect the adsorbed protein would have on cellular uptake (Figure 2.16A). To study this, emulsions were treated with either PBS or BSA before being added to RAW cells. After 3 hours, the cells were washed and analyzed by flow cytometry. We found that the presence of BSA affected the overall uptake of nanoemulsions stabilized by **2.1**, **2.9**, **2.11** and **2.16**, but not **2.5** or **2.6** (Figure 2.16A). The nanoemulsions showed no significant difference in size or fluorescence (Figure 2.17), suggesting these results are due to varied amphiphiles. To further analyze the effect of the protein corona on cellular uptake, we treated RAW cells with media, emulsions, and the cellular internalization inhibitors tested in Figure 4. The presence of BSA showed no effect on the

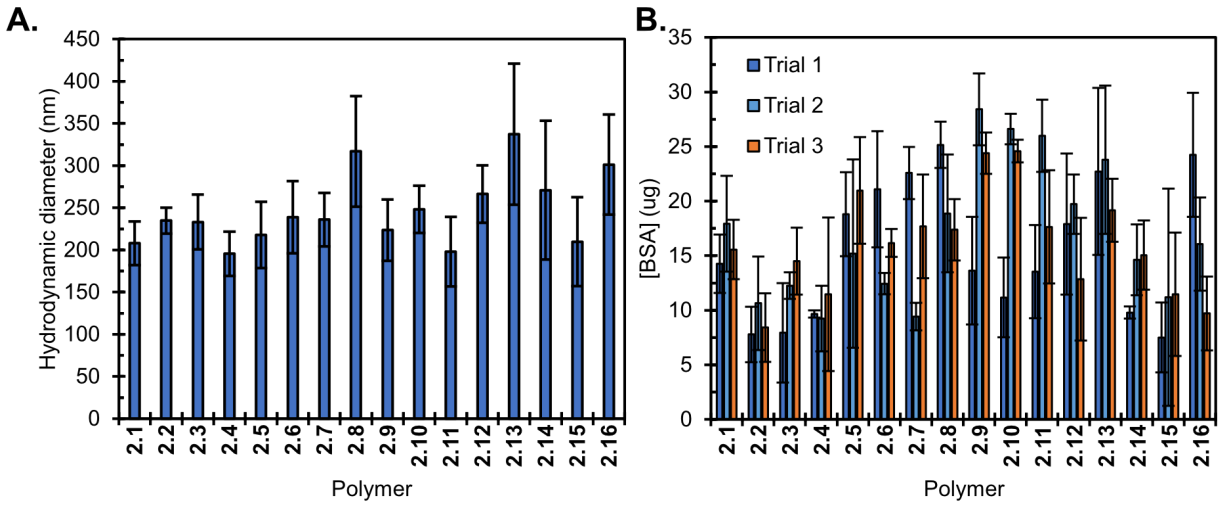

Figure 2.14. Adsorption of BSA on PFC nanoemulsions stabilized by polymer amphiphiles **2.1**—**2.16**. (A) Hydrodynamic diameter of PFC nanoemulsions. Bars represent the average of three independent samples, error bars represent the product of the Z-average and the PDI. (B) Bradford analysis of protein adsorption on PFC nanoemulsions. Bars represent the average of three wells, and are shown for three independent experiments (trial 1-trial 3). Error bars represent the standard deviation of the three wells from each individual trial.

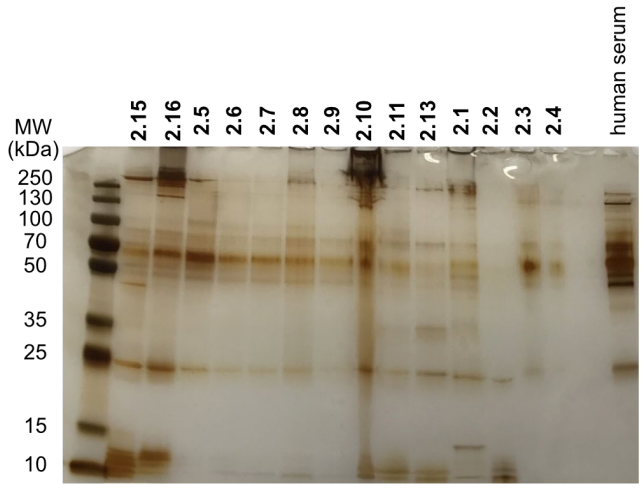

Figure 2.15. Silver stained SDS-PAGE gel representing protein adsorption of Human Serum on PFC nanoemulsions stabilized by polymer amphiphiles **2.1** (PF68), **2.2** (PF127), **2.3** (Zonyl FSO), **2.4** (Zonyl FSN), **2.5** [P(MeOx$_{30}$-*b*-NonOx$_{10}$)], **2.6** [P(MeOx$_{60}$-*b*-NonOx$_{10}$)], **2.7** [P(MeOx$_{90}$-*b*-NonOx$_{10}$)], **2.8** [P(MeOx$_{90}$-*b*-NonOx$_{10}$)], **2.9** [P(MeOx$_{30}$-*b*-NonOx$_{10}$-*b*-MeOx$_{30}$)], **2.10** [P(MeOx$_{90}$-*b*-NonOx$_{10}$-*b*-MeOx$_{90}$)], **2.11** [P(EtOx$_{30}$-*b*-NonOx$_{10}$)], **2.13** [P(EtOx$_{90}$-*b*-NonOx$_{10}$)], **2.15** (PEG$_{2K}$-*b*-NonOx$_{10}$), **2.16** (PEG$_{5K}$-*b*-NonOx$_{10}$).

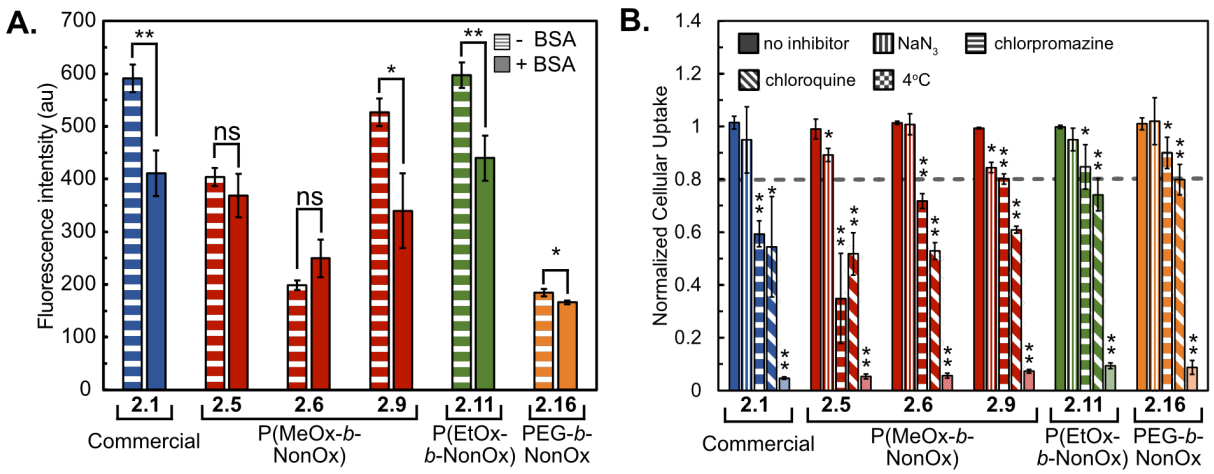

Figure 2.16. (A) Comparative endocytosis of PFC nanoemulsions in the presence or absence of a protein corona (+/- BSA). PFC nanoemulsions were treated with 60 mg/mL BSA or PBS for two hours at room temperature, washed by centrifugation 2x and added to cells (3 hr, 37 ˚C, 5% CO_2). Fluorous rhodamine fluorescence was measured via FL2 channel by FACS. Bars represent the average of two replicate experiments performed in triplicate. Error bars represent the standard deviation. (B) FACS analysis of the uptake of PFC nanoemulsions containing fluorous rhodamine. RAW264.7 cells were treated with inhibitors (NaN_3 (10 mM), Chlorpromazine (60 μM), and, Chloroquine (100 μM)) in complete media (DMEM, 10% FBS, 1% PenStrep) for 1 hour at 37 ˚C before addition of nanoemulsions and treatment for a further 3 hours. Cells were washed and analyzed for fluorous rhodamine fluorescence. Data are the average of three replicate experiments performed in triplicate and normalized to cells treated with emulsions but no inhibitor. Error bars represent the standard deviation. One tailed student T-test with unequal variance was performed in relation to no inhibitor. $p \leq 0.05$ * $p \leq 0.01$ **

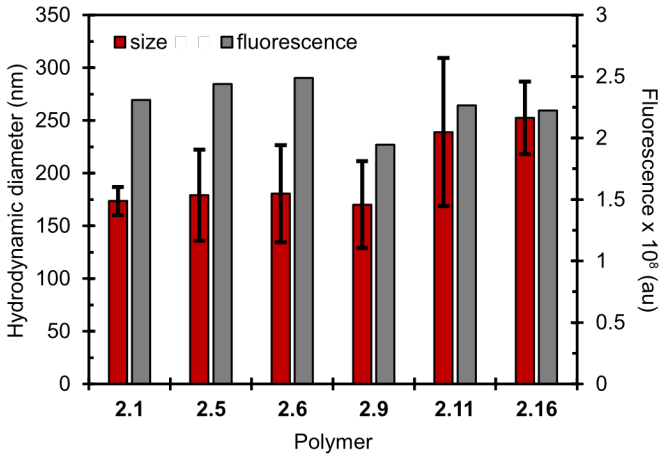

Figure 2.17. Cellular uptake of nanoemulsions stabilized by **2.1** (PF68), **2.5** [P(MeOx$_{30}$-*b*-NonOx$_{10}$)], **2.6** [P(MeOx$_{60}$-*b*-NonOx$_{10}$)], **2.9** [P(MeOx$_{30}$-*b*-NonOx$_{10}$-*b*-MeOx$_{30}$)], **2.11** [P(EtOx$_{30}$-*b*-NonOx$_{10}$)], **2.16** (PEG$_{5K}$-*b*-NonOx$_{10}$). Initial size shown in red. Bars represent the average of three DLS sample runs on the same sample and error bars represent the product of the Z-average and the PDI. The fluorescence of each nanoemulsion was measured (gray).

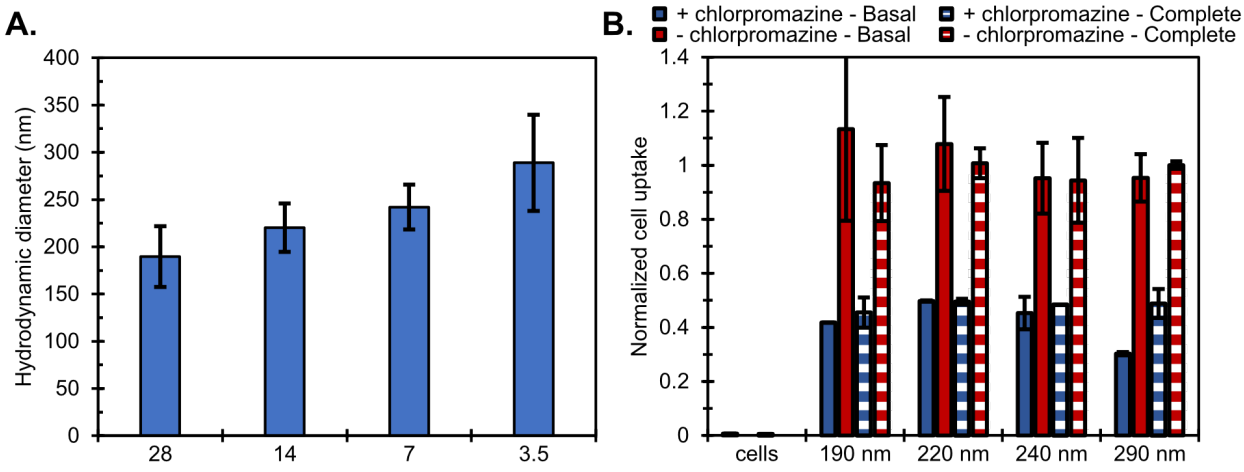

Figure 2.18. Cellular uptake of nanoemulsions ranging from 150—300 nm emulsions. (A) Hydrodynamic diameter of PFC nanoemulsions stabilized by different concentrations of P(MeOx$_{30}$-*b*-NonOx$_{10}$) (**5**). Bars represent the average of three independent samples, error bars represent the product of the Z-average and the PDI. (B) RAW264.7 cell uptake of nanoemulsions in A in the presence or absence of chlorpromazine and the presence (complete) or absence (basal) of protein. Bars represent the average of three independent samples and error bars represent the standard deviation of three independent samples.

route of endocytosis (Figures 2.16B, Figure 2.18), indicating that the presence of protein does not influence the mechanism of endocytosis.

2.4 Conclusion

In this work, we utilized a polymer library to investigate the effect of polymer amphiphiles on stabilizing PFC nanoemulsions through the systematic variation of the hydrophilic block of the surfactants. From this study, when determining the best polymer amphiphile to stabilize nanoemulsions, the length of the A block, the hydrophilic: lipophilic balance (HLB), the polymer architecture and the molecular identity should be considered. Each of these properties plays a role in the initial size, stability, payload retention, cellular endocytosis, and protein adsorption of PFC nanoemulsions. We envision these design principles can be applied to other polymer amphiphile stabilized nanoemulsion systems.

The initial size of PFC nanoemulsions is influenced by the size and sterics of the hydrophilic (A) block of the polymer amphiphiles. In most cases, longer A blocks produce larger initial nanoemulsions. This is particularly evident when considering the P(EtOx) series in which P(EtOx$_{30}$-*b*-NonOx$_{10}$) (**2.11**) are initially 200 nm, while both P(EtOx$_{90}$-*b*-NonOx$_{10}$) (**2.12**) and P(EtOx$_{90}$-*b*-NonOx$_{30}$) (**2.13**) are 300 nm and 320 nm respectively. The commercial and P(MeOx) follow this trend, with the PEG$_n$-*b*-NonOx$_{10}$ displaying similar initial sizes, with large dispersities.

The stability of the droplets over 30 days can be attributed to the HLB of the polymer. The P(MeOx) diblock polymers (**2.5**–**2.8**) and P(EtOx) (**2.11**–**2.13**) display this trend. As the ratio increases from 3:1 (P(MeOx$_{30}$-*b*-NonOx$_{10}$) (**2.5**)) to 6:1 (P(MeOx$_{60}$-*b*-NonOx$_{10}$) (**2.6**)) and 9:1 (P(MeOx$_{90}$-*b*-NonOx$_{10}$) (**2.7**)) the change in volume of the droplets over 30 days increases from 1.5x10^7 nm^3 to 2.75x10^7 nm^3. However, when the ratio returns to 3:1 with P(MeOx$_{90}$-*b*-NonOx$_{30}$)

(**2.8**) the droplets display similar stability to **2.5**. This holds true for the P(EtOx) series as well in which **2.11** and **2.13** have a 3:1 ratio.

The retention of payload is determined by the size of the hydrophilic (A) block, and the molecular identity of the A block. Both of these factors determine the overall hydrophilicity of the A block. P(MeOx) is more hydrophilic than PEG, which is more hydrophilic than P(EtOx). This is displayed with the commercial polymers in which the long PEG triblock copolymers (**2.1**, **2.2**) display superior retention (<10% release over 14 days) compared to the shorter diblock Zonyl polymers (**2.3**, **2.4**). In addition, all P(MeOx) polymers retain 80% of the fluorous coumarin over 14 days compared to the P(EtOx) polymers that retain ~50% of the fluorous coumarin after 3 days. The PEG_n-*b*-$NonOx_{10}$ polymers showcase that the hydrophilicity can also be tuned through increasing the length of the hydrophilic block, in which **2.16** retains 80% of the cargo after 3 days but **2.14** only retains 20% after 3 days.

Lastly, the cellular endocytosis and the protein adsorption are controlled by the molecular identity and the polymer architecture. The more hydrophilic polymers, the commercial and P(MeOx) polymers, undergo clathrin mediated endocytosis while the more hydrophobic polymers, P(EtOx) and PEG_n-*b*-$NonOx_{10}$, are internalized by several mechanisms. Overall, the triblock copolymers behave similarly to the diblock copolymers, with slight differences in the identity of the proteins that are adsorbed.

This study provides necessary background on the structure—property relationship of polymer amphiphiles for the stabilization of PFC nanoemulsions. Through the identification of four criteria– hydrophilic block size, hydrophilic: lipophilic balance (HLB), molecular identity and polymer architecture– the ideal nanomaterial can be more easily realized. Future work involves

combining the amphiphile design rules established here with fluorous-tagged therapeutics to enable efficient, personalized, drug delivery with nanoemulsions.

2.5 Experimental Procedures

2.5.1 General nanoemulsion formation procedure

Polymer surfactant (5.6 mg, 2.8 wt%) was dissolved in cosolvent (20 μL, DMF, MeOH or THF) and sonicated in a bath sonicator (~15 minutes) until fully dissolved, at which point 7:3 perfluorodecalin : perfluorotripropylamine (10 vol%, 20 μL) was added, followed by PBS buffer pH 7.4 (200 μL). Pluronic F-68 (**2.1**), Pluronic F-127 (**2.2**), Zonyl FSO (**2.3**), Zonyl FSN (**2.4**) required no cosolvent. P($MeOx_x$-*b*-$NonOx_y$-*b*-$MeOx_z$) (**2.5**–**2.10**), P($EtOx_x$-*b*-$NonOx_y$) (**2.11**–**2.13**) and PEG_{1K}-*b*-$NonOx_{10}$ (**2.14**) were dissolved in DMF. PEG_{2K}-*b*-$NonOx_{10}$ (**2.15**) and PEG_{5K}-*b*-$NonOx_{10}$ (**2.16**) were dissolved in THF and MeOH, respectively. The mixture was sonicated at 35% amplitude for 90 seconds at 0 °C on a QSonica (Q125) sonicator. For P($EtOx_x$-*b*-$NonOx_y$) (**2.11**–**2.13**) and PEG_n-*b*-$NonOx_m$ (**2.14**–**2.16**) polymers the mixture was sonicated at 35% amplitude for 90 seconds pulsed on for 2 seconds, off for 10 seconds at 0 °C. Sonication was performed by lowering the probe directly at the liquid-liquid interface of the two immiscible solvents. To remove cosolvents, emulsions are washed by centrifugation (5.6 x *g*, 3 min, 2x).

2.5.2 Nanoemulsion size analysis

The bulk emulsion solution was diluted in MilliQ H_2O (20 μL emulsions in 2 mL MilliQ H_2O) in a plastic 1 cm cuvette. Size was analyzed with a Malvern Zetasizer Nano dynamic light scattering. Data are representative of three replicate measurements. Size error bars represent the product of the dispersity and the z-average of the measurements.

2.5.3 Payload release experiment

Perfluorocarbon nanoemulsions (**2.1–2.16**) containing fluorous coumarin **2.24** were prepared by dissolving coumarin in acetone to make a stock solution (2.3 mg/mL). Coumarin **2.24 (**0.05 mg, 0.04 μmol, 20 μL) was then aliquoted in to eppendorf tubes and the acetone was dried. Once dried, perfluorocarbons (7:3 PFD: PFTPA, 20 μL) were added to dissolve the coumarin, and deionized water (200 μl) was added. Separately, the polymers were dissolved with required cosolvent. The PFC / water mixture was placed on the sonication probe, and immediately before starting the probe, the polymer solution (see general nanoemulsion formation procedure) was added. The mixture was sonicated for 90 s either continuously or pulsed as described in the general nanoemulsion formation procedure. Immediately after formation, emulsion solution (40 μL) was diluted with PBS (960 μL) and 1-octanol (500 μL) was layered on top of the water and placed on an orbital rocker at 40 rpm.

The 1-octanol (200 μL) was removed with a syringe (250 μL Hamilton) at 3 h, 1 day, 3 days, 7 days, 10 days, and 14 days and the fluorescence were measured in a 0.3 cm quartz cuvette. After measurement, the 1-octanol was carefully replaced to minimize loss during transfer and placed back on the rocker until the next measurement.

The control was fluorous coumarin **2.24** (3.2 μL, 0.007 mg, 6.09 nmol) dissolved in 1-octanol (500 μL) directly, and bath sonicated for 10 min to dissolve. This is the amount of fluorous coumarin that is expected to come into contact with the 1-octanol after the emulsions were diluted with PBS. Photoluminescence spectra were obtained on a Horiba Instruments PTI QuantaMaster Series fluorometer.

2.5.4 General photophysics procedures

Photoluminescence spectra were obtained on a Horiba Instruments PTI QuantaMaster Series fluorometer. Quartz cuvettes (0.3 cm path length) were used for photoluminescence measurements unless otherwise noted.

2.5.5 General cell culture procedures

RAW264.7 cells (ATCC cat# TIB-71) were cultured in Dulbecco's Modified Eagle Media (DMEM, Life Technologies, cat# 11995073) supplemented with 10% fetal bovine serum (Corning, lot# 35016109) and 1% penicillin-streptomycin (Life Technologies, cat# 15070063). Cells were washed with PBS, or PBS supplemented with 1% fetal bovine serum (FBS, FACS buffer). Cells were incubated at 37 ˚C, 5% CO_2, during treatments and throughout culturing, in HERACell 150i CO2 incubators. Cells were pelleted through use of Sorvall ST 40R centrifuge. All cell work was performed in 1300 Series A2 biosafety cabinets.

For cell viability experiments: following incubation, cells were washed three times by centrifugation (526 x *g*, 3 min, 4˚C). Propidium iodide solution (PI, 2 μL of 1 mg/mL in PBS) was added to each well. Cells treated with PI were transferred to FACS tubes with a final volume of 200 μL FACS buffer (PBS + 1% FBS). Cells were incubated on ice for 15 minutes prior to flow cytometry measurement. PI fluorescence was measured on FL2 channel. Data were analyzed by splitting the population at 10^2 as a live/dead line. Flow cytometry was performed on a BDBiosciences FACSCalibur equipped with 488 nm and 635 nm lasers. For assessment of the statistical significance of differences, a one-tailed Student's t-test assuming unequal sample variance was employed.

For inhibition experiments: Media was removed and replaced with DMEM (100 μL of either basal or complete) and inhibitors NaN_3 (10 mM), Chlorpromazine (60 μM), Wortmannin (0.4 μM), MβCD (20 μM), Chloroquine (100 μM). After 1 h, emulsions (10 μL) were added to the cells and incubated for 3 h at 37 ˚C, 5% CO_2. For 4 ˚C, emulsions were added to cells and placed at 4 ˚C for 1 h to prevent excessive cell death. Cells were then washed with media 3x, sterile lithium chloride buffer (LiCl: 0.25 M LiCl, 1 mM EDTA, 10 mM Tris-HCl) 3x, PBS 1x, then lifted with trypsin and transferred to a v-bottom 96-well plate. Note: PFC nanoemulsions are dense and settle on top of cells. Slight rocking was necessary to successfully remove excess emulsions. Cells were washed by centrifugation (2x, 526 x *g*, 3 min) and resuspended in FACS buffer (PBS + 1% FBS) to a final volume of 200 μL. Uptake was analyzed by FL2 channel on a FACSCalibur flow cytometer. 15,000 cells were collected per sample. Each emulsion was normalized to one of the replicates in the samples with no inhibitors present. Error bars represent the standard deviation of 3 replicate experiments.

2.6 Figure experimental procedures

Figure 2.2 C/D.

Perfluorocarbon nanoemulsions (**2.1**, **2.5–2.6**, **2.9**, **2.16**) were prepared following the **general nanoemulsion formation procedure** containing either perfluorooctyl bromide (PFOB), perfluoro-15-crown-5-ether (PFCE) or, 7:3 perfluorodecalin (PFD) perfluorotripropylamine (PFTPA) (10 vol%, 20 μL). Size was measured on day 0, day 1, day 2, day 3, day 7, and day 14 by resuspending emulsions via vortexing briefly (~5 s) and pipetting up and down, then diluting 1:1000 following **nanoemulsion size analysis**. Reported is the change in volume from day 0 to day 14. Error bars represent the standard deviation of the measurements.

$$V = \frac{4}{3}\pi r^3 \tag{2.3}$$

where r = radius of nanoemulsions

Figure 2.2 E/F.

Perfluorocarbon nanoemulsions stabilized by each surfactant (**2.1**–**2.16**) were prepared as described in the **general nanoemulsion formation procedure**. Emulsion size was then monitored on day 1, 2, 3, 7, 14, and 30 following the **general nanoemulsions analysis procedure**. Bars represent the average of three samples and error bars represent the standard deviation of three samples.

Volume is a more accurate description of Ostwald ripening over time. Thus, diameter on day 0 and day 30 were converted to volume of a sphere.

where r is radius. Bars represent the difference of volume on day 30 and day 0 of three samples. Error bars represent the propagation of error of three separate samples.

Figure 2.3.

Perfluorocarbon nanoemulsions (**2.1**–**2.5**, **2.7**–**2.9**, **2.11**–**2.13**) were prepared through ultrasonication (35% amp, 90 sec) of solutions containing 7:3 perfluorodecalin (PFD) perfluorotripropylamine (PFTPA) (10 vol%, 20 μL) and polymer surfactant 28 mg/mL (2.8 wt%, blue), 14 mg/mL (1.4 wt%, red), 7 mg/mL (0.7 wt%, orange), and 3.5 mg/mL (0.35 wt%, grey) in phosphate buffered saline (PBS, pH 7.4, 200 μL). Error bars represent the average of the product of the $Z_{average}$ and the polydispersity index of three replicate samples. Size was measured following the **nanoemulsion size analysis**.

Stock solutions of PF68 (**2.1**), PF127 (**2.2**), Zonyl FSN-100 (**2.3**), and Zonyl FSO (**2.4**) were made in PBS (phosphate buffered saline) pH 7.4 at 28 mg/mL. Stock solutions of the POx polymers (**2.7**–**2.9**, **2.11**–**2.13**) were made in PBS with 10% DMF at 28 mg/mL.

Figure 2.4.

Perfluorocarbon nanoemulsions (**2.1–2.16**) were prepared through ultrasonication following the **general nanoemulsion formation procedure**. Size was measured on day 0 (grey), day 1 (purple), day 2 (blue), day 3 (green), day 7 (yellow), day 14 (orange), and day 30 (red) by resuspending emulsions via vortexing briefly (~5 s) and pipetting up and down, following the **nanoemulsion size analysis**. Error bars represent the average of the product of the $Z_{average}$ and the polydispersity index of three replicate samples.

Stock solutions of PF68 (**2.1**), PF127 (**2.2**), Zonyl FSN-100 (**2.3**), and Zonyl FSO (**2.4**) were made in PBS (phosphate buffered saline) pH 7.4 at 28 mg/mL. Stock solutions of the POx polymers were made in PBS with 10% DMF at 28 mg/mL. Stock solutions of PEG_{1K}-*b*-NonOx (**2.14**), PEG_{2K}-*b*-NonOx (**2.15**), and PEG_{5K}-*b*-NonOx (**2.16**) were made in PBS with 10% MeOH, THF, and DMF respectively at 28 mg/mL.

Figure 2.6B.

Perfluorocarbon nanoemulsions (**2.1–2.16**) containing fluorous coumarin **2.24** were prepared by dissolving coumarin in acetone to make a stock solution (2.3 mg/mL). Coumarin **2.24 (**0.05 mg, 0.04 μmol, 20 μL) was then partioned to eppendorf tubes and the acetone was dried. Once dried, perfluorocarbons (7:3 PFD : PFTPA, 20 μL) were added to dissolve the coumarin, and deionized water (200 μL) was added. Separately, the polymers were dissolved with required cosolvent. The PFC/water mixture was placed on the sonication probe, and immediately before starting the probe, the polymer solution (see **general nanoemulsion formation procedure**) was added. The mixture was sonicated for 90s either continuously or pulsed as described in the **general nanoemulsion formation procedure**. Immediately after formation, emulsions solution (40 μL) was diluted with PBS (960 μL). 1-octanol (500 μL) was layered on top of the water and placed on an orbital rocker at 40 rpm.

The 1-octanol (200 μL) was removed with a syringe (250 μL Hamilton) at 3 h, 1 day, 3 days, 7 days, 10 days, and 14 days and the fluorescence was measured in a 0.3 cm cuvette as described in the **general photophysics procedures**. After measurement, the 1-octanol was then carefully replaced to minimize loss during transfer and placed back on the rocker until next measurement.

The control was fluorous coumarin **2.24** (3.2 μL, 0.007 mg, 6.1 nmol) dissolved in 1-octanol (500 μL) directly, and bath sonicated for 10 min to dissolve. This is the amount of fluorous coumarin that is expected to come into contact with the 1-octanol after the emulsions were diluted with PBS.

Fluorimeter settings: Path length: 0.3 cm, Exc: 375 nm, collect: 400-700 nm, all slits: 2nm, Integration: 0.1 sec.

Figure 2.7.

Perfluorocarbon nanoemulsions (**2.1**, **2.5–2.6**, **2.11**, **2.16**) containing fluorous rhodamine were prepared by making nanoemulsions following the **general nanoemulsion formulation procedure**. After washing by centrifugation, fluorous rhodamine dissolved in acetone (0.4 μL of 9.2 mg/mL stock, 0.4 mg) was added and emulsions were resonicated.

RAW264.7 cells (30,000 cells/well) were plated on a μ-Slide 8 Well ibiTreat tissue culture treated slides (Ibidi Cat# 80826). Cells were allowed to adhere overnight. Media was replaced with complete DMEM and treated with emulsions (**2.1**, **2.5–2.6**, **2.11**, **2.16**). Treatment was incubated for 3 h (37 ˚C, 5% CO_2). After treatment, cells were washed with media 3x, LiCl buffer 3x and replaced with OptiMEM containing cellular stains. PFC emulsions are dense and settle onto the cells, to remove the emulsions, slight rocking was necessary. Cells were stained with Hoechst (3.24 μM, ThermoFisher Cat# PI62249), LysoTracker Green DND-26 (200 nM, Cell Signaling Technologies Cat# 8783S). Cells were incubated with Hoescht at room temperature for 30 minutes prior to imaging, Hoescht in OptiMEM was removed and replaced with OptiMEM containing LysoTracker stains and imaged immediately.

PFC nanoemulsions stabilized by polymer surfactants (**2.1**, **2.5–2.6**, **2.11**, **2.16**) were labeled with fluorous rhodamine (red – B, E, H, K, N). Cells were stained with Hoescht (blue) and LysoTracker (green – C, F, I, L, O). Cells were imaged via excitation at 488 nm to visualize the LysoTracker green (C), 532 nm to visualize the rhodamine (D), and merged to show colocalization (A, D, G, J, M). Scale bars represent 7.5 μm.

Confocal settings were as follows: Hoechst (405 laser-50%, 800 gain, offset -0.4, collection 420-500nm), LysoTracker Green DMD-26 (488 laser-50%, 800 gain, offset -0.4, collection 500-550 nm), Rhodamine (532 laser-50%, 800 gain, offset -0.4, collection 540-700nm), DIC (scan-BF, 450 gain, offset -0.4). Scale bar represents 7.5 μm. Images were processed in ImageJ. Confocal microscopy was performed on a TCS SPE Leica confocal microscope containing 405 nm, 488 nm, 532 nm and 635 nm lasers.

Figure 2.8A-E.

Perfluorocarbon nanoemulsions (**2.1**–**2.16**) containing fluorous rhodamine were prepared by making nanoemulsions following the **general nanoemulsion formulation procedure**. After washing by centrifugation, fluorous rhodamine dissolved in acetone (0.4 μL of 9.2 mg/mL stock, 0.4 mg) was added and emulsions were resonicated.

RAW264.7 cells (100,000 cells/well) were plated on a flat bottom 96-well plate (Fisher, Cat# 07-201-94). Cells were allowed to adhere overnight. Media was replaced with basal DMEM and inhibitors: NaN_3 (10 mM), Chlorpromazine (60 μM), Wortmannin (0.4 μM), MβCD (20 μM), Chloroquine (100 μM) and incubated for 1 h (37 ˚C, 5% CO_2). Emulsions were added (10 μL) and

incubated for a further 3 h (37 ˚C, 5% CO_2). For 4 ˚C, emulsions were added to cells and placed at 4 ˚C for 1 h to prevent excessive cell death. Cells were then washed with media 3x, LiCl buffer 3x, PBS 1x, then lifted with trypsin and transferred to a v-bottom 96-well plate (Fisher, Cat# 07-200-96). Cells were washed by centrifugation (2x, 526 x *g*, 3 min) and resuspended in FACS buffer (PBS + 1% FBS) to a final volume of 200 μL. Uptake was analyzed by FL2 channel on a FACSCalibur flow cytometer. 15,000 cells were collected per sample. Error bars represent the standard deviation of three replicate experiments.

Figure 2.9.

Media was removed and replaced with 100 μL of basal DMEM containing inhibitors NaN_3 (10 mM), Chlorpromazine (60 μM), Wortmannin (0.4 μM), MβCD (20 μM), Chloroquine (100 μM). Cells were incubated with inhibitors for 4 h at 37 ˚C, 5% CO_2. Cells were placed at 4 ˚C for 1 h to prevent excessive cell death. Cells were then washed with media 3x, LiCl buffer 3x, PBS 1x, then lifted with trypsin and transferred to a v-bottom 96-well plate. Cells were washed by centrifugation (2x, 526 x *g*, 3 min) and resuspended in FACS buffer (PBS + 1% FBS) to a final volume of 200 μL. Cells were stained with propidium iodide (2 μL, 1 mg/mL, 15 min) on ice. Viability was analyzed by FL2 channel on a FACSCalibur flow cytometer. 15,000 cells were collected per sample. Error bars represent the standard deviation of three replicate experiments.

Figure 2.10.

Perfluorocarbon nanoemulsions stabilized by (P($MeOx_{30}$-*b*-$NonOx_{10}$) (**2.5**) and PEG_{5K}-*b*-$NonOx_{10}$ (**2.16**)) containing fluorous rhodamine were prepared by making nanoemulsions following the **general nanoemulsion formulation procedure**. After washing by centrifugation,

fluorous rhodamine dissolved in acetone (0.4 μL of 9.2 mg/mL stock, 0.4 mg) was added and emulsions were resonicated.

RAW264.7 cells (30,000 cells/well) were plated on a μ-Slide 8 Well ibiTreat tissue culture treated slides (Ibidi Cat# 80826). Cells were allowed to adhere (O/N). Media was replaced with either basal DMEM or basal DMEM and chlorpromazine (60 μM). Cells were incubated with chlorpromazine for 1 h before addition of emulsions and then further incubated for 3 h at 37 ˚C, 5% CO_2. After treatment, cells were washed with media 3x, LiCl buffer 3x and replaced with OptiMEM containing cellular stains. PFC emulsions are dense and settle onto the cells, to remove the emulsions, slight rocking was necessary. Cells were stained with Hoechst (3.24 μM, ThermoFisher Cat# PI62249), LysoTracker Green DND-26 (200 nM, Cell Signaling Technologies Cat# 8783S). Cells were incubated with Hoescht at room temperature for 30 minutes prior to imaging, Hoescht in OptiMEM was removed and replaced with OptiMEM containing LysoTracker stains and imaged immediately. Scale bar represents 25 μm.

ImageJ was used to analyze the total pixel intensity of the emulsions (rhodamine channel, red). Bars represent the average of three independent images, and error bars represent the standard deviation.

Figure 2.11.

Perfluorocarbon nanoemulsions stabilized by **2.1**–**2.16** containing fluorous rhodamine were prepared by making nanoemulsions following the **general nanoemulsion formulation**

procedure. After washing by centrifugation, fluorous rhodamine dissolved in acetone (0.4 μL of 9.2 mg/mL stock, 0.4 mg) was added and emulsions were resonicated.

RAW264.7 cells (100,000 cells/well) were plated on a flat bottom 96-well plate (Fisher, Cat# 07-201-94). Cells were allowed to adhere (O/N). Media was replaced with complete DMEM and inhibitors: Wortmannin (0.4 μM, purple), MβCD (20 μM, black). Cells were incubated with inhibitors for 1 h at 37 ˚C, 5% CO_2. After 1 h, emulsions (10 μL) were added to the cells and incubated for 3 h at 37 ˚C, 5% CO_2. Cells were then washed with media 3x, LiCl buffer 3x, PBS 1x, then lifted with trypsin and transferred to a v-bottom 96-well plate (Fisher, Cat# 07-200-96). Cells were washed by centrifugation (2x, 526 x *g*, 3 min) and resuspended in FACS buffer (PBS + 1% FBS) to a final volume of 200 μL. Uptake was analyzed by FL2 channel on a FACSCalibur flow cytometer. 15,000 cells were collected per sample. Each emulsion was normalized to no inhibitors present. Error bars represent the standard deviation of 3 replicate experiments.

Figure 2.12.

P($MeOx_{30}$-*b*-$NonOx_{10}$) (**2.5**) emulsions containing fluorous rhodamine were prepared by making nanoemulsions following the **general nanoemulsion formulation procedure**. After washing by centrifugation, fluorous rhodamine dissolved in acetone (0.4 μL of 9.2 mg/mL stock, 0.4 mg) was added and emulsions were resonicated.

A. P($MeOx_{30}$-*b*-$NonOx_{10}$) (**2.5**) emulsions were prepared following **the general nanoemulsion formulation protocol.** Prior to addition of fluorous rhodamine, size was

measured by following the **nanoemulsion size analysis**. Error bars represent the average of the product of the $Z_{average}$ and the polydispersity index of three replicate samples.

B. RAW264.7 cells were plated in a 96-well plate (100,00 cells/well). Chlorpromazine (60 μM) was added to the cells and incubated for 1 h at 37˚C, 5% CO_2. After 1 h, emulsions (10 μL) were added to the cells and incubated for 3 h at 37˚C, 5% CO_2. Cells were then washed with media 3x, LiCl buffer 3x, PBS 1x, then lifted with trypsin and transferred to a v-bottom 96-well plate (Fisher, Cat# 07-200-96). Cells were washed by centrifugation (2x, 526 x *g*, 3 min) and resuspended in FACS buffer (PBS + 1% FBS) to a final volume of 200 μL. Uptake was analyzed by FL2 channel on a FACSCalibur flow cytometer. 15,000 cells were collected per sample. Each emulsion size was normalized to one of the replicates in the samples without chlorpromazine. Error bars represent the standard deviation of 3 replicate samples.

Figure 2.13B/Figure 2.14.

Perfluorocarbon nanoemulsions (**2.1**–**2.16**) were prepared by following the **general nanoemulsion formulation procedure**. After washing, emulsions (100 μL) were diluted with deionized water (1 mL DI H_2O) or 60 mg/mL BSA dissolved in water (1 mL). Emulsions were rocked on an orbital rocker for 2 h at 40 rpm. Following treatment, emulsions are washed with DI H_2O by centrifugation 2x (5.6 x *g*, 3 min), to remove unbound protein. Following the last wash, emulsions were resuspended in dichloromethane (DCM, 100 μL) and sonicated with the probe sonicator for 30 s. The DCM was then evaporated to leave a film of polymer and protein. Protein was then dissolved in DI H_2O (100 μL) and cold acetone (400 μL). The mixture was cooled for 2 h (-20 ˚C) to precipitate the protein. The tubes were then centrifuged (17.7 x *g*, 10 min), to pellet

protein. The supernatant was removed and the process was repeated to precipitate the protein again. Following precipitation, samples were dissolved in DI H_2O (150 μL).

Protein concentration was measured via Bradford assay. A standard curve of BSA from 0–30 μg/mL was made following manufacturer specifications (VWR, Cat# P123200). Samples were measured by diluting 10 μL sample with 290 μL Bradford reagent. Absorbance was measured on plate reader at 595 nm.

Absorbance of emulsions treated with DI H_2O was subtracted from absorbance of emulsions treated with BSA. Data represents the average of three independent experiments, each experiment was performed in triplicate. Error bars represent the standard deviation of the trials.

Figure 2.13C.

Perfluorocarbon nanoemulsions **(2.1**–**2.12**, **2.14**–**2.15**) were prepared by following the **general nanoemulsion formulation procedure**. After washing, emulsions (100 μL) were diluted with complete DMEM (1 mL, 10 % FBS, 1% PenStrep). Emulsions were rocked on an orbital rocker for 2 h at 40 rpm. Following treatment, emulsions are washed with DI H_2O by centrifugation 2x (5.6 x *g*, 3min), to remove unbound protein. Following the last wash, emulsions were resuspended in Laemmli buffer (BioRad, Cat# 1610737) containing β-mercaptoethanol (βME) and heated (95 ˚C, 5 min) to denature proteins. Emulsions were pelleted (5.6 x *g*, 3 min), and supernatant was loaded onto 12% SDS-PAGE gel (BioRad, Cat# 5671043). The gel was run at 120 V for 50 min, and stained with silver stain (ThermoFisher, Cat# PI24612) for visualization.

Figure 2.15.

Perfluorocarbon nanoemulsions (**2.1**–**2.13**, **2.15**–**2.16**) were prepared by following the **general nanoemulsion formulation procedure**. After washing, emulsions (100 μL) were diluted with 10% human serum diluted in PBS (1 mL, pH 7.4). Emulsions were rocked on an orbital rocker for 2 h at 40 rpm. Following treatment, emulsions were washed with DI H_2O by centrifugation 2x (3 rpm, 3 min), to remove unbound protein. Following the last wash, emulsions were resuspended in Laemmli buffer (BioRad, Cat# 1610737) containing β-mercaptoethanol (βME) and heated (95 ˚C, 5 min) to denature proteins. Emulsions were pelleted (5.6 x *g*, 3 min), and the supernatant was loaded onto 12% SDS-PAGE gel (BioRad, Cat# 5671043). The gel was stained with silver stain (ThermoFisher, Cat# PI24612) for visualization.

Figure 2.16A/Figure 2.17.

Perfluorocarbon nanoemulsions (**2.1**, **2.5–2.6**, **2.9**, **2.11**, **2.16**) containing fluorous rhodamine were prepared by making nanoemulsions following the **general nanoemulsion formulation procedure**. After washing by centrifugation, fluorous rhodamine dissolved in acetone (0.4 μL of 9.2 mg/mL stock, 0.4 mg) is added and emulsions are re-sonicated. Emulsions (100 μL) were treated with either 60 mg/mL BSA in H_2O (+ serum) or H_2O (- serum) (1 mL each). The emulsions were rocked for 2 hours at room temperature, washed by centrifugation (3.0 rpm, 3 min, 3x), resuspended in 100 μL of H_2O and added to cells.

RAW264.7 cells (100,000 cells/well) were plated on a flat bottom 96-well plate (Fisher, Cat# 07-201-94). Cells were allowed to adhere (O/N). Media was replaced with 100 μL of basal media. Emulsions (+/- serum) were added and incubated for 3 h (10 μL, 37 ˚C, 5% CO_2). Cells were then

washed with media 3x, LiCl buffer 3x, PBS 1x, then lifted with trypsin and transferred to a v-bottom 96-well plate (Fisher, Cat# 07-200-96). Cells were washed by centrifugation (2x, 526 x *g*, 3 min) and resuspended in FACS buffer (PBS + 1% FBS) to a final volume of 200 μL. Uptake was analyzed by FL2 channel on a FACSCalibur flow cytometer. 15,000 cells were collected per sample. Error bars represent the standard deviation of three replicate experiments.

Figure 2.16B/Figure 2.17.

Perfluorocarbon nanoemulsions (**2.1**, **2.5**–**2.6**, **2.9**, **2.11**, **2.16**) containing fluorous rhodamine were prepared by making nanoemulsions following the **general nanoemulsion formulation procedure**. After washing by centrifugation, fluorous rhodamine dissolved in acetone (0.4 μL of 9.2 mg/mL stock, 0.4 mg) was added and emulsions were re-sonicated.

RAW264.7 cells (100,000 cells/well) were plated on a flat bottom 96-well plate (Fisher, Cat# 07-201-94). Cells were allowed to adhere (O/N). Media was replaced with complete DMEM and inhibitors: NaN_3 (10 mM), Chlorpromazine (60 μM), Wortmannin (0.4 μM), MβCD (20 μM), Chloroquine (100 μM) and incubated for 1 h (37 ˚C, 5% CO_2). Emulsions were added (10 μL) and incubated for a further 3 h (37 ˚C, 5% CO_2). For 4 ˚C, emulsions were added to cells and placed at 4 ˚C for 1 h to prevent excessive cell death. Cells were then washed with media 3x, LiCl buffer 3x, PBS 1x, then lifted with trypsin and transferred to a v-bottom 96-well plate (Fisher, Cat# 07-200-96). Cells were washed by centrifugation (2x, 526 x *g*, 3 min) and resuspended in FACS buffer (PBS + 1% FBS) to a final volume of 200 μL. Uptake was analyzed by FL2 channel on a FACSCalibur flow cytometer. 15,000 cells were collected per sample. Error bars represent the standard deviation of three replicate experiments.

Figure 2.18

Perfluorocarbon nanoemulsions (**2.1**, **2.5**–**2.6**, **2.9**, **2.11**, **2.16**) containing fluorous rhodamine were prepared by making nanoemulsions following the **general nanoemulsion formulation procedure**. After washing by centrifugation, fluorous rhodamine dissolved in acetone (0.4 μL of 9.2 mg/mL stock, 0.4 mg) was added and emulsions were re-sonicated.

RAW264.7 cells (100,000 cells/well) were plated on a flat bottom 96-well plate (Fisher, Cat# 07-201-94). Cells were allowed to adhere (O/N). Media was replaced with complete DMEM and inhibitors: NaN_3 (10 mM), Chlorpromazine (60 μM), Wortmannin (0.4 μM), MβCD (20 μM), Chloroquine (100 μM) and incubated for 1 h (37 ˚C, 5% CO_2). Emulsions were added (10 μL) and incubated for a further 3 h (37 ˚C, 5% CO_2). For 4 ˚C, emulsions were added to cells and placed at 4 ˚C for 1 h to prevent excessive cell death. Cells were then washed with media 3x, LiCl buffer 3x, PBS 1x, then lifted with trypsin and transferred to a v-bottom 96-well plate (Fisher, Cat# 07-200-96). Cells were washed by centrifugation (2x, 526 x *g*, 3 min) and resuspended in FACS buffer (PBS + 1% FBS) to a final volume of 200 μL. Uptake was analyzed by FL2 channel on a FACSCalibur flow cytometer. 15,000 cells were collected per sample. Error bars represent the standard deviation of three replicate experiments.

2.7 Supplemental figures

2.7.1 FACS Histograms

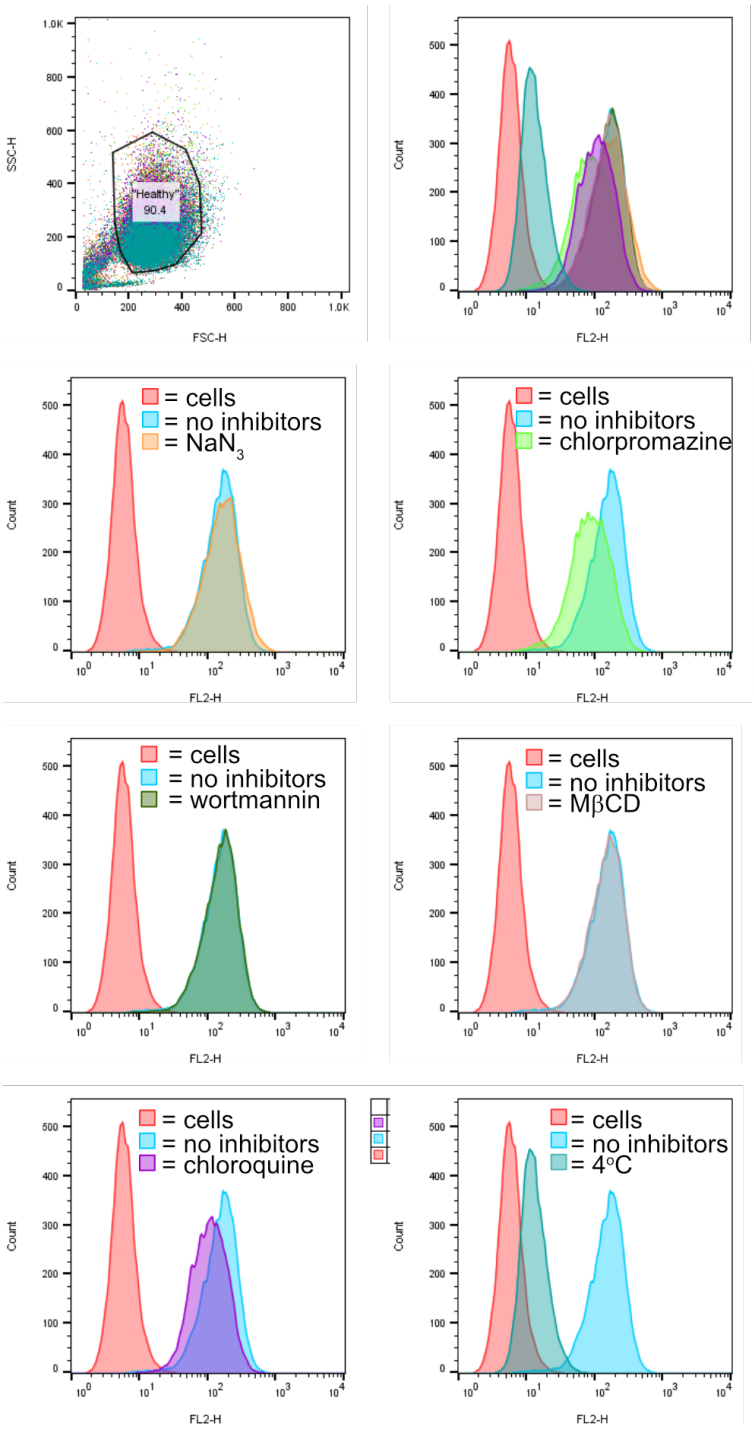

Figure S2.1. Histograms for flow cytometry data of Pluronic F-68 (**2.1**) in Figure 2.8.

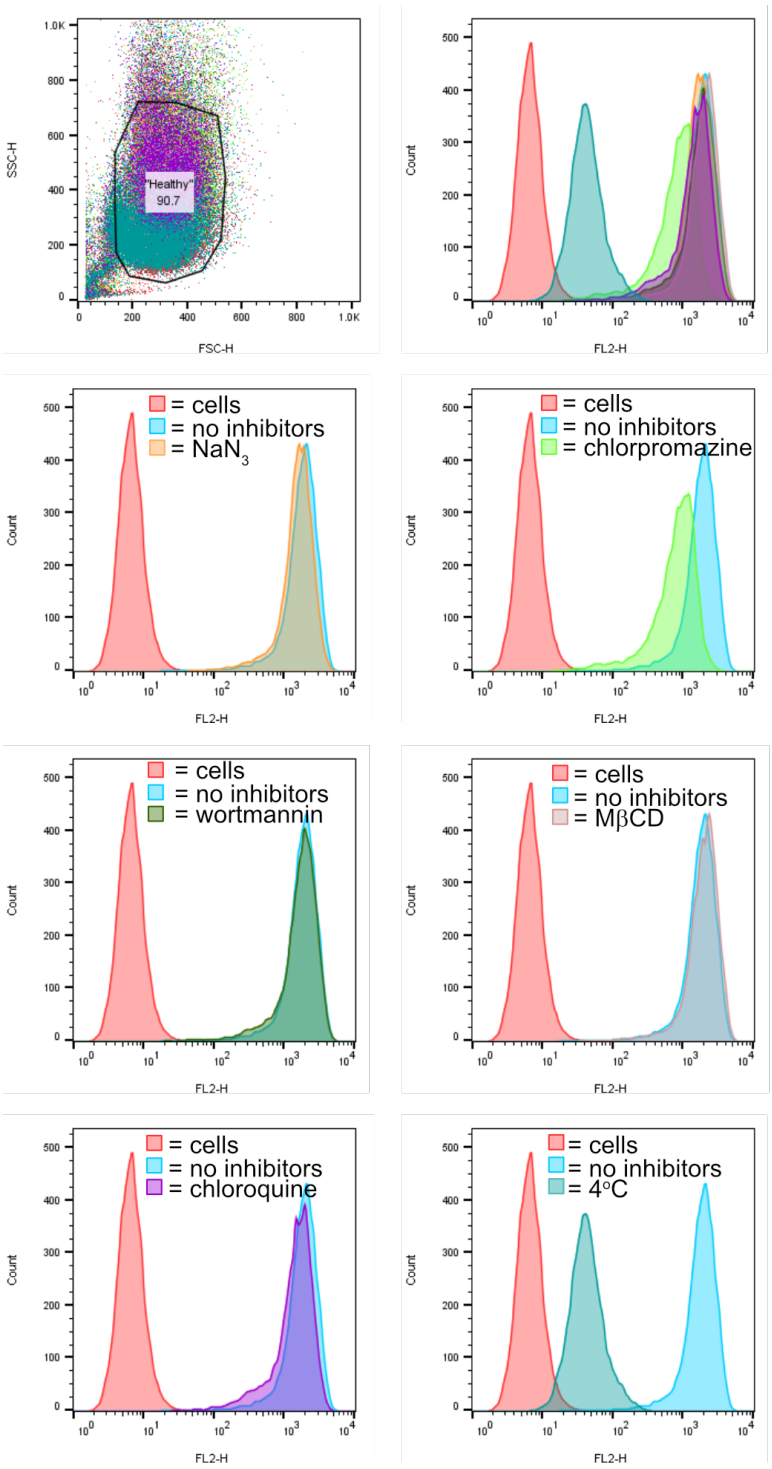

Figure S2.2 P(MeOx$_{30}$-*b*-NonOx$_{10}$) (**2.5**) histograms for flow cytometry data in Figure 2.8.

2.7.2 Single channel microscopy

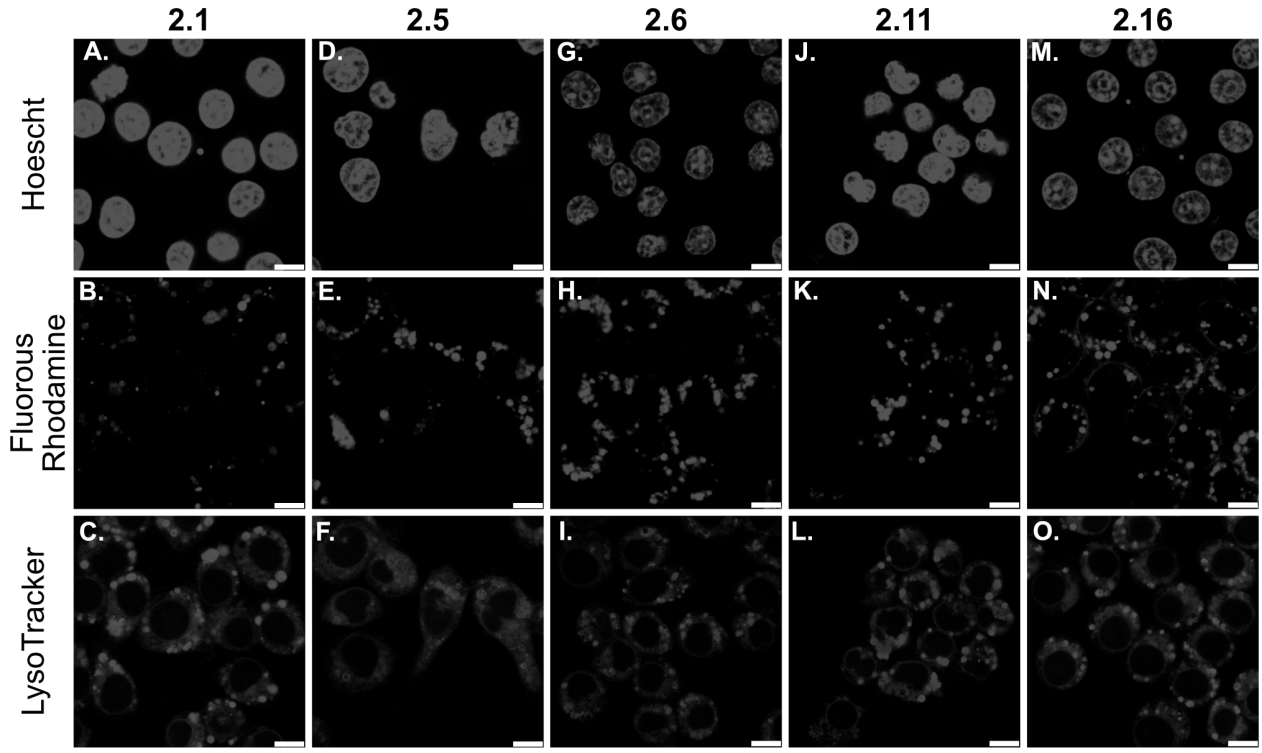

Figure S2.3 Single channel images for Figure 2.7.

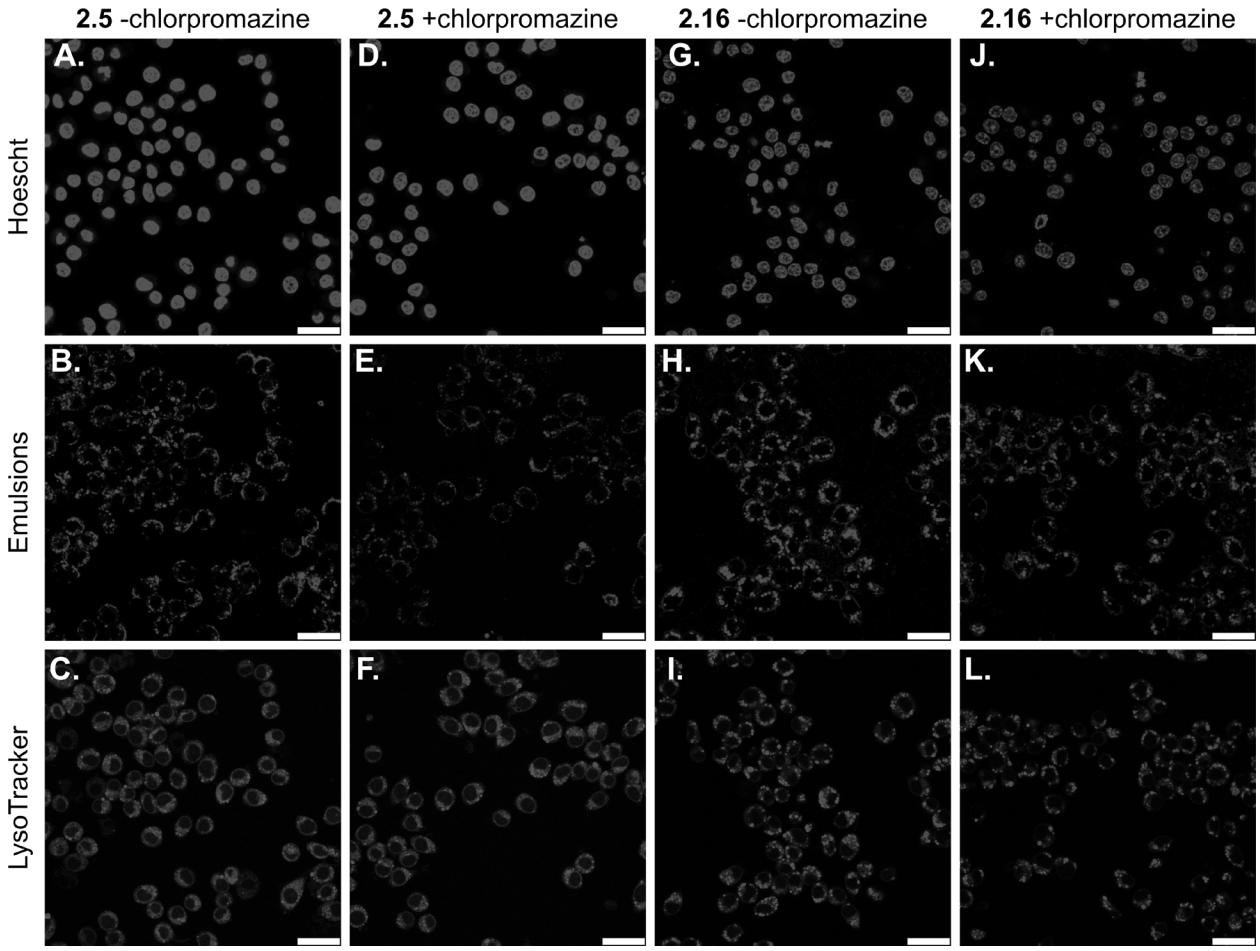

Figure S2.4 Single channel images for Figure 2.10.

2.8 References and Notes

(1) Shi, J.; Kantoff, P. W.; Wooster, R.; Farokhzad, O. C. Cancer Nanomedicine: Progress, Challenges and Opportunities. *Nat. Rev. Cancer* **2017**, *17*, 20–37.

(2) Bobo, D.; Robinson, K. J.; Islam, J.; Thurecht, K. J.; Corrie, S. R. Nanoparticle-Based Medicines: A Review of FDA-Approved Materials and Clinical Trials to Date. *Pharm. Res.* **2016**, *33*, 2373–2387.

(3) De Jong, W. H.; JA Borm, B. Drug Delivery and Nanoparticles : Applications and Hazards. *Int. J. Nanomed.* **2008**, *3*, 133–149.

(4) Haute, D. Van; Liu, A. T.; Berlin, J. M. Coating Metal Nanoparticle Surfaces with Small Organic Molecules Can Reduce Nonspecific Cell Uptake. *ACS Nano* **2018**, *12*, 117–127.

(5) Linares, J.; Concepcio, M.; Marques, P. A. A. P.; Portole, M. T. Endocytic Mechanisms of Graphene Oxide Nanosheets in Osteoblasts, Hepatocytes and Macrophages. *ACS Appl. Mater. Interfaces* **2014**, *6*, 13697–13706.

(6) Francia, V.; Yang, K.; Deville, S.; Reker-smit, C.; Nelissen, I.; Salvati, A. Corona Composition Can Affect the Mechanisms Cells Use to Internalize Nanoparticles. *ACS Nano* **2019**, *13*, 11107–11121.

(7) Chithrani, B. D.; Ghazani, A. A.; Chan, W. C. W. Determining the Size and Shape Dependence of Gold Nanoparticle Uptake into Mammalian Cells. *Nano Lett.* **2006**, *6*, 662–668.

(8) Albanese, A.; Tang, P. S.; Chan, W. C. W. The Effect of Nanoparticle Size, Shape, and Surface Chemistry on Biological Systems. *Annu. Rev. Biomed. Eng.* **2012**, *14*, 1–16.

(9) Su, G.; Zhou, H.; Mu, Q.; Zhang, Y.; Li, L.; Jiao, P.; Jiang, G.; Yan, B. Effective Surface Charge Density Determines the Electrostatic Attraction between Nanoparticles and Cells. *J. Phys. Chem. C* **2012**, *116*, 4993–4998.

(10) Bai, X.; Liu, F.; Liu, Y.; Li, C.; Wang, S.; Zhou, H.; Wang, W.; Zhu, H.; Winkler, D. A.; Yan, B. Toward a Systematic Exploration of Nano-Bio Interactions. *Toxicol. Appl. Pharmacol.* **2017**, *323*, 66–73.

(11) Beduneau, A.; Ma, Z.; Grotepas, C. B.; Kabanov, A.; Rabinow, B. E.; Gong, N.; Mosley, R. L.; Dou, H.; Boska, M. D.; Gendelman, H. E. Facilitated Monocyte-Macrophage Uptake and Tissue Distribution of Superparmagnetic Iron-Oxide Nanoparticles. *PLoS One* **2009**, *4*, e4343.

(12) Hauck, T. S.; Ghazani, A. A.; Chan, W. C. W. Assessing the Effect of Surface Chemistry on Gold Nanorod Uptake, Toxicity, and Gene Expression in Mammalian Cells. *Small* **2008**, *4*, 153–159.

(13) Vertegel, A. A.; Siegel, R. W.; Dordick, J. S. Silica Nanoparticle Size Influences the Structure and Enzymatic Activity of Adsorbed Lysozyme. *Langmuir* **2004**, *20*, 6800–6807.

(14) Durán, N.; Silveira, C. P.; Durán, M.; Martinez, D. S. T. Silver Nanoparticle Protein Corona and Toxicity: A Mini-Review. *J. Nanobiotechnology* **2015**, *13*, 55–72.

(15) Lu, F.; Wu, S. H.; Hung, Y.; Mou, C. Y. Size Effect on Cell Uptake in Well-Suspended, Uniform Mesoporous Silica Nanoparticles. *Small* **2009**, *5*, 1408–1413.

(16) Barenholz, Y. Doxil® - The First FDA-Approved Nano-Drug: Lessons Learned. *J. Control. Release* **2012**, *160*, 117–134.

(17) Peer, D.; Karp, J. M.; Hong, S.; Farokhzad, O. C.; Margalit, R.; Langer, R. Nanocarriers as an Emerging Platform for Cancer Therapy. *Nat. Nanotechnol.* **2007**, *2*, 751–760.

(18) Tadros, T.; Izquierdo, P.; Esquena, J.; Solans, C. Formation and Stability of Nano-Emulsions. *Adv. Colloid Interface Sci.* **2004**, *108–109*, 303–318.

(19) Gupta, A.; Eral, H. B.; Hatton, T. A.; Doyle, P. S. Nanoemulsions: Formation, Properties and Applications. *Soft Matter* **2016**, *12*, 2826–2841.

(20) Hörmann, K.; Zimmer, A. Drug Delivery and Drug Targeting with Parenteral Lipid Nanoemulsions - A Review. *J. Control. Release* **2016**, *223*, 85–98.

(21) Takino, T.; Konishi, K.; Takakura, Y.; Hashida, M. Long Circulating Emulsion Carrier Systems for Highly Lipophilic Drugs. *Biol. Pharm. Bull.* **1994**, *17*, 121–125.

(22) Day, R. A.; Estabrook, D. A.; Logan, J. K.; Sletten, E. M. Fluorous Photosensitizers Enhance Photodynamic Therapy with Perfluorocarbon Nanoemulsions. *Chem. Commun.* **2017**, *53*, 13043–13046.

(23) Gladysz, J. A.; Jurisch, M. *Structural, Physical, and Chemical Properties of Fluorous Compounds*; 2012; Vol. 308.

(24) Krafft, M; Riess, J. Perfluorocarbons: Life Sciences and Biomedical Uses. *J. Polym. Sci. Part A Polym. Chem.* **2007**, *45*, 1185–1198.

(25) Riess, J. G.; Riess, J. G. Oxygen Carriers ("blood Substitutes") - Raison d'etre, Chemistry,

and Some Physiology. *Chem. Rev.* **2001**, *101*, 2797–2919.

(26) Tirotta, I.; Dichiarante, V.; Pigliacelli, C.; Cavallo, G.; Terraneo, G.; Bombelli, F. B.; Metrangolo, P.; Resnati, G. 19F Magnetic Resonance Imaging (MRI): From Design of Materials to Clinical Applications. *Chem. Rev.* **2015**, *115*, 1106–1129.

(27) Janjic, J. M.; Ahrens, E. T. Fluorine-Containing Nanoemulsions for MRI Cell Tracking. *Nanomedicine* **2009**, *1*, 492–501.

(28) Tirotta, I.; Mastropietro, A.; Cordiglieri, C.; Gazzera, L.; Baggi, F.; Baselli, G.; Grazia Bruzzone, M.; Zucca, I.; Cavallo, G.; Terraneo, G.; Baldelli Bombelli, F.; Metrangolo, P.; Resnati, G. A Superfluorinated Molecular Probe for Highly Sensitive in Vivo 19F-MRI. *J. Am. Chem. Soc.* **2014**, *136*, 8524–8527.

(29) Tran, T. D.; Caruthers, S. D.; Hughes, M.; Marsh, J. N.; Cyrus, T.; Winter, P. M.; Neubauer, A. M.; Wickline, S. A.; Lanza, G. M. Clinical Applications of Perfluorocarbon Nanoparticles for Molecular Imaging and Targeted Therapeutics. *Int. J. Nanomedicine* **2007**, *2*, 515–526.

(30) Rapoport, N.; Nam, K. H.; Gupta, R.; Gao, Z.; Mohan, P.; Payne, A.; Todd, N.; Liu, X.; Kim, T.; Shea, J.; Scaife, C.; Parker, D. L.; Jeong, E. K.; Kennedy, A. M. Ultrasound-Mediated Tumor Imaging and Nanotherapy Using Drug Loaded, Block Copolymer Stabilized Perfluorocarbon Nanoemulsions. *J. Control. Release* **2011**, *153*, 4–15.

(31) Patrick, M. J.; Janjic, J. M.; Teng, H.; Hear, M. R. O.; Brown, C. W.; Stokum, J. A.; Schmidt, B. F.; Ahrens, E. T.; Waggoner, A. S. Intracellular PH Measurements Using Perfluorocarbon Nanoemulsions. *J. Am. Chem. Soc.* **2013**, *135*, 18445–18457.

(32) Kaneda, M. M.; Sasaki, Y.; Lanza, G. M.; Milbrandt, J.; Wickline, S. A. Mechanisms of Nucleotide Trafficking during SiRNA Delivery to Endothelial Cells Using Perfluorocarbon Nanoemulsions. *Biomaterials* **2010**, *31*, 3079–3086.

(33) Janjic, J. M.; Srinivas, M.; Kadayakkara, D. K. K.; Ahrens, E. T. Self-Delivering Nanoemulsions for Dual Fluorine-19 MRI and Fluorescence Detection. *J. Am. Chem. Soc.* **2008**, *130*, 2832–2841.

(34) Partlow, K. C.; Lanza, G. M.; Wickline, S. A. Exploiting Lipid Raft Transport with Membrane Targeted Nanoparticles : A Strategy for Cytosolic Drug Delivery. *Biomaterials* **2008**, *29*, 3367–3375.

(35) Gould, S. A.; Rosen, A. L.; Sehgal, L. R.; Sehgal, H. L.; Langdale, L. A.; Krause, L. M.; Rice, C. L.; Chamberlin, W. H.; Moss, G. S. Fluosol-DA as a Red-Cell Substitute in Acute Anemia. *N. Engl. J. Med.* **1986**, *314*, 1653–1656.

(36) Viegas, T. X.; Bentley, M. D.; Harris, J. M.; Fang, Z.; Yoon, K.; Dizman, B.; Weimer, R.; Mero, A.; Pasut, G.; Veronese, F. M. Polyoxazoline : Chemistry , Properties , and Applications in Drug Delivery. *Bioconjugate* **2011**, *22*, 976–986.

(37) Hoogenboom, R. Poly(2-Oxazoline)s: A Polymer Class with Numerous Potential Applications. *Angew. Chemie - Int. Ed.* **2009**, *48*, 7978–7994.

(38) Estabrook, D. A.; Ennis, A. F.; Day, R. A.; Sletten, E. M. Controlling Nanoemulsion Surface Chemistry with Poly(2-Oxazoline) Amphiphiles. *Chem. Sci.* **2019**, *10*, 3994–4003.

(39) Feng, H.; Lu, X.; Wang, W.; Kang, N. G.; Mays, J. W. Block Copolymers: Synthesis, Self-Assembly, and Applications. *Polymers (Basel).* **2017**, *9*, 494–525.

(40) Tadros, T. Principles of Emulsion Stabilization with Special Reference to Polymeric Surfactants. *J. Cosmet. Sci.* **2006**, *57*, 153–169.

(41) Hoogenboom, R.; Wiesbrock, F.; Huang, H.; Leenen, M. A.M.; Thijs, H. M.L.; Van Nispen, S. F. G. M.; Van Der Loop, M.; Fustin, C. A.; Jonas, A. M.; Gohy, J. F.; Schubert, U. S. Microwave-Assisted Cationic Ring-Opening Polymerization of 2-Oxazolines: A Powerful Method for the Synthesis of Amphiphilic Triblock Copolymers. *Macromolecules* **2006**, *39*, 4719–4725.

(42) Lava, K.; Verbraeken, B.; Hoogenboom, R. Poly (2-Oxazoline) s and Click Chemistry : A Versatile Toolbox toward Multi-Functional Polymers. *Eur. Polym. J.* **2015**, *65*, 98–111.

(43) Day, R. A.; Estabrook, D.; Wu, C.; Chapman, J. O.; Togle, A. J.; Sletten, E. M. Systematic Study of Perfluorocarbon Nanoemulsions Stabilized by Polymer Amphiphiles. *ACS Appl. Mater. Interfaces* **2020**, *12*, 38887–38898.

(44) Castro, C. I.; Briceno, J. C. Perfluorocarbon-Based Oxygen Carriers: Review of Products and Trials. *Artif. Organs* **2010**, *34*, 622–634.

(45) Duncanson, W. J.; Arriaga, L. R.; Ung, W. L.; Kopechek, J. A.; Porter, T. M.; Weitz, D. A. Microfluidic Fabrication of Perfluorohexane-Shelled Double Emulsions for Controlled Loading and Acoustic-Triggered Release of Hydrophilic Agents. *Langmuir* **2014**, *30*, 13765–13770.

(46) Hannah, A. S.; VanderLaan, D.; Chen, Y.-S.; Emelianov, S. Y. Photoacoustic and Ultrasound Imaging Using Dual Contrast Perfluorocarbon Nanodroplets Triggered by Laser Pulses at 1064 Nm. *Biomed. Opt. Express* **2014**, *5*, 3042–3053.

(47) Spence, R K; Norcross, E D; Costabile, Joseph; Mccoy, Sue; Cernaianu, Aurel C; Alexander, James B; Pello, Mark J; Atabek, Umur; Camishion, Rudolph C; Norcross, E D; Costabile, Joseph; Mccoy, S.; Aurel, C. Perfluorocarbons as Blood Substitutes : The Early Years : Experience with Fluosol DA-20 % in The. *Artif. Cells, Blood Substitutes, Biotechnol.* **1994**, *22*, 955–963.

(48) Barres, A. R.; Molugu, S. K.; Stewart, P. L.; Mecozzi, S. Droplet Core Intermolecular Interactions and Block Copolymer Composition Heavily Influence Oil-In-Water Nanoemulsion Stability. *Langmuir* **2019**, *35*, 12765–12772.

(49) Levin, Aviad; Mason, Thomas O.; Adler-Abramovich, Lihi; Buell, Alexander K.; Meisl, George; Galvagnion, Celine; Bram, Yaron; Stratford, Samuel A.; Dobson, Christopher M.; Knowles, Tuomas P. J.; Gazit, E. Ostwald's Rule of Stages Governs Structural Transitions and Morphology of Dipeptide Supramolecular Polymers. *Nat. Commun.* **2014**, *5*, 5219.

(50) Tadros, T. F. *Emulsion Formation and Stability*; 2013.

(51) Lowe, K. C. Perfluorinated Blood Substitutes and Artificial Oxygen Carriers. *Blood Rev.* **1999**, *13*, 171–184.

(52) Griffin, W. C. Classification of Surface-Active Agents by HLB. *J. Soc. Cosmet. Chem.* **1949**, *1*, 311–326.

(53) Pasquali, R. C.; Taurozzi, M. P.; Bregni, C. Some Considerations about the Hydrophilic-Lipophilic Balance System. *Int. J. Pharm.* **2008**, *356*, 44–51.

(54) Delage, B.; Briou, B.; Brossier, T.; Catrouillet, S.; Robin, J. J.; Lapinte, V. Polyoxazoline Associated with Cardanol for Bio-Based Linear Alkyl Benzene Surfactants. *Polym. Int.* **2019**, *68*, 755–763.

(55) Giardi, C.; Lapinte, V.; Charnay, C.; Robin, J. J. Nonionic Polyoxazoline Surfactants Based on Renewable Source: Synthesis, Surface and Bulk Properties. *React. Funct. Polym.* **2009**, *69*, 643–649.

(56) Sletten, E. M.; Swager, T. M. Readily Accessible Multifunctional Fluorous Nanoemulsions. *Chem. Sci.* **2016**, *7*, 5091–5097.

(57) Sletten, E. M.; Swager, T. M. Fluorofluorophores: Fluorescent Fluorous Chemical Tools Spanning the Visible Spectrum. *J. Am. Chem. Soc.* **2014**, *136*, 13574–13577.

(58) Miller, M. A.; Sletten, E. M. A General Approach to Biocompatible Branched Fluorous Tags for Increased Solubility in Perfluorocarbon Solvents. *Org. Lett.* **2018**, *20*, 6850–6854.

(59) Boija, E.; Johansson, G. Interactions between Model Membranes and Lignin-Related Compounds Studied by Immobilized Liposome Chromatography. *Biochim. Biophys. Acta* **2006**, *1758*, 620–626.

(60) Delmas, T.; Piraux, H.; Couffin, A. C.; Texier, I.; Vinet, F.; Poulin, P.; Cates, M. E.; Bibette, J. How to Prepare and Stabilize Very Small Nanoemulsions. *Langmuir* **2011**, *27*,

1683–1692.

(61) Allen, C.; Dos Santos, N.; Gallagher, R.; Chiu, G. N. C.; Shu, Y.; Li, W. M.; Johnstone, S. A.; Janoff, A. S.; Mayer, L. D.; Webb, M. S.; Bally, M. B. Controlling the Physical Behavior and Biological Performance of Liposome Formulations through Use of Surface Grafted Poly(Ethylene Glycol). *Biosci. Rep.* **2002**, *22*, 225–250.

(62) Marzio, L. Di; Marianecci, C.; Cinque, B.; Nazzarri, M.; Cimini, A. M.; Cristiano, L.; Cifone, M. G.; Alhaique, F.; Carafa, M. PH-Sensitive Non-Phospholipid Vesicle and Macrophage-like Cells : Binding , Uptake and Endocytotic Pathway. *Biochem. Biophys. Acta* **2008**, *1778*, 2749–2756.

(63) Almalik, A.; Karimi, S.; Ouasti, S.; Donno, R.; Wandrey, C.; Day, P. J.; Tirelli, N. Hyaluronic Acid (HA) Presentation as a Tool to Modulate and Control the Receptor-Mediated Uptake of HA-Coated Nanoparticles. *Biomaterials* **2013**, *34*, 5369–5380.

(64) Chithrani, B. D.; Chan, W. C. W. Elucidating the Mechanism of Cellular Uptake and Removal of Protein-Coated Gold Nanoparticles of Different Sizes and Shapes. *Nano Lett.* **2007**, *7*, 1542–1550.

(65) Misinzo, G.; Delputte, P. L.; Nauwynck, H. J. Inhibition of Endosome-Lysosome System Acidification Enhances Porcine Circovirus 2 Infection of Porcine Epithelial Cells. *J. Virol.* **2008**, *82*, 1128–1135.

(66) Wang, L.; Rothberg, K. G.; Anderson, R. G. W. Mis-Assembly of Clathrin Lattices on Endosomes Reveals a Regulatory Switch for Coated Pit Formation Materials and Methods. *J. Cell Biol.* **1993**, *123*, 1107–1117.

(67) Konradi, R.; Acikgoz, C.; Textor, M. Polyoxazolines for Nonfouling Surface Coatings — A Direct Comparison to the Gold Standard PEG. *Macromol. Rapid Commun.* **2012**, *33*, 1663–1676.

(68) Konradi, R.; Pidhatika, B.; Mu, A.; Textor, M. Poly-2-Methyl-2-Oxazoline : A Peptide-like Polymer for Protein-Repellent Surfaces. *Langmuir* **2008**, *23*, 613–616.

(69) Tong, J.; Luxenhofer, R.; Yi, X.; Jordan, R.; Kabanov, A. V. Protein Modification with Amphiphilic Block Copoly (2-Oxazoline) s as a New Platform for Enhanced Cellular Delivery. *Mol. Pharm.* **2010**, *7*, 984–992.

(70) Woodle, M. C.; Engbers, C. M.; Zalipsky, S. New Amphipatic Polymer—Lipid Conjugates Forming Long-Circulating Reticuloendothelial System-Evading Liposomes. *Bioconjug. Chem.* **1994**, *5*, 493–496.

(71) Wilson, P.; Ke, P. C.; Davis, T. P.; Kempe, K. Poly(2-Oxazoline)-Based Micro- and Nanoparticles: A Review. *Eur. Polym. J.* **2017**, *88*, 486–515.

(72) Koshkina, Olga; Westmeier, Dana; Lang, Thomas; Bantz, Christoph; Hahlbrock, Angelina; Würth, Christian; Resch-genger, Ute; Braun, Ulrike; Thiermann, Raphael; Weise, Christoph; Eravci, Murat; Mohr, Benjamin; Schlaad, Helmut; Stauber, Roland H; Docter, Domi, M. Tuning the Surface of Nanoparticles : Impact of Poly (2-Ethyl-2-Oxazoline) on Protein Adsorption in Serum and Cellular Uptake. *Macromol. Biosci.* **2016**, *16*, 1287–1300.

(73) Chem, P.; Barz, M.; Luxenhofer, R. Overcoming the PEG-Addiction: Well-Defined Alternatives to PEG, from Structure–Property. *Polym. Chem.* **2011**, *2*, 1900–1918.

(74) Suk, J. S.; Xu, Q.; Kim, N.; Hanes, J.; Ensign, L. M.; Sciences, H.; Sciences, M. PEGylation as a Strategy for Improving Nanoparticle-Based Drug and Gene Delivery. *Adv. Drug Deliv. Rev.* **2016**, *99*, 28–51.

(75) Schöttler, S.; Becker, G.; Winzen, S.; Steinbach, T.; Mohr, K.; Landfester, K.; Mailänder, V.; Wurm, F. R. Protein Adsorption Is Required for Stealth Effect of Poly(Ethylene Glycol)- and Poly(Phosphoester)- Coated Nanocarriers. *Nat. Nanotechnol.* **2016**, *11*, 372–377.

CHAPTER THREE

Perfluorocarbon nanomaterials for photodynamic therapy

Adapted from: Rachael A. Day, Daniel A. Estabrook, Jessica K. Logan and Ellen M. Sletten.* Fluorous photosensitizers enhance photodynamic therapy with perfluorocarbon nanoemulsions. *Chem. Commun.* **2017**, *53*, 13043-13046. DOI: 10.1039/c7cc07038a

and

Rachael A. Day, and Ellen M. Sletten.* Perfluorocarbon nanomaterials for photodynamic therapy. *Curr. Opin. Colloid Interface Sci.* **2021**, *54*, 101454, DOI: 10.1016/j.cocis.2021.101454.

3.1 Abstract

Photodynamic therapy (PDT) is a treatment modality in which a photosensitizer is irradiated with light, producing reactive oxygen species, often via energy transfer with oxygen. As it is common for tumors to be hypoxic, methods to deliver photosensitizer and oxygen are desirable. One such approach is the use of perfluorocarbons, molecules in which all C—H bonds are replaced with C—F bonds, to co-deliver oxygen due to the high solubility of gases in perfluorocarbons. This chapter highlights the benefits and limitations of several fluorinated nanomaterial architectures for use in PDT.

3.2 Introduction

The harsh, chaotic, and hypoxic environments of solid tumors continue to be a difficult target for classic small molecule therapeutics. Traditional chemotherapeutics often clear rapidly and have significant off-target effects. To combat these limitations, nanomaterials have been designed to solubilize and mask insoluble cargoes, increase the serum half-lives of drugs, allow for stimuli induced release of therapeutics, and facilitate tumor uptake through the addition of active targeting groups.[1] In addition, nanomedicine boasts many scaffolds that can be tuned to a specific target or cargo based on the desired application.

A complementary approach to limiting off-target effects is to apply an external stimulus that triggers a therapeutic effect only at a tumor site. A member of this class of therapies is photodynamic therapy (PDT), the use of light to induce cell death. PDT requires three components: i) light ii) photosensitizer (PS) and iii) oxygen, the latter of which is transformed into cytotoxic reactive oxygen species (ROS, Figure 3.1A).[2] The first FDA-approved iteration of PDT employed Photofrin™ (**3.1**), a systemically administered oligomeric photosensitizer, which has been used to treat bladder, esophageal, lung, and endobronchial cancers.[3] A limitation of Photofrin™ is that, similar to other small molecule chemotherapeutics, it undergoes broad biodistribution and accumulates in the skin and reticuloendothelial system, in addition to the tumor. When patients are exposed to sunlight, the photosensitizer is activated, resulting in side effects. To minimize the light sensitivity during PDT, the benefits of nanomaterials– originally studied for classic chemotherapeutics– are being leveraged to help selectively deliver the photosensitizer to the tumor. This approach provides two layers of targeting to increase specificity: targeting via the nanomaterial and the external stimuli.

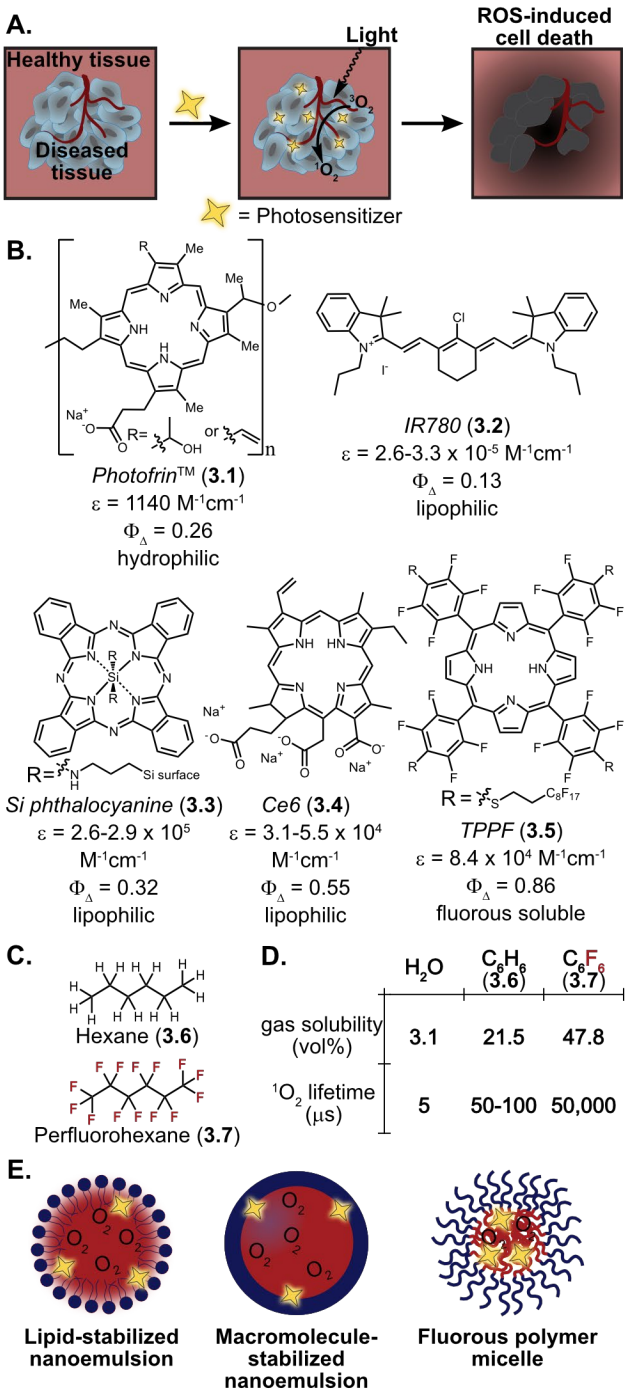

Figure 3.1. (A) Photodynamic therapy (PDT) involves the introduction of a photosensitizer, which generates reactive oxygen species (ROS) upon irradiation with light to result in cell death. (B) Structures of common photosensitizers. (C) Molecular structures of hydrocarbon (**3.6**) and perfluorocarbon (**3.7**). (D) Table of gas solubilities and singlet oxygen lifetimes in water, hexanes (**3.6**) and perfluorohexanes (**3.7**). (E) Common perfluorocarbon nanomaterials for PDT discussed herein.

Nanoparticles for PDT traditionally contain hydrophobic photosensitizers (Figure 3.1B) such as cyanine dyes (**3.2**), phthalocyanines (**3.3**) chlorins (**3.4**) or porphyrins (**3.5**).[4] Ideal photosensitizers for PDT absorb near-infrared light with high absorption coefficients (ε) and efficiently convert the majority of the absorbed light into reactive oxygen species (ROS), which is most commonly classified by the singlet oxygen quantum yield (Φ_Δ). Cyanine dyes, phthalocyanines, and chlorins have excellent absorption properties, while the phthalocyanines, chlorins, and porphyrins have the highest Φ_Δ. One limitation of these hydrophobic photosensitizers is they are prone to self-aggregation, decreasing the efficiency of the photosensitizer by reducing the absorption coefficient (ε) and/or singlet oxygen quantum yield (Φ_Δ). Aggregation is evident by the broadening and blue shift of the absorbance of the PS and multiple strategies are highlighted in this review to maximize PDT efficiency by preventing photosensitizer aggregation.

A particularly promising nanomaterial scaffold for PDT are those that contain perfluorocarbons. Perfluorocarbons (PFCs) are molecules in which all C—H bonds have been replaced with C—F bonds (such as hexanes (**3.6**) vs. perfluorohexanes (**3.7**)). PFCs form a separate, extremely hydrophobic and lipophobic phase termed the "fluorous phase" (Figure 3.1C). Perfluorocarbon nanomaterials are advantageous for PDT due to the fluorous phase boasting up to 20-fold higher dissolved gas concentrations compared to aqueous phases allowing oxygen, one of the three essential components for PDT, to be delivered alongside the photosensitizer. The high gas solubility in the fluorous phase is due to the weak van der Waals interactions between perfluorocarbon chains (Figure 3.1D).[5–8] Indeed the high oxygen solubility in PFCs has been used clinically in the 1980s and 1990s when perfluorocarbon nanoemulsions were employed as blood substitutes.[5,9]

In addition, fluorous nanomaterials are an attractive scaffold for PDT due to the extremely long singlet oxygen lifetimes in perfluorocarbons. The strength of the C—F bond renders it stable to the highly reactive singlet oxygen, leading to half-lives 1000 times longer than in water (Figure 3.1D).[10] The increased lifetime of the singlet oxygen provides a higher probability that singlet oxygen will diffuse into the water in which it can react with surrounding biomolecules.[11,12] In this chapter, we will highlight recent advances in fluorous photodynamic therapy focusing on the various ways to deliver oxygen via perfluorinated architectures. We will cover three main architectures: lipid-stabilized nanoemulsions, macromolecule-stabilized nanoemulsions, and fluorous micelles (Figure 3.1E).

3.3 Results and Discussion

Perfluorocarbon (PFC) nanoemulsions, droplets of fluorous solvent stabilized by a surfactant, are a compelling platform for PDT owing to the high oxygen content in perfluorocarbons (Figure 3.2A).[5,9] Previously, we have shown that fluorophores can be localized inside PFC nanoemulsions when fluorous chains are appended to the chromophore scaffold.[13] We imagined that a similar strategy could be employed to load PFC nanoemulsions with a photosensitizer to result in an exceptional nanomaterial for PDT (Figure 3.2B). Efforts to enhance PDT with perfluorocarbons began in 1988 when Henderson and co-workers co-injected a porphyrin photosensitizer with PFC nanoemulsions.[14] Despite promising results, this approach remained dormant for 25 years until cyanine dyes were embedded into the surfactant layer of PFC nanoemulsions to facilitate dual oxygen and photosensitizer delivery.[11,15–17] Contemporary variants of co-administration of photosensitizer and PFC nanoemulsions have also been pursued.[18]

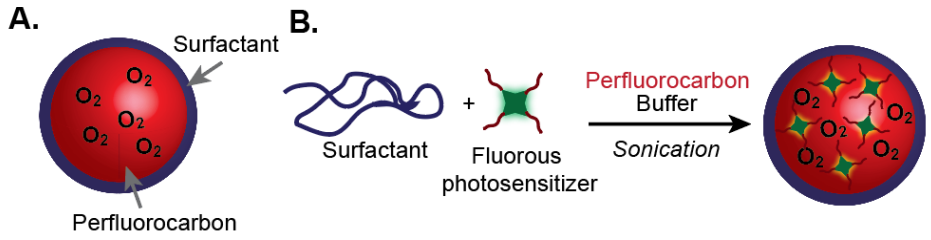

Figure 3.2 (A) Photodynamic therapy (PDT) involves the introduction of a photosensitizer which generates reactive oxygen species (ROS) upon irradiation with light to result in cell death. (B) Perfluorocarbon (PFC) nanoemulsions are droplets of fluorous solvent stabilized with surfactant. They have high oxygen content. (C) One step formulation of PFC nanoemulsions for PDT.

Collectively, these reports demonstrate the potential of PFC nanoemulsions for PDT. However, organic photosensitizers are not compatible with the fluorous solvent, which can lead to inefficient photosensitization and leaching. Here, we establish that the use of a fluorous soluble photosensitizer localized within PFC nanoemulsions enhances the efficacy of PDT.

To probe the influence of fluorous soluble photosensitizers on PFC nanoemulsion-based PDT, we prepared fluorous porphyrin **3.8** along with a control hydrocarbon analogue **3.9** (Figure 3.3A, Scheme 3.1).[19] Photophysical characterization of **3.8** and **3.9** in Dimethylformamide (Figure 3.6) indicates that the absorption, emission, and oxygen sensitization of the porphyrins are minimally altered by the fluorous or alkyl chain appendages (Figure 3.3B). Next, we tested the solubility of **3.8** and **3.9** in numerous fluorous and organic solvents (Figures 3.4-3.5), and thoroughly investigated their photophysics in hexanes (HEX, **3.6**) and perfluorohexanes (PFH, **3.7**) as model solvents for each phase (Figure 3.3C). Fluorous porphyrin **3.8** can be solubilized in both HEX and PFH, as evidenced by robust absorption and emission in each solvent. Distinctly different results are obtained with **3.9**, which is soluble in HEX but not PFH. We further explored

Scheme 3.1. Synthesis of 5,10,15,20-Tetrakis[4-(10H,10H,20H,20H-perfluorododecyl) -2,3,5,6- tetrafluorophenyl] porphyrin **3.8**, and 5,10,15,20-Tetrakis[4-(10H,10H,20H,20H-dodecyl) -2,3,5,6- tetrafluorophenyl] porphyrin **3.9**.

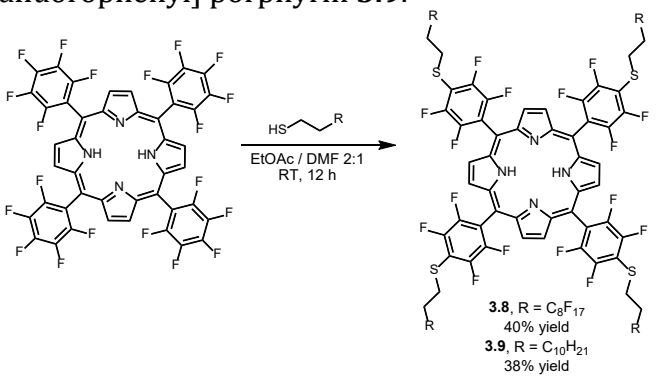

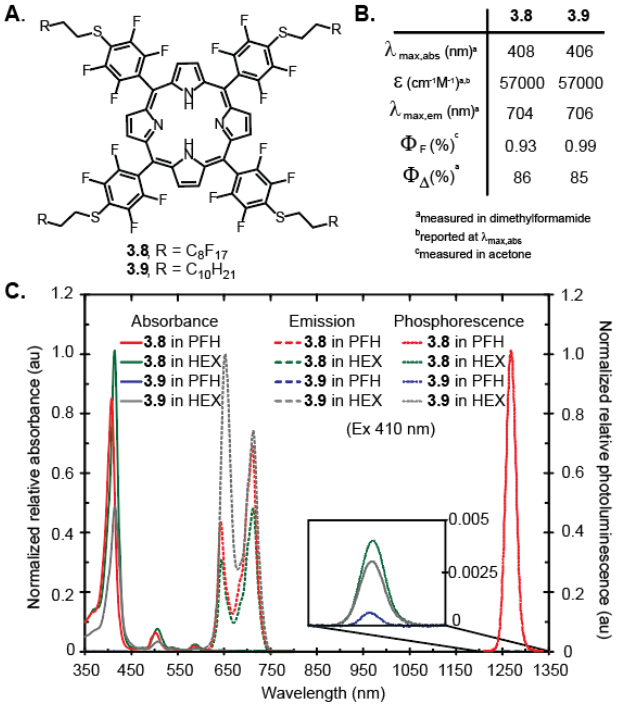

Figure 3.3 (A) Structures of fluorous-tagged (**3.8**) and hydrocarbon-tagged (**3.9**) porphyrin photosensitizers. (B) Photophysical characterization of **3.8** and **3.9** in dimethylformamide. See Figure 3.6 for spectra in dimethylformamide. (C) Normalized relative absorbance, emission, and phosphorescence spectra of the photosensitizers in hexanes (HEX) and perfluorohexanes (PFH). Solid line = absorbance; Dashed line = emission (Ex 410 nm); Dotted line = singlet oxygen phosphorescence (Ex 410 nm, 1000 nm longpass filter). Red = **3.8** in PFH; Green = **3.8** in HEX; Blue = **3.9** in PFH; Grey = **3.9** in HEX.

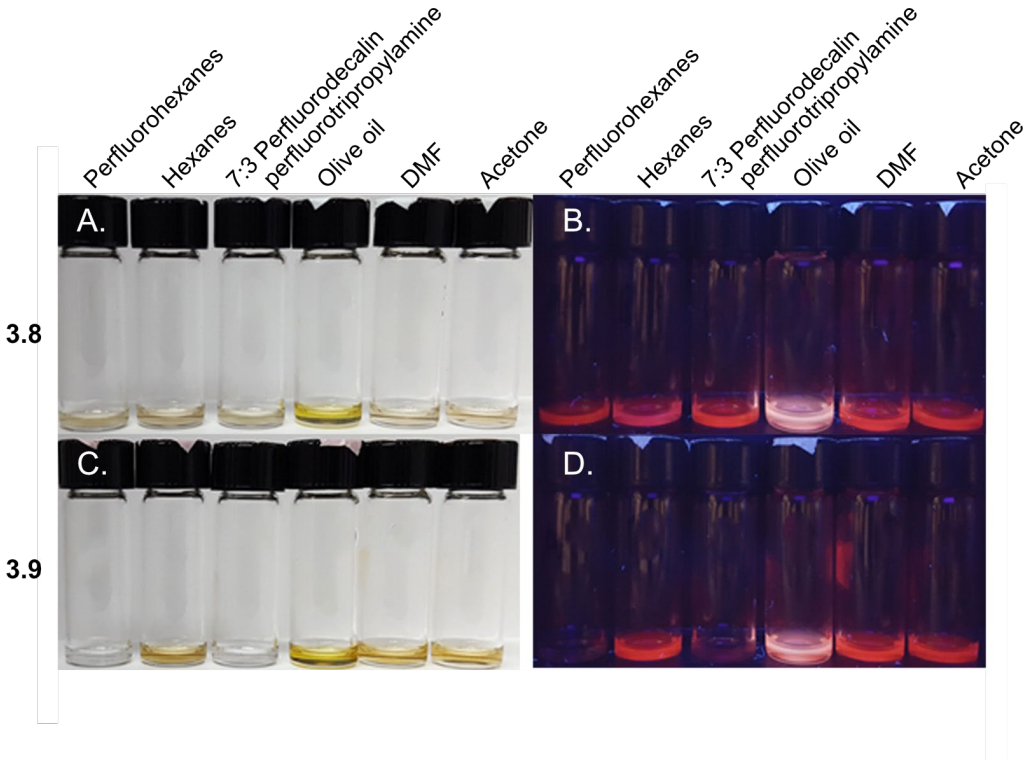

Figure 3.4 Solubility of photosensitizers.
Porphyrins **3.8** (A, B) or **3.9** (C, D) (18.6 nmol) were dissolved in selected solvents (200 μL). Photographs were taken in either visible (A, C) or long-wave UV light (B, D).

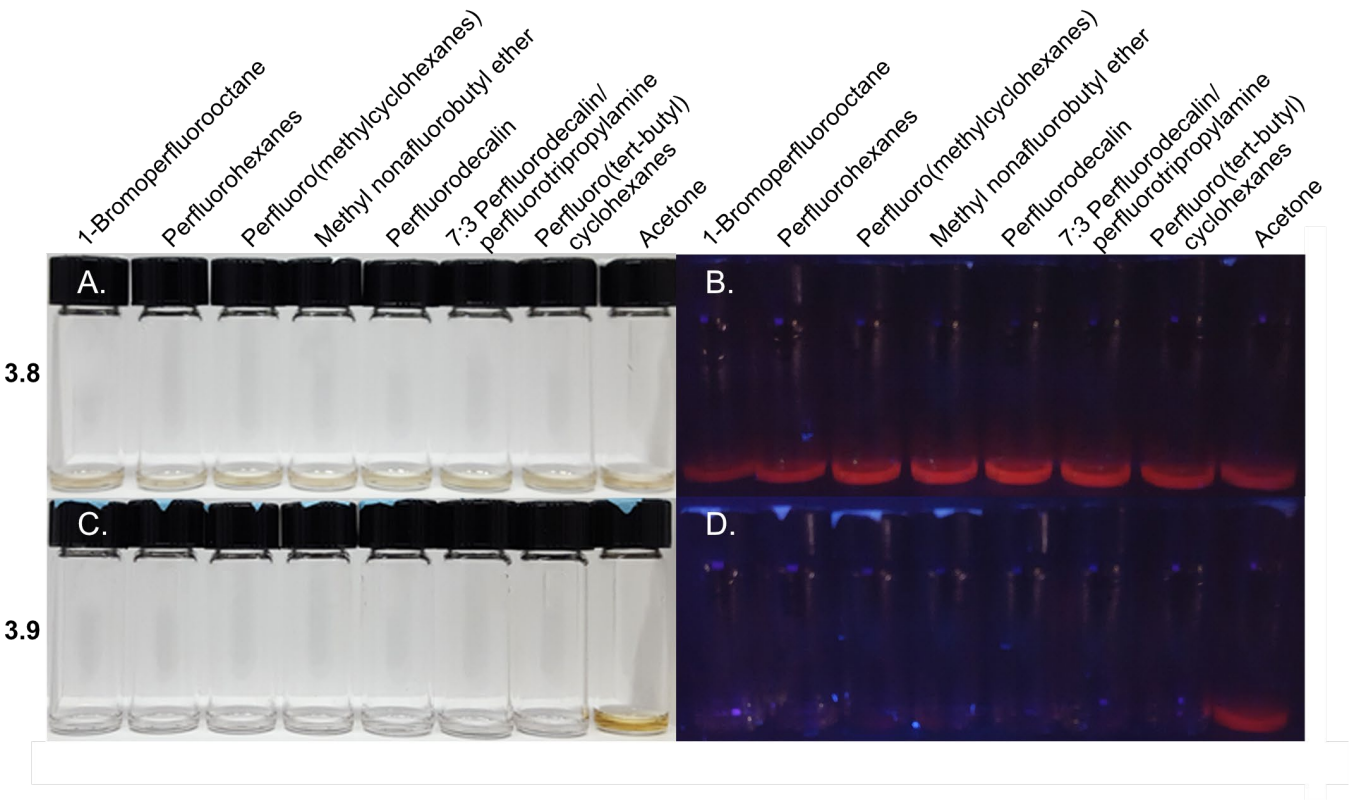

Figure 3.5 Solubility of photosensitizers.
Porphyrins **3.8** (A, B) or **3.9** (C, D) (18.6 nmol) were dissolved in selected fluorous solvents (200 μL). Photographs were taken in either visible (A, C) or long-wave UV light (B, D).

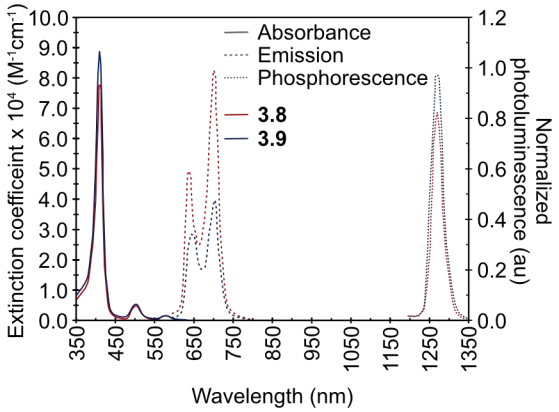

Figure 3.6 Characterization of porphyrins **3.8** and **3.9** in dimethylformamide (30 □M).

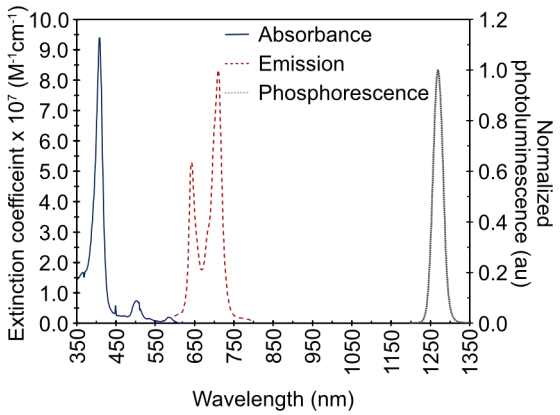

Figure 3.7 Characterization of fluorous porphyrin **3.8** in 7:3 perfluorodecalin/perfluorotripropylamine (30 μM). Absorbance (blue), fluorescence (red-dashed, Ex 410 nm), and singlet oxygen phosphorescence were measured (grey-dotted, Ex 410 nm, collected with 1000 nm longpass filter).

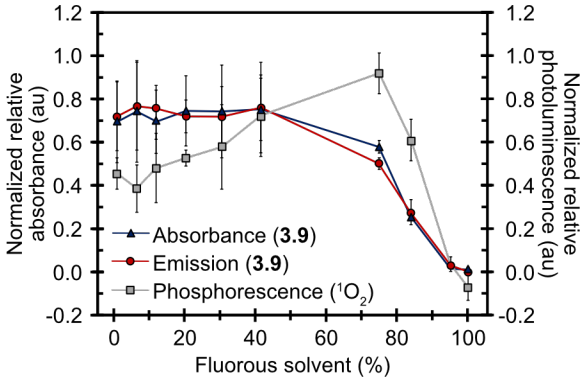

Figure 3.8 Aggregation of hydrophobic porphyrin **3.9** in fluorous solvent.
Porphyrin **3.9** (1.16 nmol) was dissolved in DMF with increasing amounts of methoxyperfluorobutane added (total volume = 0.75 mL). All data were normalized relative to $\lambda_{max,\ abs}$, $\lambda_{max,\ em}$, and $\lambda_{max,\ phos}$. Plotted are the averages of the normalized $\lambda_{max,abs}$ (blue, $\lambda_{max,abs}$ = 410 nm), $\lambda_{max,em}$ (red, Ex 410 nm, $\lambda_{max,em}$ = 705 nm), and $\lambda_{max,phos}$ (grey, Ex 410 nm, collected with 1000 nm longpass filter, $\lambda_{max,phos}$ = 1274 nm). Error bars represent the standard deviation of three samples.

the aggregation of **3.9** in the presence of fluorous solvent and found that a significant decrease in absorption and emission begins in solutions containing greater than 50% fluorous solvent (Figure 3.8). Aggregation is a common occurrence with chromophores that leads to low quantum yields of emission (Φ_F) and oxygen sensitization (Φ_Δ).[20] Thus, these data suggest that when organic photosensitizers are employed in PFC emulsions, aggregation will decrease $^1O_2$ production.

The most striking data observed in the photophysical characterization of **3.8** and **3.9** is the superior production of $^1O_2$ with fluorous photosensitizer **3.8** in PFH (Figure 3.3C), assayed via the direct detection of $^1O_2$ phosphorescence at 1274 nm.[21] These data are attributed to the high oxygen content in PFH relative to HEX (4.23 vs. 1.99 mM),[22] the long half-life of $^1O_2$ in perfluorocarbons[10] as well as the ability for **3.8** to readily come into contact with O_2. Similar photophysics of **3.8** were observed when measured in the 7:3 mixture of perfluorodecalin (PFD) : perfluorotripropylamine (PFTPA) that makes up the inner phase of the PFC nanoemulsions (Figure 3.7). Oxygen sensitization is a Dexter-type energy transfer which requires the two species to be within 10-20 Å of each other.[23,24] Therefore, solubilizing O_2 and photosensitizer in the same phase should lead to enhanced Φ_Δ. Efficient sensitization of oxygen in perfluorocarbons has been observed in synthetic chemistry[25,26] and is also supported by PDT with surfaces[27] and polymer micelles[28,29] containing fluorous segments and photosensitizers.

With positive initial photophysical characterization of **3.8** and **3.9**, we prepared PFC and oil emulsions containing each photosensitizer (Figure 3.9A, emulsions **A**–**D**). PFC nano-emulsions were prepared with a mixture of 7:3 PFD : PFTPA (10 vol%) stabilized by

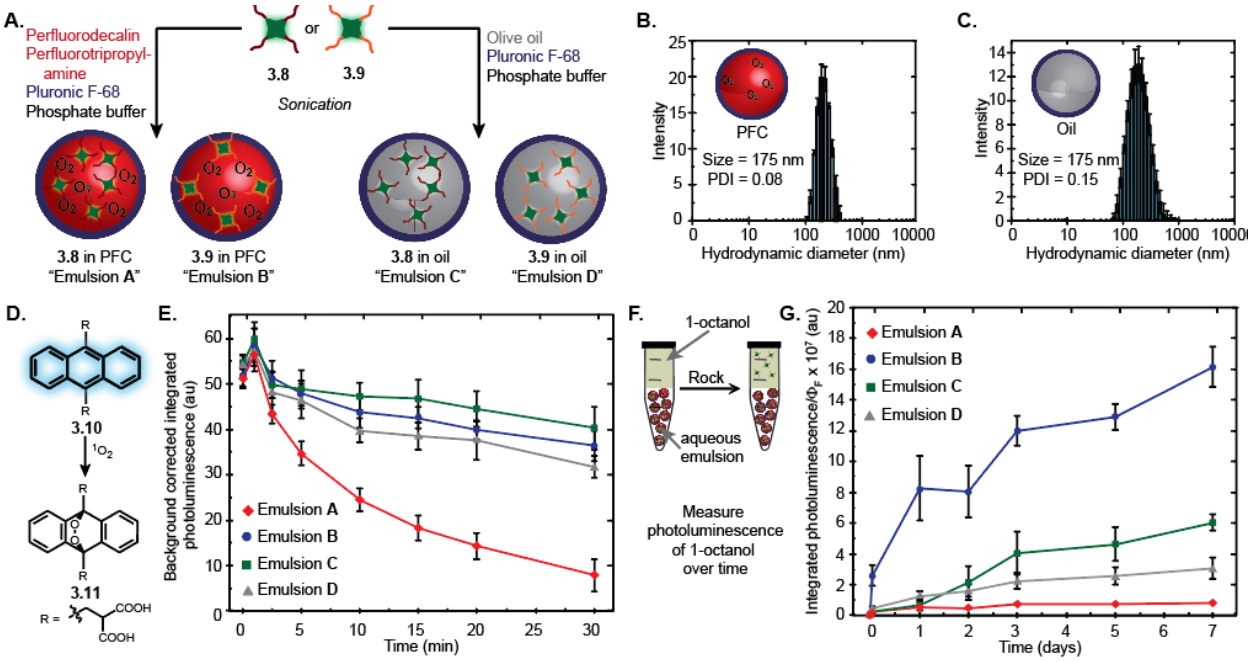

Figure 3.9 (A) Preparation of perfluorocarbon (PFC) and oil emulsions containing fluorous-and hydrocarbon-tagged photosensitizers. Porphyrin **3.8** or **3.9** was pre-dissolved in 7:3 perfluorodecalin/perfluorotripropylamine or olive oil. 10 vol% of the porphyrin solutions was combined with phosphate buffer containing 2.8 wt% Pluronic F-68. Sonication produced the emulsions. (B/C) Dynamic light scattering data for empty PFC (B) and oil (C) emulsions. (D) Anthracene trap assay. (E) Background-corrected photoluminescence of **3.10** (Ex 410 nm) vs. time of solutions containing emulsion **A-D** and **3.10**. The solutions were irradiated with 420 nm light at 8.5 mW/cm^2. (F) Schematic of partition experiment to determine the degree of photosensitizer leaching. (G) The integrated photoluminescence of **3.8** or **3.9** in the 1-octanol normalized by Φ_F vs. time. (E/G) Emulsion **A** (red, diamond), **B** (blue, circle), **C** (green, square), or **D** (grey, triangle). Error bars represent the standard deviation of 3 replicate samples.

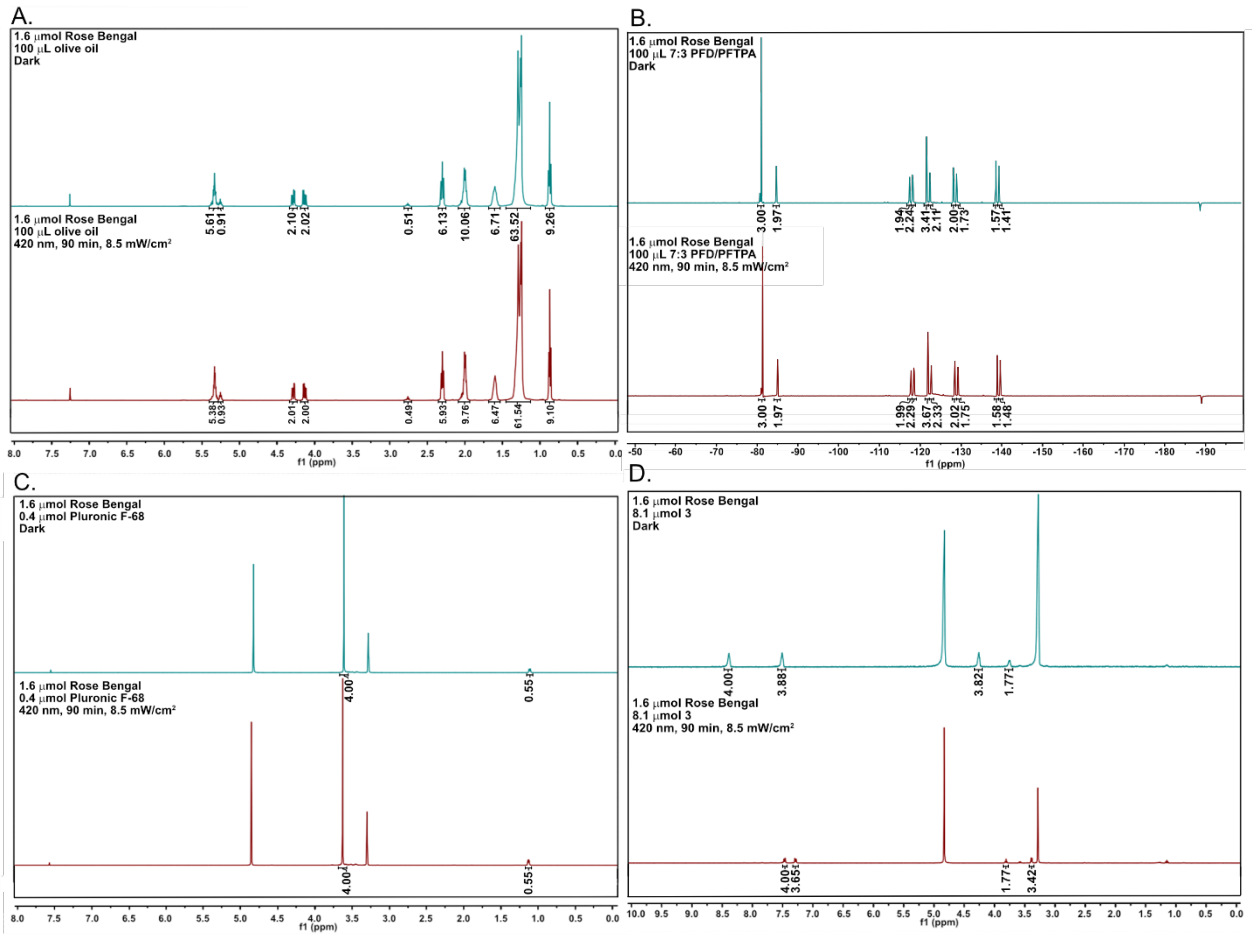

Figure 3.10 Stability of oil, perfluorocarbon solvents and Pluronic F-68 in the presence of $^1O_2$. (A) Rose Bengal (1.6 µmol) and olive oil (100 µL) were combined in $CDCl_3$ (0.5 mL) and kept in the dark or irradiated with light. ^1H-NMR spectra were collected. (B) Rose Bengal (1.6 µmol) and 7:3 perfluorodecalin/perfluorotripropylamine (100 µL) were combined in $CDCl_3$ and kept in the dark or irradiated with light. ^{19}F-NMR spectra were collected. (C) Rose Bengal (1.6 µmol) and Pluronic F-68 (0.4 µmol) were combined in CD_3OD (0.5 mL) and kept in the dark or irradiated with light. ^1H-NMR spectra were collected. (D) Rose Bengal (1.6 µmol) and **3.10** (8.1 µmol) were combined in $CDCl_3$ (0.5 mL) and kept in the dark or irradiated with light. ^1H-NMR spectra were collected. (A-D) Dark samples are in the top panel (blue) and irradiated samples are in the bottom panel (red). Irradiation was performed with 420 nm, 90 min, 8.5 mW/cm^2.

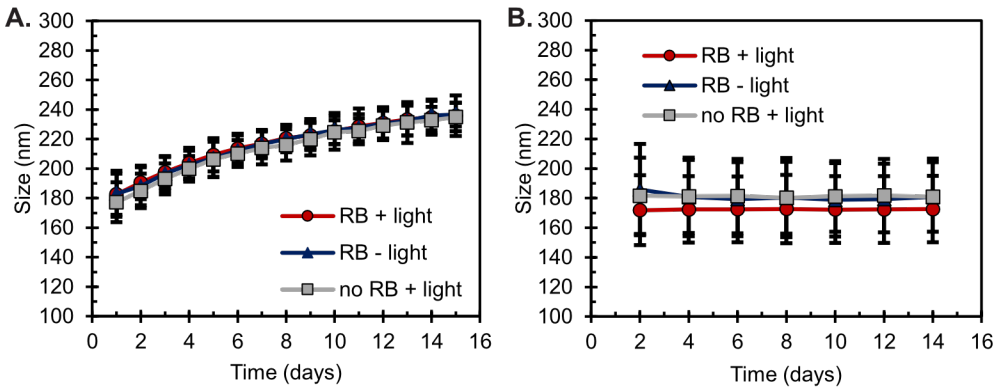

Figure 3.11 Stability of emulsions in the presence of $^1O_2$
(A) Perfluorocarbon nanoemulsions and (B) olive oil emulsions were prepared through ultrasonication (35% amp, 90 sec) of solutions containing fluorous or organic phase (10 vol%) and Pluronic F-68 (2.8 wt%) in phosphate buffered saline (PBS, pH 7.4). Rose Bengal (RB, 4 μM) was added to the aqueous phase (red, blue) and the size of the emulsions was monitored by dynamic light scattering (DLS) over two weeks. Emulsions were exposed to light (420 nm, 30 min, 8.5 mW/cm^2) prior to every measurement (red, grey). A no light control was also performed (blue). Error bars represent standard deviation of the product of the $Z_{average}$ and the polydispersity index of three replicate samples.

Pluronic F-68 (2.8 wt%) in phosphate buffered saline (PBS) to result in 175 nm emulsions with a polydispersity of 0.08 (Figure 3.9B). Oil emulsions were prepared with olive oil (10 vol%) and Pluronic F-68 (2.8 wt%) in PBS to yield 175 nm emulsions with a polydispersity of 0.15 (Figure 3.9C). We assayed the emulsions and all components for stability to $^1O_2$ and did not observe any significant $^1O_2$-induced degradation of the components (Figure 3.10) or instability of the emulsions (Figure 3.11).

Next, we investigated the ability of emulsions **A**–**D** to deliver $^1O_2$ to the surrounding aqueous media. For these studies, we employed water-soluble, anthracene **3.10**, which undergoes a Diels-Alder reaction with $^1O_2$ to produce non-emissive adduct **3.11** (Figure 3.9D).[30] Mixtures of **3.10** and emulsions **A–D** in PBS were irradiated with 420 nm light (8.5 mW/cm^2), and their photoluminescence was monitored over time. The data show (Figure 3.9E) that the PFC nanoemulsion containing **3.8** (emulsion **A**) delivers the most $^1O_2$ to the surrounding environment, with the oil emulsions (emulsions **C**,**D**) and the PFC nanoemulsion containing **3.9** (emulsion **B**) displaying similar, lower levels of $^1O_2$ production. In contrast to the photophysical characterization of **3.9** in PFH, we found that some **3.9** could be incorporated into PFC emulsions (Figure 3.12). This result is likely due to interactions between **3.9** and the Pluronic F-68 surfactant. Similar interactions have enabled the preparation of cyanine-dye loaded PFC nanoemulsions for PDT. [11,15–17]

We suspected that **3.9** within emulsion **B** would readily leach into surrounding lipophilic media, while **3.8** would be retained inside the PFC nanoemulsions. Leaching and premature drug release are significant problems in nanomedicine and should be considered alongside efficacy when evaluating new therapeutic materials.[31] To demonstrate that the use of a

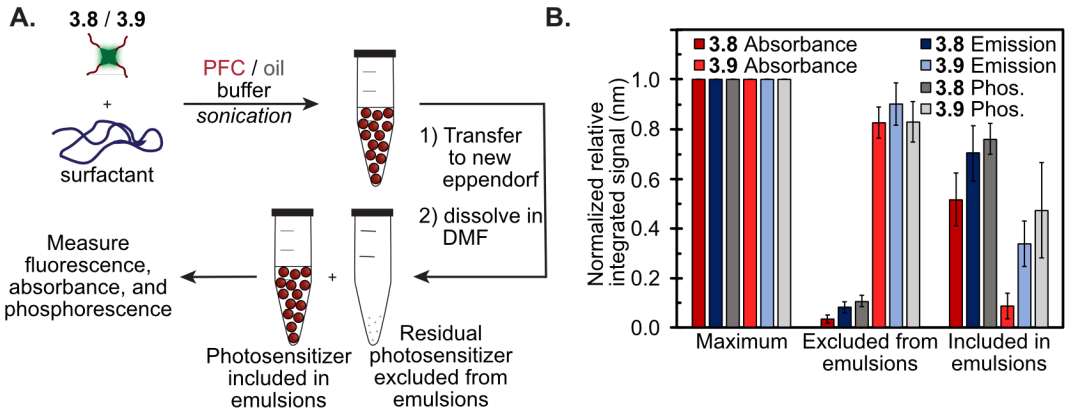

Figure 3.12 Analysis of the uptake of porphyrins **3.8** and **3.9** into perfluorocarbon nanoemulsions. Porphyrin **3.8** or **3.9** (6 nmol) was dissolved in 7:3 perfluorodecalin/perfluorotripropylamine (20 μL, 10 vol%) and emulsified in the presence of Pluronic F-68 (2.8 wt%) in PBS (35% amp, 90 s, 0 ˚C). Emulsions were transferred from the Eppendorf tube in which emulsification occurred into a new Eppendorf tube. The emulsions were diluted with dichloromethane (1 mL) and then evaporated to dryness. DMF (500 μL) was added to the original Eppendorf tube as well as the dry emulsions. Absorbance (red), fluorescence (blue, Ex 410 nm), and singlet oxygen phosphorescence (grey, Ex 410) were measured. Error bars represent the standard deviation of three samples.

fluorous soluble photosensitizer also enhances the stability of the nanomaterial, we continuously partitioned aqueous suspensions of emulsions **A**–**D** with 1-octanol, a lipid bilayer mimic.[32] We monitored the photoluminescence of the 1-octanol over time (Figure 3.9F) and found that **3.9** was rapidly released from the PFC nanoemulsions (emulsion **B**) while **3.8** showed minimal leaching from emulsion **A** over 7 days (Figure 3.9G). The oil emulsions **C** and **D** were also subjected to these conditions and **3.9** (emulsion **D**) showed better retention than **3.8** (emulsion **C**). These data indicate that the solubility match is important for photosensitizer stabilization within either PFC or oil emulsions. Notably, the core structure of both emulsions appeared stable in these studies (Figure 3.13). Taken together, these *in vitro* results suggest PFC nanoemulsions containing fluorous soluble photosensitizers will be superior agents for PDT due to their enhanced oxygen sensitization capabilities and the minimal leaching of the fluorous porphyrin to surrounding hydrophilic or lipophilic environments.

Following promising characterization, we proceeded to assay the efficacy of PDT with the photosensitizer-containing emulsions *in cellulo.* In order to visualize the PFC nanoemulsions, emulsion **E** was prepared which contained fluorous rhodamine **3.12**[13] along with porphyrin **3.8** (Figures 3.14A,B). Emulsion **E** was readily accessed by pre-dissolving both **3.8** and **3.12** in PFD : PFTPA prior to sonication, showcasing the modularity of PFC nanoemulsions for nanomedicine.[33–37] We subjected emulsion **E** (**3.8** = 30 μM; **3.12** = 0.57 mM) to human malignant melanoma (A375) cells for 3 hours. Confocal microscopy visualizing rhodamine **3.12** established that the emulsions were internalized (Figure 3.14C), which was further verified by colocalization with LysoTracker Green (Figure 3.15; S3.4). The viability of these cells was verified by NucGreen™, a cell-death marker[38] (Figure

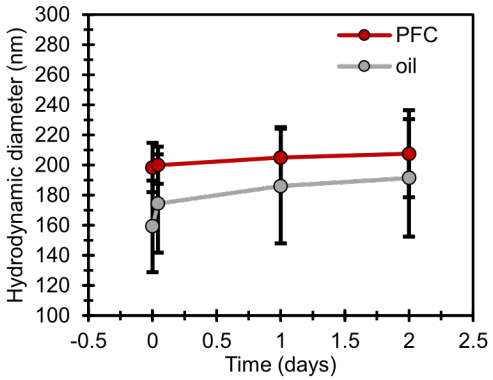

Figure 3.13 Stability of emulsions in presence of 1-octanol.
Perfluorocarbon (red, circle) and olive oil (grey, square) emulsions were prepared (10 vol% fluorous or organic phase, 2.8 wt% Pluronic F-68, 35% amp, 90 s) and diluted to 2 mL. Half the sample (1 mL) was taken and placed in the presence of 1-octanol (0.5 mL). The size of PFC and oil emulsions were measured before and after addition of 1-octanol, and then over three days of continuous rocking in the presence of 1-octanol. Hydrodynamic diameters were determined by dynamic light scattering. Error bars represent the standard deviation of the product of the $Z_{average}$ and the polydispersity index of three samples.

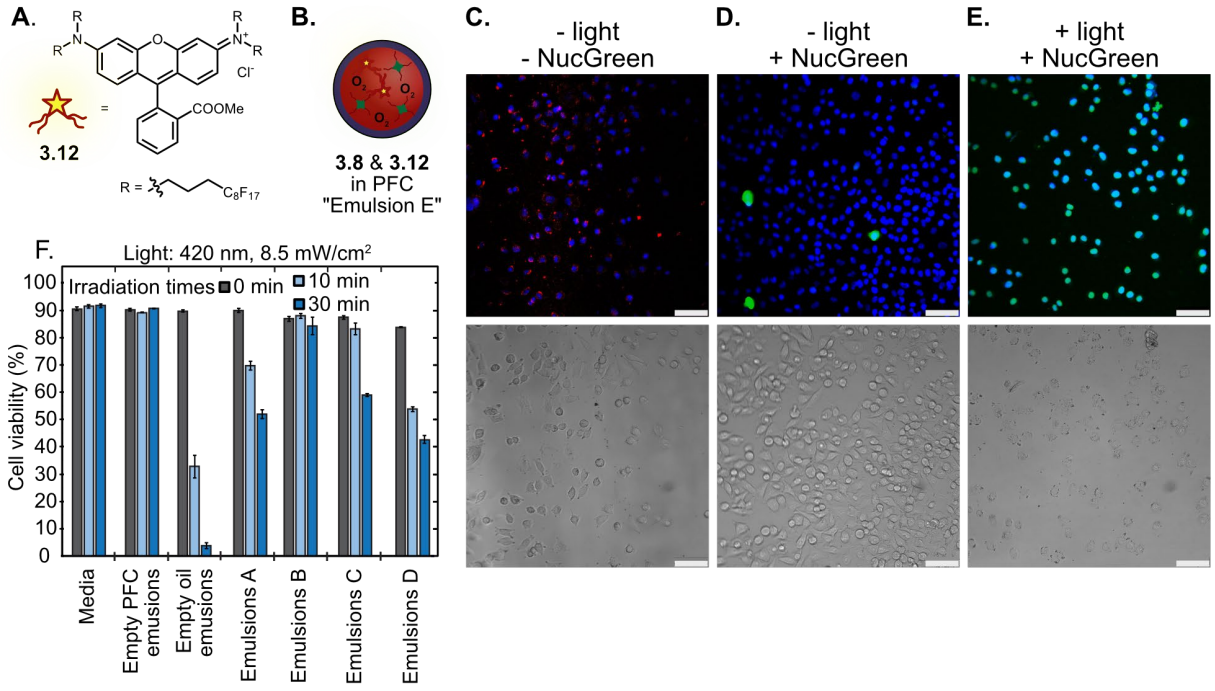

Figure 3.14 (A) Fluorous rhodamine **3.12**. (B) PFC nanoemulsions containing rhodamine **3.12** (0.57 mM) and fluorous photosensitizer **3.8** (30 μM). (C/D/E) Confocal microscopy of A375 cells stained and incubated with emulsion E for 3 h, washed, and stained with Hoescht dye. These cells were analyzed for rhodamine (C, Ex 532 nm), then subjected to the viability marker NucGreenTM and analyzed for cell death before (D, Ex 488) and after (E, Ex 488) light treatment (420 nm, 8.5 mW/cm^2, 30 min). (C/D/E) Scale bar indicates 75 μm. (F) Flow cytometry of A375 cells incubated with no emulsions, empty PFC or oil emulsions, or emulsions A–D containing 30 μM **3.8** or **3.9**. The cells were washed via centrifugation, irradiated with 420 nm light (8.5 mW/cm^2) for 0 (gray), 10 (light blue), or 30 min (dark blue), stained with propidium iodide and analyzed by flow cytometry. Dead cells were characterized as exhibiting fluorescence greater than 10^2. Error bars represent the standard deviation of 3 replicate samples.

3.14D). Upon irradiation with light (420 nm, 8.5 mW/cm^2, 30 min), cell death was observed as indicated by the NucGreen^{TM} fluorescence and the loss of cell adherence (Figures 3.14E; S3.5). An analogous experiment was performed with emulsions containing only **3.12** and showed minimal cell death upon irradiation (Figure 3.16; S3.6).

The microscopy studies illustrated that emulsion **E** was performing as expected, and we proceeded to a flow cytometry assay for further optimization and analysis. Dose-dependent experiments revealed that the efficacy of PDT plateaued at a 1:3 dilution of emulsion **A** containing 30 μM **3.8** in the PFD/PFTPA (Figure 3.17). We employed these conditions to perform a comparative study of the PFC and oil emulsions containing no porphyrin, **3.8**, or **3.9**. A375 (Figure 3.14), MCF7 (Figure 3.18), and HEK293 (Figure 3.19) cells were incubated with the requisite emulsions or media alone, washed, and treated with light (420 nm, 8.5 mW/cm^2) for 0, 10, or 30 min. The cells were stained with propidium iodide and analysed by flow cytometry. Minimal dark toxicity was observed in all samples and time-dependent light toxicity was only evident with emulsions that contained photosensitizer (Figures 3.14F, S3.1-S3.3). The PFC nanoemulsions containing fluorous-tagged porphyrin **3.8** (emulsion **A**) displayed 140 times more cell death upon 30 min of treatment than the PFC nanoemulsion containing **3.9** (emulsion **B**) These data correlate with the $^1O_2$ trapping experiments (Figure 3.9E) and confirm that the use of fluorous soluble photosensitizers is the most promising avenue for PDT with PFC nanoemulsions.

In summary, we have demonstrated that fluorous photosensitizers sequestered inside PFC nanoemulsions allow the simultaneous delivery of oxygen and photosensitizer to cells. Upon irradiation, the photosensitizer can efficiently produce $^1O_2$ due to its minimally aggregated state and close proximity to the solubilized oxygen in the fluorous solvent.

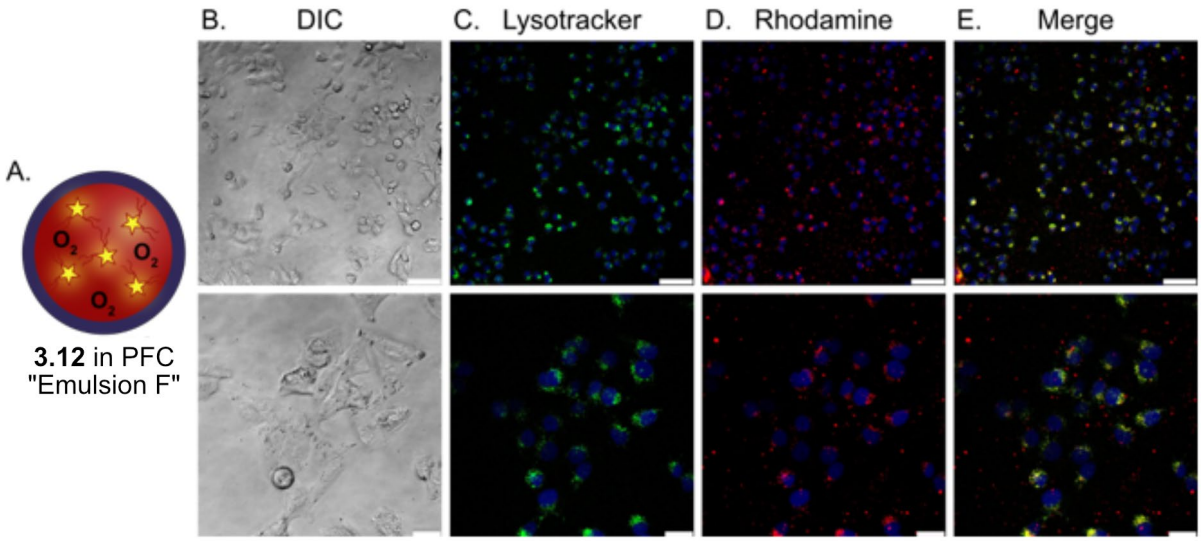

Figure 3.15 Colocalization of Emulsion F and Lysotracker green.
(A) Emulsion **F**. PFC emulsions containing rhodamine **3.12** (0.57 mM). (B/C/D/E) A375 cells were incubated with emulsion **F** for 3 h, washed, and stained with Hoechst dye and Lysotracker green. Cells were imaged via excitation at 488 nm to visualize the lysotracker green (C), 532 nm to visualize the rhodamine (D), and merged to show colocalization (E). Differential interference contrast (DIC) is shown in (B). Scale bars represent 75 μm (top panel), 25 μm (bottom panel).

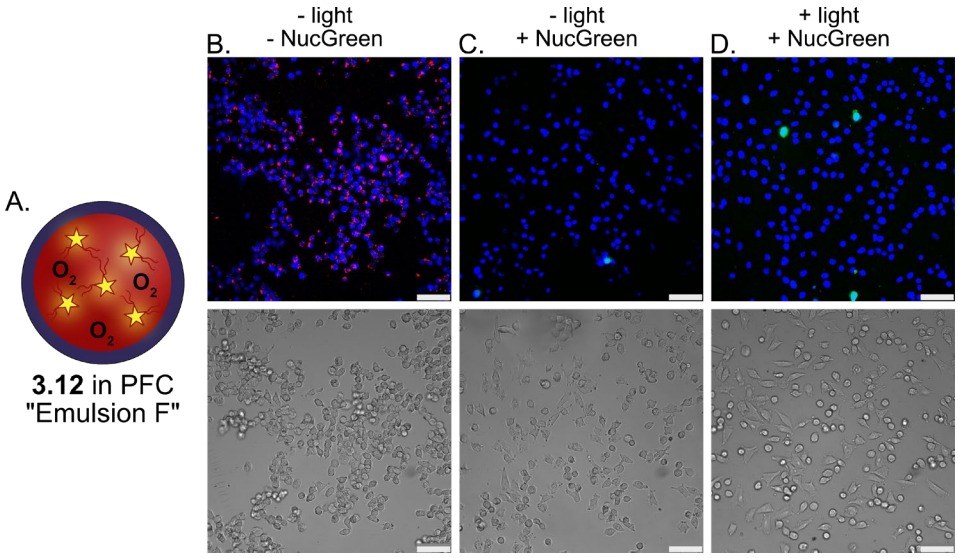

Figure 3.16 Control experiment for Figure 3.9B-E performed with emulsions containing rhodamine **3.12** but no photosensitizer. (A) Emulsion **F**. PFC emulsions containing rhodamine **5** (0.57 mM). (B/C/D) A375 cells were incubated with emulsion **F** for 3 h, washed, and stained with Hoechst dye. Cells were imaged via excitation at 532 nm to visualize the rhodamine (B), then subjected to the cell death stain NucGreen™ and excited at 488 nm to visualize NucGreen™ (C), then irradiated (420 nm light, 30 min, 8.5 mW/cm^2) and again excited at 488 nm to visualize cell death via NucGreen™ (D). Scale bars represent 75 μm.

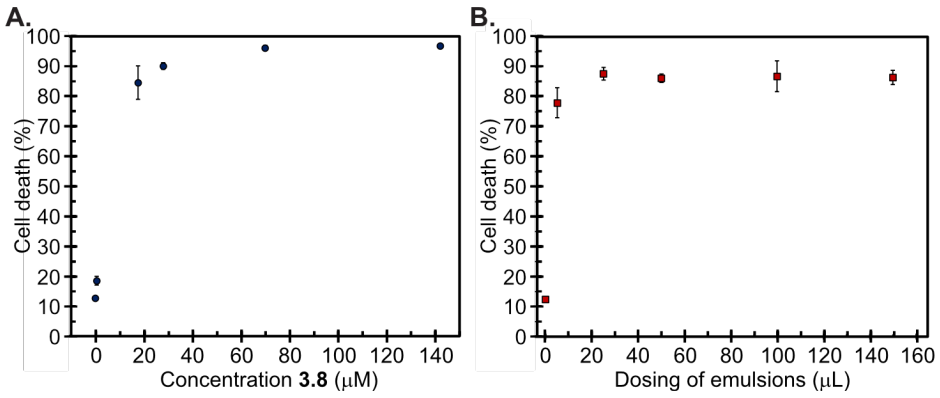

Figure 3.17 Dose-dependent photodynamic therapy response of emulsion **A**.
HEK293 cells were placed in a v-bottom 96-well plate (200,000 cells/150 μL/well). (A) PFC emulsions were prepared with varying concentrations of **3.8** (0–155 μM). The emulsions were diluted 1:5 and this dilution (50 μL) was added to HEK cells for a final volume of 200 μL per well or (B) cells were treated with varying amounts of emulsion **A** (30 μM), diluted 1:5 and varying amounts of this dilution (5-150 μL) were added to the HEK cells. The volume in each well was adjusted to 200 μL. (A/B) Cells were incubated in the presence of emulsions (37 ˚C, 5% CO_2, 3 h), washed by centrifugation (3x, 526xg, 3 min) and resuspended in FACS buffer (PBS with 1% FBS) to a final volume of 200 μL. Cells were irradiated (30 min, 420 nm, 8.5 mW/cm^2). After irradiation, cells were diluted to 300 μL FACS buffer and incubated (0 ˚C, 15 min) with propidium iodide (2 μL, 1 mg/mL solution). Cell death was analyzed by FL2 channel on FACSCalibur flow cytometer. 10,000 cells were collected per sample. Error bars represent standard deviation of three samples.

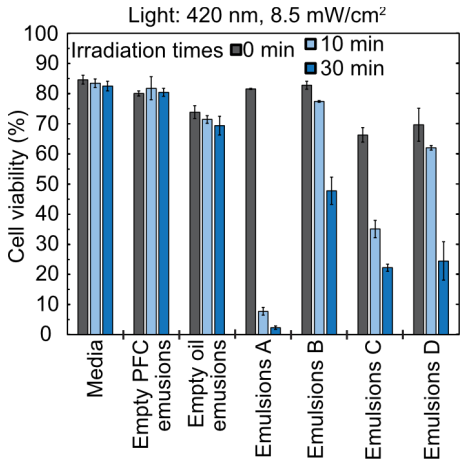

Figure 3.18 Photodynamic therapy response of emulsions **A**-**D** on MCF7 cells.
Emulsions **A**-**D** were prepared containing **3.8** or **3.9** (6 nmol). MCF7 cells were placed in a v-bottom 96-well plate (200,000 cells/150 μL/well). Emulsions were diluted 1:5 with PBS and this dilution (50 μL) was added to the MCF7 cells to give a final volume of 200 μL per well. The cells were incubated in the presence of emulsions (37 ˚C, 5% CO_2, 3 h), washed by centrifugation (3x, 526xg, 3 min) and resuspended in FACS buffer (PBS + 1% FBS) to a final volume of 200 μL. Cells were irradiated with light for 0, 10 or 30 min (420 nm, 8.5 mW/cm^2). After irradiation, cells were diluted to 300 μL with FACS buffer and incubated (0 ˚C, 15 min) with propidium iodide (2 μL, 1 mg/mL solution). Cell death was analyzed by FL2 channel on a FACSCalibur flow cytometer. 15,000 cells were collected per sample. Error bars represent the standard deviation of 3 replicate samples.

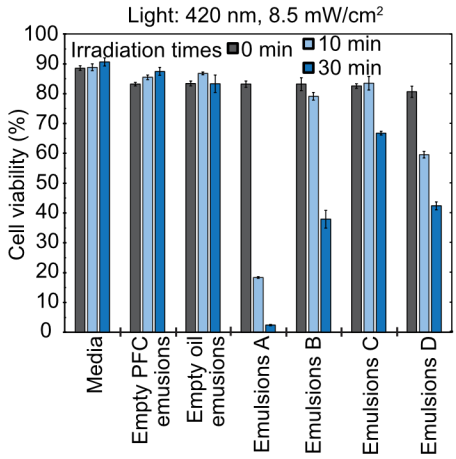

Figure 3.19 Photodynamic therapy response of emulsions **A**-**D** on HEK293 cells.
Emulsions **A**-**D** were prepared containing **3.8** or **3.9** (6 nmol). HEK cells were placed in a v-bottom 96-well plate (200,000 cells/150 μL/well). Emulsions were diluted 1:5 with PBS and this dilution (50 μL) was added to the HEK cells to give a final volume of 200 μL per well. The cells were incubated in the presence of emulsions (37 ˚C, 5% CO_2, 3 h), washed by centrifugation (3x, 526xg, 3 min) and resuspended in FACS buffer (PBS + 1% FBS) to a final volume of 200 μL. Cells were irradiated with light for 0, 10 or 30 min (420 nm, 8.5 mW/cm^2). After irradiation, cells were diluted to 300 μL with FACS buffer and incubated (0 ˚C, 15 min) with propidium iodide (2 μL, 1 mg/mL solution). Cell death was analyzed by FL2 channel on a FACSCalibur flow cytometer. 15,000 cells were collected per sample. Error bars represent the standard deviation of 3 replicate samples.

Furthermore, the addition of fluorous tags minimizes leaching of the photosensitizer from the PFC nanoemulsions. Efforts are underway to bathochromically-shift the photosensitizer and install biocompatible branched fluorous chains[39] such that the results of this proof-of-concept study can be translated *in vivo*.

3.4 Conclusion

Photodynamic therapy with fluorous materials is a promising approach to treat diseases through the co-delivery of oxygen and photosensitizers. While there are other methods to increase tumor oxygenation including the reduction of hydrogen peroxide to oxygen *in situ* and hyperbaric oxygen inhalation,[40–44] perfluorocarbons represent a simple, safe, and inert approach. In the past five years, the use of perfluorocarbons to deliver oxygen and improve photodynamic efficiencies has become an attractive method to propel photodynamic therapy into the treatment of non-surface exposed cancers and diseases.[4] Future work will continue to improve on the photosensitizer properties including reduction in aggregation, shifting the absorbance to the near-infrared region of the electromagnetic spectrum for enhanced tissue penetration, and increasing quantum yields of singlet oxygen generation.[45] Nanomaterial scaffolds will also continue to be optimized, providing means to increase perfluorocarbon/oxygen content and monomeric photosensitizer. A particularly promising approach is the use of mesoporous silica nanoparticles, which have already shown individual use for photodynamic therapy[46] and as molecular oxygen shuttles through the inclusion of fluorous solvents.[47,48] Self-assembled peptide-photosensitizer conjugates also have the potential for perfluorocarbon incorporation.[49] With continued optimization and building from the clinical precedence for photodynamic therapy and perfluorocarbons for oxygen delivery, we expect the

utility of fluorous nanomaterials for photodynamic therapy to make rapid strides in the next decade.

3.5 Summary of fluorous PDT

3.5.1 Lipid-stabilized nanoemulsion

Lipid-stabilized perfluorocarbon nanoemulsions are droplets of fluorous solvent stabilized by lipids, suspended in water (Figure 3.20A). These nanoemulsions are distinct from liposomes, which are composed of a lipid bilayer encapsulating an aqueous center. The lipid-stabilized PFC droplets are formulated primarily through a lipid film rehydration method in which a lipid film is first formed, then after the addition of buffer and fluorous solvent, energy is provided in the form of ultrasonication to form nanoemulsions ranging from 100–300 nm. These materials accumulate in the tumor via the enhanced permeability and retention effect (EPR) and are cleared through the liver. Common lipid surfactants employed can be seen in Figure 3.20B (**3.13**-**3.16**) along with common fluorous solvents for the formation of lipid-stabilized emulsions in Figure 3.20C. Perfluoro-15-crown-5-ether (PFCE, **3.17**) is often used for ^{19}F-MRI imaging. Perfluorodecalin (PFD, **3.18**), perfluorooctyl bromide (PFOB, **3.19**), perfluorohexanes (PFH, **3.7**), perfluorotripropylamine (PFTPA, **3.20**), and perfluorotributylamine (PFTBA, **3.21**) are all perfluorocarbons employed for oxygen delivery, with PFOB also being used for ^{19}F-MRI imaging and PFH for ultrasound imaging.

The first example of employing lipid-stabilized PFC nanoemulsions to deliver oxygen for use in PDT was reported in 1988 by Henderson and coworkers in which they co-injected PFC nanoemulsions encapsulating perfluorodecalin (**3.18**) and perfluorotripropylamine (**3.20**) alongside nonencapsulated porphyrin photosensitizers.[14] It took 25 years for this technology to be

revisited and advanced with the inclusion of the photosensitizer in the PFC droplets. To date, three different photosensitizers have been incorporated into the lipid tails stabilizing the water-perfluorocarbon interface. These photosensitizers are cyanine dyes IR780 (**3.2**)[11,50,51] and FDA approved ICG[52], along with Ce6 (**3.4**).[12,18] Aggregation of the photosensitizer is observed in each formulation; however, the fluorous nanomaterial does outperform the introduction of the photosensitizer alone.

The seminal paper combining a photosensitizer into a lipid-stabilized perfluorocarbon nanoemulsion was published by Hu and coworkers in 2015.[11] The specific nanomaterial, termed Oxy-PDT, included a mixture of DSPE-PEG_{2000} (**3.13**), lecithin (**3.14**), and cholesterol (**3.15**) to stabilize perfluorohexanes (PFH, **3.7**), with IR780 (**3.2**) incorporated in the surfactant layer. The implementation of PFH in lipid-stabilized droplets produced higher amounts of $^1O_2$, caused increased cell death *in cellulo* and shrunk tumors compared to controls without PFH via both intratumor and intravenous injection (Figure 3.20D). These nanoemulsions can also be used with good PDT efficiency (80-90% reduction in cellular viability upon irradiation) even under extreme hypoxic conditions due to the oxygen carrying ability of the PFC droplets.[11,50]

Following Hu's report, the benefits of lipid-stabilized perfluorocarbon nanoemulsions for PDT were quickly combined with the previously established ultrasound activity of perfluorocarbons. Ultrasound has been a useful, noninvasive, imaging modality to monitor tumor regression following PDT treatment.[53] Song et. al. employed lipid-stabilized PFCs and external ultrasound stimuli to deliver bursts of oxygen to tumor sites for combined PDT and ultrasound imaging. Nanoemulsions were delivered to tumor bearing mice via intravenous injection which accumulate in the tumor via the EPR effect. When ultrasound was applied to the tumor site, a burst of oxygen is released due to the energy provided by the sound waves, rather than slow diffusion

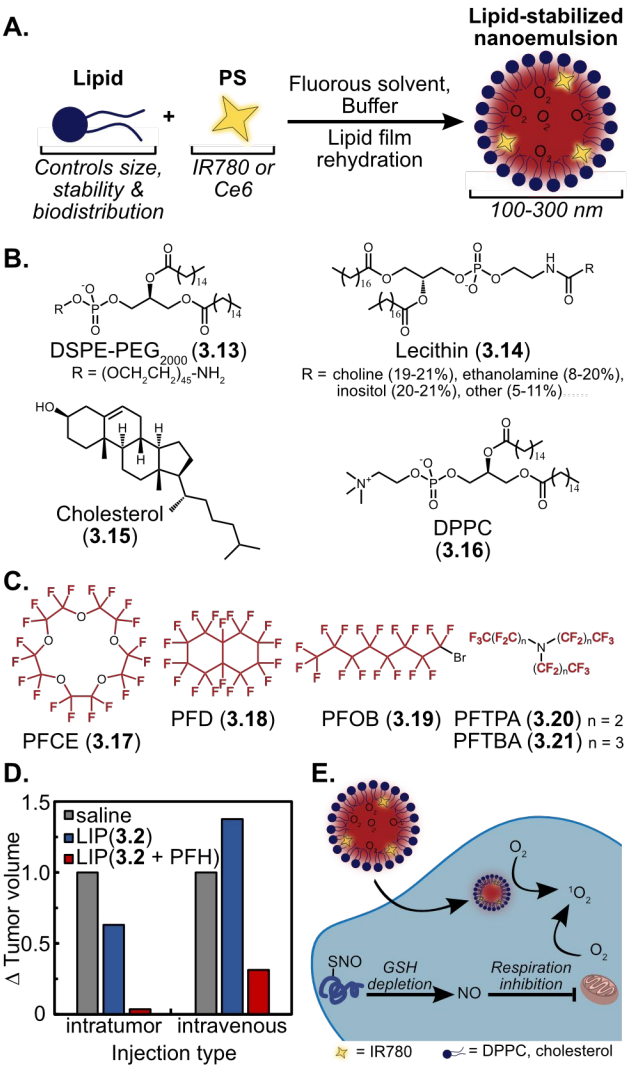

Figure 3.20. Lipid-stabilized nanoemulsions for photodynamic therapy. (A) Formulation of lipid-stabilized nanoemulsions utilize lipid rehydration and subsequent sonication. (B) Panel of common lipids used to stabilize nanoemulsions. (C) Panel of common fluorous solvents for PDT. (D) Reduction in tumor volume when treated with liposomes containing IR780 without PFH (blue) or with PFH (red) compared to the saline control (grey). Data adapted from *Nat. Commun.* **2015**, *6*, 8785. (E) Schematic showing the increase in oxygenation through delivery of lipid-stabilized PFC nanoemulsions and SNO-HSA.

of oxygen as seen without stimuli.[18] Yu et. al. prepared droplets that were designed to undergo pH-dependent coalesce upon ultrasound treatment.

In this report, the lipid-stabilized droplets were able to accumulate in the acidic environment surrounding solid tumors through the enhanced permeability and retention effect. The acidic pH protonates the lipids stabilizing the PFC nanoemulsions, promoting the membrane fusion upon the introduction of ultrasonication. With sonication, the droplet size increases to ~ 1 μm and becomes trapped inside the tumor.[12] Both responsive materials displayed enhanced photodynamic efficiencies compared to non-responsive controls.

Further combined responsive perfluorocarbon nanoemulsions have been designed to enhance the photodynamic efficiency. In one example, glutathione (GSH) concentrations were decreased through the co-delivery of S-nitrosated human serum albumin (SNO-HSA).[51] In the presence of GSH, which is upregulated in solid tumors, SNO-HSA is reduced to nitric oxide (NO) which inhibits mitochondrial respiration thereby increasing cellular oxygen. This, in addition to the oxygen delivered by the PFC droplets, enhances the photodynamic efficiency (Figure 3.20E).

Overall, lipid-stabilized perfluorocarbon nanoemulsions showcase the advantages of delivering photosensitizer and perfluorocarbon simultaneously for PDT. In all cases, perfluorinated droplets outperformed oil or nonfluorinated controls *in cellulo* and *in vivo.* Furthermore, combination with ultrasound allows for further oxygen delivery, imaging, and controlled coalescence. Disadvantages of lipid-stabilized droplets include the need for lipid rehydration methods and limited opportunities for decreasing aggregation of the photosensitizer. More customizable macromolecule-stabilized perfluorocarbon droplets have allowed some of these initial limitations to be overcome.

3.5.2 Macromolecule-stabilized nanoemulsions

Droplets of perfluorocarbon can also be effectively stabilized in water by macromolecular amphiphiles (Figure 3.21A). Indeed, the FDA-approved perfluorocarbon nanoemulsion, Fluosol-DA, employed the 8 kDa triblock copolymer Pluronic F-68 (**3.22**) as a co-surfactant. Perfluorocarbon nanoemulsions stabilized with macromolecular amphiphiles are primarily formulated via ultrasonic emulsification of a biphasic solution producing nanoemulsions ranging from 100-400 nm in diameter. The serum half-lives of the nanoemulsions are related to their size, with smaller nanoemulsions having half-lives of a few days.[54] Macromolecular amphiphiles offer many opportunities to modify the surface chemistry of the nanoemulsions, which also allows for modulation of the serum half-lives and biodistribution.[55] Notably, both lipid and macromolecular stabilized nanoemulsions are kinetically stable, and will not disassemble upon introduction to dilute environments (*e.g.* upon intravenous injection).

A variety of macromolecular surfactants, ranging from naturally occurring polymers and proteins such as hyaluronic acid and human serum albumin to synthetic polymers, have successfully yielded perfluorocarbon nanoemulsions (Figure 3.21B). Droplets stabilized by hyaluronic acid show high targeting of solid tumors *in cellulo* and *in vivo*.[56] Those stabilized by albumin,[57] and poloxamers[58,59] demonstrated biocompatibility and stability. Recently, we have focused on poly(2-oxazoline) amphiphiles (**3.24**) and found through varying the hydrophilic lipophilic balance (HLB) and architecture of polymer amphiphiles, that the size, stability, cargo retention, and cellular uptake can be predicted and controlled.[60]

One advantage of macromolecular surfactants has been decreasing aggregation of photosensitizers, leading to increased PDT efficiency (Figure 3.21C).[57,61] For example, the surface

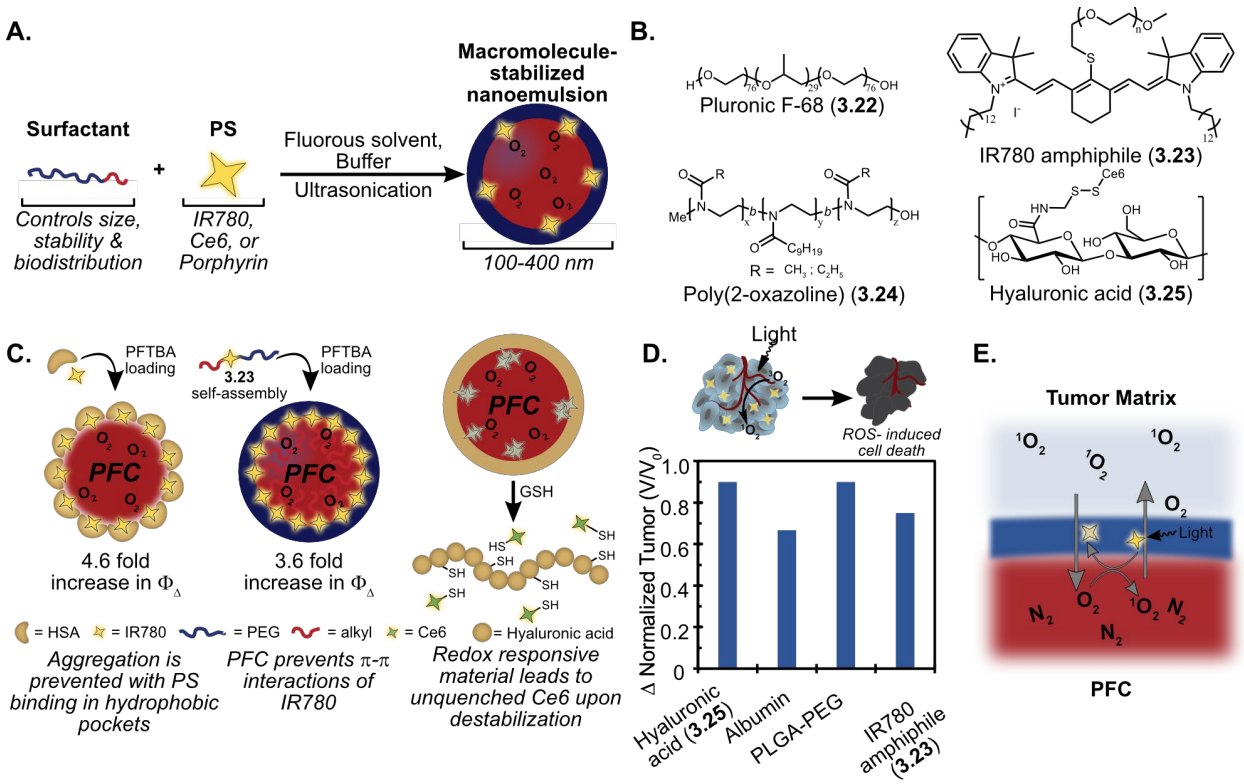

Figure 3.21 Macromolecule-stabilized nanoemulsions for PDT (A) One step formulation of PFC nanoemulsions for PDT. (B) Selected polymeric surfactants for stabilizing PFC nanoemulsions. (C) Schematic of PFC promoting an unquenched IR780 by forcing IR780 into hydrophobic pockets; Schematic of PFC promoting an unquenced IR780 through prevention of p-p interations of the amphiphile-PS; Schematic of GSH responsive nanomaterial that becomes unquenched after disassembly. (D) Solubilization of PS in the fluorous phase increases ROS-induced cell death 140 fold compared to hydrophobic control. Data adapted from *Chem. Commun*. **2017**, *53*, 13043. (E) Compilation of tumor regression. Tumors treated with saline were normalized to 1, with change in tumor volume plotted (grey). (F) Deoxygenated PFC nanoemulsions increase tumor hypoxia by absorbing the minimal oxygen found in the tumor environment.

active protein albumin can act as a surfactant to stabilize PFC nanoemulsions[36] and also provides a hydrophobic binding pocket for the photosensitizer. In this case, the perfluorocarbon core not only contributed to oxygen delivery but also helped decrease photosensitizer aggregation.[57] In other work, the photosensitizer was synthesized into an amphiphilic surfactant by the addition of a poly(ethylene glycol) chain and hydrocarbon to a heptamethine photosensitizer (**3.23**). The authors compared micelles of **3.23** to perfluorocarbon droplets stabilized by **3.23** and, following results similar to the albumin study, determined that the perfluorocarbons enhanced the PDT efficiency by both delivering oxygen and preventing aggregation.[61] A more advanced variant of a combined surfactant amphiphile is surfactant **3.25** which is composed of hyaluronic acid with photosensitizer Ce6 (**3.4**) attached via disulfide linkages. Upon self-assembly and loading of perfluorohexanes (PFH), droplets are formed that will disassemble to release free Ce6 after encountering high concentrations of glutathione found in the tumor microenvironment.[56]

Each of these materials produces ROS *in vitro*, *in cellulo*, and many were extended to tumor regression *in vivo*. By normalizing the tumor weight of saline treated tumors to one and subtracting the weight of the treated tumors, we can compare the overall tumor regression between systems (Figure 3.21D). In all cases, the materials containing perfluorocarbons outperformed the empty and oil controls, demonstrating the delivery of oxygen simultaneously with photosensitizers is critical for enhanced photodynamic efficiency. In contrast to the typical use of perfluorocarbon nanoemulsions presented in this review, deoxygenated PFC nanoemulsions can also be utilized to further increase the hypoxia found in solid tumors to increase the efficacy of hypoxia-based agents such as Tirapazamine and Salmonella. By saturating PFC nanoemulsion containing IR780 with inert gasses, the droplets will absorb the little oxygen present in solid tumors. This oxygen is then depleted by irradiating the droplets to produce ROS. The droplets are then able to absorb more

oxygen, creating a cycle increasing tumor hypoxia (Figure 3.21E). This variation in photodynamic therapy was quite effective at enhancing the efficacy of hypoxia-based agents to efficiently kill cells in culture and promote tumor regression.[62]

In summary, perfluorocarbon nanoemulsions stabilized by macromolecules are easily formulated via ultrasonication. Often the photosensitizers are localized in the surfactant layer and aggregated. However, through clever design, the photosensitizers can be forced into a monomeric state upon the addition of perfluorocarbons, the disassembly of the droplets, or solubilization within the fluorous phase with perfluorocarbon tags. In all cases, the non-aggregated photosensitizers outperform aggregated photosensitizers *in vitro*, *in cellulo* and *in vivo*.

3.5.3 Micelles

Micelles are self-assembled architectures composed solely of polymer amphiphiles with hydrophobic payloads either covalently attached to the amphiphile or non-covalently associated with the hydrophobic center of the micelle (Figure 3.22A). A key difference between micelles and nanoemulsions is the quantity of perfluorocarbon. Although fluorous solvents are not directly incorporated in the micelles as they are in lipid- and macromolecule-stabilized nanoemulsions, fluorous segments of polymer amphiphiles still have a high affinity for oxygen compared to water when saturated with oxygen (900 mM O_2 vs. 600 mM O_2)[63]. Rodionov and coworkers systematically studied the oxygen carrying ability of a range of fluorous polymers, varying the fluorous monomer (C_3F_7, C_6F_{13}, C_8F_{17}) and the overall fluorous weight percent of the polymer (10, 12, or 15 wt%). Interestingly, they found the polymer composed of the shortest fluorous containing monomer but the highest wt% fluorine incorporation had the highest oxygen saturation (C_3F_7, 15 wt%).[63]

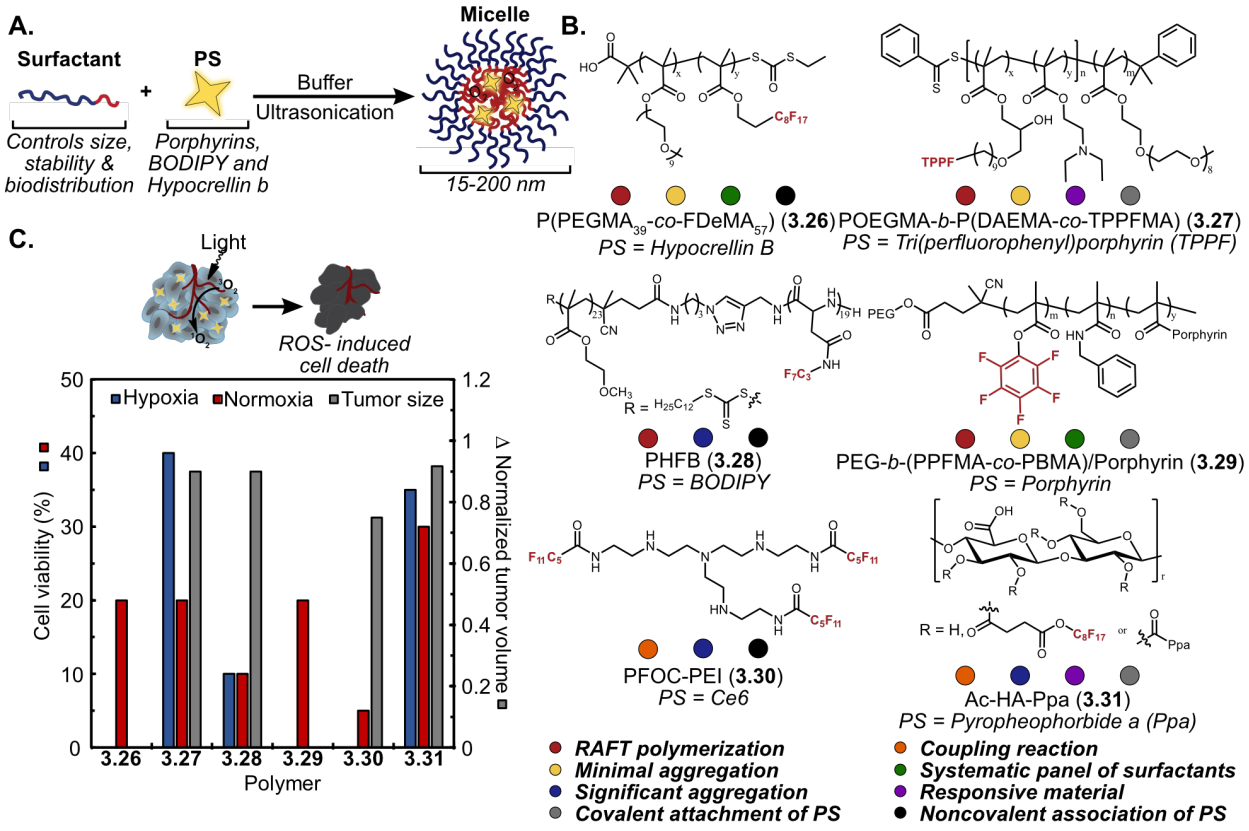

Figure 3.22 Fluorous polymer micelles for photodynamic therapy. **(**A) One step formulation of fluorine containing micelles for PDT. (B) Panel of surfactants utilized for micelle formation. (C) Compilation of cell viability and tumor regression following PDT treatment. Cell viability was measured in hypoxia (blue) and normoxia (red) conditions. Tumors treated with saline were normalized to 1, with change in tumor volume plotted (grey).

Fluorinated amphiphiles can be synthesized via living polymerizations or coupling reactions (designated with red vs. orange dots in Figure 3.22B). Photosensitizers can be covalently attached to the polymer backbone or noncovalently associated with the hydrophobic center of the micelles to render fluorous micelles active agents for photodynamic therapy (designated with gray vs. black dots in Figure 3.22B, respectively). In addition, the polymers can be designed to have additional mechanisms to decrease off-target effects through the addition of acid or esterase sensitive functional groups (designated with purple dot in Figure 3.22B). As with nanoemulsions, photosensitizers can be prone to aggregation upon self-assembly (blue dot in Figure 3.22B), but careful amphiphile design can result in the photosensitizer being in the monomeric state (yellow dot in Figure 3.22B).

The majority of fluorous amphiphiles used to formulate micelles are synthesized through RAFT polymerization (**3.26**-**3.29**).[28,64–66] This controlled radical polymerization allows precise control of block lengths, and has high functional group tolerance, which provides opportunities for post-polymerization attachment of photosensitizers. Other amphiphiles employed for micelles for PDT include the coupling of standard hydrophilic polymers (*i.e.* polyethyleneimine (**3.30**)[67] or hyaluronic acid (**3.31**)[68]) with fluorous carboxylic acids (Figure 3.22B). In all cases, the amphiphiles will self-assemble into thermodynamically stable micelles (~15 nm) or aggregates (<200 nm) when placed in water. These small nanomaterials accumulate in the tumor via the EPR effect. Due to their small size, they can exhibit long serum-half lives; however, they are prone to disassembly when diluted below the critical micelle concentration (CMC) within the body.

Approaches to photosensitizer introduction vary based on the amphiphile. Hydrophobic photosensitizers such as porphyrins,[28] chlorins,[67] and derivatives[68] have been incorporated via copolymerization with hydrophobic and fluorous containing monomers (**3.27**, **3.29**, **3.31**). The

covalent incorporation of photosensitizers prevents the undesired or premature leakage of payloads, a major limitation of perfluorocarbon nanoemulsions. In other instances, photosensitizers are non-covalently sequestered into the interior of the polymer micelles (**3.26**, **3.28**, **3.30**).[64,66,67] For both approaches, photosensitizer aggregation is observed. Even so, in all cases, the fluorinated analogs outperformed the hydrocarbon variants delivering more oxygen, thereby producing more reactive oxygen species, leading to increased cell death *in cellulo* and *in vivo.*

Polymer amphiphiles can also be modified to have responsive behavior in the presence of cellular stimuli such as the acidic microenvironment surrounding tumors and hyaluronic acid esterases. In the first example, an acrylate containing pentafluorophenyl porphyrin was copolymerized with diethylaminoethylmethacrylate and poly(ethylene glycol) to create an acid sensitive amphiphile that self-assembles into micelles (**3.27**). When **3.27** is exposed to acidic environments, the diethlyamino side chains become protonated, facilitating a hydrophobic to hydrophilic transition, which substantially changes the critical micelle concentration, leading to nanomaterial disassembly. This disassembly results in the de-aggregation of photosensitizers, increasing the fluorescence and the photodynamic efficiency *in vitro*, *in cellulo*, and *in vivo*. In the second example, hyaluronic acid was esterified with perfluorooctanoic acid and the photosensitizer pyropheophorbide a (Ppa) (**3.31**). Upon self-assembly, polymer aggregates of approximately 150 nm were formed displaying significant aggregation of Ppa. The fluorinated segments increased the photodynamic efficiency 3-fold compared to controls with no fluorination.[68]

Overall, each self-assembled, fluorinated polymer outperformed the hydrocarbon variants both in cell culture and tumor regression studies. Under hypoxic cell culture conditions, the micelles and larger polymer aggregates are able to facilitate cell death upon irradiation, suggesting

oxygen is indeed incorporated into the nanoparticles. In xenograft tumor models, the nanoparticles were all reported to reduce the tumor volume by 75-90% compared to the volume of the saline control (Figure 3.22C).

3.5.4 Other

The majority of approaches toward dual oxygen and photosensitizer delivery with fluorous nanomaterials involve nanoemulsions (both lipid- and macromolecule-stabilized) or micelles. With some apparent limitations in these nanomaterial scaffolds, other architectures that accomplish combined delivery of oxygen and photosensitizer have started to be pursued. These include Mg-Al layered double hydroxides with a photosensitizer and fluorous solvent cointercalated,[69] covalent organic polymers,[70] and superhydrophobic silica.[71] Each of these take different approaches to deliver oxygen and photosensitizer simultaneously but a unifying advantage is that their composition promotes the monomeric form of the photosensitizer, eliminating the challenges with photosensitizer aggregation that occur in droplets and micelles.

Layered double hydroxides (LDHs) are synthetic clay materials composed of layers of positively charged metal hydroxides separated by layers of anions and water. Often, these materials are used as catalysts for chemical conversions.[72] Interestingly, LDHs can enter cells and release their interlayer anions either through ion exchange with cellular anions or dissolution in the acidic environment of the lysosome. LDHs with magnesium and aluminum cations were prepared and protoporphyrin IX (ppIX) and perfluoroheptanoic acid (PFHA) were coupled to the surface. Notably, the protoporphyrin aggregated significantly with the addition of the PFHA compared to PS immobilized on LDH alone. However, this did not inhibit the photodynamic efficiency as the

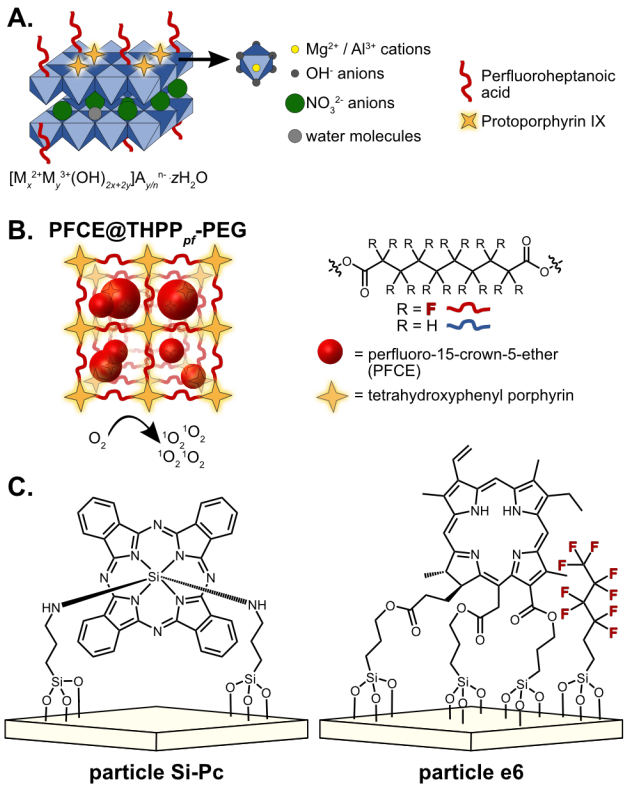

Figure 3.23 Other fluorous nanomaterial scaffolds loaded with photosensitizer for photodynamic therapy. (A) Layered double hydroxides (LDHs) decorated with PS and fluorous chains. (B) Covalent organic polymer (COP) formulated with PS and fluorous linkers for the inclusion of perfluorocarbons to enhance PDT. (C) Superhydrophobic surfaces for the treatment of bacterial biofilms.

fluorous containing LDH-ppIX oxidized two substrates specific for reaction with singlet oxygen faster than non-fluorous containing LDH or PS alone (Figure 3.23A).[69]

The covalent organic polymer (COP) was cleverly designed with tetra(hydroxyphenyl)porphyrin (THPP) vertices bridged with perfluorosebacic acid (PFSEA) to create a crosslinked fluorous polyester. Due to the fluorinated linkages, perfluoro-15-crown-5-ether (PFCE) could be loaded into the COP (Figure 3.23B). The fluorinated COP loaded with PFCE outperformed the fluorinated COP and a hydrophobic control COP in dissolved oxygen loading, singlet oxygen production, cellular toxicity and tumor regression.[70]

Superhydrophobic silica surfaces for biofilm reduction were formulated through coupling either a phthalocyanine or a combination of Chlorin e6 and a silyl perfluorobutane to a glass slide. Both surfaces were effective at reducing biofilm formation through PDT; however, in this case the phthalocyanine-decorated surface outperformed the Chlorin e6/perfluorobutane functionalized surface. The authors attribute this to increased loading of the phthalocyanine photosensitizer as compared to the Chlorin e6 (4.1 vs 1.4 mmol/g). As biofilms are commonly hypoxic, one would expect optimization of the photosensitizer loading accompanied with fluorous chains, will in the future, be a superior material (Figure 3.23C).

Each of these architectures display the importance of co-delivery of photosensitizer and oxygen. When designing novel platforms separate from the traditional emulsions and micelles, the most important factor is the biocompatibility of the platform utilized. From there, it has been shown that fluorous small molecules can be functionalized to the surface of materials or used as building blocks to further load with more fluorous solvent and oxygen.

3.5.5 Summary and Outlook

Photodynamic therapy with fluorous materials is a promising approach to treat diseases through the co-delivery of oxygen and photosensitizers. While there are other methods to increase tumor oxygenation including the reduction of hydrogen peroxide to oxygen *in situ* and hyperbaric oxygen inhalation,[40–44] perfluorocarbons represent a simple, safe, and inert approach. In the past five years, the use of perfluorocarbons to deliver oxygen and improve photodynamic efficiencies has become an attractive method to propel photodynamic therapy into the treatment of non-surface exposed cancers and diseases.[4] Future work will continue to improve on the photosensitizer properties including reduction in aggregation, shifting the absorbance to the near-infrared region of the electromagnetic spectrum for enhanced tissue penetration, and increasing quantum yields of singlet oxygen generation.[45] Nanomaterial scaffolds will also continue to be optimized, providing means to increase perfluorocarbon/oxygen content and monomeric photosensitizer. A particularly promising approach is the use of mesoporous silica nanoparticles, which have already shown individual use for photodynamic therapy[46] and as molecular oxygen shuttles through the inclusion of fluorous solvents.[47,48] Self-assembled peptide-photosensitizer conjugates also have the potential for perfluorocarbon incorporation.[49] With continued optimization and building from the clinical precedence for photodynamic therapy and perfluorocarbons for oxygen delivery, we expect the utility of fluorous nanomaterials for photodynamic therapy to make rapid strides in the next decade.

3.6 Experimental Procedures

3.6.1 General experimental procedures

Chemical reagents were purchased from Sigma-Aldrich, TCI America or Acros Organics and used without purification unless noted otherwise. Anhydrous and deoxygenated dimethylformamide (DMF) was dispensed from a Grubb's-type Phoenix Solvent Drying System. Thin layer chromatography was performed using Silica Gel 60 F_{254} (EMD Millipore) plates. Flash chromatography was performed with technical grade silica gel with 60 Å pores and 40–63 μm mesh particle size (Sorbtech Technologies). Solvent was removed under reduced pressure with a Büchi Rotovapor with a Welch self-cleaning dry vacuum pump and further dried with a Welch DuoSeal pump. Bath sonication was performed using a Branson 3800 ultrasonic cleaner. Emulsions were prepared using a QSonica (Q125) sonicator. Nuclear magnetic resonance (^{1}H NMR and ^{19}F NMR) spectra were taken on Bruker Avance 500 (^{1}H NMR), Bruker Avance 400 (^{1}H NMR, ^{19}F NMR) or Bruker Avance 300 (^{19}F NMR) instruments and processed with TopSpin or MNova software. Size and surface charge were measured with Malvern Zetasizer Nano instrument.

3.6.2 General photophysics procedures

Absorbance spectra were collected on a JASCO V-770 UV-Visible/NIR spectrophotometer with a 4000 nm/min scan rate after blanking with the appropriate solvent. Photoluminescence spectra were obtained on a Horiba Instruments PTI QuantaMaster Series fluorometer. Quartz cuvettes (1 cm) were used for absorbance and photoluminescence measurements unless otherwise noted. Extinction coefficients were calculated with serial dilutions in DMF in volumetric glassware. Error was taken as the standard deviation of the triplicate measurement. Relative singlet oxygen quantum

yields were determined in DMF as described in relative quantum yield experimental procedure. Absolute quantum yields were determined in acetone with an integrating sphere as described in absolute quantum yield experimental procedure.

All irradiation was performed with THORLabs M420L3 (420 nm) LED with SM1P25-A lens. Power was supplied with a KORAD KD3005D Digital-control DC Power Supply: 0-30V, 0-5A. Samples were placed 18 cm from the lens and kept in the center of the light. Power densities were measured with a FieldMate Laser Power Meter + Iris.

3.6.3 General cell culture procedures

HEK293 cells were donated by the lab of Professor Jorge Torres. A375 and MCF7 cells were purchased from ATCC.

HEK293 cells and A375 cells were cultured in Dulbecco's Modified Eagle Media (Life Technologies, cat# 11995073) supplemented with 10% fetal bovine serum (Corning, lot# 35016109) and 1% penicillin-streptomycin (Life Technologies, cat# 15070063). MCF7 cells were cultured in Minimal Essential Medium supplemented with 10% fetal bovine serum (Corning, lot# 35016109) and 1% penicillin-streptomycin (Life Technologies, cat# 15070063). Cells were washed with PBS, or PBS supplemented with 1% fetal bovine serum (FACS buffer). Cells were incubated at 37 ˚C, 5% CO_2, during treatments and throughout culturing, in HERACell 150i CO_2 incubators. Cells were pelleted through use of Sorvall ST 40R centrifuge. All cell work was performed in 1300 Series A2 biosafety cabinets.

For cell viability experiments: following incubation, cells were washed three times by centrifugation (526xg, 3 min, 4 ˚C). 2 μL of propidium iodide solution (1 mg/mL in PBS) was added to each well. Cells/PI were transferred to FACS tubes with a final volume of 300 □L FACS buffer (PBS + 1% FBS). Cells were incubated on ice for 15 minutes prior to flow cytometry measurement. PI fluorescence was measured on FL2 channel. Data was analyzed by splitting the population at 10^2 as a live/dead line. Flow cytometry was performed on a BDBiosciences FACSCalibur equipped with 488 nm and 635 nm lasers. For assessment of the statistical significance of differences, a one-tailed Student's t-test assuming unequal sample variance was employed.

Confocal microscopy was performed on a TCS SPE Leica confocal microscope containing 405 nm, 488 nm, 532 nm and 635 nm lasers.

3.6.4 Calculating quantum yield procedures

1. Relative measures of singlet oxygen quantum yield

The singlet oxygen quantum yield of a photosensitizer is defined as follows

$$QY_{\Delta s} = \left(\frac{I_{\Delta r}}{I_{\Delta s}}\right) * QY_{\Delta r} \qquad (3.1)$$

Where $I_{\Delta r}$ is the integral from 1200-1350 nm of singlet oxygen phosphorescence of the reference, and $I_{\Delta s}$ is of the sample. $QY_{\Delta r}$ is the known singlet oxygen quantum yield of the reference in a specified solvent.

Rose Bengal and zinc phthalocyanine were used as references in DMF. References of Rose Bengal (47%, DMF) and zinc phthalocyanine (56%, DMF)[73] were used to check the method, then used to calculate the singlet oxygen quantum yields of **3.8** and **3.9**. The following parameters were used:

ex_{slits} 5 nm, em_{slits} 30 nm, step size 1 nm, integration time, 0.1 s. (ex: 560 nm, 660 nm, collection 1200-1350 nm).

Each photosensitizer was excited at their respective absorbance λ_{max}, and phosphorescence was collected at a 90˚ angle to excitation. Excitation slit widths were 5 nm, and the emission slit widths were opened to 30 nm to allow maximum detection. A 1000 nm longpass filter was placed before the entrance slit of the detector to block any emission below 1000 nm, and the trace was integrated for 0.1 seconds.

2. Absolute measures of fluorescence quantum yield

The photoluminescence quantum yield of a dye or material is defined as follows

$$QY = \frac{P_E}{P_A} \tag{3.2}$$

Where $P_{E,}$ P_A are the number of photons absorbed and emitted respectively. To determine absolute quantum yield, we either use a known standard (relative method), or measure the number of photons absorbed and emitted independently (absolute method).

An integrating sphere is utilized to measure the absolute quantum yields, in which a standard cuvette is illuminated on all sides by scattering a laser against white Teflon. The direct scatter is diminished by a baffle, and a side port is used with a large-area detector (Horiba Instruments PTI QuantaMaster Series fluorometer). Excitation is provided by a xenon lamp and excitation monochromator, both of which are shared with the steady state system. The sample compartment and excitation correction fixture (RCQC) are shared. An emission correction file (in quanta/nm) for the sphere/fiber/mono/PMT combination is provided (EMCORsphere). The measurement consists of two emission scans, which are excitation and emission corrected during the acquisition.

Emission corrections are necessary to correct for the wavelength dependent efficiency of the detection system and to convert to quanta. Excitation corrections are recommended since they correct for fluctuation in lamp power and for intensity drifts.

The number of fluorescence quanta is found by integrating the sample emission curve without a neutral density filter over all the fluorescence. The number of absorbed quanta is given by the integral of (blank excitation curve – sample excitation curve) over the excitation wavelength. The number of emitted quanta is given by the integral of (blank emission curve – sample emission curve) over the emission range. PTI software contains an integration function. The product of the scaling factor and the absorbed/emitted quanta accounts for potential attenuation of the scattered excitation peak.

Scaling factors for the filter were calculated by finding the integration of the reference excitation without the filter divided by the reference excitation with the filter. All calculations were done through the Trace Math function of the software. The excitation traces were integrated over several ranges, giving a range of scaling factors that all gave the same quantum yield in further calculations.

Experiments were performed on 0.45 μM, 0.9 μM, and 1.8 μM of both **1** and **2** in DMF, all giving the same values.

3.7 Figure experimental procedures

Figure 3.3B.

The $\lambda_{max,abs}$ values were obtained in dimethylformamide (DMF) on a JASCO V-770 UV-Visible/NIR spectrophotometer with a 2000 nm/min scan rate. Extinction coefficient values were obtained from serial dilutions using volumetric flasks. All masses were determined on a Sartorius MSE6.6S-000-DM Cubis Micro Balance. $\lambda_{max,em}$ values were obtained in DMF on a Horiba Instruments PTI QuantaMaster Series fluorometer. For the emission of **3.8** and **3.9**, the following parameters were used: slits 5 nm, step size 1 nm, integration time, 0.1 s. Emission collection were as follows: **3.8** and **3.9** (Ex 410, collection 600 – 800 nm). For the $^1O_2$ phosphorescence of **3.8** and **3.9**, the following parameters were used: ex_{slits} 5 nm, em_{slits} 30 nm, step size 1 nm, integration time, 0.1 s. The $^1O_2$ phosphorescence settings were as follows: **1** and **2** (Ex 410, collection 1200 – 1350 nm, 1000 nm longpass filter). The Φ_F for **3.8** and **3.9** in DMF, the following parameters were used: slits 5 nm, step size 1 nm, integration time 1.0 s. Excitation were: **3.8** and **3.9** (Ex 410, collection 390-430 nm). Emission were: **3.8** and **3.9** (Ex 410, collection 600-750 nm). Scaling factor measurements were as follows: ex_{slits} 3 nm, em_{slits} 4.2 nm, step size 1 nm, integration time, 1.0 s. Excitation were: **3.8** and **3.9** (Ex 410, collection 390-430 nm). Excitation and emission were collected of **3.8** and **3.9,** and blanks of DMF. The Φ_Δ were calculated through integration of the $^1O_2$ phosphorescence peak at 1274 nm. The following parameters were used: ex_{slits} 5 nm, em_{slits} 30 nm, step size 1 nm, integration time, 0.1 s. Emission were: **3.8** and **3.9** (Ex 410, collection 1200–1350 nm). References of Rose Bengal (47%, DMF) and zinc phthalocyanine (56%, DMF)[73] with the following parameters were used: ex_{slits} 5 nm, em_{slits} 30 nm, step size 1 nm, integration time, 0.1 s. (Ex 560 nm, 660 nm, collection 1200-1350 nm).

Figure 3.3C.

Spectra were taken in hexanes and perfluorohexanes (6 nmol, 0.02 mg **3.8**, 0.011 mg **3.9**). Absorbance values were obtained on a JASCO V-770 UV-Visible/NIR spectrophotometer with a 2000 nm/min scan rate. Emission values were obtained on a Horiba Instruments PTI QuantaMaster Series fluorometer with the following settings: slits 5 nm, step size 1 nm, integration time 0.1 s (Ex 410 nm, collection 600-800 nm). $^1O_2$ phosphorescence were obtained on a Horiba Instruments PTI QuantaMaster Series fluorometer with the following settings: ex_{slits} 5 nm, em_{slits} 30 nm, step size 1 nm, integration time 0.1 s, 1000nm longpass filter (Ex 410 nm, collection 1200-1350nm).

Figure 3.4-3.5

Photosensitizer **3.8** or **3.9** (18.6 nmol, 0.06 mg **3.8**, 0.03 mg **3.9**) were dissolved in the indicated solvents (200 μL) through inversion or minimal sonication (<10 sec, bath sonicator). Photographs were taken in either visible or long-wave UV light (UVGL-25, 365 nm).

Figure 3.6

Characterization of photosensitizer **3.8** and **3.9** in dimethylformamide (DMF) (30 μM, 6 nmol in 200 μL). Spectra were taken in a 300 μL quartz cuvette. Extinction coefficient was calculated through serial dilution of **3.8** and **3.9** in DMF, performed in a 1 mL volumetric flask. Extinction coefficient was measured on a JASCO V-770 UV-Visible/NIR spectrophotometer with a 2000 nm/min scan rate. Photoluminescence spectra were obtained on a Horiba Instruments PTI QuantaMaster Series fluorometer. Emission spectra: slits 5 nm, step size 1 nm, integration time 0.1 s (Ex: 410 nm, collection 600-750 nm). Phosphorescence spectra (grey, dotted): ex_{slits} 5 nm,

em_{slits} 30 nm, step size 1 nm, integration time 0.1 s (Ex: 410 nm, collection 1200-1350 nm, 1000 nm long-pass filter).

Figure 3.7.

Photosensitizer **3.9** (1.16 nmol, 0.002 mg) was dissolved in dimethylformamide with increasing percentages of methoxyperfluorobutane (0-100%, TCI America). The total volume was kept consistent at 0.75 mL. Absorbance was measured on a JASCO V-770 UV-Visible/NIR spectrophotometer with a 2000 nm/min scan rate. Photoluminescence spectra were obtained on a Horiba Instruments PTI QuantaMaster Series fluorometer. Emission spectra: slits 5 nm, step size 1 nm, integration time 0.1 s (Ex 410 nm, collection 600-750nm). Phosphorescence spectra: ex_{slits} 5 nm, em_{slits} 30 nm, step size 1 nm, integration time 0.1 s (Ex 410 nm, collection 1200-1350nm, 1000 nm longpass filter). All data was normalized to $\lambda_{max,abs}$, $\lambda_{max,em}$, and $\lambda_{max,phos}$. The average of the normalized data is plotted. Error bars represent the standard deviation of three samples.

Figure 3.9A.

Emulsions A-D were prepared by predissolving **3.8** or **3.9** (6 nmol, 0.02 mg **3.8** or 0.011 mg **3.9**) in 7:3 perfluorodecalin/perfluorotripropylamine or in olive oil (10 vol%, 20 μL) in an Eppendorf tube. Pluronic F-68 was predissolved in PBS pH 7.4 (28 mg/mL) and this solution (200 μL, 2.8 wt%) was added to the fluorous solvent or olive oil. Sonication (35% amp, 90 s, 0 ˚C) resulted in emulsions of sizes shown in Figure 3.9B and Figure 3.9C without filtration.

Figure 3.9B/C.

Empty emulsions were prepared by sonicating 7:3 perfluorodecalin/ perfluorotripropylamine (10 vol%, 20 μL) with Pluronic F-68 predissolved in PBS pH 7.4 (28 mg/mL, 2.8 wt%, 200 μL). Emulsions were diluted in MilliQ H_2O (20 μL emulsions in 2 mL MilliQ H_2O, **Ω** = -18 mV) in a plastic cuvette. The size was monitored with Malvern Zetasizer Nano dynamic light scattering and data is representative of three replicate measurements. Error bars represent the standard deviation of three measurements.

Figure 3.9E.

Emulsions containing **3.8** and **3.9** were prepared as described in Figure 3.9A**.** Emulsions were diluted in PBS (200 μL emulsion in 3 mL PBS). To this dilution was added **3.10** (25 μL of 1 mg/mL stock, 61 μM final concentration). This solution (1 mL) was irradiated (420 nm, 8.5 mW/cm^2) for 30 min. Emission values were collected over 30 min on a Horiba Instruments PTI QuantaMaster Series fluorometer with the following settings: ex_{slits} 5 nm, em_{slits} 2, step size 1 nm, integration time 0.1 s (ex: 375 nm, collection 390-500 nm). A control of **3.10** alone was irradiated (420 nm, 8.5 mW/cm^2) to determine background photobleaching. The data was integrated from 390-500 nm, and the control photobleaching of **3.10** was added to each data set to account for the photobleaching of **3.10** alone. Emulsion A is statistically significant from emulsions B-D with $p<0.001$. Statistical significance was determined with a one tailed, unequal variance T-test.

Figure 3.9F/G.

Emulsions containing **3.8** or **3.9** were prepared as described in Figure 3.9A except the concentration of **3.8** and **3.9** was 0.04 μmol (0.13 mg **3.8** or 0.07 mg **3.9** in 20 μL 7:3 PFD/PFTPA

or oil, 10 vol%) and diluted (200 μL emulsions in 5 mL). A portion of these solutions (1 mL) was taken and placed in the presence of 1-octanol (0.5 mL) in an Eppendorf tube. The biphasic samples were then rocked for 1 week. The Eppendorf tubes containing the samples were allowed to roll freely on a KJ-201BD Orbital shaker at 20 rpm. The fluorescence of the 1-octanol layer was monitored to determine the amount of **3.8** and **3.9** that diffused out of the emulsions (Figure 3.9F). Emission values were obtained by taking an aliquot (200 μL) of the 1-octanol in a 0.3 mL quartz cuvette and measuring the fluorescence on a Horiba Instruments PTI QuantaMaster Series fluorometer with the following settings: slits 5 nm, step size 1 nm, integration time 0.1 s (Ex 410 nm, collection 600-750nm). The 1-octanol was returned to the sample after the measurement. Emulsion B is statistically significant from emulsions A, C and D with $p<0.001$. Statistical significance was determined with a one tailed, unequal variance T-test.

Figure 3.10.

NMR samples were prepared with each of the components of PFC or oil emulsions in the presence of Rose Bengal (1.6 μmol, 1 mg), a known photosensitizer. A final volume of 0.5 mL for each of the NMRs were prepared, with 100 μL of either 7:3 perfluorodecalin (PFD)/ perfluorotripropylamine (PFTPA) or olive oil, or Pluronic F-68 (0.4 μmol, 1.1 mg). Anthracene, **3.10**, was used as a control (8.1 μmol, 2 mg) to ensure $^1O_2$ was being produced in high enough quantities to interact with the fluorous solvent, oil, or Pluronic F-68. NMR samples were then kept in the dark or irradiated (420 nm, 90 min, 8.5 mW/cm^2). NMRs were taken on Bruker AV-500 or AV-300 instruments.

Figure 3.11.

Emulsions were prepared as described in Figure 3.9B/C. Emulsions were diluted (20 μL emulsions in 2 mL MilliQ H_2O, **Ω** = -18 mV), and Rose Bengal was added (0.4 μM, 2 μL of 1 mM stock). Size measurements of the emulsions were taken over a period of two weeks in the presence of Rose Bengal, with and without light (420 nm, 30 min, 8.5 mW/cm^2). Size was monitored with Malvern Zetasizer Nano dynamic light scattering and data is representative of three replicate measurements. Error bars represent the standard deviation of the product of the $Z_{average}$ and the polydispersity index of three measurements.

Figure 3.12.

Emulsions A-D were prepared as described in Figure 3.9A. The emulsions were transferred to a new Eppendorf tube and diluted with dichloromethane (1 mL) and evaporated to dryness. Dimethylformamide (0.5 mL) was added to the dried emulsions (denoted "included in emulsions"), and the original Eppendorf tube the emulsions were prepared in (denoted "excluded from emulsions"). The maximum control was **3.8** or **3.9** (6 nmol, 0.02 mg **3.8** or 0.011 mg **3.9**) dissolved in dimethylformamide (0.5 mL). Absorbance was measured on a JASCO V-770 UV-Visible/NIR spectrophotometer with a 2000 nm/min scan rate. Photoluminescence spectra were obtained on a Horiba Instruments PTI QuantaMaster Series fluorometer. Emission spectra: slits 5 nm, step size 1 nm, integration time 0.1 s (Ex 410 nm, collection 600-750 nm). Phosphorescence spectra: ex_{slits} 5 nm, em_{slits} 30 nm, step size 1 nm, integration time 0.1 s (ex: 410 nm, collection 1200-1350 nm, 1000 nm longpass filter). Data was normalized relative to the maximum control. Error bars represent the standard deviation of three samples.

Figure 3.13.

Emulsions were prepared as in Figure 3.9 B/C. A portion of these solutions (1 mL) was taken and placed in the presence of 1-octanol (0.5 mL) in an Eppendorf tube. The biphasic samples were then rocked for three days. The Eppendorf tubes containing the samples were allowed to roll freely on a KJ-201BD Orbital shaker at 20 rpm. Each day, the aqueous layer was removed and placed in a 1 mL plastic cuvette and the size of the emulsions was measured by dynamic light scattering. After the measurement, the emulsions were replaced and returned to rocking. Error bars represent the standard deviation of the product of the $Z_{average}$ and the polydispersity index of three samples.

Figure 3.14C-E/Figure S3.4

Emulsion E was prepared by predissolving **3.8** (6 nmol, 0.02 mg) and **3.12** (0.11 μmol, 0.25 mg) in 7:3 perfluorodecalin / perfluorotripropylamine (10 vol%, 20 μL) in an Eppendorf tube. Pluronic F-68 predissolved in PBS pH 7.4 (28 mg/mL, 2.8 wt%, 200 μL) was added to the fluorous solvent. Sonication (35% amp, 90 s, 0 ˚C) resulted in emulsion E. Emulsions were diluted in FACS buffer (200 μL in 1 mL, PBS buffer + 1% FBS).

A375 cells (30,000 cells/50 μL) were plated on a single well glass microscope slide (VWR 10118-600) that had been treated with FBS (2 mL, 30 min) and allowed to dry at RT in a biosafety cabinet to maintain sterility. Cells were allowed to adhere (O/N) and were washed with FACS buffer (PBS buffer + 1% FBS, 3x). Cells were treated with emulsion E (50 μL dilution in 100 μL media, 3 h). Cells were stained with Hoechst and NucGreen™ from ReadyProbes Cell Viability Imaging Kit (ThermoFisher, ref # R37609). Cells were stained with Hoechst (1 drop/1mL media, 15 min) before confocal images were taken. Cells were imaged before light treatment without NucGreen™.

Cells were then stained with NucGreen™ (1 drop/1mL media, 15 min) and imaged before and after light treatment. Confocal settings were as follows: Rhodamine (532 laser-51%, 970 gain, offset -0.4, collection 540-700nm), Hoechst (405 laser-51%, 970 gain, offset -0.4, collection 420-500nm), NucGreen™ (488 laser-51%, 970 gain, 0ffset -0.4, collection 500-550 nm), DIC (scan-BF, 450 gain, offset -0.7). Scale bar represents 75 μm. Images were processed in ImageJ.

Figure 3.14F/Figure 3.17

Emulsions A-D were prepared as described in Figure 3.9A. A375 cells were placed in a 96-well plate (200,000 cells per 150 μL/well). Emulsions were diluted in FACS buffer (200 μL in 1 mL, PBS buffer + 1% FBS). Cells suspended in 150 μL media were treated with 50 μL of the diluted emulsions. Cells were incubated in the presence of emulsions (37 ˚C, 5% CO_2, 3 h). Cells were washed by centrifugation (3x, 526xg, 3 min) and resuspended in FACS buffer (PBS with 1% FBS) to a final volume of 200 μL. Cells were irradiated (30 min, 420 nm, 8.5 mW/cm^2). After irradiation, cells were diluted to 300 μL with FACS buffer and incubated (0 ˚C, 15 min) with propidium iodide (2 μL, 1 mg/ml solution). Cell death was analyzed by FL2 channel on FACSCalibur. 15,000 cells were collected per sample. Emulsions A, B, and C were statistically significant after 10 min irradiation from the dark control with $p<0.05$. All emulsions were statistically significant after 30 min irradiation from the dark control with $p<0.0001$. Statistical significance was determined with a one tailed, unequal variance T-test.

Figure 3.15/S3.4.

Emulsion F was prepared by predissolving **3.12** (0.11 μmol, 0.25 mg) in 7:3 perfluorodecalin / perfluorotripropylamine (10 vol%, 20 μL) in an Eppendorf tube. A solution of Pluronic F-68 in

PBS pH 7.4 (28 mg/mL, 2.8 wt%, 200 μL) was added to the fluorous solvent. Sonication (35% amp, 90 s, 0 ˚C) resulted in emulsion F.

A375 cells (30,000 cells/50 μL) were plated on a single welled glass microscope slide (VWR 10118-600) that had been treated with FBS (2 mL, 30 min) and allowed to dry at RT in biosafety cabinet to maintain sterility. Cells were allowed to adhere (O/N) and were washed with FACS buffer (PBS buffer + 1% FBS, 3x). Cells were treated with emulsion F (50 μL in 100 μL media, 3 h). Cells were stained with Hoechst from ReadyProbes Cell Viability Imaging Kit (ThermoFisher, ref # R37609) (1 drop/1mL media, 15 min) before confocal images were taken. Cells were stained with LysoTracker Green DND-26 (Cell Signaling #8783, 1:20,000 in PBS buffer, 100 μL, 5 min) and washed with FACS buffer (PBS buffer + 1% FBS, 3x). Cells were imaged via excitation at 405 nm (Hoescht), 488 nm (LysoTracker Green), and 532 nm (Rhodamine). Images were processed in ImageJ. Scale bar represents 75 μm (top panel), 25 μm (bottom panel).

Figure 3.16/S3.6

Emulsion F was prepared by predissolving **3.12** (0.11 μmol, 0.25 mg) in 7:3 perfluorodecalin/perfluorotripropylamine (10 vol%, 20 μL) in an Eppendorf tube. A solution of Pluronic F-68 in PBS pH 7.4 (28 mg/mL, 2.8 wt%, 200 μL) was added to the fluorous solvent. Sonication (35% amp, 90 s, 0 ˚C) resulted in emulsion F.

A375 cells (30,000 cells/50 μL) were plated on a single welled glass microscope slide (VWR 10118-600) that had been treated with FBS (2 mL, 30 min) and allowed to dry at RT in biosafety cabinet to maintain sterility. Cells were allowed to adhere (O/N) and were washed with FACS

buffer (PBS buffer + 1% FBS, 3x). Cells were treated with emulsion F (50 μL in 100 μL media, 3 h). Cells were stained with Hoechst and NucGreen™ from ReadyProbes Cell Viability Imaging Kit ThermoFisher, (ref # R37609). Cells were stained with Hoechst (1 drop/1mL media, 15 min) before confocal images were taken. Cells were imaged before light treatment without NucGreen™. Cells were stained with NucGreen™ (1 drop/1mL media, 15 min) and imaged before and after light treatment (30 min, 420 nm, 8.5 mW/cm^2). Confocal settings were as follows: Rhodamine (532 laser-51%, 970 gain, offset -0.4, collection 540-700 nm), Hoechst (405 laser-51%, 970 gain, offset -0.4, collection 420-500 nm), NucGreen™ (488 laser-51%, 970 gain, offset -0.4, collection 500-550 nm), DIC (scan-BF, 450 gain, offset -0.7). Images were processed in ImageJ. Scale bar represents 75 μm.

Figure 3.17.

200,000 HEK cells/150 μL media were placed in 96-well plates.

(A) Emulsion A was prepared with varying amount of **3.8** (0-155 μM, 0-0.1 mg). Emulsions were diluted with FACS buffer (PBS, 1% FBS, 200 μL emulsions in 1 mL). Cells suspended in 150 μL media were treated with 50 μL diluted emulsions.

(B) Emulsions containing **3.8** were prepared as described in Figure 3.9A**.** Emulsions were diluted in PBS (200 μL emulsion in 1 mL PBS). HEK cells suspended in media were treated with varying amounts of diluted emulsions (5-150 μL, 200 μL emulsion diluted in 1 mL FACS buffer) to a final volume of 200 μL.

Cells were incubated in the presence of emulsions (37 °C, 5% CO_2, 3 h). Cells were washed by centrifugation (3x, 526xg, 3 min) and resuspended in FACS buffer (PBS with 1% FBS) at a final

volume of 200 μL. Cells were irradiated (30 min, 420 nm, 8.5 mW/cm^2). After irradiation, cells were diluted to 300 μL FACS buffer and incubated (0 ˚C, 15 min) with propidium iodide (2 μL, 1 mg/mL solution). Cell death was analyzed by FL2 channel on FACSCalibur. The live/dead line was drawn at 10^2. 10,000 cells were collected per sample. Error bars represent the standard deviation of three samples.

Figure 3.18-S3.2.

Emulsions A-D were prepared as described in Figure 3.9. MCF7 cells were placed in a 96-well plate (200,000 cells per 150 μL/well). Emulsions were diluted in FACS buffer (200 μL in 1 mL, PBS buffer + 1% FBS). Cells suspended in 150 μL media were treated with 50 μL of the diluted emulsions. Cells were incubated in the presence of emulsions (37 ˚C, 5% CO_2, 3 h). Cells were washed by centrifugation (3x, 526xg, 3 min) and resuspended in FACS buffer (PBS with 1% FBS) to a final volume of 200 μL. Cells were irradiated (30 min, 420 nm, 8.5 mW/cm^2). After irradiation, cells were diluted to 300 μL with FACS buffer and incubated (0 ˚C, 15 min) with propidium iodide (2 μL, 1 mg/ml solution). Cell death was analyzed by FL2 channel on FACSCalibur. 15,000 cells were collected per sample. Emulsions A, B, and C were statistically significant after 10 min irradiation from the dark control with $p<0.05$. All emulsions were statistically significant after 30 min irradiation from the dark control with $p<0.0001$. Statistical significance was determined with a one tailed, unequal variance T-test.

Figure 3.19-3.28.

Emulsions A-D were prepared as described in Figure 3.9. HEK293 cells were placed in a 96-well plate (200,000 cells per 150 μL/well). Emulsions were diluted in FACS buffer (200 μL in 1 mL,

PBS buffer + 1% FBS). Cells suspended in 150 μL media were treated with 50 μL of the diluted emulsions. Cells were incubated in the presence of emulsions (37 °C, 5% CO_2, 3 h). Cells were washed by centrifugation (3x, 526xg, 3 min) and resuspended in FACS buffer (PBS with 1% FBS) to a final volume of 200 μL. Cells were irradiated (30 min, 420 nm, 8.5 mW/cm^2). After irradiation, cells were diluted to 300 μL with FACS buffer and incubated (0 ˚C, 15 min) with propidium iodide (2 μL, 1 mg/ml solution). Cell death was analyzed by FL2 channel on FACSCalibur. 15,000 cells were collected per sample. Emulsions A, B, and C were statistically significant after 10 min irradiation from the dark control with $p<0.05$. All emulsions were statistically significant after 30 min irradiation from the dark control with $p<0.0001$. Statistical significance was determined with a one tailed, unequal variance T-test.

Figure 3.29.

Characterization of photosensitizer **3.8** in 7:3 perfluorodecalin (PFD)/ perfluorotripropylamine (PFTPA) (30 μM **3.8,** 6 nmol in 200 μL). Spectra were taken in a 300 μL quartz cuvette. Extinction coefficient was calculated through serial dilution of **3.8** in 7:3 PFD/PFTPA, performed in a 1 mL volumetric flask. Extinction coefficient was measured on a JASCO V-770 UV-Visible/NIR spectrophotometer with a 2000 nm/min scan rate. Photoluminescence spectra were obtained on a Horiba Instruments PTI QuantaMaster Series fluorometer. Emission spectra: slits 5 nm, step size 1 nm, integration time 0.1 s (Ex: 410 nm, collection 600-750 nm). Phosphorescence spectra (grey, dotted): ex_{slits} 5 nm, em_{slits} 30 nm, step size 1 nm, integration time 0.1 s (Ex: 410 nm, collection 1200-1350 nm, 1000 nm long-pass filter).

3.8 Scheme experimental procedures

Fluorous Porphyrin (3.8)

5,10,15,20-Tetrakis[4- (10H,10H,20H,20H-perfluorododecyl) -2,3,5,6-tetrafluorophenyl] porphyrin[19] 5,10,15,20-Tetrakis(pentafluorophenyl)porphyrin (11.5 mg, 11.8 μmol, 1 equiv., TCI America) was dissolved in DMF (1 mL, anhydrous). 1H, 1H, 2H, 2H-perflurododecane-1-thiol (38 mL, 112 μmol, 9.5 equiv.) and diethylamine (20 μL, 194 μmol, 16 equiv.) were dissolved in 2:1 ethyl acetate/DMF under nitrogen (3 mL). The 5,10,15,20-Tetrakis(pentafluorophenyl)porphyrin dissolved in DMF was added to the solution of 1H, 1H, 2H, 2H-perflurododecane-1-thiol and diethylamine. The resulting solution was stirred overnight at room temperature and evaporated onto silica gel. Photosensitizer **1** was purified via silica gel chromatography, eluting with hexane/acetone. (R_f = 0.6 in 20:1 hexane/acetone). This procedure gave pure **1** (37.9 mg, 11.8 μmol, 39.6%). ^{1}H NMR (300 MHz, $CDCl_3$, 5% TFA): δ 8.98 (s, 8H), 3.61 (t, *J* = 9 Hz, 8H), 2.78-2.73 (m, 8H), -0.72 (br s, 2H). ^{19}F (282 MHz, $CDCl_3$, 5% TFA): δ -81.08 (t, *J* = 10 Hz, 12F), -114.09 (m, 8F), -121.77 (m, 8F), -122.04 (m, 16F), -122.88 (m, 8F), -123.31 (m, 8F), -126.32 (m, 8F), -132.22 (m, 8F), -137.80 (m, 8F). HRMS (MALDI): Calculated for $C_{84}H_{27}F_{84}N_4S_4^+$ $[M+H]^+$: 2814.9772; found: 2814.9798. Absorbance (DMF): 408 nm (ε = $8.4x10^4$ $M^{-1}cm^{-1}$). Emission (DMF, Ex 410 nm): 704 nm, Φ_F = 0.02 ± 0.03 (DMF), Φ_Δ = 86 ± 0.8 % (DMF).

Hydrophobic Porphyrin (3.9)

5,10,15,20-Tetrakis[4- (10H,10H,20H,20H-dodecyl) -2,3,5,6-tetrafluorophenyl] porphyrin 5,10,15,20-Tetrakis(pentafluorophenyl)porphyrin (11.5 mg, 11.8 μmol, 1 equiv.) was dissolved in DMF (1 mL, anhydrous). Dodecane-1-thiol (150 μL, 600 μmol, 50 equiv.) and diethylamine (36 μL, 354 μmol, 30 equiv.) were dissolved in 2:1 ethyl acetate/DMF under nitrogen (3 mL). The 5,10,15,20-tetrakis(pentafluorophenyl)porphyrin dissolved in DMF was added to the solution of dodecane-1-thiol and diethylamine. The resulting mixture was stirred overnight at room temperature and evaporated onto silica gel. Photosensitizer **2** was purified via silica gel chromatography, eluting with pentane ether solvent gradient of: pentane, 1000:1 pentane: ether, 500:1 pentane: ether, 250:1 pentane: ether. This procedure gave pure **2** (7.5 mg, 2.0 μmol, 38%). ^{1}H NMR (500 MHz, $CDCl_3$): δ 8.93 (s, 8H), 3.29 (t, J = 8 Hz, 8H), 1.86 (m, 8H), 1.61 (m, 8H), 1.36-1.19 (m, 64H), 0.87 (m, 12H), -2.86 (s, 2H). ^{19}F NMR (377 MHz, $CDCl_3$): δ -134.26 (m, 8F), -137.22 (m, 8F). HRMS (MALDI): Calculated for $C_{92}H_{111}F_{16}N_4S_4^+$ $[M+H]^+$: 1703.7431; found: 1703.7426. Absorbance (DMF): 406 nm ($\varepsilon = 9x10^4\ M^{-1}cm^{-1}$). Emission (DMF, Ex. 410 nm): 706 nm, $\Phi_F = 0.02 \pm 0.03$ (DMF), $\Phi_\Delta = 85 \pm 3.6$ % (DMF).

3.9 Supplemental figures

3.9.1 FACS Histograms

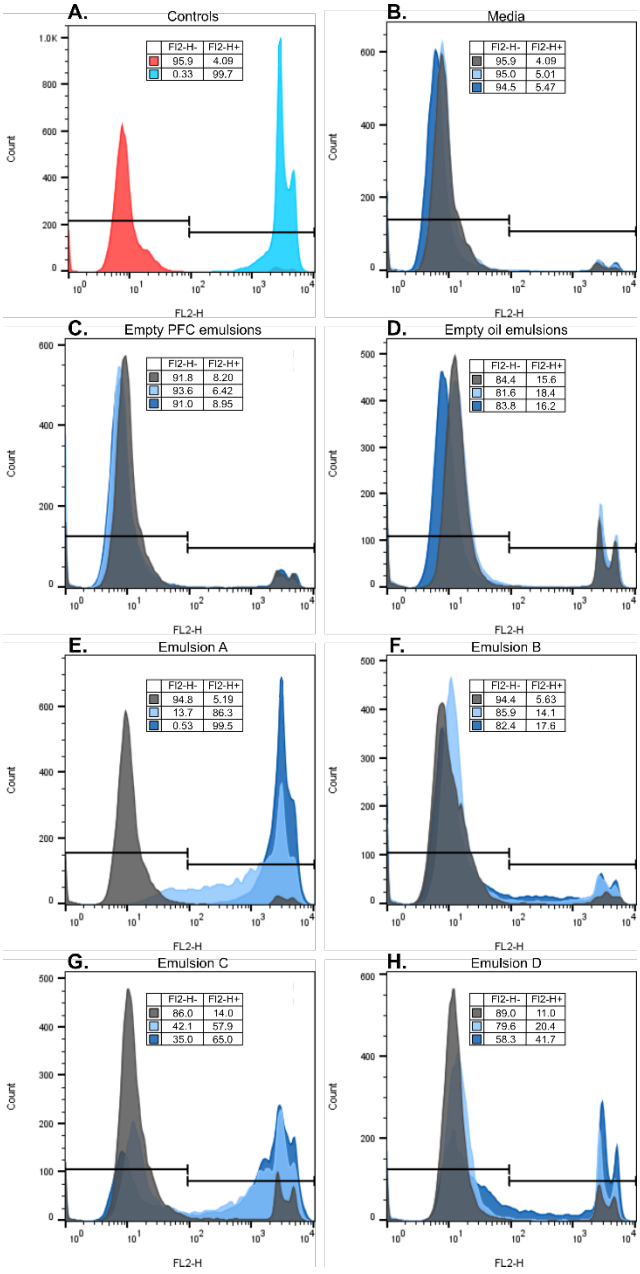

Figure S3.1 Histograms for flow cytometry data in Figure 3.14F.

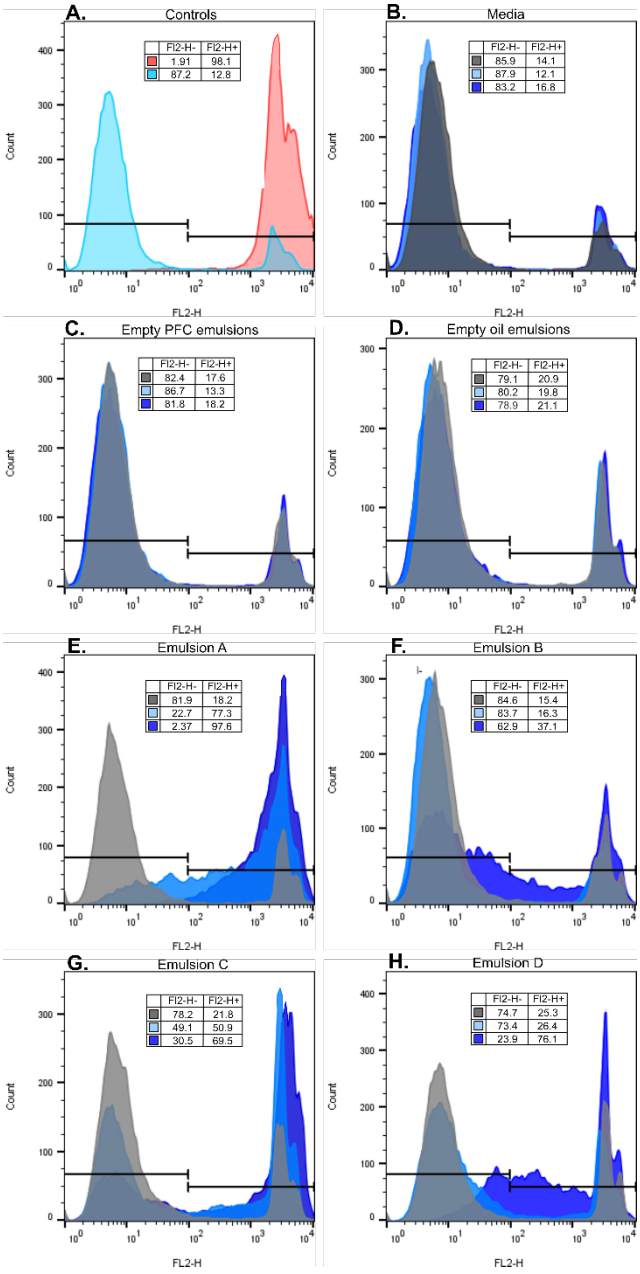

Figure S3.2 Histograms for flow cytometry data in Figure 3.18.

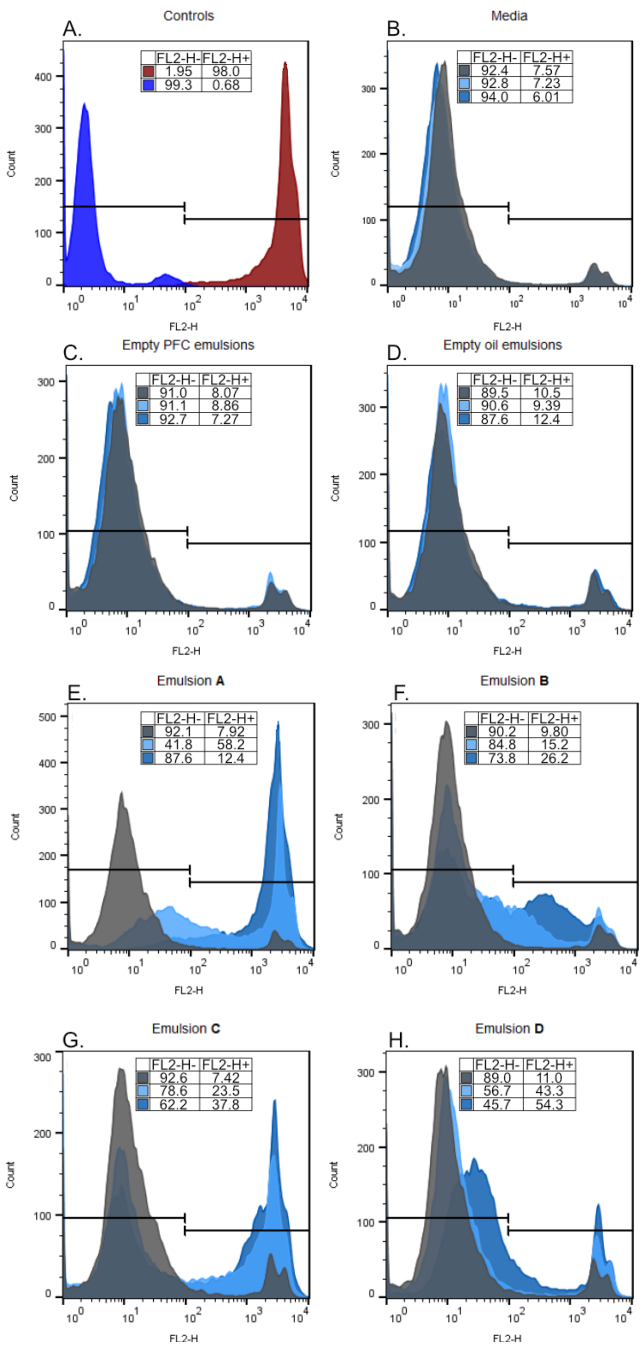

Figure S3.3 Histograms for flow cytometry data in Figure S3.19.

3.9.2 Single channel microscopy

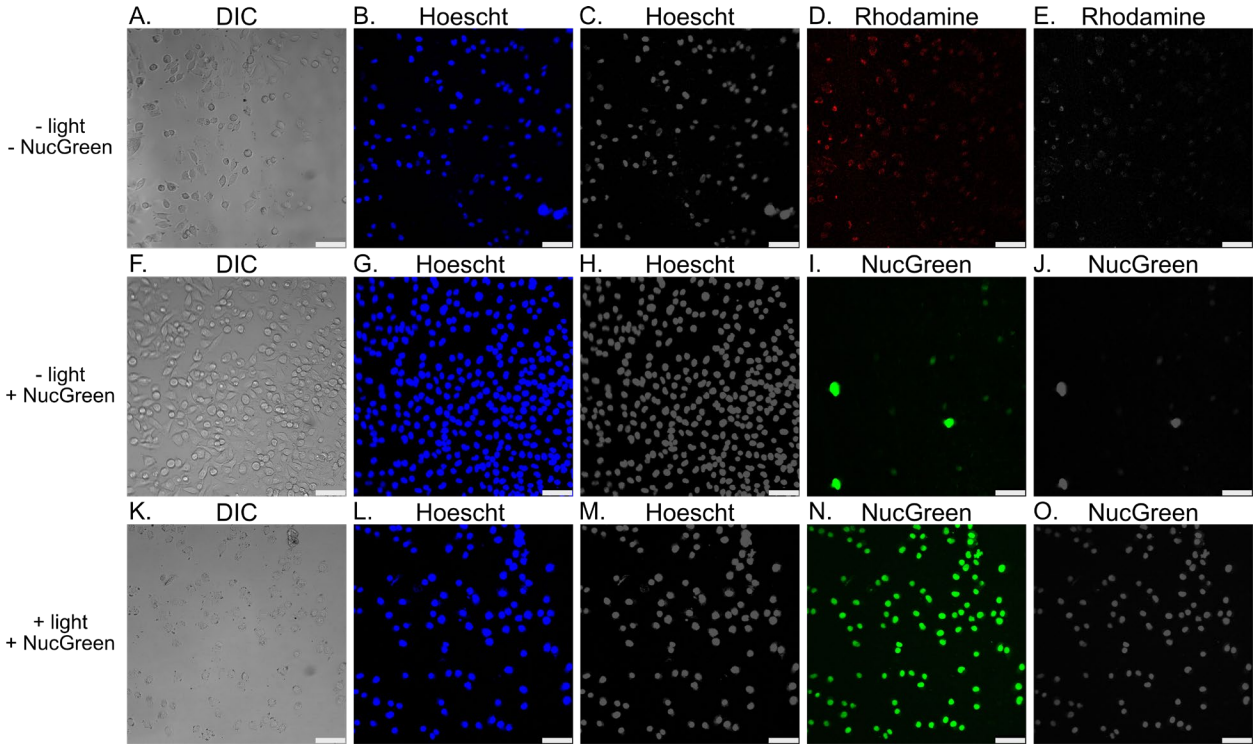

Figure S3.5 Single channel images for Figure 3.14C-E.

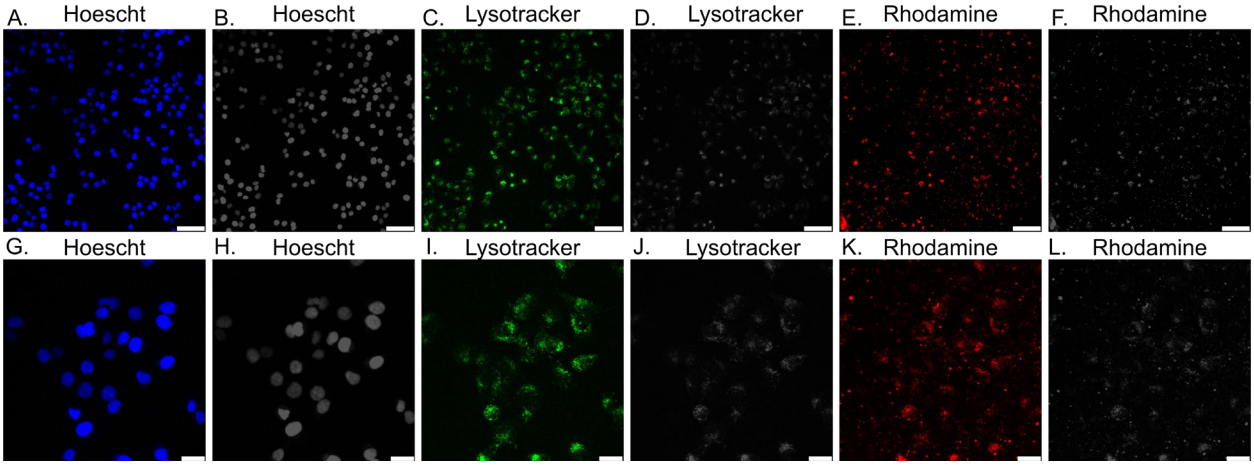

Figure S3.4 Single channel images for Figure 3.15.

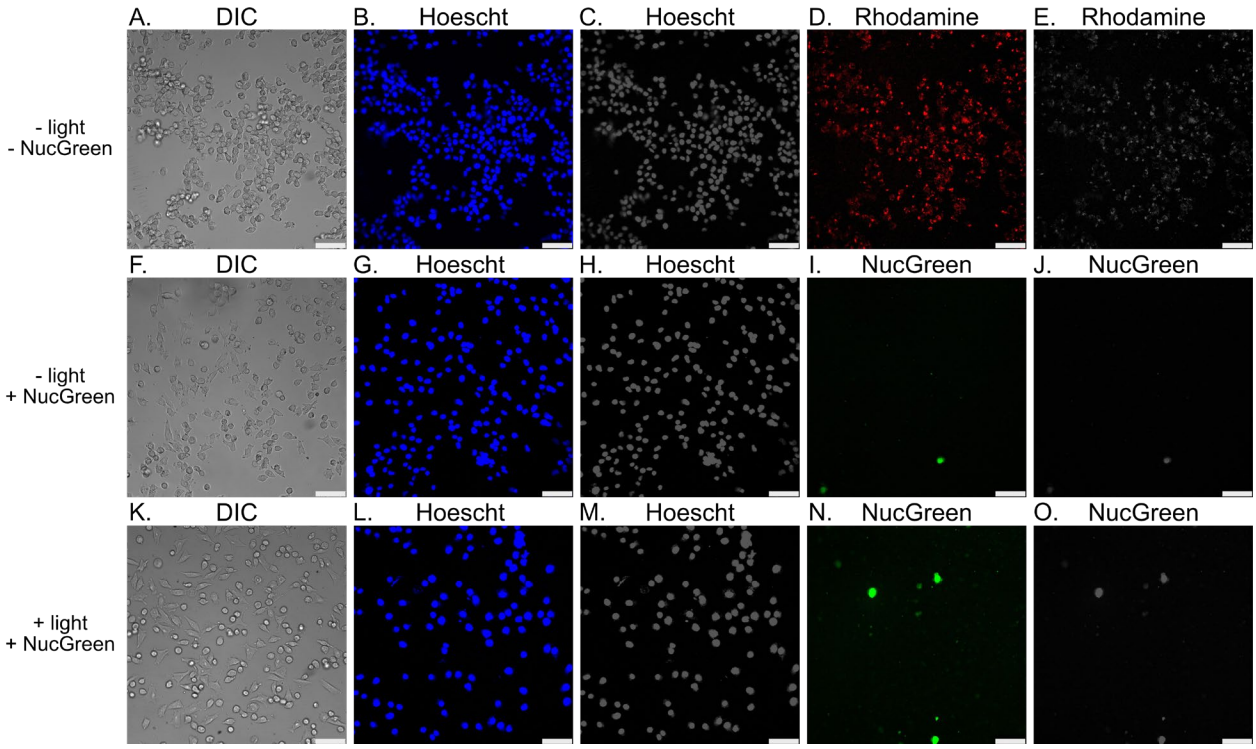

Figure S3.6 Single channel images for Figure 3.16

3.10 NMR Characterization

3.10.1 ^{1}H NMR Spectra

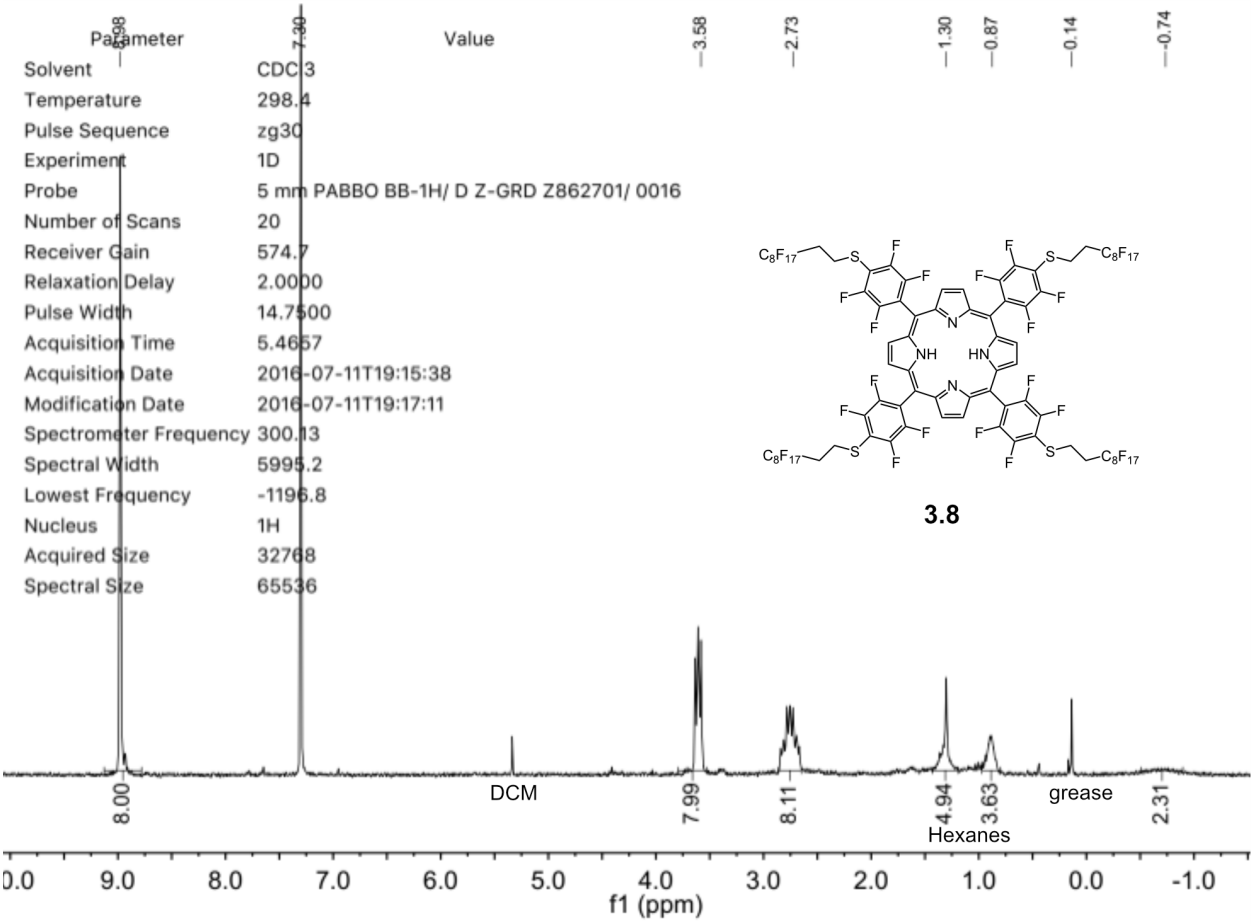

3.8

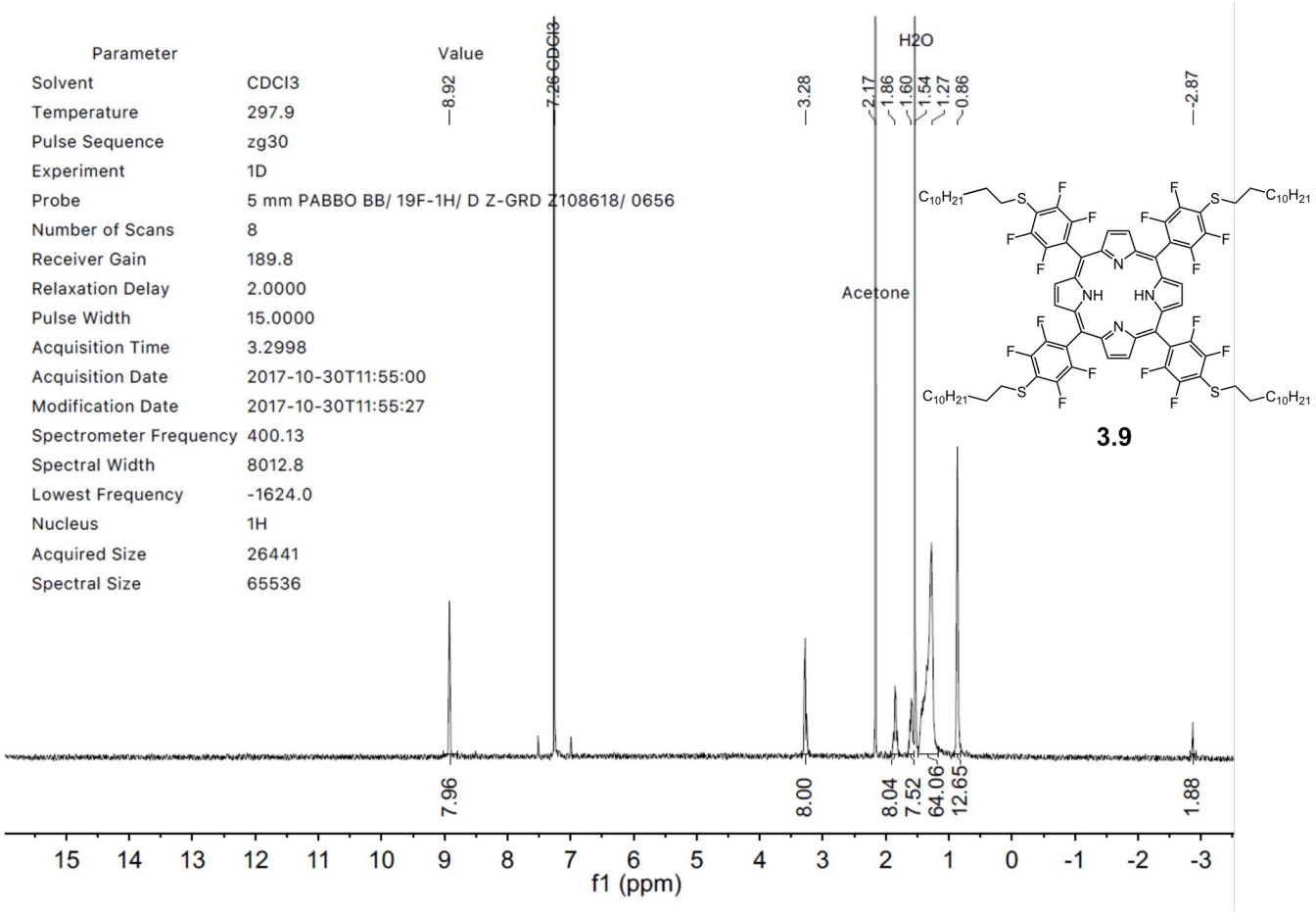
Parameter Value
Solvent CDCl3
Temperature 297.9
Pulse Sequence zg30
Experiment 1D
Probe 5 mm PABBO BB/ 19F-1H/ D Z-GRD Z108618/ 0656
Number of Scans 8
Receiver Gain 189.8
Relaxation Delay 2.0000
Pulse Width 15.0000
Acquisition Time 3.2998
Acquisition Date 2017-10-30T11:55:00
Modification Date 2017-10-30T11:55:27
Spectrometer Frequency 400.13
Spectral Width 8012.8
Lowest Frequency -1624.0
Nucleus 1H
Acquired Size 26441
Spectral Size 65536
8.92
7.26 CDCl3
3.28
2.17
1.86
1.60
1.54
1.27
0.86
-2.87
H2O
Acetone
7.96
8.00
8.04
7.52
64.06
12.65
1.88
15 14 13 12 11 10 9 8 7 6 5 4 3 2 1 0 -1 -2 -3
f1 (ppm)
3.9

3.10.2 ^{19}F NMR Spectra

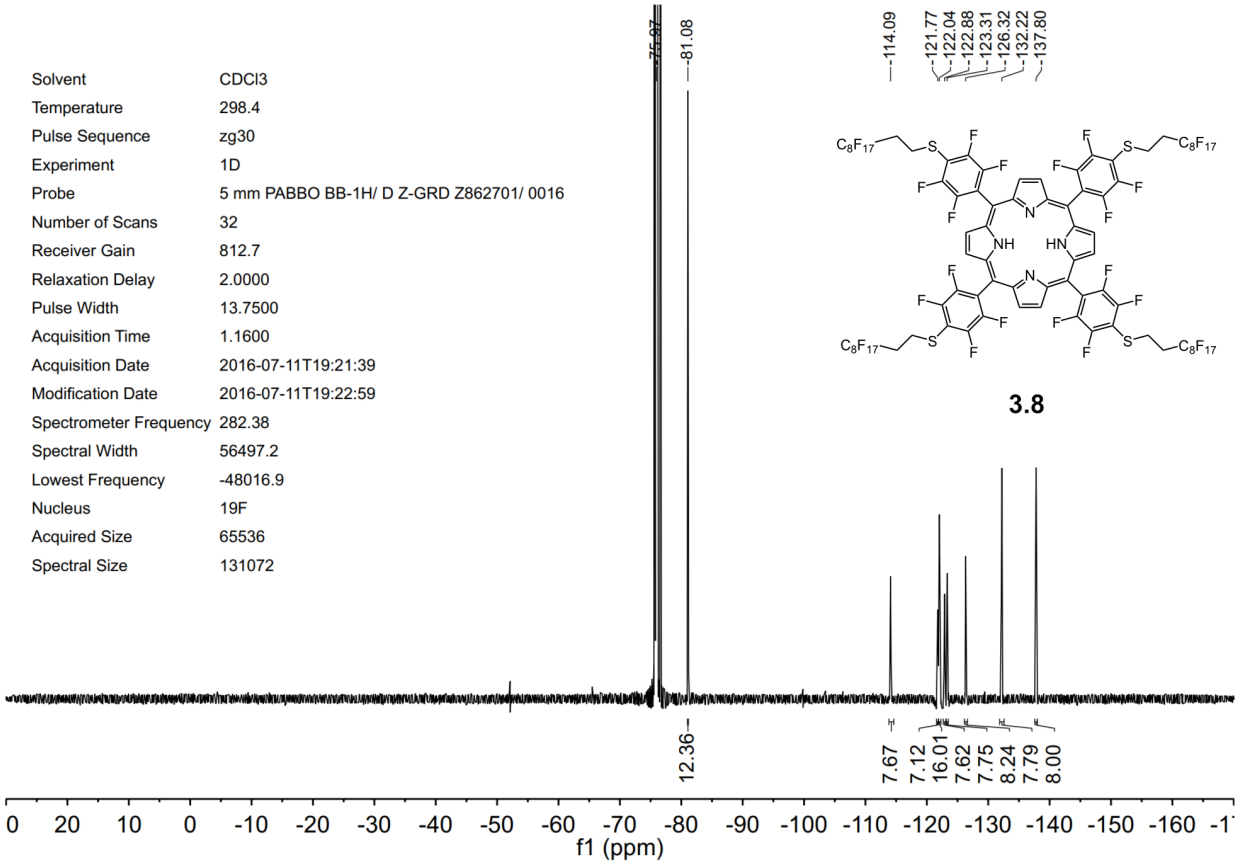

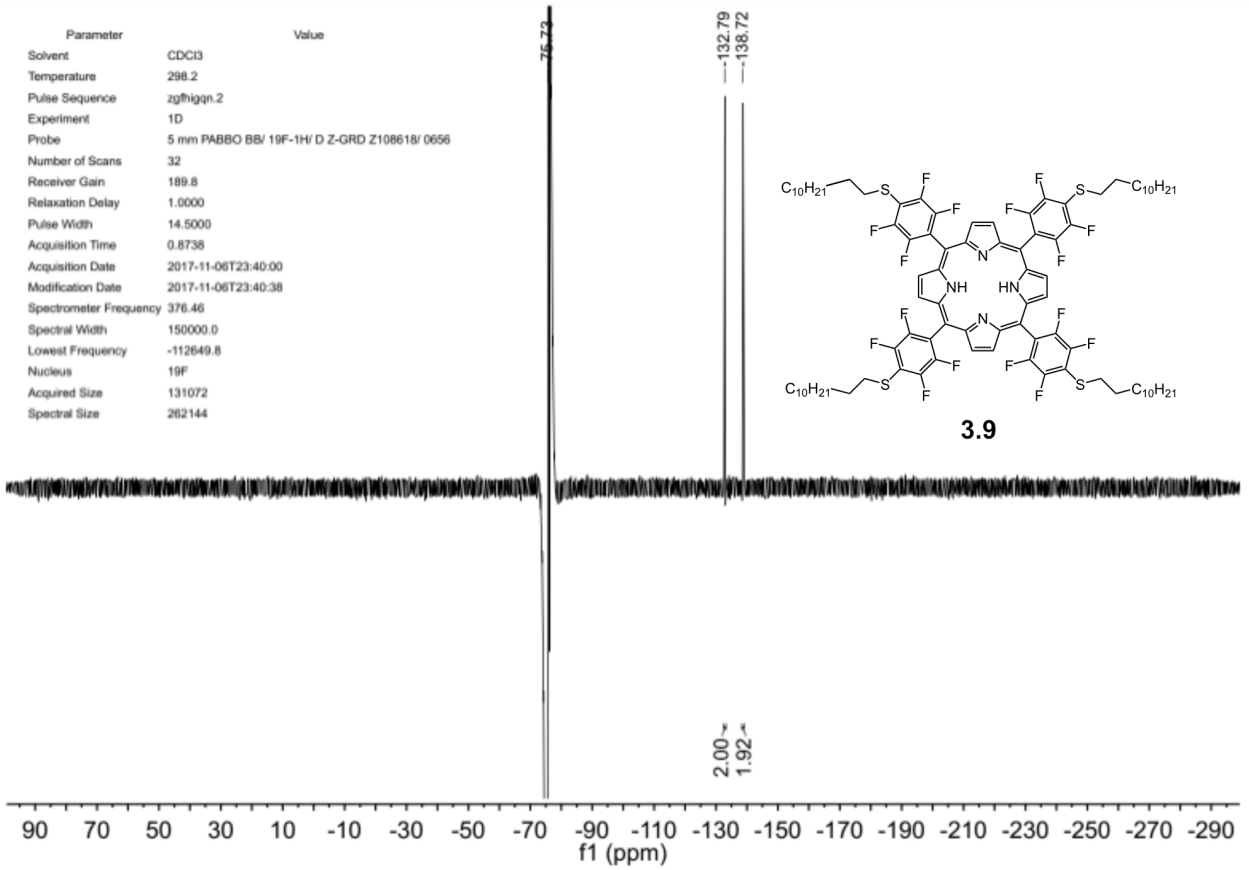
Parameter Value
Solvent CDCl3
Temperature 298.2
Pulse Sequence zgfhigqn.2
Experiment 1D
Probe 5 mm PABBO BB/ 19F-1H/ D Z-GRD Z108618/ 0656
Number of Scans 32
Receiver Gain 189.8
Relaxation Delay 1.0000
Pulse Width 14.5000
Acquisition Time 0.8738
Acquisition Date 2017-11-06T23:40:00
Modification Date 2017-11-06T23:40:38
Spectrometer Frequency 376.46
Spectral Width 150000.0
Lowest Frequency -112649.8
Nucleus 19F
Acquired Size 131072
Spectral Size 262144
-76.73
-132.79
-138.72
2.00
1.92
90 70 50 30 10 -10 -30 -50 -70 -90 -110 -130 -150 -170 -190 -210 -230 -250 -270 -290
f1 (ppm)

3.9

3.11 References and Notes

(1) Shi, J.; Kantoff, P. W.; Wooster, R.; Farokhzad, O. C. Cancer Nanomedicine: Progress, Challenges and Opportunities. *Nat. Rev. Cancer* **2017**, *17*, 20–37.

(2) Bacellar, I. O. L.; Tsubone, T. M.; Pavani, C.; Baptista, M. S. Photodynamic Efficiency: From Molecular Photochemistry to Cell Death. *Int. J. Mol. Sci.* **2015**, *16*, 20523–20559.

(3) Li, X.; Zheng, B. De; Peng, X. H.; Li, S. Z.; Ying, J. W.; Zhao, Y.; Huang, J. D.; Yoon, J. Phthalocyanines as Medicinal Photosensitizers: Developments in the Last Five Years. *Coord. Chem. Rev.* **2019**, *379*, 147–160.

(4) Lucky, S. S.; Soo, K. C.; Zhang, Y. Nanoparticles in Photodynamic Therapy. *Chem. Rev.* **2015**, *115*, 1990–2042.

(5) Riess, J. G.; Riess, J. G. Oxygen Carriers ("blood Substitutes") - Raison d'etre, Chemistry, and Some Physiology. *Chem. Rev.* **2001**, *101*, 2797–2919.

(6) Fraker, C. A.; Mendez, A. J.; Stabler, C. L. Complementary Methods for the Determination of Dissolved Oxygen Content in Perfluorocarbon Emulsions and Other Solutions. *J. Phys. Chem. B* **2011**, *115*, 10547–10552.

(7) Krafft, M. P. Alleviating Tumor Hypoxia with Perfluorocarbon-Based Oxygen Carriers. *Curr. Opin. Pharmacol.* **2020**, *53*, 117–125.

(8) Krafft, M. P. *The Curious World of Fluorinated Molecules*; 2020.

(9) Krafft, M; Riess, J. Perfluorocarbons: Life Sciences and Biomedical Uses. *J. Polym. Sci. Part A Polym. Chem.* **2007**, *45*, 1185–1198.

(10) Fuchs, J. T. J. The Role of Oxygen in Cutaneous Photodynamic Therapy. *Free Radic. Biol. Med.* **1998**, *24*, 835–847.

(11) Cheng, Y.; Cheng, H.; Jiang, C.; Qiu, X.; Wang, K.; Huan, W.; Yuan, A.; Wu, J.; Hu, Y. Perfluorocarbon Nanoparticles Enhance Reactive Oxygen Levels and Tumour Growth Inhibition in Photodynamic Therapy. *Nat. Commun.* **2015**, *6*, 8785–8793.

(12) Yu, M.; Xu, X.; Cai, Y.; Zou, L.; Shuai, X. Perfluorohexane-Cored Nanodroplets for Stimulations-Responsive Ultrasonography and O2-Potentiated Photodynamic Therapy. *Biomaterials* **2018**, *175*, 61–71.

(13) Sletten, E. M.; Swager, T. M. Fluorofluorophores: Fluorescent Fluorous Chemical Tools Spanning the Visible Spectrum. *J. Am. Chem. Soc.* **2014**, *136*, 13574–13577.

(14) Fingar, V. H.; Mang, T. S.; Henderson, B. W. Modification of Photodynamic Therapy-Induced Hypoxia by Fluosol-DA (20%) and Carbogen Breathing in Mice. *Cancer Res.* **1988**, *48*, 3350–3354.

(15) Wang, Y.-G.; Kim, H.; Mun, S.; Kim, D.; Choi, Y. Indocyanine Green-Loaded Perfluorocarbon Nanoemulsions for Bimodal (19)F-Magnetic Resonance/Nearinfrared Fluorescence Imaging and Subsequent Phototherapy. *Quant. Imaging Med. Surg.* **2013**, *3*, 132–140.

(16) Ren, H.; Liu, J.; Su, F.; Ge, S.; Yuan, A.; Dai, W.; Wu, J.; Hu, Y. Relighting Photosensitizers by Synergistic Integration of Albumin and Perfluorocarbon for Enhanced Photodynamic Therapy. *ACS Appl. Mater. Interfaces* **2017**, *9*, 3463–3473.

(17) Tang, X.; Cheng, Y.; Huang, S.; Zhi, F.; Yuan, A.; Hu, Y.; Wu, J. Overcome the Limitation of Hypoxia against Photodynamic Therapy to Treat Cancer Cells by Using Perfluorocarbon Nanodroplet for Photosensitizer Delivery. *Biochem. Biophys. Res. Commun.* **2017**, *487*, 483–487.

(18) Song, X.; Feng, L.; Liang, C.; Yang, K.; Liu, Z. Ultrasound Triggered Tumor Oxygenation with Oxygen-Shuttle Nanoperfluorocarbon to Overcome Hypoxia-Associated Resistance in Cancer Therapies. *Nano Lett.* **2016**, *16*, 6145–6153.

(19) Varotto, A.; Todaro, L.; Vinodu, M.; Koehne, J.; Liu, G.; Drain, C. M. Self-Organization of a New Fluorous Porphyrin and C60 Films on Indium-Tin-Oxide Electrode. *Chem. Commun.* **2008**, *1*, 4921–4923.

(20) Tanielian, C.; Schweitzer, C.; Mechin, R.; Wolff, C. Quantum Yield of Singlet Oxygen Production by Monomeric and Aggregated Forms of Hematoporphyrin Derivative. *Free Radic. Biol. Med.* **2001**, *30*, 208–212.

(21) Mathai, S.; Smith, T. A.; Ghiggino, K. P. Singlet Oxygen Quantum Yields of Potential Porphyrin-Based Photosensitisers for Photodynamic Therapy. *Photochem. Photobiol. Sci.* **2007**, *6*, 995–1002.

(22) Dias, A. M. A.; Bonifácio, R. P.; Marrucho, I. M.; Pádua, A. A. H.; Costa Gomes, M. F. Solubility of Oxygen in N-Hexane and in n-Perfluorohexane. Experimental Determination and Prediction by Molecular Simulation. *Phys. Chem. Chem. Phys.* **2003**, *5*, 543–549.

(23) You, Z. Q.; Hsu, C. P.; Fleming, G. R. Triplet-Triplet Energy-Transfer Coupling: Theory and Calculation. *J. Chem. Phys.* **2006**, *124*, 044506.

(24) Skourtis, S. S.; Liu, C.; Antoniou, P.; Virshup, A. M.; Beratan, D. N. Dexter Energy Transfer Pathways. *Proc. Natl. Acad. Sci.* **2016**, *113*, 8115–8120.

(25) Gladysz, J. A.; Jurisch, M. *Structural, Physical, and Chemical Properties of Fluorous Compounds*; 2012; Vol. 308.

(26) DiMagno, S. G.; Dussault, P. H.; Schultz, J. A. Fluorous Biphasic Singlet Oxygenation with a Perfluoroalkylated Photosensitizer. *J. Am. Chem. Soc.* **1996**, *118*, 5312–5313.

(27) Ghogare, A. A.; Miller, J. M.; Mondal, B.; Lyons, A. M.; Cengel, K. A.; Busch, T. M.; Greer, A. Fluorinated Photodynamic Therapy Device Tips and Their Resistance to Fouling for in Vivo Sensitizer Release. *Photochem. Photobiol.* **2016**, *92*, 166–172.

(28) Que, Y.; Liu, Y.; Tan, W.; Feng, C.; Shi, P.; Li, Y.; Xiaoyu, H. Enhancing Photodynamic Therapy Efficacy by Using Fluorinated Nanoplatform. *ACS Macro Lett.* **2016**, *5*, 168–173.

(29) Wallat, J. D.; Wek, K. S.; Chariou, P. L.; Carpenter, B. L.; Ghiladi, R. A.; Steinmetz, N. F.; Pokorski, J. K. Fluorinated Polymer-Photosensitizer Conjugates Enable Improved Generation of ROS for Anticancer Photodynamic Therapy. *Polym. Chem.* **2017**, *8*, 3195–3202.

(30) Bresolí-obach, R.; Nos, J.; Mora, M.; Lluïsa, M.; Ruiz-gonzález, R.; Nonell, S. Anthracene-Based Fluorescent Nanoprobes for Singlet Oxygen Detection in Biological Media. *Methods* **2016**, *109*, 64–72.

(31) De Jong, W. H.; JA Borm, B. Drug Delivery and Nanoparticles : Applications and Hazards. *Int. J. Nanomed.* **2008**, *3*, 133–149.

(32) Boija, E.; Johansson, G. Interactions between Model Membranes and Lignin-Related Compounds Studied by Immobilized Liposome Chromatography. *Biochim. Biophys. Acta* **2006**, *1758*, 620–626.

(33) Chen, J.; Pan, H.; Lanza, G. M.; Wickline, S. A. Perfluorocarbon Nanoparticles for Physiological and Molecular Imaging and Therapy. *Adv Chronic Kidney Dis* **2013**, *20*, 466–478.

(34) Kaneda, M. M.; Caruthers, S.; Lanza, G. M.; Wickline, S. A. Perfluorocarbon Nanoemulsions for Quantitative Molecular Imaging and Targeted Therapeutics. *Ann. Biomed. Eng.* **2009**, *37*, 1922–1933.

(35) O'Hanlon, C. E.; Amede, K. G.; O'Hear, M. R.; Janjic, J. M. NIR-Labelend Perfluoropolyether Nanoemulsions for Drug Delivery and Imaging. *J Fluor Chem* **2012**, *127*, 27–33.

(36) Sletten, E. M.; Swager, T. M. Readily Accessible Multifunctional Fluorous Nanoemulsions. *Chem. Sci.* **2016**, *7*, 5091–5097.

(37) Janjic, J. M.; Srinivas, M.; Kadayakkara, D. K. K.; Ahrens, E. T. Self-Delivering Nanoemulsions for Dual Fluorine-19 MRI and Fluorescence Detection. *J. Am. Chem. Soc.* **2008**, *130*, 2832–2841.

(38) Kolostova, K.; Spicka, J.; Matkowski, R.; Bobek, V. Isolation , Primary Culture , Morphological and Molecular Characterization of Circulating Tumor Cells in Gynecological Cancers. *Am J Transl Res* **2015**, *7*, 1203–1213.

(39) Edwards, H. D.; Nagappayya, S. K.; Pohl, N. L. B. Probing the Limitations of the Fluorous Content for Tag-Mediated Microarray Formation. *Chem. Commun.* **2012**, *48*, 510–512.

(40) Sun, Y.; Zhao, D.; Wang, G.; Wang, Y.; Cao, L.; Sun, J.; Jiang, Q.; He, Z. Recent Progress of Hypoxia-Modulated Multifunctional Nanomedicines to Enhance Photodynamic Therapy: Opportunities, Challenges, and Future Development. *Acta Pharm. Sin. B* **2020**, *10*, 1382–1396.

(41) Sahu, A.; Kwon, I.; Tae, G. Improving Cancer Therapy through the Nanomaterials-Assisted Alleviation of Hypoxia. *Biomaterials* **2020**, *228*, 119578.

(42) Li, X.; Kwon, N.; Guo, T.; Liu, Z.; Yoon, J. Innovative Strategies for Hypoxic-Tumor Photodynamic Therapy. *Angew. Chemie - Int. Ed.* **2018**, *57*, 11522–11531.

(43) Dang, J.; He, H.; Chen, D.; Yin, L. Manipulating Tumor Hypoxia toward Enhanced Photodynamic Therapy (PDT). *Biomater. Sci.* **2017**, *5*, 1500–1511.

(44) Larue, L.; Myrzakhmetov, B.; Ben-Mihoub, A.; Moussaron, A.; Thomas, N.; Arnoux, P.; Baros, F.; Vanderesse, R.; Acherar, S.; Frochot, C. Fighting Hypoxia to Improve PDT. *Pharmaceuticals* **2019**, *12*, 1–115.

(45) Master, A.; Livingston, M.; Sen Gupta, A. Photodynamic Nanomedicine in the Treatment of Solid Tumors: Perspectives and Challenges. *J. Control. Release* **2013**, *168*, 88–102.

(46) Yang, Z.; Wang, J.; Ai, S.; Sun, J.; Mai, X.; Guan, W. Self-Generating Oxygen Enhanced Mitochondriontargeted Photodynamic Therapy for Tumor Treatment with Hypoxia

Scavenging. *Theranostics* **2019**, *9*, 6809–6823.

(47) Vu, K. B.; Chen, T.; Almahdali, S.; Bukhryakov, K. V.; Rodionov, V. O. Hollow Nanospheres with Fluorous Interiors for Transport of Molecular Oxygen in Water. *ChemPubSoc Eur.* **2016**, *1*, 3306–3309.

(48) Teeple E Shrestha S, Dennerlein J, et al, C. J. Oxygen Sensing with Perfluorocarbon-Loaded Ultraporous Mesostructured. *ACS Nano* **2017**, *11*, 5623–5632.

(49) Sun, B.; Chang, R.; Cao, S.; Yuan, C.; Zhao, L.; Yang, H.; Li, J.; Yan, X.; van Hest, J. C. M. Acid-Activatable Transmorphic Peptide-Based Nanomaterials for Photodynamic Therapy. *Angew. Chemie - Int. Ed.* **2020**, *59*, 20582–20588.

(50) Tang, X.; Cheng, Y.; Huang, S.; Zhi, F.; Yuan, A.; Hu, Y.; Wu, J. Overcome the Limitation of Hypoxia against Photodynamic Therapy to Treat Cancer Cells by Using Perfluorocarbon Nanodroplet for Photosensitizer Delivery. *Biochem. Biophys. Res. Commun.* **2017**, *487*, 483–487.

(51) Li, W.; Yong, J.; Xu, Y.; Wang, Y.; Zhang, Y.; Ren, H.; Li, X. Glutathione Depletion and Dual-Model Oxygen Balance Disruption for Photodynamic Therapy Enhancement. *Colloids Surfaces B Biointerfaces* **2019**, *183*, 110453.

(52) Sheng, D.; Liu, T.; Deng, L.; Zhang, L.; Li, X.; Xu, J.; Hao, L.; Li, P.; Ran, H.; Chen, H.; Wang, Z. Perfluorooctyl Bromide & Indocyanine Green Co-Loaded Nanoliposomes for Enhanced Multimodal Imaging-Guided Phototherapy. *Biomaterials* **2018**, *165*, 1–13.

(53) Hester, S. C.; Kuriakose, M.; Nguyen, C. D.; Mallidi, S. Role of Ultrasound and

Photoacoustic Imaging in Photodynamic Therapy for Cancer. *Photochem. Photobiol.* **2020**, *96*, 260–279.

(54) Maiti; Bidinger. Solubility and Transport Phenomena in Perfluorochemicals Relevant to Blood Substitution and Other Biomedical Applications. *Pure Appl. Chem.* **1982**, *54*, 2383–2406.

(55) Schmieder, A. H.; Caruthers, S. D.; Keupp, J.; Wickline, S. A.; Lanza, G. M. Recent Advances in 19Fluorine Magnetic Resonance Imaging with Perfluorocarbon Emulsions. *Engineering* **2015**, *1*, 475–489.

(56) Hu, D. R.; Zhong, L.; Wang, M. Y.; Li, H. H.; Qu, Y.; Liu, Q. Y.; Han, R.; Yuan, L. P.; Shi, K.; Peng, J. R.; Qian, Z. Y. Perfluorocarbon-Loaded and Redox-Activatable Photosensitizing Agent with Oxygen Supply for Enhancement of Fluorescence/Photoacoustic Imaging Guided Tumor Photodynamic Therapy. *Adv. Funct. Mater.* **2019**, *29*, 1806199.

(57) Ren, H.; Liu, J.; Su, F.; Ge, S.; Yuan, A.; Dai, W.; Wu, J.; Hu, Y. Relighting Photosensitizers by Synergistic Integration of Albumin and Perfluorocarbon for Enhanced Photodynamic Therapy. *ACS Appl. Mater. Interfaces* **2017**, *9*, 3463–3473.

(58) Day, R. A.; Estabrook, D. A.; Logan, J. K.; Sletten, E. M. Fluorous Photosensitizers Enhance Photodynamic Therapy with Perfluorocarbon Nanoemulsions. *Chem. Commun.* **2017**, *53*, 13043–13046.

(59) Li, N.; Xu, F.; Cheng, J.; Zhang, Y.; Huang, G.; Zhu, J.; Shen, X.; He, D. Perfluorocarbon Nanocapsules Improve Hypoxic Microenvironment for the Tumor Ultrasound Diagnosis

and Photodynamic Therapy. *J. Biomed. Nanotechnol.* **2018**, *14*, 2162–2171.

(60) Day, R. A.; Estabrook, D.; Wu, C.; Chapman, J. O.; Togle, A. J.; Sletten, E. M. Systematic Study of Perfluorocarbon Nanoemulsions Stabilized by Polymer Amphiphiles. *ACS Appl. Mater. Interfaces* **2020**, *12*, 38887–38898.

(61) Ke Jiang, Haoran Wang, Huanhuan Zhang, Yiqiao Hu, J. W. Enhanced Photodynamic Therapy by Encapsulation of Perfluorocarbon into PEGylated Near-Infared Dyes. *Cell. Mol. Biol.* **2018**, *64*, 66–72.

(62) Wang, W.; Cheng, Y.; Yu, P.; Wang, H.; Zhang, Y.; Xu, H.; Ye, Q.; Yuan, A.; Hu, Y.; Wu, J. Perfluorocarbon Regulates the Intratumoural Environment to Enhance Hypoxia-Based Agent Efficacy. *Nat. Commun.* **2019**, *10*, 1580.

(63) Patil, Y.; Almahdali, S.; Vu, K. B.; Zapsas, G.; Hadjichristidis, N.; Rodionov, V. O. PH-Sensitive Amphiphilic Block-Copolymers for Transport and Controlled Release of Oxygen. *Polym. Chem.* **2017**, *8*, 4322–4326.

(64) Hu, H.; Yan, X.; Wang, H.; Tanaka, J.; Wang, M.; You, W.; Li, Z. Perfluorocarbon-Based O 2 Nanocarrier for Efficient Photodynamic Therapy. *J. Mater. Chem. B* **2019**, *7*, 1116–1123.

(65) Liu, Z.; Xue, Y.; Wu, M.; Yang, G.; Lan, M.; Zhang, W. Sensitization of Hypoxic Tumor to Photodynamic Therapy via Oxygen Self-Supply of Fluorinated Photosensitizers. *Biomacromolecules* **2019**, *20*, 4563–4573.

(66) Yuan, P.; Ruan, Z.; Jiang, W.; Liu, L.; Dou, J.; Li, T.; Yan, L. Oxygen Self-Sufficient

Fluorinated Polypeptide Nanoparticles for NIR Imaging-Guided Enhanced Photodynamic Therapy. *J. Mater. Chem. B* **2018**, *6*, 2323–2331.

(67) Wang, Q.; Li, J. M.; Yu, H.; Deng, K.; Zhou, W.; Wang, C. X.; Zhang, Y.; Li, K. H.; Zhuo, R. X.; Huang, S. W. Fluorinated Polymeric Micelles to Overcome Hypoxia and Enhance Photodynamic Cancer Therapy. *Biomater. Sci.* **2018**, *6*, 3096–3107.

(68) Li, J.; Xue, Y.; Tian, J.; Liu, Z.; Zhuang, A.; Gu, P.; Zhou, H.; Zhang, W.; Fan, X. Fluorinated-Functionalized Hyaluronic Acid Nanoparticles for Enhanced Photodynamic Therapy of Ocular Choroidal Melanoma by Ameliorating Hypoxia. *Carbohydr. Polym.* **2020**, *237*, 116119.

(69) Kantonis, G.; Trikeriotis, M.; Ghanotakis, D. F. Biocompatible Protoporphyrin IX-Containing Nanohybrids with Potential Applications in Photodynamic Therapy. *J. Photochem. Photobiol. A Chem.* **2007**, *185*, 62–66.

(70) Tao, D.; Feng, L.; Chao, Y.; Liang, C.; Song, X.; Wang, H.; Yang, K.; Liu, Z. Covalent Organic Polymers Based on Fluorinated Porphyrin as Oxygen Nanoshuttles for Tumor Hypoxia Relief and Enhanced Photodynamic Therapy. *Adv. Funct. Mater.* **2018**, *28*, 180491.

(71) Pushalkar, S.; Ghosh, G.; Xu, Q.; Liu, Y.; Ghogare, A. A.; Atem, C.; Greer, A.; Saxena, D.; Lyons, A. M. Superhydrophobic Photosensitizers: Airborne 1O2 Killing of an in Vitro Oral Biofilm at the Plastron Interface. *ACS Appl. Mater. Interfaces* **2018**, *10*, 25819–25829.

(72) Pinnavaia, T. J.; Chibwe, M.; Constantino, V. R. L.; Yun, S. K. Organic Chemical

Conversions Catalyzed by Intercalated Layered Double Hydroxides (LDHs). *Appl. Clay Sci.* **1995**, *10*, 117–129.

(73) Redmond, R. W.; Gamlin, J. N. A Compilation of Singlet Oxygen Yields from Biologically Relevant Molecules. *Photochem. Photobiol.* **1999**, *70*, 391–475.

CHAPTER FOUR

Redox responsive materials for payload delivery via perfluorocarbon nanoemulsions

Adapted from:

Margeaux A. Miller,[±] Rachael A. Day,[±] Daniel A. Estabrook[±] and Ellen M. Sletten.* A reduction-sensitive fluorous fluorogenic coumarin. *Synlett*, **2020**, *31*, 450-454.

DOI: 10.1055/s-0039-1690770 [±] denotes equal contribution

and

Daniel A. Estabrook, Rachael A. Day, and Ellen M. Sletten.* Redox-responsive gene delivery from perfluorocarbon nanoemulsions through cleavable poly(2-oxazoline) surfactants. *Angew. Chem. Int. Ed.* **2021**, *Accepted.* DOI: 10.1002/anie.202102413.

4.1 Abstract

In order to deliver active therapeutics to the cytosol of cells, a responsive payload and surfactant to stabilize nanoemulsions is desired. The concentration of glutathione in the cytosol is 5-10 mM and the concentration of glutathione in the extracellular matrix is in the micromolar range. Thus, we looked to design a payload that will become fluorescent, and a polymer surfactant that will release payload when exposed to the high concentrations of glutathione in the cytosol. To do this, we used strategically placed disulfide bonds. We use these tools to study how payloads encapsulated in perfluorocarbon nanoemulsions experience the environment surrounding the nanoemulsions, and ways to predictably, and with control, release payloads from the perfluorocarbon core.

4.2 Introduction

Emulsions, a class of soft nanomaterials, have been explored for drug delivery since World War II.[1] Nanoemulsions – droplets less than ~200 nm – are well-suited to biomedical applications due to their small size and long-term kinetic stability.[2] While the former results in extended half-lives *in vivo* and tumor accumulation,[3] the latter allows for stability and tolerance to environmental changes (*e.g.,* pH, temperature)[4] with the *in vivo* fate being controlled by the interior lipophilic core and surface properties.[5] Currently, all five FDA-approved emulsion formulations involve passive release of small molecule payloads.[4,6] Taking inspiration from stimuli that are present within the cytosol of cells, but not present in the extracellular environment, we looked to design materials that would be responsive to the high concentrations of glutathione found within cells.[7] Here, we design a fluorogenic, fluorous soluble fluorophore (Figure 4.1A; *Sections 4.3.1)* and a redox responsive polymer for the controlled release and delivery of plasmid DNA (Figure 4.1B; *Sections 4.3.2)*.

As introduced in prior chapters, we are interested in studying nanoemulsions in which the inner phase is composed of perfluorocarbons (PFCs). The orthogonality of perfluorocarbons to aqueous and organic solution prevents the leaching of fluorous soluble molecules into biological environments,[8] which is a limitation of traditional oil emulsions and has hindered the translation to the clinic. The extreme hydrophobicity and nonpolarizability of perfluorocarbons[9,10] necessitate the use of fluorous tags[11] to solubilize payloads and fluorous soluble fluorophores for the visualization of PFC nanoemulsions.[12,13]

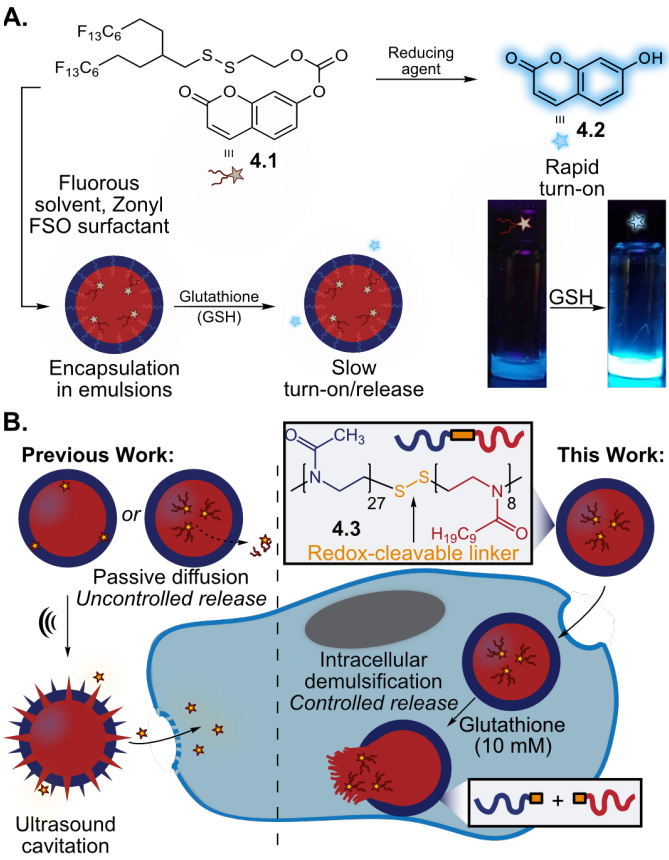

Figure 4.1 Redox responsive tools for the study of PFC nanoemulsions. (A) Redox sensitive, fluorogenic coumarin **4.1**, becomes fluorescent coumarin **4.2** after exposure to reducing agents. Coumarin **4.1** can be incorporated in PFC nanoemulsions. (B) Controlled release of payload through PFC nanoemulsions stabilized by responsive polymer **4.3**, compared to previous work which relied on passive diffusion or ultrasound treatment for release of payload.

4.3 Results and Discussion

4.3.1 Fluorogenic coumarin

Chromophores that undergo changes in their photophysical properties in response to environmental or chemical perturbations are valuable tools to gain quantitative information in complex systems.[14–17] These probes are designed such that they either undergo a shift in $\lambda_{max,abs}$ or $\lambda_{max,em}$, deemed solvatochromic or ratiometric, respectively, or an enhancement in quantum yield, deemed fluorogenic (Figure 1A). Thousands of solvatochromic, ratiometric, and fluorogenic probes have been prepared to measure polarity changes,[14–18] quantify ion concentrations,[19–22] image cellular compartments,[23,24] detect metabolites,[25–27] sense chemical warfare agents,[28–31] etc. The medium that these probes can function in varies from gas phase to organic solvents to aqueous buffers; however, applications in the fluorous phase are scarce.

We chose coumarin as a scaffold for the development of a fluorogenic fluorous fluorophore due to literature precedent for solubilizing coumarin in perfluorocarbons,[12,32–34] in addition to the large body of work demonstrating that coumarin fluorescence can be modulated by changes in substituents at the 7-position.[35–37] We envisioned that the hydroxyl group of 7-hydroxycoumarin could be alkylated with a chemically sensitive linkage connected to a fluorous tag. The branched fluorous tag imparts fluorous solubility to the starting fluorophore, while the chemically sensitive linker facilitates fluorescence turn-on. For our initial work, we chose a disulfide as the chemically sensitive linkage, which was connected to the coumarin via a self-immolating carbonate linker[38] to facilitate release of 7-hydroxycoumarin (**4.2**).

We looked to a commonly used, self-immolative, redox responsive linker[38,39] and reasoned that we could use previously developed chemistry in the Sletten lab to form a fluorous soluble self-immolative linker. With this linker in hand, we synthesized the first fluorous soluble, fluorogenic

fluorophore, a coumarin (**4.1**). We evaluated the response of coumarin **4.1** to a variety of reducing agents. We anticipated that disulfide cleavage via a reducing agent would lead to thiol **4.4** and **4.5**, which would spontaneously eliminate 1,3-oxathiolane-2-one (**4.6**) to release fluorescent **4.2** (Figure 4.2A). To test an initial panel of reducing agents, we dissolved **4.1** in acetone. Acetone was chosen as we have found it to be sufficient to solubilize many partially fluorinated compounds and it is miscible with water, allowing polar reducing agents to be analyzed. As can be seen in Figure 4.2B, upon addition of 10 mM β-mercaptoethanol (BME, dark blue), dithiothrietol (DTT, green), glutathione (GSH, purple), or tris(carboxyethyl phosphine) (TCEP, orange) significant fluorescence is observed, becoming similar to that of free 7-hydroxycoumarin, suggested that efficient cleavage of the disulfide in **4.1** was readily obtained.[40] Importantly, if reagents that are not able to reduce disulfide bonds are added, such as oxidized glutathione (ox GSH, gray) or ethylene glycol (black), little fluorescence is observed.

Next, we moved to evaluating the fluorogenic nature of **4.1** in fluorous solvents. Coumarin **4.1** was dissolved in perfluorooctyl bromide (PFOB, **3.19**), methoxyperfluorobutane (MPFB), perfluorodecalin (PFD, **3.18**), or perfluorohexanes (PFH, **3.7**) and partitioned with phosphate buffered saline (PBS). It is important to note, although **4.1** was soluble in fluorous solvent, there was aggregation seen via a hypsochromic shoulder in the absorbance spectra in all solvents tested (Figure 4.3). Minimal signal is observed until the addition of β-mercaptoethanol (BME), at which point robust emission from the aqueous layer is apparent (Figure 4.2C).

Of particular interest is the response to glutathione, as glutathione levels are very high intracellularly (5–10 mM) but low extracellularly (10 μM).[7,41] We further probed the turn-on kinetics of **4.1** under various concentrations of glutathione and found that when treated with micromolar concentrations of glutathione there was less than 10-fold turn-on over the course

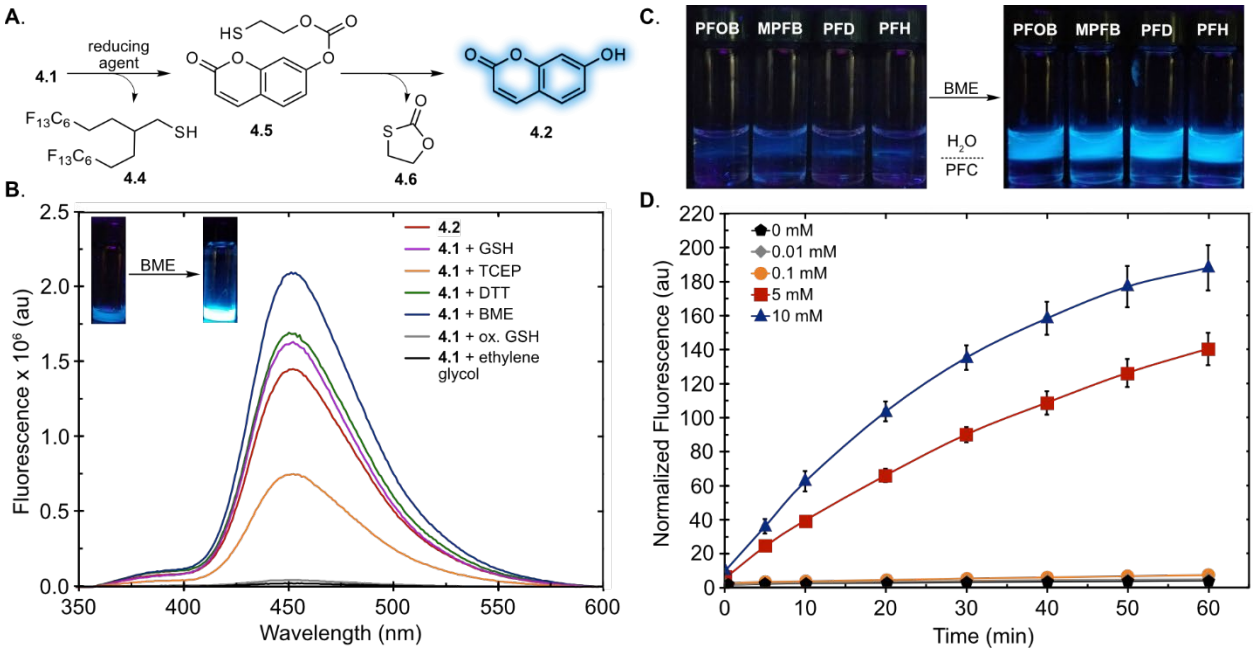

Figure 4.2 (A) Cleavage of disulfide bond in the presence of reducing agent to release a free thiol that rapidly undergoes self-immolation to give fluorescent 7-hydroxycoumarin. (B) Fluorescence spectra of **4.1** (49.1 μM, 1:1 acetone/PBS pH 7.4) after 30 min treatment with 10 mM: glutathione (GSH, purple), tris(carboxyethylphosphine) (TCEP, orange), dithiothreitol (DTT, green), β-mercaptoethanol (BME, blue), oxidized glutathione (ox. GSH, gray), and ethylene glycol (black). 7-hydroxycoumarin 3 (49.1 μM in 1:1 acetone/PBS) is shown in red. Inset: Long-wave UV image of **4.1** in 1:1 acetone /PBS before and after the adition of 10 mM β-mercaptoethanol (BME). (C) Long-wave UV images of **4.1** (0.05 mg in 0.75 mL fluorous solvent partitioned against 0.75 mL PBS pH 7.4) before and after reduction with 10 mM BME. Fluorous solvent = perfluorooctyl bromide (PFOB, **3.19**), methoxyperfluorobutane (MPFB), perfluorodecalin (PFD), perfluorohexane (PFH). (D) Time-dependent turn-on of **4.1** (19.1 μM, 1:1 acetone/PBS pH 7.4) in the presence of intra- (5–10 mM) and extracellular (0–0.1 mM) concentrations of glutathione: (0 mM, black hexagon; 0.01 mM, gray diamond; 0.1 mM, orange circle; 5 mM, red square; 10 mM, blue triangle)

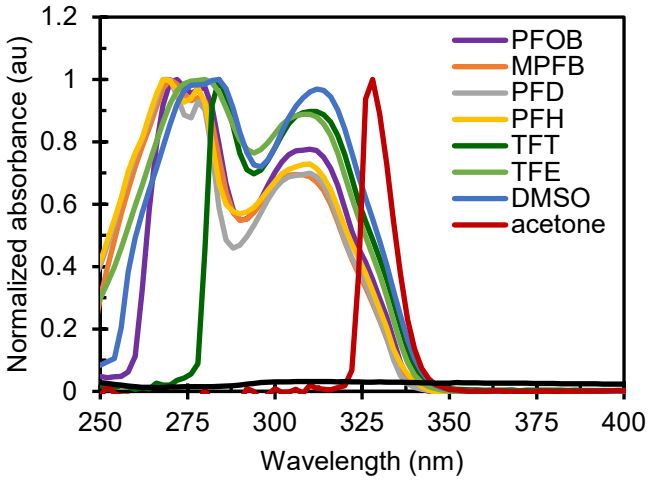

Figure 4.3 Normalized UV/Vis spectra of **4.1** (78.6 μM) in perfluorooctyl bromide (**3.19**, purple), methoxyperfluorobutane (MPFB, orange), perfluorodecalin (PFD, gray), perfluorohexanes (PFH, yellow), trifluorotoluene (TFT, dark green), trifluoroethanol (TFE,light green), dimethylsulfoxide (DMSO, blue), acetone (red), and phosphate buffered saline (PBS, black).

of an hour compared to the control (Figure 4.2D, orange, gray vs. black). When exposed to either 5 mM or 10 mM glutathione, the fluorescence increased over 100-fold within an hour (Figure 4.2D, red, blue vs. black). These data suggest that fluorogenic coumarin **4.1** can differentiate between biologically relevant glutathione levels.

One application of **4.1** is as a probe to measure the response of fluorous nanomaterials to intra- and extracellular conditions. Towards this end, we compared the properties of **4.1** encapsulated in two different delivery vehicles: (i) droplets of fluorous solvent stabilized in water, (i.e., perfluorocarbon nanoemulsions) and (ii) fluorous coreshell micelles. Our group is interested in exploiting the orthogonal nature of the fluorous phase to create advanced nanotherapeutics.[8,11,12,42,43] An important component of fluorous nanotherapeutics is the ability for fluorous-tagged molecules to be protected inside the biologically inert and nontoxic fluorous core.[44,45] Fluorogenic coumarin **4.1** allowed us to directly test if cargo loaded into the center of the perfluorocarbon nanoemulsions or micelles sense the surrounding environment.

Perfluorocarbon nanoemulsions containing **4.1** were prepared by first solubilizing **4.1** in **3.19** (982 μM) and then combining with PBS to make a biphasic solution of 10 vol% fluorous oil. A commercially available nonionic fluorosurfactant, Zonyl FSN-100 (**2.4**), was added to a surfactant loading of 2.8 wt% in PBS (Figure 4.4A). Emulsions were then formed through ultrasonication at the liquid–liquid interface for 90 s at 0 °C. This procedure resulted in weakly fluorescent emulsions with a diameter of 185 nm and a polydispersity of 0.13 (Figures 4.5A). To prepare micelles, **2.4** was dissolved in a stock solution of MilliQ water at 2.8 wt% (far above the critical micelle concentration), and **4.1** was added via an acetone stock, yielding weakly fluorescent 6 nm micelles with a polydispersity of 0.04 (Figures 4.5B).[46]

To probe the role of these delivery vehicles in protecting the fluorogenic dye from the surrounding environment, nanomaterials were treated with no, low (e.g., extracellular, 0.1 mM), or high (e.g., intracellular, 10 mM) levels of glutathione in PBS. The fluorescence was then monitored over 48 h at 25 °C (Figure 4.4B and 4.6A, 4.6B). As expected, when encapsulated in either micelles or nanoemulsions, **4.1** shows reduced turn-on. After a 12 h incubation in 10 mM GSH at 25 °C, micelles and emulsions show similar levels of cargo protection, having 79% and 83% less fluorescence than the free dye, respectively. After 48 h, micelles and emulsions exhibit 85% and 70% less release than the free dye, indicating that, at room temperature, micelles show delayed release kinetics over time compared to emulsions. However, after 48 h at physiological temperature (37 °C), similar levels of protection are observed for the two vehicles (Figures 4.7A/B). As seen in Figure 4.4C, which compares 48 h fluorescence measurements at 25 °C or 37 °C, the micelles and emulsions both effectively reduce fluorescence by roughly 40% compared to free dye, although there is more significant turn-on of **4.1** at elevated temperatures. Together, these data demonstrate that encapsulation of a fluorogenic dye within the perfluorocarbon droplets or fluorous micelles effectively shields cargo from environmental stimuli. Yet, different turn-on kinetics are observed for the two vehicles, suggesting opportunities for engineering slow release of drugs by tuning the fluorous delivery vehicle.

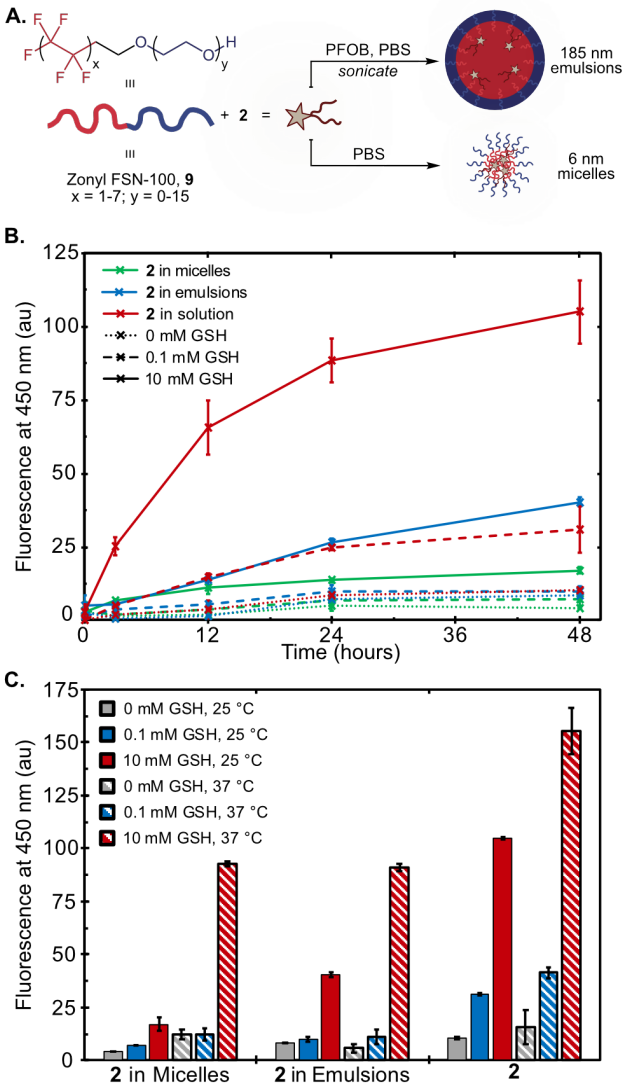

Figure 4.4 (A) Fluorogenic coumarin **4.1** was loaded into either perfluorooctylbromide-in-water emulsions or micelles formed from fluorosurfactant 9. See Figures 4.5A, 4.5B for size analysis of emulsions and micelles, respectively. See Figures 4.6A, 4.7A for emission spectra of emulsions and micelles containing **4.1** at 25 °C and 37 °C, respectively. (B) Emulsions and micelles were exposed to no, low (0.1 mM, extracellular), or high (10 mM, intracellular) levels of glutathione (GSH) in PBS, and fluorescence was monitored over 48 h at 25 °C. See Figure 4.6B for inset. (C) Fluorescence turn-on of **4.1** in emulsions, micelles, or free in solution after 48 h at both 25 °C and 37 °C. See Figures 4.7B for fluorescence traces over time at 37 °C.

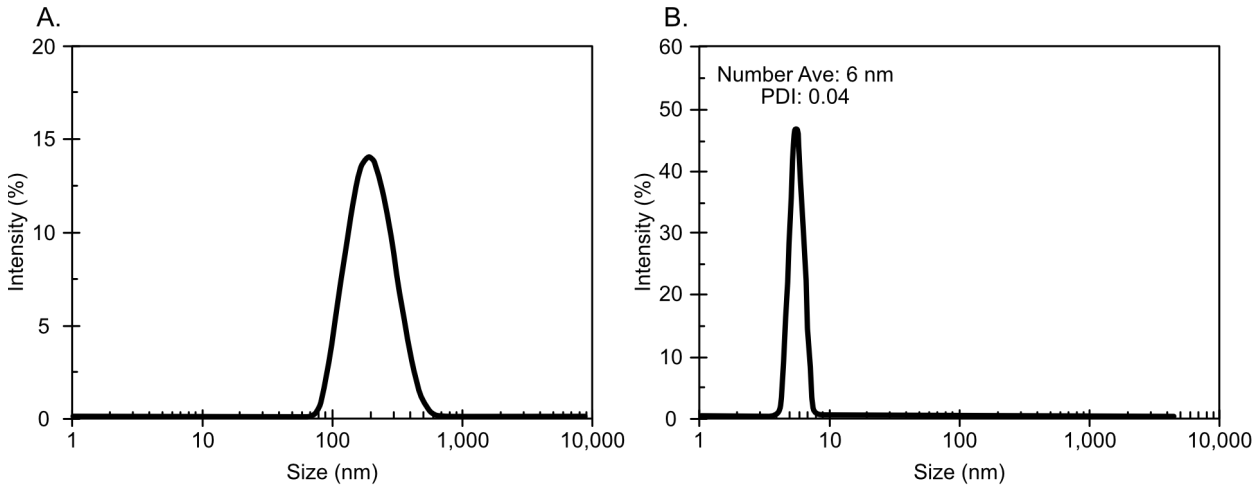

Figure 4.5 (A) Dynamic light scattering data for the **2.4** emulsions in MilliQ water. Data are an average of five replicate measurements. See general nanoemulsion formation and analysis procedures for more information. (B) Dynamic light scattering data for the **2.4** micelles in MilliQ water (2.8 mg/mL). Data are an average of five replicate measurements. See general micelle formation and analysis procedures for more information.

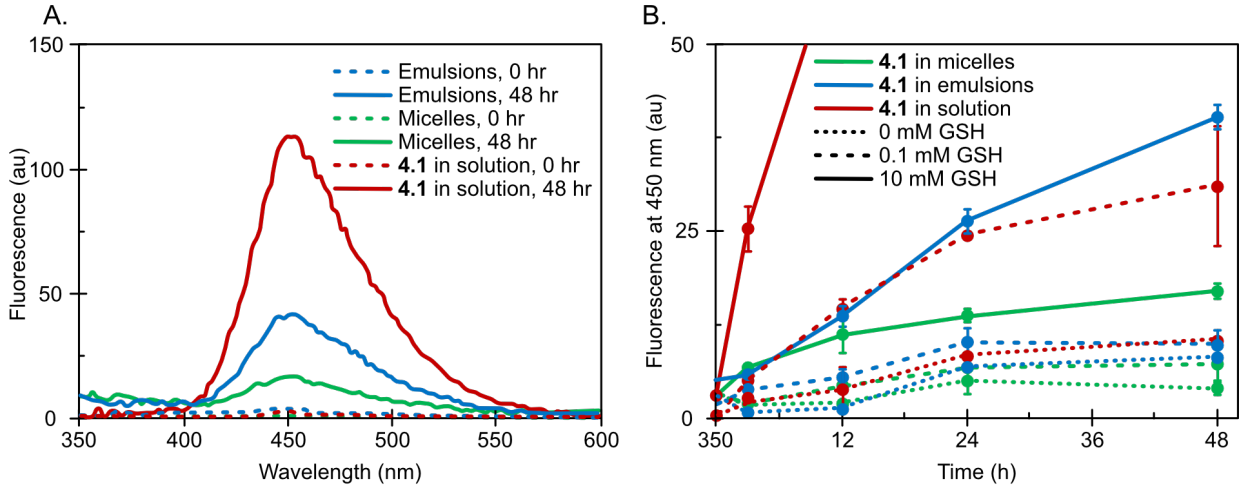

Figure 4.6 (A) Fluorescence of **4.1** either free in solution (red) or loaded in **2.4** stabilized micelles (green) or perfluorooctylbromide-in-water nanoemulsions (982 μM in **3.19**, blue). All samples are incubated with 10 mM GSH at 25 °C and fluorescence was monitored over 48 hours (see Figure 4.4B). Data are representative of three replicate measurements. (B) Zoom in of Figure 4.4B. Fluorescence at 450 nm of **4.1** either free in solution (red) or loaded in **2.4** stabilized micelles (green) or perfluorooctylbromide-in-water nanoemulsions (982 μM in **3.19**, blue). All samples are incubated with 0 (dotted line), 0.1 (dashed line) or 10 mM (solid line) GSH at 25 °C and fluorescence was monitored over 48 hours. Data are an average of three replicate measurements. Error bars represent the standard deviation of three replicates.

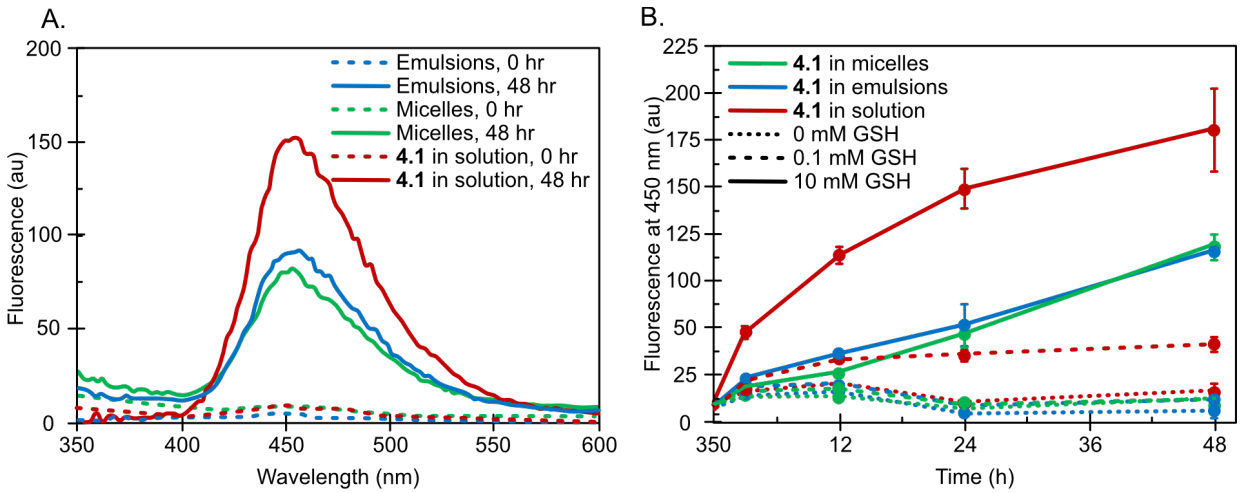

Figure 4.7 (A) Fluorescence of **4.1** either free in solution (red) or loaded in **2.4** stabilized micelles (green) or perfluorooctylbromide-in-water nanoemulsions (982 μM in **3.19**, blue). All samples are incubated with 10 mM GSH at 37 °C and fluorescence was monitored over 48 hours (see Figure 4.4C). Data are representative of three replicate measurements. (B) Fluorescence at 450 nm of **4.1** either free in solution (red) or loaded in **2.4** stabilized micelles (green) or perfluorooctylbromide-in-water nanoemulsions (982 μM in **3.19**, blue). All samples are incubated with 0 (dotted), 0.1 (dashed) or 10 (solid) mM GSH at 37 °C and fluorescence was monitored over 48 hours. Data are an average of three replicate measurements. Error bars represent the standard deviation of three replicates.

4.3.2 Redox-responsive nanoemulsions for pDNA delivery

To obtain a stimuli-responsive surfactant, we envisioned that a cleavable bond could link the hydrophilic and hydrophobic blocks of a diblock copolymer such that, upon stimulus, the surfactant would be irreversibly cleaved. The separated hydrophilic and hydrophobic homopolymers, having no surface activity, would no longer stabilize droplets, leading to demulsification. Previous work on responsive emulsions has involved a variety of stimuli, including pH[47–49], ions[50], gases[51,52], temperature[53,54], and redox agents[55,56]. Among these, redox agents are appealing for intracellular delivery vehicles due to the high concentration of reducing agents within the cell. Redox-responsive surfactants have been reported that contain functionalities such as ferrocenes[57,58], selenium atoms[55,59], and disulfide bonds[56,60,61]. However, these surfactants were not explored as emulsifiers for nanoemulsions.

We modified a previously developed poly(2-oxazoline) (POx) block copolymer scaffold[43,62] to form redox-responsive polymer surfactant **4.3**. We confirmed that **4.3** stabilized nanoemulsions had a similar size distribution to the control, non-responsive surfactant (**2.5**), and confirmed the responsive nature of **4.3** and **2.5** stabilized nanoemulsions.

Inspired by Medina and coworkers[63] who rendered fluorescent protein, GFP, fluorous soluble through the use of non-covalent fluorinated anionic tags, we looked to solubilize a GFP plasmid in the fluorous phase for *in cellulo* delivery via responsive nanoemulsions stabilized by **4.3**. Efforts within gene delivery using polymeric materials, *e.g.* polyethyleneimine (PEI) are often limited by inefficient gene release.[64] Nucleic acid delivery with oil nanoemulsions has been explored since the mid-90s, with the major loading strategy being electrostatic adsorption of cationic surfactants with the phosphodiester backbone.[65] More recently, plasmid encapsulation in a hydrocarbon oil core was reported and compared to surface adsorption loading methods.[66] While

adsorption suffered from burst release behavior, encapsulation suffered the inverse—plasmid was not released even after 48 h of media incubation. Herein, we demonstrate the ability to selectively release pDNA from a bioorthogonal fluorinated liquid core and drive protein expression *in cellulo*, representing a significant advance in nonviral gene delivery. This first required a strategy to solubilize hydrophilic DNA into the non-polarizable fluorous phase. Fundamental studies by Bühlmann and coworkers have quantified ion pairs to be ~10^5 times stronger in fluorous solvents than organic solvents,[67] suggesting electrostatic interactions between the anionic backbone of DNA and a cationic fluorous tag would be a fruitful approach to loading PFC nanoemulsions with DNA.

We employed ammonium **4.7** with two C_6F_{13} chains[11] as a fluorous tag to solubilize plasmid (pDNA) in the fluorous phase (Figure 4.8A). Importantly, this tag is designed to maximize fluorous solubility while retaining biocompatible perfluorocarbon tags.[68] For the pDNA, we chose an eGFP plasmid such that a fluorescence readout could measure payload delivery. Notably, cytosolic delivery and nuclear entry of the pDNA are essential for gene expression (Figure 4.8B). We combined **4.7** (7.7 mg) with eGFP pDNA (4.3, 15 or 30 μg) and freeze-dried overnight. The pDNA/**4.7** polyplex was then dissolved in a PFC mixture and sonicated (Figure 4.8A). Model poly(2-oxazoline) amphiphile poly(2-ethyl-2-oxazoline)$_{90}$-*b*-poly(2-nonyl-2-oxazoline)$_{10}$ (**2.12**)[62] was solubilized in dimethylformamide and diluted with PBS (pH 7.4) to a loading of 2.8 wt%. This solution was combined with 10 vol% of the PFC/pDNA/**4.7** mixture and ultrasonicated. To verify encapsulation, supernatant was separated and solution corresponding to eGFP loaded within PFC nanoemulsions was analyzed on an agarose gel (Figure 4.8C). DNA bands were assigned following literature precedent.[69] These data showed that eGFP pDNA could be loaded into PFC

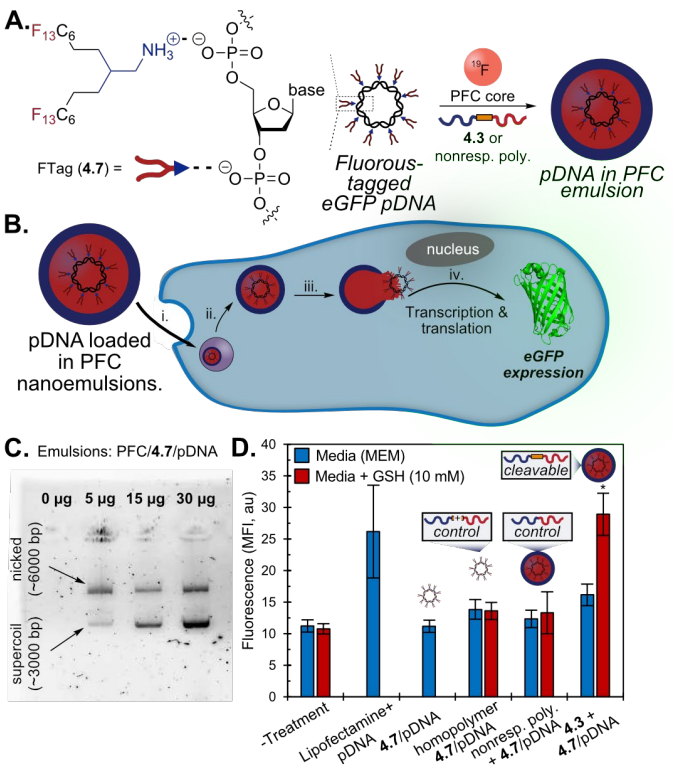

Figure 4.8 Delivery of eGFP pDNA with GSH-responsive nanoemulsions. (A) Fluorous amine tag (**4.7**) complexes with pDNA, solubilizing it within a PFC core that is sonicated in the presence of **4.3** or nonresponsive polymer (**2.5**) to form **4.7**/eGFP PFC nanoemulsions. (B) Schematic of delivery and eGFP expression. (C) Gel electrophoresis of destroyed PFC emulsions loaded with different amounts of pDNA complexed with **4.7**. (D) Flow cytometry of HEK-293 cells incubated with PFC/**4.7**/pDNA nanoemulsions for 3 hours in MEM media with or and without GSH (10 mM). Cells were washed and incubated with MEM media with or without GSH (10 mM) overnight. Cells were trypsonized, washed, resuspended in FACS buffer and analyzed for eGFP fluorescence. Data is representative of four independent experiments. See Fig. 4.13–4.15 for histograms of independent experiments. Statistical significance is defined by ANOVA test followed by Tukey HSD test for significance. α is defined as 0.05. See Fig. 4.11 for analysis.

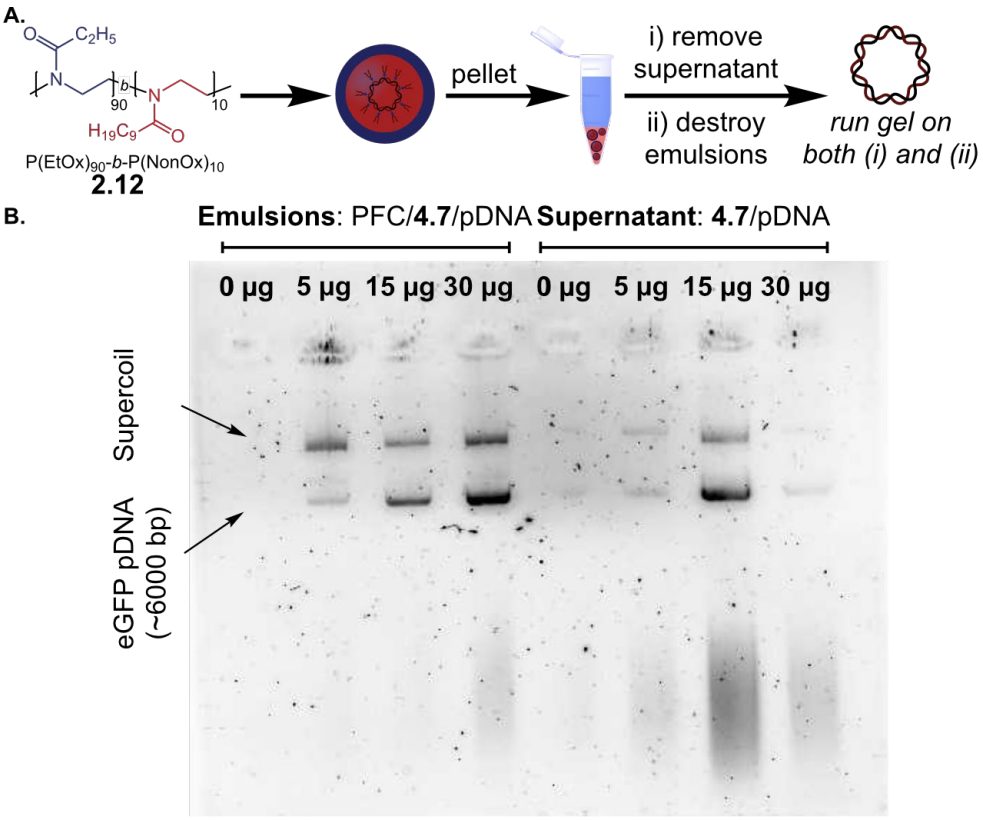

Figure 4.9 (A) Schematic showing emulsions were pelleted, (i) supernatant was isolated and (II) remaining emulsions were destroyed. Solutions isolated from both phases were run on agarose gel. (B) Agarose gel electrophoresis (1.2%) of **4.7**/eGFP pDNA solubilized within $P(EtOx)_{90}$-*b*-$P(NonOx)_{10}$ (**2.12**) stabilized PFD : PFTPA nanoemulsions at varying concentrations of pDNA (5 µg, 15 µg, 30 µg). Gel was run at 120V for 45 min and stained with ethidium bromide. Data is representative of three independent experiments. For detailed information, see supplemental figure experimental protocols. **2.12** was synthesized as previously reported.[62]

droplets in a dose-dependent manner from 5–30 μg. By comparison, electrophoresis of the supernatant solution showed reduced pDNA (Figure 4.9). These data were verified by fluorescence experiments using Thiazole Orange, a DNA-binding dye suggesting that 40 ± 4% of the pDNA was encapsulated in the 30 μg sample (Figure 4.10).

With **4.7** loaded into PFC nanoemulsions, we investigated the ability of responsive surfactant **4.3** to promote eGFP expression (Figure 4.8B). Emulsion formation was accomplished with responsive surfactant **4.3** or control surfactant **2.5**. Large aggregates were also made with homopolymers, as these are not amphiphiles, they were unable to stabilize PFC nanoemulsions. To monitor transfection efficiency, eGFP pDNA complexed with lipofectamine was added as a positive control. Human embryonic kidney cells (HEK-293) were treated with pDNA-loaded nanomaterials for 3 hours in media. After emulsions were washed away, the cells were incubated in the presence or absence of GSH (10 mM) overnight.[70,71] The following day, cells were washed and analyzed by flow cytometry (Figure 4.8D). Incubation with control **2.5**-stabilized droplets resulted in statistically insignificant expression regardless of GSH treatment. By contrast, responsive **4.3**-stabilized emulsions showed effective eGFP expression only in cells treated with GSH buffer, while untreated cells had fluorescence similar to that of control **2.5**. These data suggest that the cleavable disulfide within **4.3**-stabilized droplets enables release of encapsulated eGFP pDNA. Treating cells with endosomal escape agent chloroquine had no benefit over treatments with GSH buffer alone (Figure S4.1-S4.3).

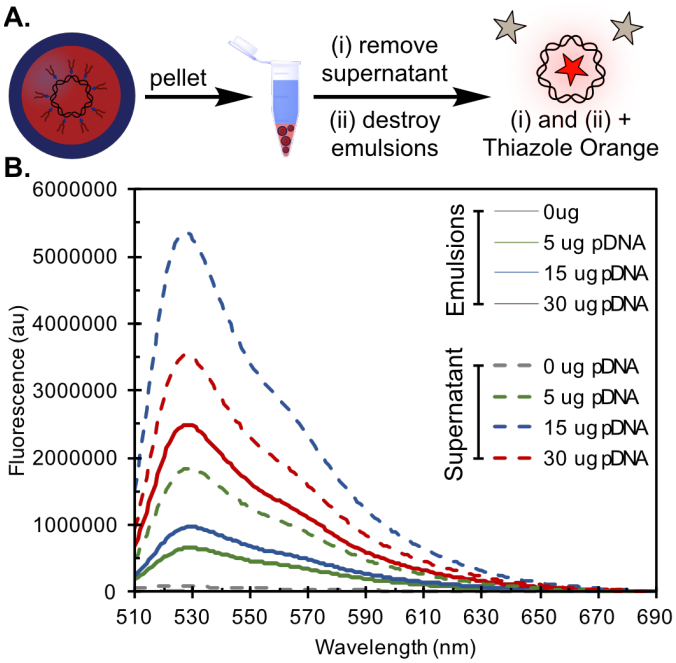

C.

	Emulsions (AUC, au)	Supernatant (AUC, au)	Encapsulation (%)
Expt. 1	138952147	197374020	41.3
Expt. 2	6143	8175	42.9
Expt. 3	5024	9239	35.2

Figure 4.10 (A) Fluorescence measurements of thiazole orange dye incubated with solutions isolated from **4.7** (4.5 mM)/eGFP pDNA solubilized within **2.11**-stabilized PFD : PFTPA nanoemulsions at varying concentrations of pDNA (5 µg, 15 µg, 30 µg). As schematized, emulsions were pelleted, (i) supernatant was isolated and (ii) remaining emulsions were destroyed. Solutions isolated from both phases were incubated with thiazole orange (1.9 mM). (B) Fluorescence measurement of thiazole orange stained pDNA (Ex: 500 nm, Em: 510-700 nm). Data are representative of three independent experiments. For detailed information, see supplemental figure experimental protocols. (C) DNA encapsulation efficiencies, as referenced in the main text, were calculated by comparing area under the curve (AUC) values of PFC/**4.7** emulsions + 30 µg pDNA to the AUC sum of both emulsions and supernatant for that experiment. The average and standard deviation were calculated from three independent experiments to be 39.8 ± 4.1%. **2.12** was synthesized as previously reported.[62]

A. **Analysis of Variance** $\alpha = 0.05$

Source	DF	Sum of Squares	Mean Square	F Ratio	Prob > F
Condition	5	1214.2935	242.859	27.9239	<.0001*
Error	63	547.9212	8.697		
C. Total	63	1762.2147			

B.

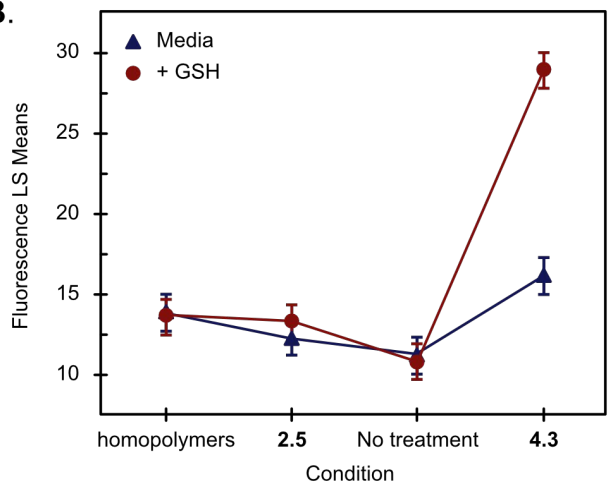

C. **LSMeans Differences Tukey HSD**

Level	Letter grade	Least Sq. Mean
4.3, GSH	A	28.916667
4.3, Media	B	16.158333
homopolymer, GSH	B C	13.85000
homopolymer, Media	B C D	13.60000
2.5, GSH	C D E	13.308333
2.5, Media	C D E	12.333333
No treat, GSH	D E	11.229167
No treat, Media	E	10.82000

Figure 4.11 Statistical tests of significance for Figure 4.7D. (A) Anova test of significance showing there is statistical significance with an alpha value of 0.05 across all samples. (B/C) Tukey HSD post hoc analysis showing **4.3**, GSH are statistically significant from all other conditions.

4.4 Conclusions

With both redox-responsive payloads and surfactants in hand, we are able to determine payloads solubilized with the PFC core do not significantly experience the environment surrounding the PFC nanoemulsions. This provides us the ability to deliver sensitive payloads, such as pDNA, that can then be released into the cytosol upon destabilization of the surfactant and therefore nanoemulsion. We found that self-immolative fluorous tags can readily solubilize small molecule fluorophores and promote a fluorescence turn-on upon destabilization, and non-covalent fluorous tags can form ionic interactions with the backbone of plasmid DNA resulting in ~40% encapsulation within PFC nanoemulsions. These studies have provided valuable insight into the use of PFC nanoemulsions for drug delivery.

4.5 Experimental Procedures

4.5.1 General experimental procedures

Chemical reagents were purchased from Sigma-Aldrich, Alfa Aesar, Fisher Scientific, SynQuest Laboratories, Chem-Impex International or Acros Organics and used without purification unless noted otherwise. Zonyl FSN-100 was obtained from DuPont. Perfluorooctylbromide was obtained from SynQuest Laboratories. Anhydrous dimethyl sulfoxide (DMSO) was obtained from a Sure-Seal™ bottle (Aldrich). Anhydrous and deoxygenated solvents dichloromethane (DCM), dimethylformamide (DMF), acetonitrile (MeCN), methanol (MeOH), and tetrahydrofuran (THF) were dispensed from a Grubb's-type Phoenix Solvent Drying System.[72] Solvent was removed under reduced pressure with a Büchi Rotovapor with a Welch self-cleaning dry vacuum pump and further dried with a Welch DuoSeal pump. Lyophilization was performed with Labconco FreeZone Benchtop Freeze Dryer, 4.5 L -84 °C, operating with an Edwards RV5 Rotary Vane pump 10:03 Vacuum, set point 0.000 mbar. Dialysis was performed with pre-wetted Spectra/Por regenerated cellulose dialysis membranes with a 1 kDa molecular weight cutoff purchased from Spectrum Laboratories. Bath sonication was performed using a Branson 3800 ultrasonic cleaner. Nuclear magnetic resonance (^{1}H NMR, ^{13}C NMR, and ^{19}F NMR) spectra were taken on Bruker Avance 500 (^{1}H NMR) instrument and processed with MestReNova 11.0.1 software. All ^{1}H NMR peaks are reported in reference to $CDCl_3$ at 7.26 ppm.

4.5.2 General photophysics procedure

4.3.1 Absorbance spectra were collected on a JASCO V-770 UV-Visible/NIR spectrophotometer with a 4000 nm/min scan rate after blanking with the appropriate solvent. Fluorescence was performed on Falcon 96-well black, flat-bottom plates on a Tecan M1000 Plate Reader.

Photoluminescence spectra were obtained on a Horiba Instruments PTI QuantaMaster Series fluorometer.

4.3.2 Values were obtained in a 0.3 mL quartz cuvette on a Horiba Instruments PTI QuantaMaster Series fluorometer with the following settings:

Thiazole Orange, Figure 4.9: Emission Scan. Slits 3 nm, step size 1 nm, integration time 0.1 s (Ex 500 nm, collection: 510–700 nm).

4.5.3 General nanoemulsion formation procedure

4.3.1 Zonyl FSN-100 (**2.4**, 5.6 mg) was dissolved in PBS (1x, pH 7.4, 200 μL) and perfluorooctylbromide (10 vol%, 20 μL) was added. The mixture was sonicated at 35% amplitude for 15 minutes at 0 °C on a QSonica (Q125) sonicator. Sonication was performed by lowering the probe directly at the liquid-liquid interface of the two immiscible solvents.

4.3.2 Polymer surfactant (3.0 mg) was pre-solubilized in DMF (20 μL) and vortexed gently until fully dissolved. In a separate 2 mL eppendorf tube, oil (10 vol%, 20 μL of either perfluorooctylbromide or olive oil) was added, followed by PBS buffer pH 7.4 (200 μL), 15 wt% total surfactant. The mixture was quickly sonicated at 35% amplitude for at least 90 seconds at 0 °C on a QSonica (Q125) sonicator. Sonication was performed by lowering the probe directly to the liquid-liquid interface of the two immiscible solvents.

4.5.4 General micelle formation procedure

4.3.1 Zonyl FSN-100 (28 mg) was dissolved in PBS (1x, pH 7.4, 1 mL) and vortexed briefly to dissolve.

4.5.5 General nanoemulsion analysis procedure

4.3.1 and 4.3.2 Size analysis: The bulk emulsion solution was diluted in MilliQ H_2O (20 µL emulsions in 2 mL MilliQ H_2O) in a plastic 1 cm cuvette. Size was analyzed with a Malvern Zetasizer Nano dynamic light scattering. SOP parameters: 10 runs, 10 seconds/run, three measurements, no delay between measurements, 25 °C with 120 second equilibration time. Collection parameters: Lower limit = 0.6, Upper limit = 1000, Resolution = High, Number of size classes = 70, Lower size limit = 0.4, Upper size limit = 1000, Lower threshold = 0.05, Upper threshold = 0.01. Data are representative of three replicate measurements.

4.5.6 General micelle analysis procedure

4.3.1 The micelle solution (28 mg/mL) was diluted in MilliQ H2O (20 µL micelles in 2 mL MilliQ H2O) in a plastic 1 cm cuvette. Size was analyzed with a Malvern Zetasizer Nano dynamic light scattering. SOP parameters: 10 runs, 10 seconds/run, three measurements, no delay between measurements, 25 °C with 120 second equilibration time. Collection parameters: Lower limit = 0.6, Upper limit = 1000, Resolution = Normal, Number of size classes = 70, Lower size limit = 0.4, Upper size limit = 1000, Lower threshold = 0.05, Upper threshold = 0.01. Data are representative of five replicate measurements.

4.5.7 Fluorous tagging and encapsulation of eGFP pDNA in nanoemulsions procedure

A fluorous ammonium **4.7** stock (10 mM) was prepared by dissolving **4.7** (7.7 mg, 0.010 mmol) in MeOH (1 mL). This was diluted to a 1 mM stock in water. DNA (30 µg, eGFP, addgene: 13031) (as measured by nanodrop) was placed in Eppendorf tubes, 1 mL 1 mM stock **4.7** was added and freeze dried overnight. Emulsions were prepared by dissolving the pDNA/**4.7** in 20 µL 7:3

PFD:PFTPA (vol%) and bath sonicating for 5 min. Phosphate buffered saline (PBS, 200 μL) was added, and polymer **4.3** or **2.5** (5.6 mg dissolved in 20 μL DMF) was added immediately before sonication. Emulsions were sonicated for 3 min, pulsed on for 2 s, off for 5 s. Emulsions were centrifuged (5.6 x g, 3 min) to separate un-encapsulated eGFP pDNA and resuspended in PBS.

4.5.8 Cell culture experimental procedures

HEK-293 cells were purchased from ATCC (Cat# CRL-1573). Chloroquine hydrochloride was purchased from Sigma-Aldrich.

HEK-293 cells were cultured in Minimum Essential Media (Gibco, cat# 11095080) supplemented with 10% fetal bovine serum (Corning, lot# 35016109) and 1% penicillin-streptomycin (Life Technologies, cat# 15070063). Cells were washed with PBS. Cells were incubated at 37 ˚C, 5% CO_2, during treatments and throughout culturing, in HERACell 150i CO_2 incubators. Cells were pelleted through use of Sorvall ST 40R centrifuge. All cell work was performed in 1300 Series A2 biosafety cabinets.

eGFP pDNA was purchased from AddGene (13031). Thiazole Orange was purchased from Fisher (Cat# 50-176-3367). Lipofectamine 2000 was purchased from Fisher (Cat# 11668030).

For transfection experiments: Media was removed and replaced with media + emulsions. Positive control (lipofectamine) followed Invitrogen's Lipofectamine® 2000 DNA Transfection Reagent Protocol. The cells were incubated with treatment for 3 hours at 37 °C and then washed gently to remove treatment. Media or GSH (10 mM) was added back and cells were incubated overnight at

37 ˚C. The next day, cells were lifted via trypsonization, washed via centrifugation (526 x *g*, 3 min) and resuspended in 200 µL FACS buffer (PBS, 1% FBS). The cells were analyzed for GFP (FL-1) fluorescence via flow cytometry. Error bars represent the standard deviation of 3 replicate experiments.

4.6 Figure experimental procedures

Figure 4.2B

Either 7-hydroxycoumarin (3, 0.01 mg, 20 nmol) or fluorous coumarin (2, 0.02 mg, 20 nmol) were place in vials and dissolved in acetone (0.5 mL, 50 μM solution). A stock solution (20 mM) of the indicated reducing agent or control was prepared and the pH was adjusted to 7.4. To the solutions of 2 or 3, 0.5 mL of the stock solution of reducing agent was added (pH 7.4, final concentration 10 mM) and rocked for 30 min at room temperature. The fluorescence was collected on a Horiba Instruments PTI QuantaMaster Series fluorometer. Excitation: 325 nm, collect 350–600nm, all slits were 2 nm, with an integration time of 0.1 sec. B inset) Two aliquots of fluorous coumarin 2 (0.02 mg, 20 nmol) was placed in a vial sand dissolved in acetone (0.5 mL). To one aliquot, 0.5 mL PBS, pH 7.4 was added. To the other vial 20 mM BME in PBS (0.5 mL, pH 7.4) was added. Long-wave UV images were taken of each vial after preparation.

Figure 4.2C

Fluorous coumarin 2 (0.1 mg, 100 nmol) was dissolved in the indicated fluorous solvents (0.75 mL) and PBS (pH 7.4, 0.75 mL). Neat BME (7 μL) was added to the vials and shaken (final concentration 660 mM). Visible and Long-wave UV images were taken before and after the addition of BME.

Figure 4.2D

Fluorous coumarin 2 (0.02 mg, 20 nmol) was dissolved in acetone (1 mL) in a 1 cm cuvette. A glutathione stock in PBS was prepared (20 mM, pH 7.4) and was added to the cuvette (10mM-1 mL stock, 5 mM-0.5 mL stock, 0.1 mM- 10 μL stock, 0.01 mM- 1 μL stock) and diluted to a final

volume of 2 mL with PBS. Immediately after the addition of GSH, the cuvettes were sealed, mixed thoroughly and monitored via fluorescence. The solutions were monitored every 10 minutes for 1 hour. Fluorescence spectra were collected on a Horiba Instruments PTI QuantaMaster Series fluorometer. Excitation: 325 nm, collect 350–600nm, all slits were 2 nm, with an integration of 0.1 sec.

Figure 4.3

Fluorous coumarin 2 (0.08 mg, 80 nmol) was dissolved in the indicated solvent (1 mL). The solution was sonicated briefly followed by analysis via UV/Vis blanked on the indicated solvent. A 0.3 mL cuvette, with a 1 mL path length was utilized. Spectra were taken from 250–400 nm.

Figure 4.4A

Emulsions: Perfluorocarbon nanoemulsions containing 2 were prepared by first solubilizing 2 in perfluorooctyl bromide (PFOB, 20 μL, 982 μM). Phosphate buffered saline (PBS, pH 7.4, 200 μL) was then added to make a biphasic solution of 10 vol% fluorous oil. **2.4**, was added to a surfactant loading of 2.8 wt% in PBS. Emulsions were then formed through ultrasonication at the liquid-liquid interface for 90 seconds at 0 °C. Micelles: A stock solution of 28 mg/mL **2.4** was made in PBS pH 7.4. This solution was vortexed briefly to dissolve. For a 200 μL aliquot of micellar solution, 20 μL of fluorous coumarin 2 in acetone (982 μM stock) was added directly and rocked briefly to encapsulate.

Figure 4.4B/C A solution of PFOB-in-water nanoemulsions loaded with 2 (220 μL) were formed as described in (A). Zonyl micellar solution was made as described in (B). A stock of reduced

glutathione in PBS (20 mM, pH 7.4) was prepared. The experiment was then set up on black, flat bottomed, 96-well plates from BD Falcon. To each well, the following was performed, with the final volume of each well being 200 μL. If relevant, GSH solution was added directly before measurements began. All samples were performed in triplicate:

Emulsions: Emulsion solution formed in (A) (10 μL) was added to each well and diluted with either PBS or 20 mM GSH stock to a final concentration of either 0, 0.1 or 10 mM GSH. S14

Micelles: **2.4** solution formed in (A) (10 μL) was added to each well and diluted with either PBS or 20 mM GSH stock to a final concentration of either 0, 0.1 or 10 mM GSH. Free dye: Fluorous coumarin 2 in acetone (1 μL of 982 μM stock) was added to each well and diluted with either PBS or 20 mM GSH stock to a final concentration of either 0, 0.1 or 10 mM GSH.

Prior to measurements, the plate was shaken for 60 seconds. Between measurements, plates were rocked at either (i) 37 °C on a New Brunswick Scientific Innova 4230 incubator shaker at 40 rpm, or (ii) 25 °C on an orbital shaker at 40 rpm. Measurements were taken on a Tecan M1000 Plate Reader with the following settings: Emission settings: Ex: 325 nm; Em. range: 350-600 nm; Step size: 2; Bandwidth: 5.0 nm; Mode: top; Gain: Manual, 100; Z-Position: Manual, 20000 μm; Flashes: Mode 1 [400 Hz]: 50; Settle Time: 0 ms. For the first 12 hours, measurements were taken every hour, then measurements were taken at the 24- and 48-hour time points. Data are an average of three replicate measurements.

Figure 4.5

See general nanoemulsion and micelle formation and analysis procedures.

Figure 4.6-4.7

See Figure 4.4 experimental information. Solutions were diluted 1:20 in PBS pH 7.4 and transferred to a microwell plate for fluorimeter measurements. The microwell plate was a black, flat bottomed, 96-well plates from BD Falcon. Measurements were taken on a Tecan M1000 Plate Reader with the following settings: Emission settings: Ex: 325 nm; Em. range: 350-600 nm; Step size: 2; Bandwidth: 5.0 nm; Mode: top; Gain: Manual, 100; Z-Position: Manual, 20000 µm; Flashes: Mode 1 [400 Hz]: 50; Settle Time: 0 ms. Data are an average of three replicate measurements. Error bars represent the standard deviation between replicates.

Figure 4.8A.

Fluorous ammonium **4.7** stock (10 mM) was made by dissolving **4.7** in MeOH. This was diluted to a stock in water (1 mM). pDNA (eGFP, addgene: 13031, 30 µg) (as measured by nanodrop) was placed in Eppendorf tubes, 1 mL 0.1 mM stock **4.7** was added, freeze dried overnight. Emulsions were prepared by dissolving the pDNA/**4.7** in 20 µL 7:3 PFD:PFTPA (vol%) and bath sonicating for 5 min. Phosphate buffered saline (PBS, 200 µL) was added, and polymer **4.3** or **2.5** (5.6 mg dissolved in 20 µL DMF) was added immediately before sonication. Emulsions were sonicated for 3 min, pulsed on for 2 s, off for 5 s. Emulsions were centrifuged (5.6 x g, 3 min) and supernatant was discarded.

Figure 4.8C

Emulsions were formed as described in Fig. 4.8A. **2.11** was used as a model polymeric surfactant. The emulsions were then centrifuged (5.6 x *g*, 3 min) and the supernatant was collected. The emulsions were resuspended with 200 µL PEG-8k (100 mg/mL). Phenol and chloroform (~200

μL each) were added to the resuspended emulsions and the supernatant, and vortexed followed by immediate centrifugation (18 x *g*, 5 min). The aqueous (top) layer was removed and placed in new vials, chloroform (~200 μL) was added, vortexed, and centrifuged (18 x *g*, 5 min). The aqueous (top) layer was removed again and placed in new vials with 20 μL acetate buffer (5 mM, pH 5.5) and 500 μL ethanol. This was placed in -80 °C freezer overnight. The next day, the eppendorf tubes were centrifuged to pellet any DNA present (18 x *g*, 5 min) and the supernatant was decanted. The pellet was washed with 70% ethanol, centrifuged (18 x *g*, 5 min), supernatant decanted, and dried at room temperature (~10 min). DNA pellets were dissolved in 50 μL MilliQ water. 2 μL of loading buffer was added to each sample, then loaded onto a 1.2% agarose gel. The gel was run for 45 min, 120 V and visualized with ethidium bromide.

Figure 4.8D

Emulsions were formed as described in Fig. 4.8A. Polymers **4.3** or **2.5** were used for responsive and control emulsions, respectively. Emulsions were then centrifuged (5.6 x *g*, 3 min), supernatant was discarded and emulsions were resuspended in PBS (200 μL). 200,000 HEK293 cells (ATCC: CRL-1573) were plated in 12 well plate (Fisher, cat# FB012928), and allowed to adhere overnight. Media (MEM, Gibco cat# 11095080) was removed and replaced with two treatments (media + emulsions, or media + emulsions + glutathione (GSH, 10 mM)) with a total volume of 1 mL. Positive control (lipofectamine) followed Invitrogen's Lipofectamine® 2000 DNA Transfection Reagent Protocol. The cells were incubated with treatment for 3 hours at 37 °C and then washed gently to remove treatment. Media or GSH (10 mM) was added back and cells were incubated overnight at 37 ˚C. The next day, cells were lifted via trypsonization, washed via centrifugation (526 x *g*, 3 min) and resuspended in 200 μL FACS buffer (PBS, 1% FBS). The cells were analyzed

for GFP (FL-1) fluorescence via flow cytometry. ANOVA test was done to determine statistical significance across all samples, followed by a Tukey HSD analysis with $\alpha = 0.05$.

Figure 4.9

Emulsions were formed as described in Fig. 4.8A and the fluorous tagging and encapsulation of eGFP pDNA in the nanoemulsions procedure. **2.11** was used as a model polymeric surfactant. The emulsions were then centrifuged (5.6 x *g*, 3 min) and the supernatant was collected. The emulsions were resuspended with 200 µL PEG-8k (100 mg/mL). Phenol and chloroform (~200 µL each) were added to the resuspended emulsions and the supernatant, and vortexed followed by immediate centrifugation (18 x *g*, 5 min). The aqueous (top) layer was removed and placed in new vials, chloroform (~200 µL) was added, vortexed, and centrifuged (18 x *g*, 5 min). The aqueous (top) layer was removed again and placed in new vials with 20 µL acetate buffer (5 mM, pH 5.5) and 500 µL ethanol. This was placed in -80 °C freezer overnight. The next day, the eppendorf tubes were centrifuged to pellet any DNA present (18 x *g*, 5 min) and the supernatant was decanted. The pellet was washed with 70% ethanol, centrifuged (18 x *g*, 5 min), supernatant decanted, and dried at room temperature (~10 min). DNA pellets were dissolved in 50 µL MilliQ water. 2 µL of loading buffer was added to each sample, then loaded onto a 1.2% agarose gel. The gel was run for 45 min, 120 V and visualized with ethidium bromide.

Figure 4.10

Emulsions were formed as described in Fig. 4.8A and the fluorous tagging and encapsulation of eGFP pDNA in the nanoemulsions procedure. Polymer **2.11** was used as a model polymeric surfactant. The emulsions were then centrifuged (5.6 x *g*, 3 min) and the supernatant was collected.

The emulsions were resuspended with 200 µL PEG-8k (100 mg/mL). Phenol and chloroform (~200 µL each) were added to the resuspended emulsions and the supernatant, and vortexed followed by immediate centrifugation (18 x *g*, 5 min). The aqueous (top) layer was removed and placed in new vials, chloroform (~200 µL) was added, vortexed, and centrifuged (18 x *g*, 5 min). The aqueous (top) layer was removed again and placed in new vials with 20 µL acetate buffer (5 mM, pH 5.5) and 500 µL ethanol. This was placed in -80 °C freezer overnight. The next day, the eppendorf tubes were centrifuged to pellet any DNA present (18 x *g*, 5 min) and the supernatant was decanted. The pellet was washed with 70% ethanol, centrifuged (18 x *g*, 5 min), supernatant decanted, and dried at room temperature (~10 min). DNA pellets were dissolved in 50 µL MilliQ water. Thiazole orange (0.5 µL, 1.9 mM, Fisher cat# 50-176-3367) was added, fluorescence was measured. Fluorometer settings: Ex: 500 nm; Em: 510-700 nm; Slits: 3 nm; Int: 0.1 s; Step Size: 1 nm. DNA encapsulation efficiencies, as referenced in the main text, were approximated by comparing area under the curve (AUC) values of PFC/**4.7** emulsions + 30 µg pDNA to the AUC sum of both emulsions and supernatant for that experiment. The average and standard deviation were calculated from three independent experiments.

Figure S4.1–S4.3

Emulsions were formed as described in Fig. 4.8A. Polymers **4.3** or **2.5** were used for responsive and control emulsions, respectively. Emulsions were then centrifuged (5.6 x *g*, 3 min), supernatant was discarded, and emulsions were resuspended in PBS (200 µL). 200,000 HEK293 cells (ATCC: CRL-1573) were plated in 12 well plate (Fisher, cat# FB012928), and allowed to adhere overnight. Media (MEM, Gibco cat# 11095080) was removed and replaced with four treatments at a total volume of 1 mL: (i) media + emulsions, (ii) media + emulsions + chloroquine (CQ, 50 µM), (iii)

media + emulsions + glutathione (GSH, 10 mM), (iv) media + emulsions + CQ (50 μM) + GSH (10 mM). Positive control (lipofectamine) followed Invitrogen's Lipofectamine® 2000 DNA Transfection Reagent Protocol. The cells were incubated with treatment for 3 hours at 37 °C and then washed gently to remove treatment. Media or GSH (10 mM) was added back, and cells were incubated overnight at 37 ˚C. The next day, cells were lifted via trypsonization, washed via centrifugation (526 x *g*, 3 min) and resuspended in 200 μL FACS buffer (PBS, 1% FBS). The cells were analyzed for GFP (FL-1) fluorescence via flow cytometry.

Figure S4.4–S4.6

Emulsions were formed as described in Fig. 4.8A. Polymers **4.3** or **2.5** were used for responsive and control emulsions, respectively. Homopolymers were used together as controls along with free DNA delivered in media. Emulsions were then centrifuged (5.6 x *g*, 3 min), supernatant was discarded, and emulsions were resuspended in PBS (200 μL). 100,000 HEK293 cells (ATCC: CRL-1573) were plated in 96 well plate (Fisher, cat# FB012928), and allowed to adhere overnight. Complete media (MEM +10% FBS +1% PS, Gibco cat# 11095080) was removed and replaced with media + emulsions. Positive control (lipofectamine) followed Invitrogen's Lipofectamine® 2000 DNA Transfection Reagent Protocol. The cells were incubated with treatment for 3 hours at 37 °C and then washed gently to remove treatment. Media or GSH (10 mM) was added back and cells were incubated overnight at 37 ˚C. The next day, cells were lifted via trypsonization, washed via centrifugation (526 x *g*, 3 min) and resuspended in 200 μL FACS buffer (PBS, 1% FBS). The cells were analyzed for GFP (FL-1) fluorescence via flow cytometry.

Figure S4.7

Emulsions were formed as described in Fig. 4.8A. Polymers **4.3** or **2.5** were used for responsive and control emulsions, respectively. Homopolymers were used together as controls along with free DNA delivered in media. Emulsions were then centrifuged (5.6 x *g*, 3 min), supernatant was discarded, and emulsions were resuspended in PBS (200 μL). 200,000 HEK293 cells (ATCC: CRL-1573) were plated in 96 well plate (Fisher, cat# FB012928), and allowed to adhere overnight. Complete media (MEM +10% FBS +1% PS, Gibco cat# 11095080) was removed and replaced with two treatments at a total volume of 200 mL: (i) media + emulsions, (ii) media + emulsions + chloroquine (CQ, 50 μM. Positive control (lipofectamine) followed Invitrogen's Lipofectamine® 2000 DNA Transfection Reagent Protocol. The cells were incubated with treatment for 3 hours at 37 °C and then washed gently to remove treatment. Media or GSH (10 mM) was added to GSH wells and cells were incubated overnight at 37 ˚C. The next day, cells were lifted via trypsonization, washed via centrifugation (526 x *g*, 3 min) and resuspended in 200 μL FACS buffer (PBS, 1% FBS). The cells were analyzed for GFP (FL-1) fluorescence via flow cytometry.

4.7 Supplemental figures

4.7.1 FACS Histograms

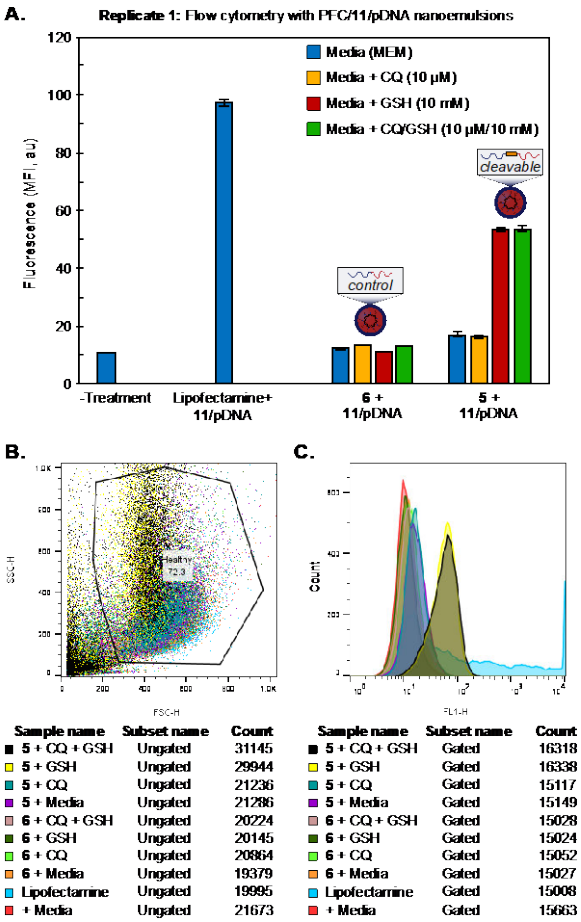

Figure S4.1 First replicate of flow cytometry results. (A) Flow cytometry of human embryonic kidney (HEK-293) cells incubated with PFC/**4.7**/pDNA nanoemulsions for 3 hours, with emulsions formed as described in the fluorous tagging and encapsulation of eGFP pDNA in nanoemulsions procedure. During treatment, cells were incubated with (i) Media (MEM + 10% FBS, Blue), (ii) MEM + chloroquine (CQ, 50 µM, Orange), (iii) MEM + Glutathione (GSH, 10 mM, Red), and (iv) MEM + CQ/GSH (50 µM/10 mM, Green) alongside emulsions for 3 hours. After treatment, cells were washed gently to remove emulsions. MEM media with and without respective GSH treatments were then added back and cells were incubated overnight at 37 °C. The cells were then lifted, washed, resuspended in FACS buffer and analyzed for eGFP (FL-1) fluorescence via flow cytometry. Data is representative of three independent experiments. For assessment of the statistical significance of differences, a one-tailed Student's t-test assuming unequal sample variance was employed. Results were considered significant/not significant versus no treatment per the following definitions: ns = $p > 0.01$, * = $p \leq 0.01$. (B) Side scatter (SSC) vs. forward scatter (FSC) overlay of HEK-293 cells incubated for 3 hours with emulsions and washed. (C) Representative FL-2 histograms of each sample, gated.

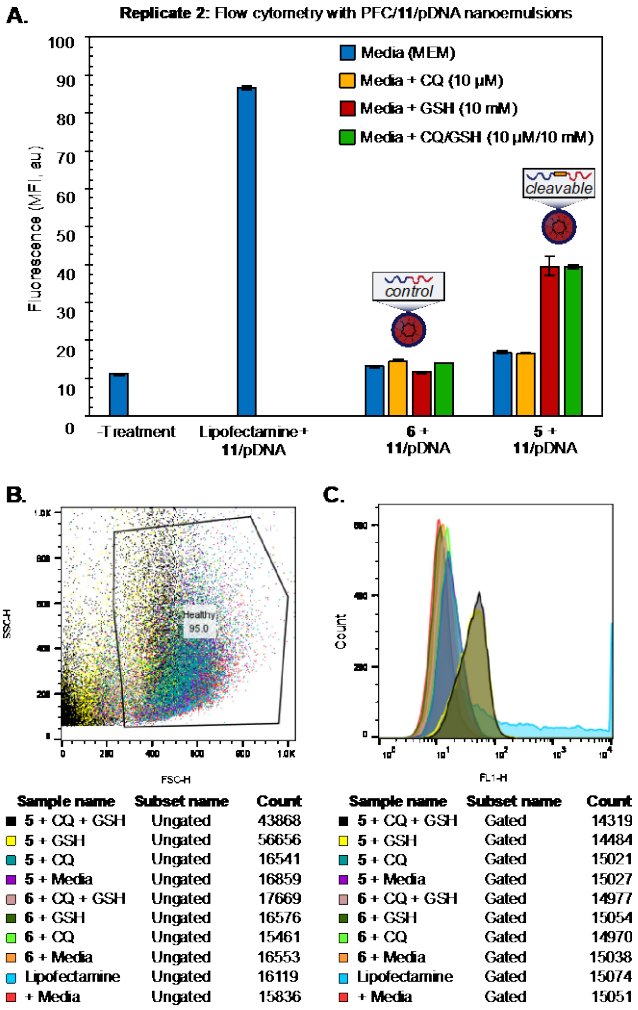

Figure S4.2 Second replicate of flow cytometry results. (A) Flow cytometry of human embryonic kidney (HEK-293) cells incubated with PFC/**4.7**/pDNA nanoemulsions for 3 hours, with emulsions formed as described in the fluorous tagging and encapsulation of eGFP pDNA in nanoemulsions procedure. During treatment, cells were incubated with (i) Media (MEM + 10% FBS, Blue), (ii) MEM + chloroquine (CQ, 50 µM, Orange), (iii) MEM + Glutathione (GSH, 10 mM, Red), and (iv) MEM + CQ/GSH (50 µM/10 mM, Green) alongside emulsions for 3 hours. After treatment, cells were washed gently to remove emulsions. MEM media with and without respective GSH treatments were then added back and cells were incubated overnight at 37 °C. The cells were then lifted, washed, resuspended in FACS buffer and analyzed for eGFP (FL-1) fluorescence via flow cytometry. Data is representative of three independent experiments. For assessment of the statistical significance of differences, a one-tailed Student's t-test assuming unequal sample variance was employed. Results were considered significant/not significant versus no treatment per the following definitions: ns = $p > 0.01$, * = $p \leq 0.01$. (B) Side scatter (SSC) vs. forward scatter (FSC) overlay of HEK-293 cells incubated for 3 hours with emulsions and washed. (C) Representative FL-2 histograms of each sample, gated.

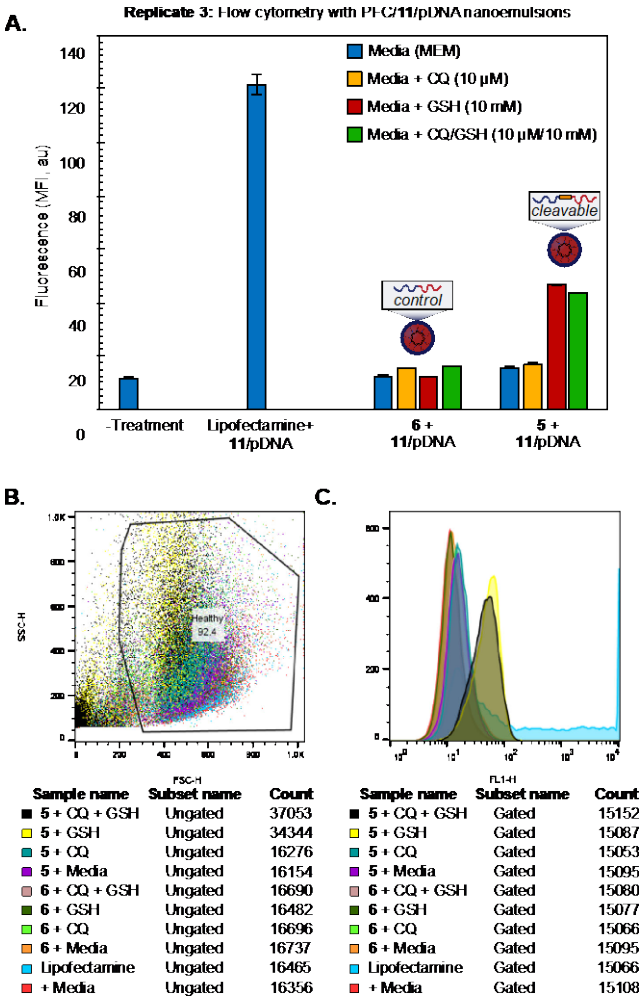

Figure S4.3 Third replicate of flow cytometry results. (A) Flow cytometry of human embryonic kidney (HEK-293) cells incubated with PFC/**4.7**/pDNA nanoemulsions for 3 hours, with emulsions formed as described in the fluorous tagging and encapsulation of eGFP pDNA in nanoemulsions procedure. During treatment, cells were incubated with (i) Media (MEM +10% FBS, Blue), (ii) MEM + chloroquine (CQ, 50 µM, Orange), (iii) MEM + Glutathione (GSH, 10 mM, Red), and (iv) MEM + CQ/GSH (50 µM/10 mM, Green) alongside emulsions for 3 hours. After treatment, cells were washed gently to remove emulsions. MEM media with and without respective GSH treatments were then added back and cells were incubated overnight at 37 °C. The cells were then lifted, washed, resuspended in FACS buffer and analyzed for eGFP (FL-1) fluorescence via flow cytometry. Data is representative of three independent experiments. For assessment of the statistical significance of differences, a one-tailed Student's t-test assuming unequal sample variance was employed. Results were considered significant/not significant versus no treatment per the following definitions: ns = $p > 0.01$, * = $p \leq 0.01$. (B) Side scatter (SSC) vs. forward scatter (FSC) overlay of HEK-293 cells incubated for 3 hours with emulsions and washed. (C) Representative FL-2 histograms of each sample, gated.

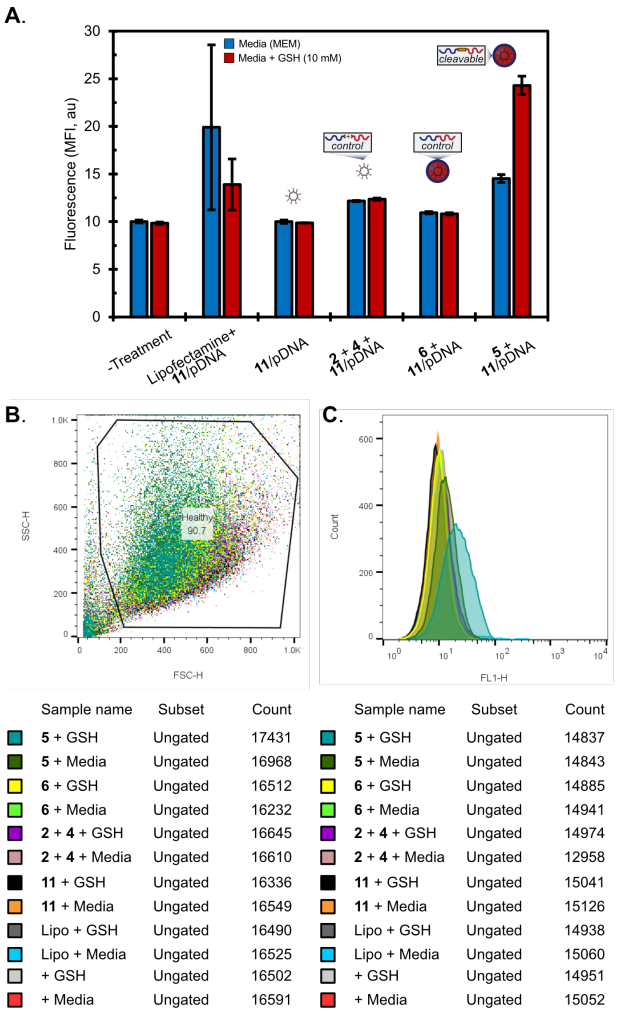

Sample name	Subset	Count	Sample name	Subset	Count
5 + GSH	Ungated	17431	**5** + GSH	Ungated	14837
5 + Media	Ungated	16968	**5** + Media	Ungated	14843
6 + GSH	Ungated	16512	**6** + GSH	Ungated	14885
6 + Media	Ungated	16232	**6** + Media	Ungated	14941
2 + **4** + GSH	Ungated	16645	**2** + **4** + GSH	Ungated	14974
2 + **4** + Media	Ungated	16610	**2** + **4** + Media	Ungated	12958
11 + GSH	Ungated	16336	**11** + GSH	Ungated	15041
11 + Media	Ungated	16549	**11** + Media	Ungated	15126
Lipo + GSH	Ungated	16490	Lipo + GSH	Ungated	14938
Lipo + Media	Ungated	16525	Lipo + Media	Ungated	15060
+ GSH	Ungated	16502	+ GSH	Ungated	14951
+ Media	Ungated	16591	+ Media	Ungated	15052

Figure S4.4 Fourth replicate of flow cytometry results, the average of which is shown in Figure 4D. (A) Flow cytometry of human embryonic kidney (HEK-293) cells incubated with PFC/**4.7**/pDNA nanoemulsions for 3 hours, with emulsions formed as described in the fluorous tagging and encapsulation of eGFP pDNA in nanoemulsions procedure. During treatment, cells were incubated in complete Media (10% FBS, 1% PS) alongside emulsions for 3 hours. After treatment, cells were washed gently to remove emulsions. MEM media with and without respective GSH (10 mM) treatments were then added back and cells were incubated overnight at 37 °C. The cells were then lifted, washed, resuspended in FACS buffer and analyzed for eGFP (FL-1) fluorescence via flow cytometry. Data is representative of three independent experiments. For assessment of the statistical significance of differences, an ANOVA test followed by Tukey HSD were performed with significance determined by alpha value of 0.05. (B) Side scatter (SSC) vs. forward scatter (FSC) overlay of HEK-293 cells incubated for 3 hours with emulsions and washed. The gate employed for Figure 4.7D is shown. (C) Representative FL-2 histograms of each sample, gated.

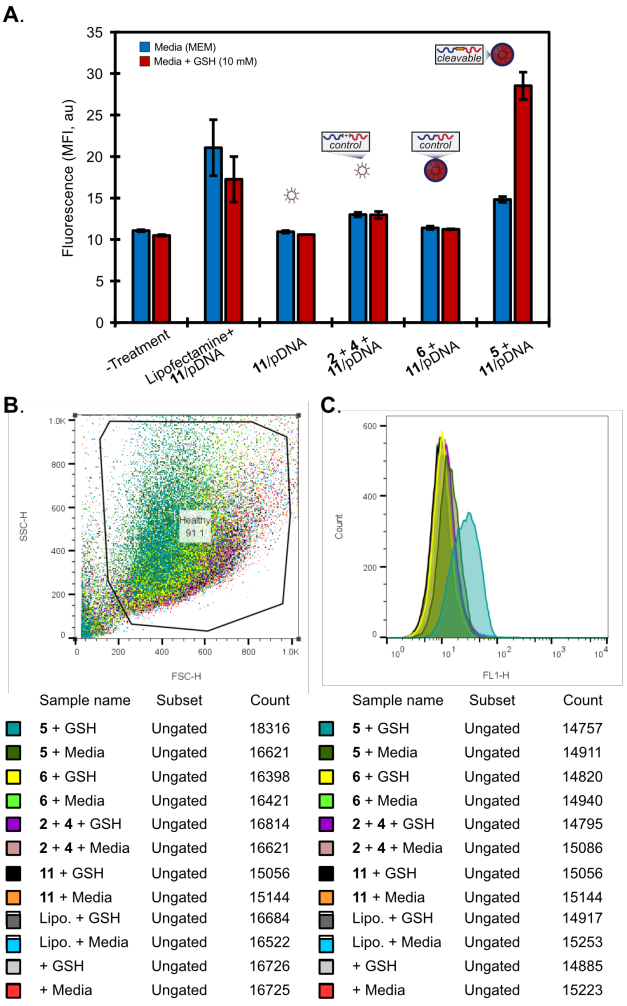

Figure S4.5 Fifth replicate of flow cytometry results, the average of which is shown in Figure 4D. (A) Flow cytometry of human embryonic kidney (HEK-293) cells incubated with PFC/**4.7**/pDNA nanoemulsions for 3 hours, with emulsions formed as described in the fluorous tagging and encapsulation of eGFP pDNA in nanoemulsions procedure. During treatment, cells were incubated in complete Media (10% FBS, 1% PS) alongside emulsions for 3 hours. After treatment, cells were washed gently to remove emulsions. MEM media with and without respective GSH (10 mM) treatments were then added back and cells were incubated overnight at 37 °C. The cells were then lifted, washed, resuspended in FACS buffer and analyzed for eGFP (FL-1) fluorescence via flow cytometry. Data is representative of three independent experiments. For assessment of the statistical significance of differences, an ANOVA test followed by Tukey HSD were performed with significance determined by alpha value of 0.05. (B) Side scatter (SSC) vs. forward scatter (FSC) overlay of HEK-293 cells incubated for 3 hours with emulsions and washed. The gate employed for Figure 4.7D is shown. (C) Representative FL-2 histograms of each sample, gated.

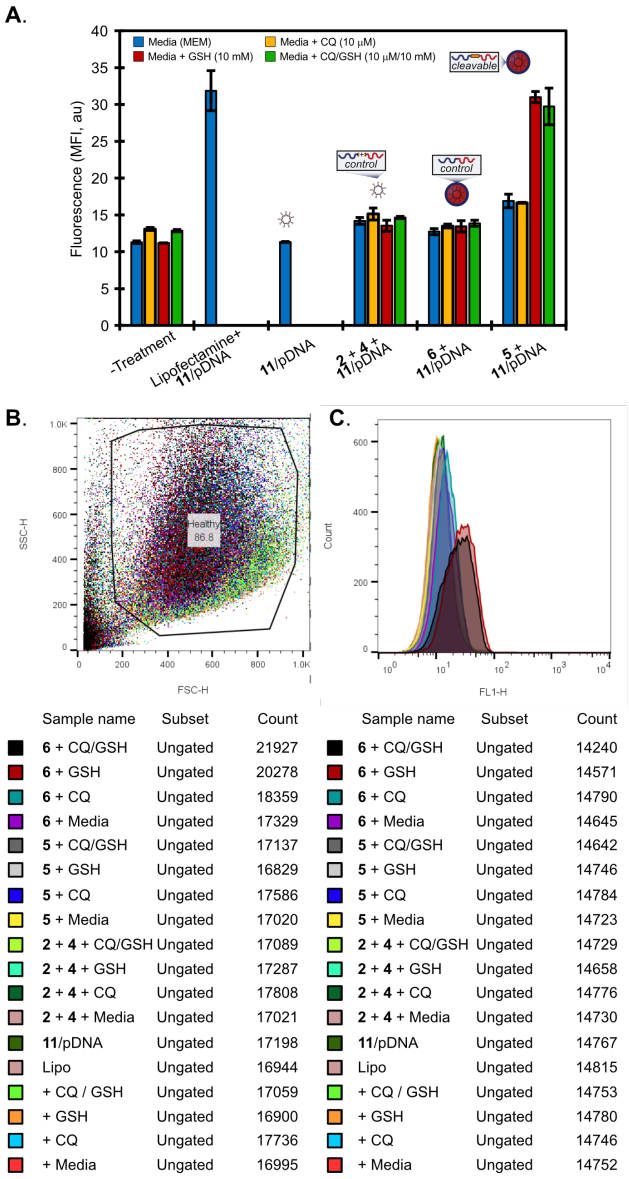

Sample name	Subset	Count
6 + CQ/GSH	Ungated	21927
6 + GSH	Ungated	20278
6 + CQ	Ungated	18359
6 + Media	Ungated	17329
5 + CQ/GSH	Ungated	17137
5 + GSH	Ungated	16829
5 + CQ	Ungated	17586
5 + Media	Ungated	17020
2 + **4** + CQ/GSH	Ungated	17089
2 + **4** + GSH	Ungated	17287
2 + **4** + CQ	Ungated	17808
2 + **4** + Media	Ungated	17021
11/pDNA	Ungated	17198
Lipo	Ungated	16944
+ CQ / GSH	Ungated	17059
+ GSH	Ungated	16900
+ CQ	Ungated	17736
+ Media	Ungated	16995

Sample name	Subset	Count
6 + CQ/GSH	Ungated	14240
6 + GSH	Ungated	14571
6 + CQ	Ungated	14790
6 + Media	Ungated	14645
5 + CQ/GSH	Ungated	14642
5 + GSH	Ungated	14746
5 + CQ	Ungated	14784
5 + Media	Ungated	14723
2 + **4** + CQ/GSH	Ungated	14729
2 + **4** + GSH	Ungated	14658
2 + **4** + CQ	Ungated	14776
2 + **4** + Media	Ungated	14730
11/pDNA	Ungated	14767
Lipo	Ungated	14815
+ CQ / GSH	Ungated	14753
+ GSH	Ungated	14780
+ CQ	Ungated	14746
+ Media	Ungated	14752

Figure S4.6 Sixth replicate of flow cytometry results, the average of which is shown in Figure 4D. (A) Flow cytometry of human embryonic kidney (HEK-293) cells incubated with PFC/**4.7**/pDNA nanoemulsions for 3 hours, with emulsions formed as described in the fluorous tagging and encapsulation of eGFP pDNA in nanoemulsions procedure. During treatment, cells were incubated in complete Media (10% FBS, 1% PS) alongside emulsions for 3 hours. After treatment, cells were washed gently to remove emulsions. MEM media with and without respective GSH (10 mM) treatments were then added back and cells were incubated overnight at 37 °C. The cells were then lifted, washed, resuspended in FACS buffer and analyzed for eGFP (FL-1) fluorescence via flow cytometry. Data is representative of three independent experiments. For assessment of the statistical significance of differences, an ANOVA test followed by Tukey HSD were performed with significance determined by alpha value of 0.05. (B) Side scatter (SSC) vs. forward scatter (FSC) overlay of HEK-293 cells incubated for 3 hours with emulsions and washed. The gate employed for Figure 4.7D is shown. (C) Representative FL-2 histograms of each sample, gated.

4.8 References and Notes

(1) Collins-Gold, L. C.; Lyons, R. T.; Bartholow, L. C. Parenteral Emulsions for Drug Delivery. *Adv. Drug Deliv. Rev.* **1990**, *5*, 189–208.

(2) Mason, T. G.; Wilking, J. N.; Meleson, K.; Chang, C. B.; Graves, S. M. Nanoemulsions: Formation, Structure, and Physical Properties. *J. Phys. Condens. Matter* **2006**, *18*, R635–R666.

(3) Nel, A.; Ruoslahti, E.; Meng, H. New Insights into "Permeability" as in the Enhanced Permeability and Retention Effect of Cancer Nanotherapeutics. *ACS Nano* **2017**, *11*, 9567–9569.

(4) Singh, Y.; Meher, J. G.; Raval, K.; Khan, F. A.; Chaurasia, M.; Jain, N. K.; Chourasia, M. K. Nanoemulsion: Concepts, Development and Applications in Drug Delivery. *J. Control. Release* **2017**, *252*, 28–49.

(5) Ganta, S.; Talekar, M.; Singh, A.; Coleman, T. P.; Amiji, M. M. Nanoemulsions in Translational Research - Opportunities and Challenges in Targeted Cancer Therapy. *AAPS PharmSciTech* **2014**, *15*, 694–708.

(6) Zhong, H.; Chan, G.; Hu, Y.; Hu, H.; Ouyang, D. A Comprehensive Map of FDA-Approved Pharmaceutical Products. *Pharmaceutics* **2018**, *10*, 263–282.

(7) Montero, D.; Tachibana, C.; Rahr Winther, J.; Appenzeller-Herzog, C. Intracellular Glutathione Pools Are Heterogeneously Concentrated. *Redox Biol.* **2013**, *1*, 508–513.

(8) Day, R. A.; Estabrook, D. A.; Logan, J. K.; Sletten, E. M. Fluorous Photosensitizers

Enhance Photodynamic Therapy with Perfluorocarbon Nanoemulsions. *Chem. Commun.* **2017**, *53*, 13043–13046.

(9) Gladysz, J. A.; Jurisch, M. *Structural, Physical, and Chemical Properties of Fluorous Compounds*; 2012; Vol. 308.

(10) Riess, J. G. Understanding the Fundamentals of Perfluorocarbons and Perfluorocarbon Emulsions Relevant to in Vivo Oxygen Delivery. *Artif. Cells. Blood Substit. Immobil. Biotechnol.* **2005**, *33*, 47–63.

(11) Miller, M. A.; Sletten, E. M. A General Approach to Biocompatible Branched Fluorous Tags for Increased Solubility in Perfluorocarbon Solvents. *Org. Lett.* **2018**, *20*, 6850–6854.

(12) Sletten, E. M.; Swager, T. M. Fluorofluorophores: Fluorescent Fluorous Chemical Tools Spanning the Visible Spectrum. *J. Am. Chem. Soc.* **2014**, *136*, 13574–13577.

(13) Lim, I.; Vian, A.; van de Wouw, H.; Day, R. A.; Gomez, C.; Liu, Y.; Rheingold, A. L.; Campas, O.; Sletten, E. M. Fluorous Soluble Cyanine Dyes for Visualizing Perfluorocarbons in Living Systems. *J. Am. Chem. Soc.* **2020**, *142*, 16072–16081.

(14) Klymchenko, A. S. Solvatochromic and Fluorogenic Dyes as Environment-Sensitive Probes: Design and Biological Applications. *Acc. Chem. Res.* **2017**, *50*, 366–375.

(15) Nadler, A.; Schultz, C. The Power of Fluorogenic Probes. *Angew. Chemie - Int. Ed.* **2013**, *52*, 2408–2410.

(16) Lavis, L. D.; Raines, R. T. Bright Building Blocks for Chemical Biology. *ACS Chem.*

Biol. **2014**, *9*, 855–866.

(17) Grimm, J. B.; Heckman, L. M.; Lavis, L. D. *The Chemistry of Small-Molecule Fluorogenic Probes*, 1st ed.; Elsevier Inc., 2013; Vol. 113.

(18) Reichardt, C. Solvatochromic Dyes as Solvent Polarity Indicators. *Chem. Rev.* **1994**, *94*, 2319–2358.

(19) Lee, M. H.; Kim, J. S.; Sessler, J. L. Small Molecule-Based Ratiometric Fluorescence Probes for Cations, Anions, and Biomolecules. *Chem. Soc. Rev.* **2015**, *44*, 4185–4191.

(20) Cotruvo, J. A.; Aron, A. T.; Ramos-Torres, K. M.; Chang, C. J. Synthetic Fluorescent Probes for Studying Copper in Biological Systems. *Chem. Soc. Rev.* **2015**, *44*, 4400–4414.

(21) Carter, K. P.; Young, A. M.; Palmer, A. E. Fluorescent Sensors for Measuring Metal Ions in Living Systems. *Chem. Rev.* **2014**, *114*, 4564–4601.

(22) Zheng, H.; Zhan, X. Q.; Bian, Q. N.; Zhang, X. J. Advances in Modifying Fluorescein and Rhodamine Fluorophores as Fluorescent Chemosensors. *Chem. Commun.* **2013**, *49*, 429–447.

(23) Malinouski, M.; Zhou, Y.; Belousov, V. V.; Hatfield, D. L.; Gladyshev, V. N. Hydrogen Peroxide Probes Directed to Different Cellular Compartments. *PLoS One* **2011**, *6*, e14564.

(24) Zhu, H.; Fan, J.; Du, J.; Peng, X. Fluorescent Probes for Sensing and Imaging within Specific Cellular Organelles. *Acc. Chem. Res.* **2016**, *49*, 2115–2126.

(25) Hammers, M. D.; Pluth, M. D. Ratiometric Measurement of Hydrogen Sulfide and Cysteine/Homocysteine Ratios Using a Dual-Fluorophore Fragmentation Strategy. *Anal.*

Chem. **2014**, *86*, 7135–7140.

(26) Yi, L.; Li, H.; Sun, L.; Liu, L.; Zhang, C.; Xi, Z. A Highly Sensitive Fluorescence Probe for Fast Thiol-Quantification Assay of Glutathione Reductase. *Angew. Chemie - Int. Ed.* **2009**, *48*, 4034–4037.

(27) Dickinson, B. C.; Huynh, C.; Chang, C. J. A Palette of Fluorescent Probes with Varying Emission Colors for Imaging Hydrogen Peroxide Signaling in Living Cells. *J. Am. Chem. Soc.* **2010**, *132*, 5906–5915.

(28) Burnworth, M.; Rowan, S. J.; Weder, C. Fluorescent Sensors for the Detection of Chemical Warfare Agents. *Chem. - A Eur. J.* **2007**, *13*, 7828–7836.

(29) Zhang, S. W.; Swager, T. M. Fluorescent Detection of Chemical Warfare Agents: Functional Group Specific Ratiometric Chemosensors. *J. Am. Chem. Soc.* **2003**, *125*, 3420–3421.

(30) Dale, T. J.; Rebek, J. Fluorescent Sensors for Organophosphorus Nerve Agent Mimics. *J. Am. Chem. Soc.* **2006**, *128*, 4500–4501.

(31) Díaz De Greñu, B.; Moreno, D.; Torroba, T.; Berg, A.; Gunnars, J.; Nilsson, T.; Nyman, R.; Persson, M.; Pettersson, J.; Eklind, I.; Wästerby, P. Fluorescent Discrimination between Traces of Chemical Warfare Agents and Their Mimics. *J. Am. Chem. Soc.* **2014**, *136*, 4125–4128.

(32) Kirrane, T. M.; Middleton, W. J. 7-Amino-4-Perfluoroheptylcoumarins: A Novel Class of Perfluorocarbon-Soluble Fluorescent Dyes. *J. Fluor. Chem.* **1993**, *62*, 289–292.

(33) Matsui. Masaki; Shibata, Katsuyoski; Muramatsu, Hiroshige; Sawada, Hideo; Nakayama, M. Synthesis, Fluorescence, and Photostabilities of 3-(Perfluoroalkyl)Coumarins. *Chem. Ber.* **1992**, *125*, 467–471.

(34) Matsui, M.; Joglekar, B.; Ishigure, Y.; Shibata, K.; Muramatsu, H.; Murata, Y. Synthesis of 3-Cyano-6-Hydroxy-5-[2-(Perfluoroalkyl)Phenylazo]-2-Pyridones and Their Application for Dye Diffusion Thermal Transfer Printing. *Bull. Chem. Soc. Jpn.* **1993**, *66*, 1790–1794.

(35) Setsukinai, K. I.; Urano, Y.; Kikuchi, K.; Higuchi, T.; Nagano, T. Fluorescence Switching by O-Dearylation of 7-Aryloxycoumarins. Development of Novel Fluorescence Probes to Detect Reactive Oxygen Species with High Selectivity. *J. Chem. Soc. Perkin Trans. 2* **2000**, No. 12, 2453–2457.

(36) Muthuramu, K.; Ramamurthy, V. 7-Alkoxy Coumarins as Fluorescence Probes for Microenvironments. *J. Photochem.* **1984**, *26*, 57–64.

(37) Taneja, L.; Sharma, A. K.; Singh, R. D. Study of Photophysical Properties of Coumarins: Substituent and Concentration Dependence. *J. Lumin.* **1995**, *63*, 203–214.

(38) Satyam, A. Design and Synthesis of Releasable Folate-Drug Conjugates Using a Novel Heterobifunctional Disulfide-Containing Linker. *Bioorganic Med. Chem. Lett.* **2008**, *18*, 3196–3199.

(39) Maiti, S.; Park, N.; Han, J. H.; Jeon, H. M.; Lee, J. H.; Bhuniya, S.; Kang, C.; Kim, J. S. Gemcitabine − Coumarin − Biotin Conjugates : A Target Speci Fi c Theranostic Anticancer Prodrug. *J. Am. Chem. Soc.* **2013**, *135*, 4567.

(40) Han, J. C.; Han, G. Y. A Procedure for Quantitative Determination of Tris(2-Carboxyethyl)Phosphine, an Odorless Reducing Agent More Stable and Effective than Dithiothreitol. *Analytical Biochemistry*. 1994, pp 5–10.

(41) Smith, C. V.; Jones, D. P.; Guenthner, T. M.; Lash, L. H.; Lauterburg, B. H. Compartmentation of Glutathione: Implications for the Study of Toxicity and Disease. *Toxicol. Appl. Pharmacol.* **1996**, *140*, 1–12.

(42) Sletten, E. M.; Swager, T. M. Readily Accessible Multifunctional Fluorous Nanoemulsions. *Chem. Sci.* **2016**, *7*, 5091–5097.

(43) Estabrook, D. A.; Ennis, A. F.; Day, R. A.; Sletten, E. M. Controlling Nanoemulsion Surface Chemistry with Poly(2-Oxazoline) Amphiphiles. *Chem. Sci.* **2019**, *10*, 3994–4003.

(44) Krafft, M; Riess, J. Perfluorocarbons: Life Sciences and Biomedical Uses. *J. Polym. Sci. Part A Polym. Chem.* **2007**, *45*, 1185–1198.

(45) Winter, P. M. Perfluorocarbon Nanoparticles : Evolution of a Multimodality and Multifunctional Imaging Agent. *Sci.* **2014**, *2014*, 746574.

(46) Škvarla, J.; Uchman, M.; Procházka, K.; Tošner, Z.; Garamus, V. M.; Pispas, S.; Štěpánek, M. Micellization of Zonyl FSN-100 Fluorosurfactant in Aqueous Solutions. *Colloids Surfaces A Physicochem. Eng. Asp.* **2014**, *443*, 209–215.

(47) Fujii, S.; Cai, Y.; Weaver, J. V. M.; Armes, S. P. Syntheses of Shell Cross-Linked Micelles Using Acidic ABC Triblock Copolymers and Their Application as PH-

Responsive Particulate Emulsifiers. *J. Am. Chem. Soc.* **2005**, *127*, 7304–7305.

(48) Tu, F.; Lee, D. Shape-Changing and Amphiphilicity-Reversing Janus Particles with PH-Responsive Surfactant Properties. *J. Am. Chem. Soc.* **2014**, *136*, 9999–10006.

(49) Liu, K.; Jiang, J.; Cui, Z.; Binks, B. P. PH-Responsive Pickering Emulsions Stabilized by Silica Nanoparticles in Combination with a Conventional Zwitterionic Surfactant. *Langmuir* **2017**, *33*, 2296–2305.

(50) Binks, B. P.; Rodrigues, J. A. Inversion of Emulsions Stabilized Solely by Ionizable Nanoparticles. *Angew. Chemie - Int. Ed.* **2005**, *44*, 441–444.

(51) Liu, Y.; Jessop, P. G.; Cunningham, M.; Eckert, C. A.; Liotta, C. L. Switchable Surfactants. *Science (80-.).* **2006**, *313*, 958–960.

(52) Jiang, J.; Zhu, Y.; Cui, Z.; Binks, B. P. Switchable Pickering Emulsions Stabilized by Silica Nanoparticles Hydrophobized in Situ with a Switchable Surfactant. *Angew. Chemie - Int. Ed.* **2013**, *52*, 12373–12376.

(53) Binks, B. P.; Murakami, R.; Armes, S. P.; Fujii, S. Temperature-Induced Inversion of Nanoparticle-Stabilized Emulsions. *Angew. Chemie - Int. Ed.* **2005**, *44*, 4795–4798.

(54) Wiese, S.; Spiess, A. C.; Richtering, W. Microgel-Stabilized Smart Emulsions for Biocatalysis. *Angew. Chemie - Int. Ed.* **2013**, *52*, 576–579.

(55) Kong, W.; Guo, S.; Wu, S.; Liu, X.; Zhang, Y. Redox-Controllable Interfacial Properties of Zwitterionic Surfactant Featuring Selenium Atoms. *Langmuir* **2016**, *32*, 9846–9853.

(56) Sivakumar, S.; Bansal, V.; Cortez, C.; Chong, S. F.; Zelikin, A. N.; Caruso, F.

Degradable, Surfactant-Free, Monodisperse Polymer-Encapsulated Emulsions as Anticancer Drug Carriers. *Adv. Mater.* **2009**, *21*, 1820–1824.

(57) Aydogan, N.; Abbott, N. L. Comparison of the Surface Activity and Bulk Aggregation of Ferrocenyl Surfactants with Cationic and Anionic Headgroups. *Langmuir* **2001**, *17*, 5703–5706.

(58) Tsuchiya, K.; Orihara, Y.; Kondo, Y.; Yoshino, N.; Ohkubo, T.; Sakai, H.; Abet, M. Control of Viscoelasticity Using Redox Reaction. *J. Am. Chem. Soc.* **2004**, *126*, 12282–12283.

(59) Zhang, Y.; Chen, H.; Liu, X.; Zhang, Y.; Fang, Y.; Qin, Z. Effective and Reversible Switching of Emulsions by an Acid/Base-Mediated Redox Reaction. *Langmuir* **2016**, *32*, 13728–13735.

(60) Jong, L. I.; Abbott, N. L. Chemodegradable Surfactant System Based on Oxidation of Disulfide Bonds Using Hypochlorite. *Langmuir* **2000**, *16*, 5553–5561.

(61) Deng, Z.; Yuan, S.; Xu, R. X.; Liang, H.; Liu, S. Reduction-Triggered Transformation of Disulfide-Containing Micelles at Chemically Tunable Rates. *Angew. Chemie - Int. Ed.* **2018**, *57*, 8896–8900.

(62) Day, R. A.; Estabrook, D.; Wu, C.; Chapman, J. O.; Togle, A. J.; Sletten, E. M. Systematic Study of Perfluorocarbon Nanoemulsions Stabilized by Polymer Amphiphiles. *ACS Appl. Mater. Interfaces* **2020**, *12*, 38887–38898.

(63) Sloand, J. N.; Nguyen, T. T.; Zinck, S. A.; Cook, E. C.; Zimudzi, T. J.; Showalter, S. A.;

Glick, A. B.; Simon, J. C.; Medina, S. H. Ultrasound-Guided Cytosolic Protein Delivery via Transient Fluorous Masks. *ACS Nano* **2020**, *14*, 4061.

(64) Grigsby, C. L.; Leong, K. W. Balancing Protection and Release of DNA: Tools to Address a Bottleneck of Non-Viral Gene Delivery. *J. R. Soc. Interface* **2010**, *7*, S67–S82.

(65) Teixeira, H. F.; Bruxel, F.; Fraga, M.; Schuh, R. S.; Zorzi, G. K.; Matte, U.; Fattal, E. Cationic Nanoemulsions as Nucleic Acids Delivery Systems. *Int. J. Pharm.* **2017**, *534*, 356–367.

(66) Fraga, M.; Bruxel, F.; Diel, D.; De Carvalho, T. G.; Perez, C. A.; Magalhães-Paniago, R.; Malachias, Â.; Oliveira, M. C.; Matte, U.; Teixeira, H. F. PEGylated Cationic Nanoemulsions Can Efficiently Bind and Transfect PIDUA in a Mucopolysaccharidosis Type i Murine Model. *J. Control. Release* **2015**, *209*, 37–46.

(67) Boswell, P. G.; Bühlmann, P. Fluorous Bulk Membranes for Potentiometric Sensors with Wide Selectivity Ranges: Observation of Exceptionally Strong Ion Pair Formation. *J. Am. Chem. Soc.* **2005**, *127* (25), 8958–8959.

(68) Krafft, M. P.; Riess, J. G. Per- and Polyfluorinated Substances (PFASs): Environmental Challenges. *Curr. Opin. Colloid Interface Sci.* **2015**, *20* (3), 192–212.

(69) Ando, S.; Putnam, D.; Pack, D. W.; Langer, R. PLGA Microspheres Containing Plasmid DNA: Preservation of Supercoiled DNA via Cryopreparation and Carbohydrate Stabilization. *J. Pharm. Sci.* **1999**, *88*, 126–130.

(70) Koo, A. N.; Lee, H. J.; Kim, S. E.; Chang, J. H.; Park, C.; Kim, C.; Park, J. H.; Lee, S. C.

Disulfide-Cross-Linked PEG-Poly(Amino Acid)s Copolymer Micelles for Glutathione-Mediated Intracellular Drug Delivery. *Chem. Commun.* **2008**, No. 48, 6570–6572.

(71) Tang, L. Y.; Wang, Y. C.; Li, Y.; Du, J. Z.; Wang, J. Shell-Detachable Micelles Based on Disulfide-Linked Block Copolymer as Potential Carrier for Intracellular Drug Delivery. *Bioconjug. Chem.* **2009**, *20*, 1095–1099.

(72) Pangborn, A. B.; Giardello, M. A.; Grubbs, R. H.; Rosen, R. K.; Timmers, F. J. Safe and Convenient Procedure for Solvent Purification. *Organometallics* **1996**, *15*, 1518–1520.

CHAPTER FIVE

Experimental perspectives on direct visualization of endosomal rupture

Adapted from: Rachael A. Day and Ellen M. Sletten.* Experimental perspectives on direct visualization of endosomal rupture. **2021**, *Submitted.*

5.1 Abstract

Endosomal escape continues to be a limiting factor in the therapeutic use of nanomaterials. Assays to visualize endosomal escape often do not decouple the endosomal disruption from the release of payload into the cytosol. Here, we focus on three approaches to directly probe endosomal rupture: calcein dye dilution, lysosome size quantification and endosome/lysosome membrane integrity visualized with a genetically engineered cell line. We apply the three assays to endosomes ruptured via osmotic pressure and photochemical internalization.

5.2 Introduction

Endosomal escape is the elephant in the room for nanomaterial studies. While nanomaterials have been hailed as the solution to many challenges in medicine, most nanomaterials are internalized by cells through endocytosis mechanisms, delivering them to the endosome (Figure 5.1A). Failure to escape the endosomal/lysosomal pathway results in degradation of the material and payload[1–3] (path 1, Figure 5.1A) or exocytosis from the cell[4,5] (path 2, Figure 5.1A). Consequently, a plethora of methods to rupture/escape the endosome and assays to visualize escape have been explored (path 3, Figure 5.1A). Common assays include transfection efficiency,[6]

Forster resonance energy transfer assays,[7] colocalization with cellular markers,[8,9] and fluorescence correlation spectroscopy (FCS) measurements.[10,11] While each of these assays have their advantages and disadvantages, they all rely on visualization of the escaped nanomaterial or payload (path 3b, Figure 5.1A). If endosomal escape is successful, these methods are convincing and even quantitative in the case of FCS; however, if no escape is observed these assays do not provide information on whether the challenge lies in rupturing the endosome/lysosome (path 3a, Figure 5.1A) or release from the ruptured endosome/lysosome (path 3b, Figure 5.1A). The ability to separately assay path 3a and 3b becomes particularly relevant for the release of large nanomaterials.

A common assay to identify endosomal rupture is calcein (**5.1**, Figure 5.1B),[12–17] an impermeable, fluorescein derivative that is self-quenched at high concentrations and low pH. Upon endosomal disruption, calcein diffuses into the cytosol resulting in an increase in fluorescence within the cell. However, the use of calcein can be complicated by premature leakage from the lysosomes and inefficient, cell-line dependent quenching[18,19] that is difficult to quantify. In addition, calcein is excited by 488 nm light without adequate equivalents at higher wavelengths, diminishing flexibility for multiplexing with common fluorescent protein markers (Figure 5.1B).

Here, we compare the use of calcein with two less explored approaches for direct visualization of endosomal rupture: lysosome swelling visualized with pH sensitive dyes (Figure 5.1C) or a genetically-engineered cell line developed by Duvall and coworkers[20,21] (Figure 5.1D). Lysosome swelling occurs when weakly basic molecules accumulate in the lysosome, preventing the natural acidification, resulting in an increase of water, protons and chloride ions pumped into the lysosome.[19,22] The genetically engineered cell line developed by Duvall and coworkers use galectins, a class of lectins that bind to β-galactoside which is localized in the inner leaflet of

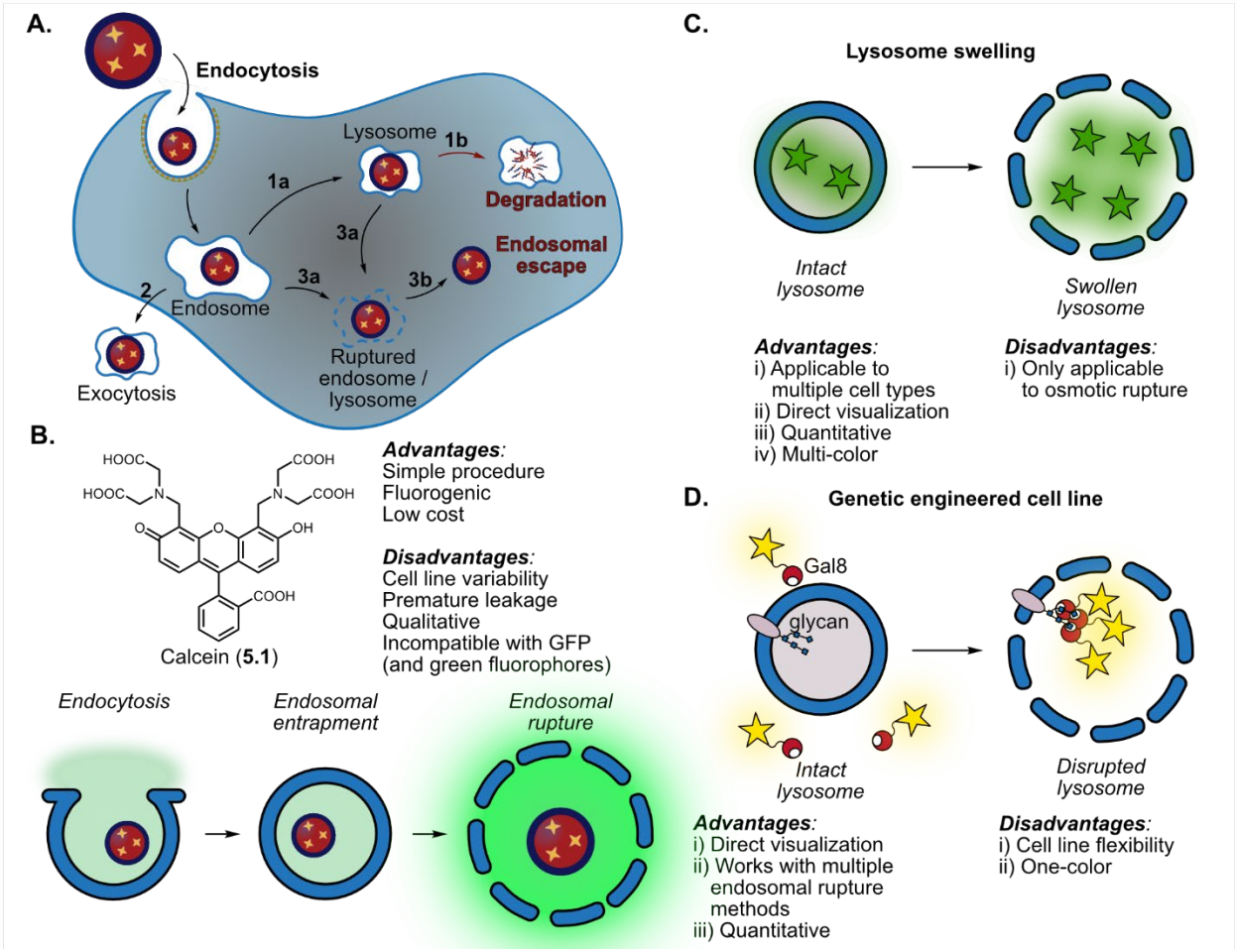

Figure 5.3. (A) Nanomaterial endocytosis pathways. (B) Advantages and disadvantages of traditional calcein dilution assays. (C) This work utilizing lysosome swelling and (D) genetic engineered cell lines to visualized endosomal disruption.

endosomes. A primary role of galectins is to sense endosomal membrane damage, resulting in the accumulation within disrupted endosomes.[23,24] This mechanism has been leveraged to visualize endosomal disruption by fusing YFP to Galectin-8 (Gal8)[20,21,23,25] and Galectin-9 (Gal9).[24,26] We showcase the benefits and limitations of these two assays, as compared to calcein, using two methods of endosomal escape: osmotic rupture and photochemical internalization (PCI).[27]

5.3 Results and Discussion

We are interested in perfluorocarbon (PFC) nanoemulsions, a class of soft nanomaterials, where an immiscible PFC solvent is stabilized by a surfactant to create particles ~100-300 nm in diameter.[28,29] PFC nanoemulsions are endocytosed via clathrin mediated pathways,[29,30] and trafficked to the lysosome. The large size of PFC nanoemulsions provide a significant challenge for endosomal escape and motivated this work exploring assays which give a direct readout of endosomal rupture.

First, we investigated the three assays using osmotic rupture to facilitate endosomal escape (Figure 5.2A). Chloroquine (**5.2**), a lysosomotropic weak base, inhibits the acidification of the lysosome through the protonation of the diethylamino group.[31–33] Cell-penetrating, cationic peptides containing arginine and lysine residues, such as the TAT-HA2 peptide (**5.3**) and derivatives, can be used alone or in combination with chloroquine to increase endosomal escape efficiencies (Figure 5.2B).[12,34,35]

We treated a macrophage cell line (RAW264.7; Figure 5.2C i.-ii.; Figure 5.3-5.5) with PFC nanoemulsions and 150 μM calcein (**5.1**) in the presence or absence of endosomal escape treatment **5.2**, **5.3,** or the combination of **5.2**/**5.3** (Figure 5.2 C-D) at non-toxic concentrations (Figure 5.6). Despite following literature reports,[15,17] in our hands the calcein assay did not produce the expected

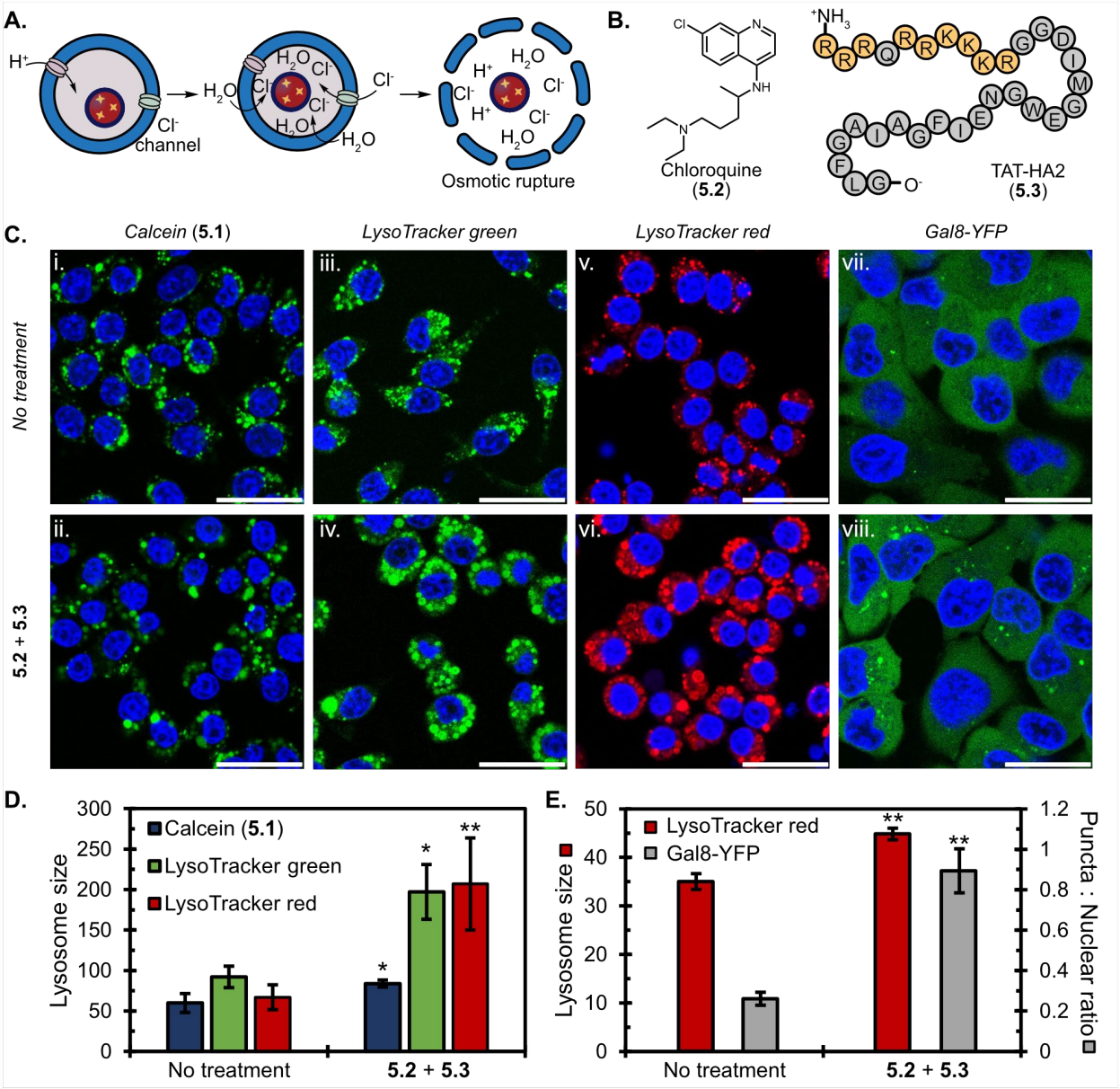

Figure 5.2. Osmotic rupture of endosomes. (A) Schematic showing osmotic rupture of endosomes. (B) Lysosomotropic molecule (**5.2**) and cell-penetrating peptide (**5.3**) used to promote osmotic rupture. (C) Confocal scanning microscopy of RAW264.7 cells +/- treatment (**5.2/5.3**). Scale bar represents 25 mm. (D) Quantification of lysosome size (calcein, blue; LysoTracker green, green; LysoTracker red, red). (E) Quantification of lysosome size in MDA-MB-231 Gal8-YFP cells stained with LysoTracker red (red, see Figure 5.20-5.21 for microscopy), and quantification of the puncta to nuclear ratio (vii.-viii.; gray). Description of quantification in ImageJ Analysis Section of Supporting Information. Statistical significance is defined by one tailed Student T's test of unequal variance compared to no treatment controls. *p<0.05, **p<0.01.

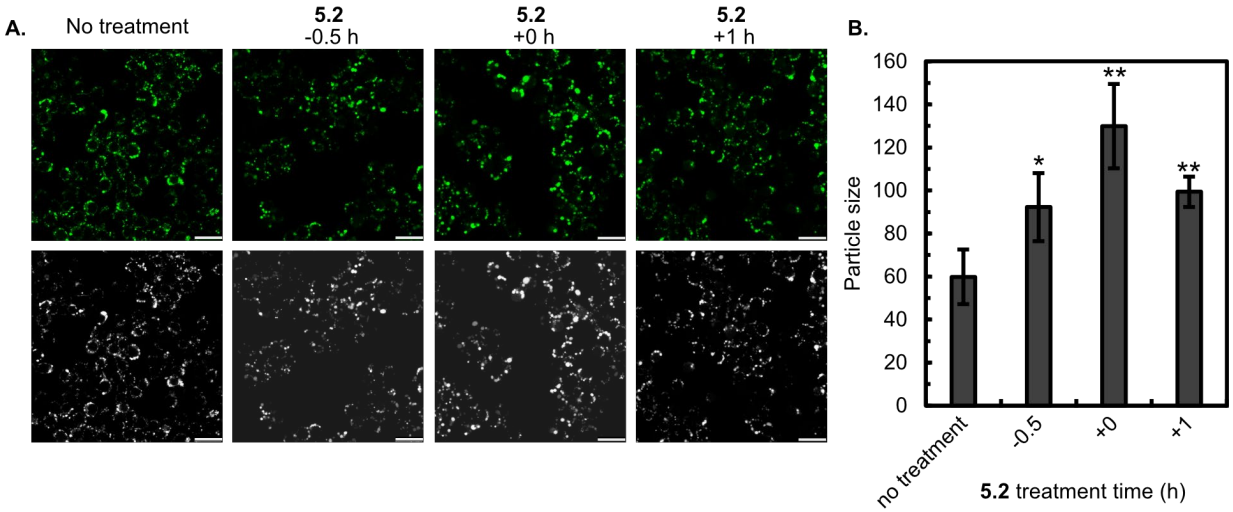

Figure 5.3. Confocal microscopy visualizing endosomal disruption via calcein (**5.1**) staining of RAW cells. (A) Single channel microscopy of calcein (green, top panel) and black and white (bottom panel). Cells were treated with chloroquine (**5.2**, 100 mM) 0.5 h before addition of emulsions (-0.5 h), at the same time as emulsions (+0 h), or one hour after emulsions (+1 h). (B) Quantification of calcein stained lysosomes. Bars represent the average of three representative images and error bars represent the standard deviation of 3 images. Statistical significance is defined by a one-sided Student T-test with unequal variance compared to no treatment control. * $p < 0.05$ ** $p < 0.01$

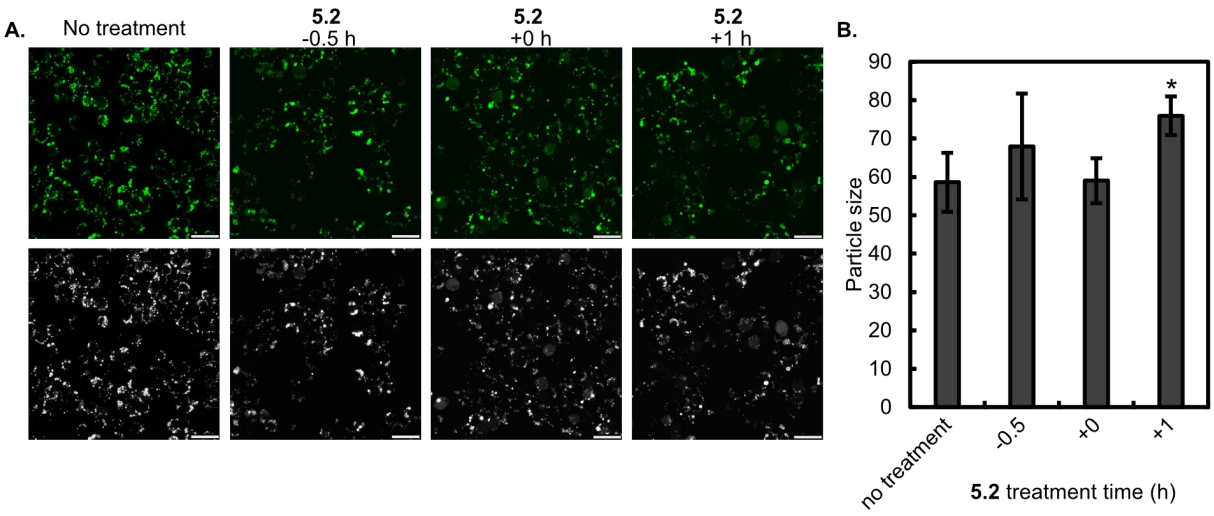

Figure 5.4. Confocal microscopy visualizing endosomal disruption via calcein (**5.1**) staining of RAW cells. (A) Single channel microscopy of calcein (green, top panel) and black and white (bottom panel). Cells were treated with chloroquine (**5.2**, 100 mM) 0.5 h before addition of emulsions (-0.5 h), at the same time as emulsions (+0 h), or one hour after emulsions (+1 h). (B) Quantification of calcein stained lysosomes. Bars represent the average of three representative images and error bars represent the standard deviation of 3 images. Statistical significance is defined by a one-sided Student T-test with unequal variance compared to no treatment control. * $p < 0.05$ ** $p < 0.01$

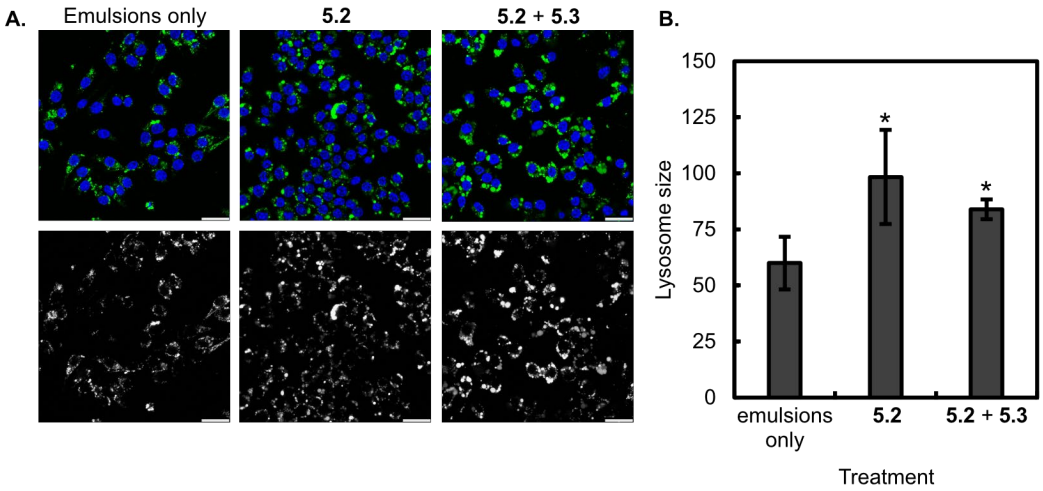

Figure 5.5. Confocal microscopy visualizing endosomal disruption via calcein (**5.1**) staining of RAW cells. (A) Multi channel microscopy of calcein (green, top panel), Hoescht (blue, top panel) and black and white staining of calcein (bottom panel). (B) Quantification of calcein stained lysosomes. Bars represent the average of three representative images and error bars represent the standard deviation of 3 images. Statistical significance is defined by a one-sided Student T-test with unequal variance compared to no treatment control. * $p < 0.05$

cytosolic labeling upon treatment with **5.2/5.3** (Figure 5.2C ii.). However, we did reliably observe larger areas of fluorescence after endosomal escape treatment which we reasoned were enlarged endosomes that resulted from swelling due to osmotic imbalance. This was supported by Verkman[22] and Braeckmans[19] who both used fluorescence microscopy to visualize the swelling of endosomes associated with endocytosis of weakly basic nanocarriers. With this precedent, we expected common endosome/lysosome markers would produce the same result and enable detection of compromised endosomes.

We proceeded to treat RAW264.7 (Figure 5.2C iii.-vi.; Figure 5.7-5.12) and A375 cell lines (Figure 5.13-5.18) with LysoTracker stains and PFC nanoemulsions in the presence or absence of **5.2/5.3**. The LysoTracker stains are quick, easy to use, and can be multiplexed as there are variants that align with the four common confocal laser channels. We found treatment with both LysoTracker green (iii.-iv.), and LysoTracker red (v.-vi.) provided similar results to the calcein-stained cells (i.-ii.; 5.7-5.18). To quantify the lysosome enlargement, a threshold was applied to each set of images, and the average number of pixels per lysosome was counted (see ImageJ analysis section in the Supporting Information). We found that before treatment, lysosome size averaged between 50-100 pixels. After treatment with **5.2/5.3,** the lysosomes stained with LysoTracker increase 2-3.5 fold (Figure 5.2D). Visually, calcein follows the same trend; however, quantification only resulted in a 1.4 fold increase in lysosome size compared to no treatment.

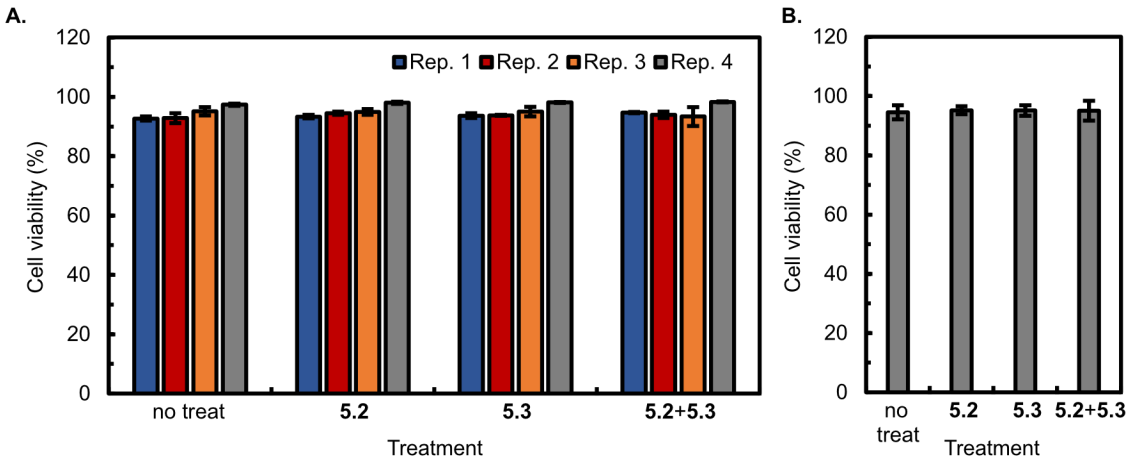

Figure 5.6. Cell viability of RAW264.7 after treatment with chloroquine (**5.2**) and TAT-HA2 peptide (**5.3**). (A) Cell viability for four identical trials. Bars represent the average of three wells per experiment. Error bars represent the standard deviation. (B) The average cell viability of the four trials. Error bars represent the standard deviation.

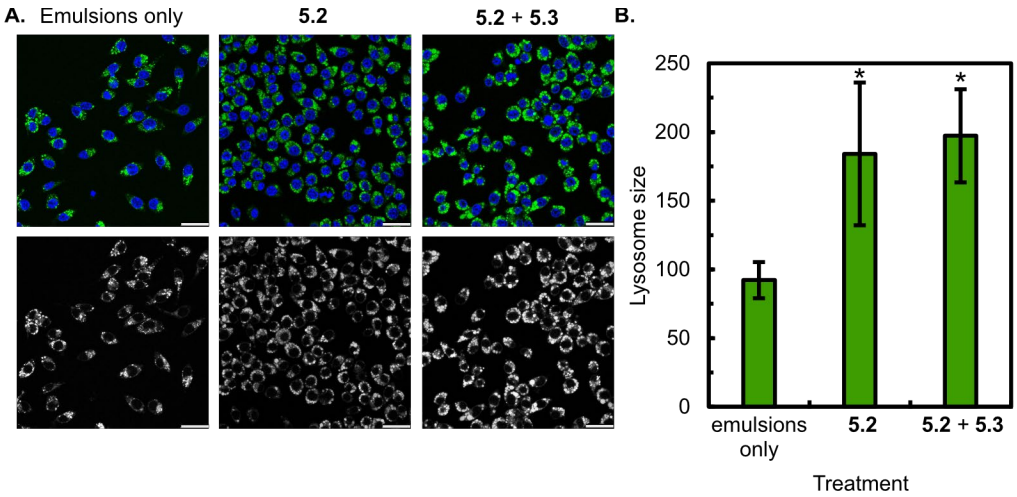

Figure 5.7. Confocal microscopy visualizing endosomal disruption via LysoTracker green staining of RAW cells. (A) Multi channel microscopy of LysoTracker (green, top panel), Hoescht (blue, top panel) and black and white staining of the lysosomes (LysoTracker green, bottom panel). (B) Quantification of stained lysosomes. Bars represent the average of three representative images and error bars represent the standard deviation of 3 images. Statistical significance is defined by a one-sided Student T-test with unequal variance compared to no treatment control. * $p < 0.05$

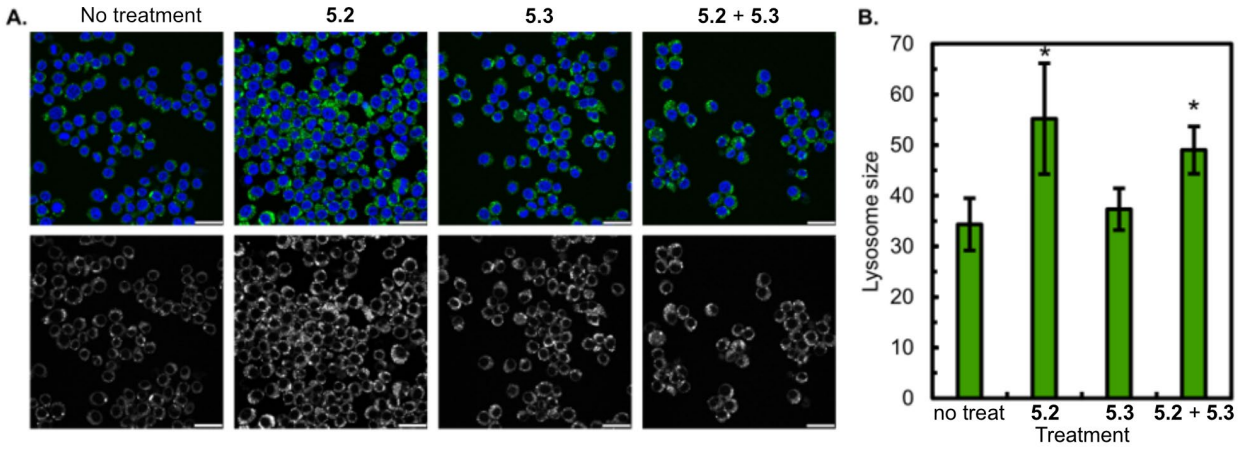

Figure 5.8. Confocal microscopy visualizing endosomal disruption via LysoTracker green staining of RAW cells. (A) Multi channel microscopy of LysoTracker (green, top panel), Hoescht (blue, top panel) and black and white staining of the lysosomes (bottom panel). (B) Quantification of stained lysosomes. Bars represent the average of three representative images and error bars represent the standard deviation of 3 images. Statistical significance is defined by a one-sided Student T-test with unequal variance compared to no treatment control. * $p < 0.05$

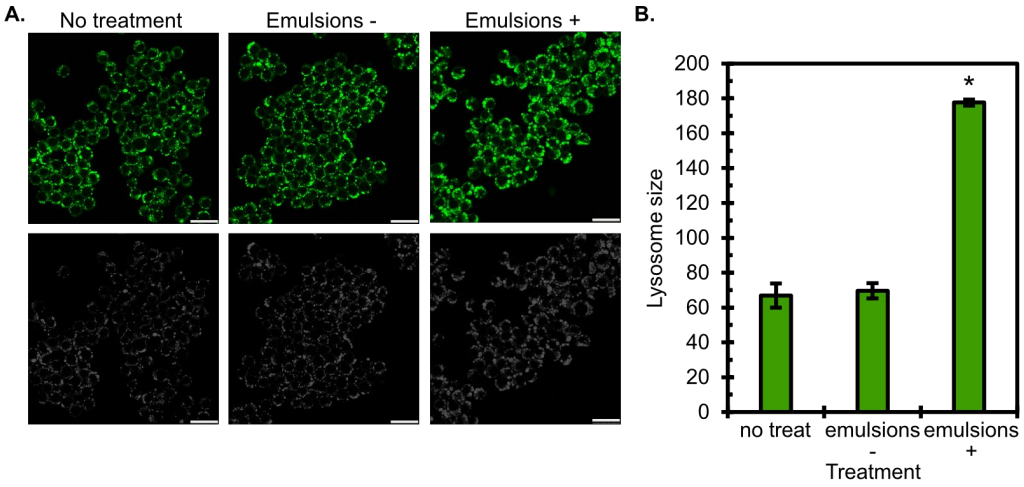

Figure 5.9. Confocal microscopy visualizing endosomal disruption via LysoTracker green staining of RAW cells. (A) Single channel microscopy of LysoTracker (green, top panel) and black and white (bottom panel). (B) Quantification of stained lysosomes. Bars represent the average of three representative images and error bars represent the standard deviation of 3 images. Statistical significance is defined by a one-sided Student T-test with unequal variance compared to no treatment control. * $p < 0.05$

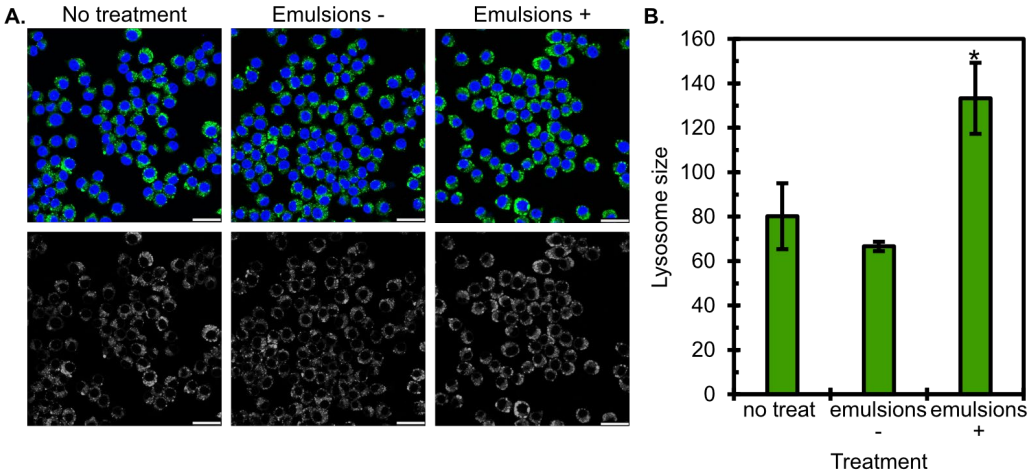

Figure 5.10. Confocal microscopy visualizing endosomal disruption via LysoTracker green staining of RAW cells. (A) Multi channel microscopy of LysoTracker (green, top panel), Hoescht (blue, top panel) and black and white staining of the lysosomes (bottom panel). (B) Quantification of stained lysosomes. Bars represent the average of three representative images and error bars represent the standard deviation of 3 images. Statistical significance is defined by a one-sided Student T-test with unequal variance compared to no treatment control. * $p < 0.05$

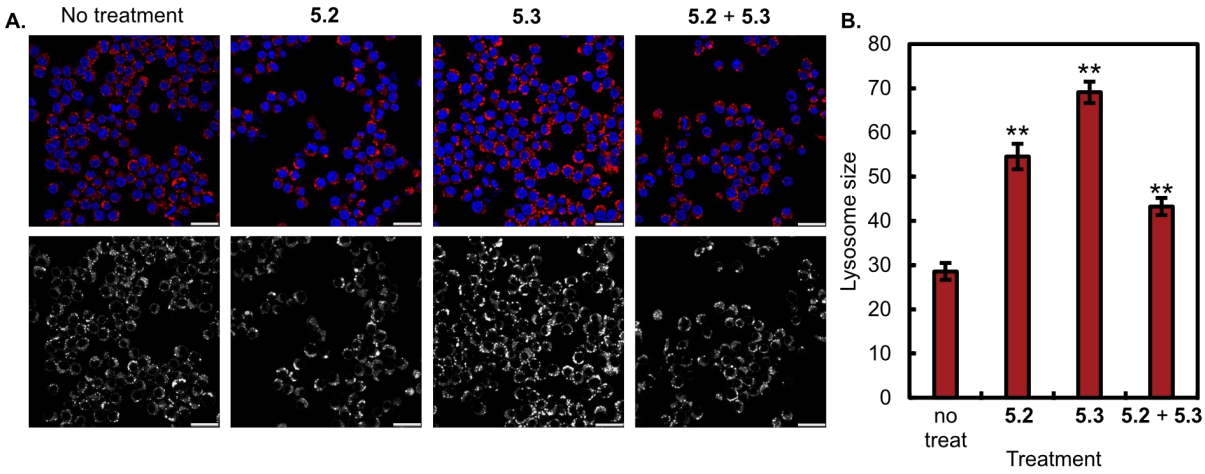

Figure 5.11. Confocal microscopy visualizing endosomal disruption via LysoTracker red staining of RAW cells. (A) Multi channel microscopy of LysoTracker (red, top panel), Hoescht (blue, top panel) and black and white staining of the lysosomes (bottom panel). (B) Quantification of stained lysosomes. Bars represent the average of three representative images and error bars represent the standard deviation of 3 images. Statistical significance is defined by a one-sided Student T-test with unequal variance compared to no treatment control. * $p < 0.05$ ** $p < 0.01$

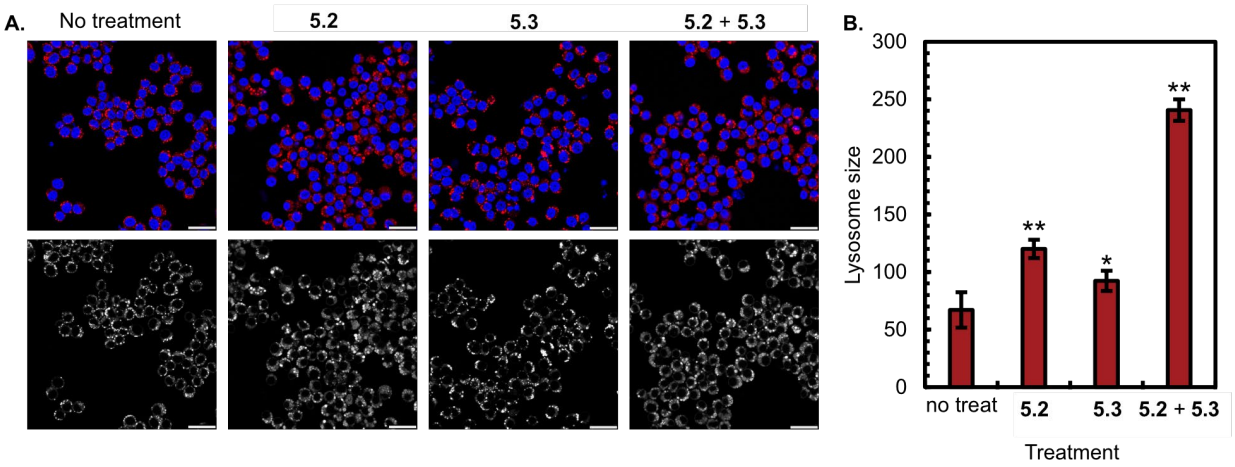

Figure 5.12. Confocal microscopy visualizing endosomal disruption via LysoTracker red staining of RAW cells. (A) Multi channel microscopy of LysoTracker (red, top panel), Hoescht (blue, top panel) and black and white staining of the lysosomes (bottom panel). (B) Quantification of stained lysosomes. Bars represent the average of three representative images and error bars represent the standard deviation of 3 images. Statistical significance is defined by a one-sided Student T-test with unequal variance compared to no treatment control. * $p < 0.05$ ** $p < 0.01$

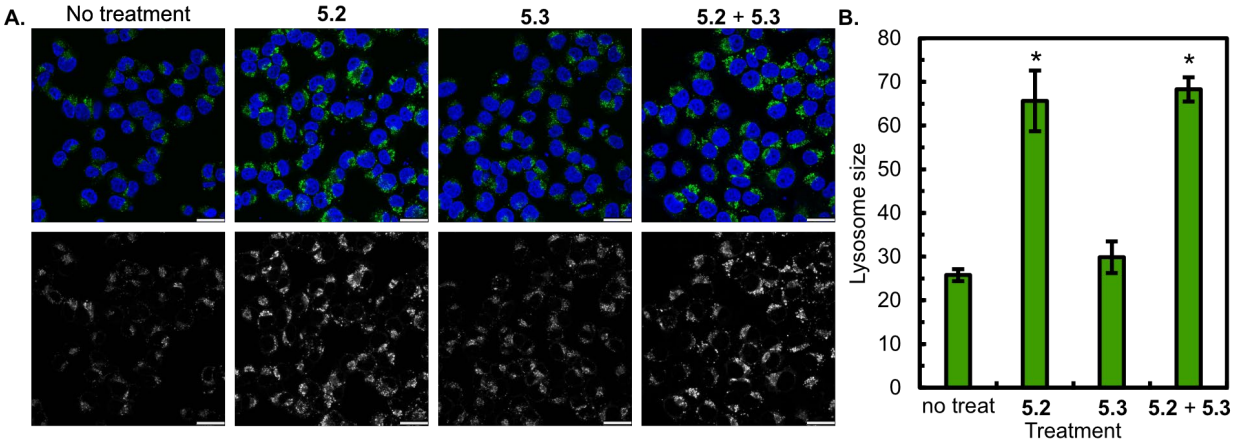

Figure 5.13. Confocal microscopy visualizing endosomal disruption via LysoTracker green staining of A375 cells. (A) Multi channel microscopy of LysoTracker (green, top panel), Hoescht (blue, top panel) and black and white staining of the lysosomes (bottom panel). (B) Quantification of stained lysosomes. Bars represent the average of three representative images and error bars represent the standard deviation of 3 images. Statistical significance is defined by a one-sided Student T-test with unequal variance compared to no treatment control. * $p < 0.05$

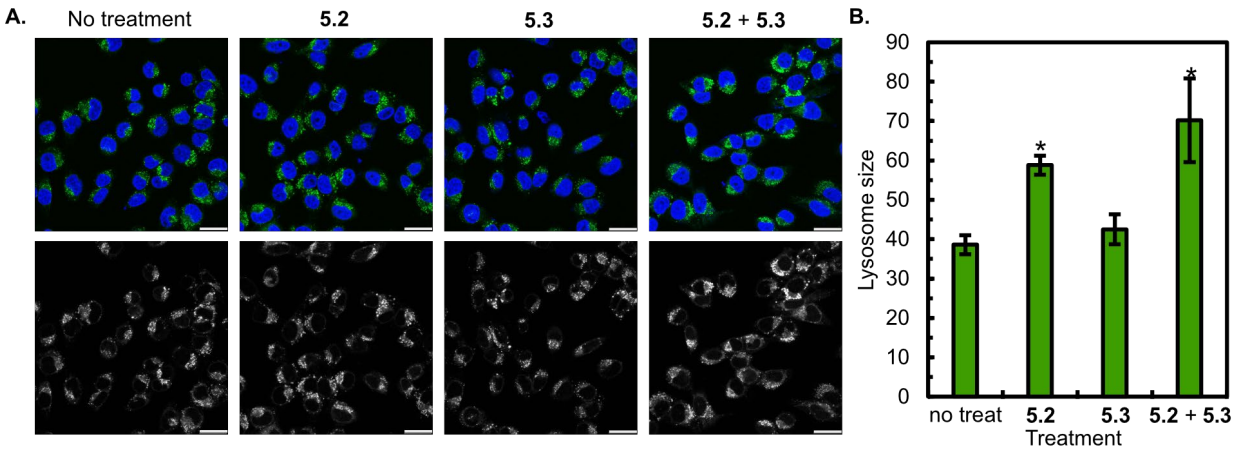

Figure 5.14. Confocal microscopy visualizing endosomal disruption via LysoTracker green staining of A375 cells. (A) Multi channel microscopy of LysoTracker (green, top panel), Hoescht (blue, top panel) and black and white staining of the lysosomes (bottom panel). (B) Quantification of stained lysosomes. Bars represent the average of three representative images and error bars represent the standard deviation of 3 images. Statistical significance is defined by a one-sided Student T-test with unequal variance compared to no treatment control. * $p < 0.05$

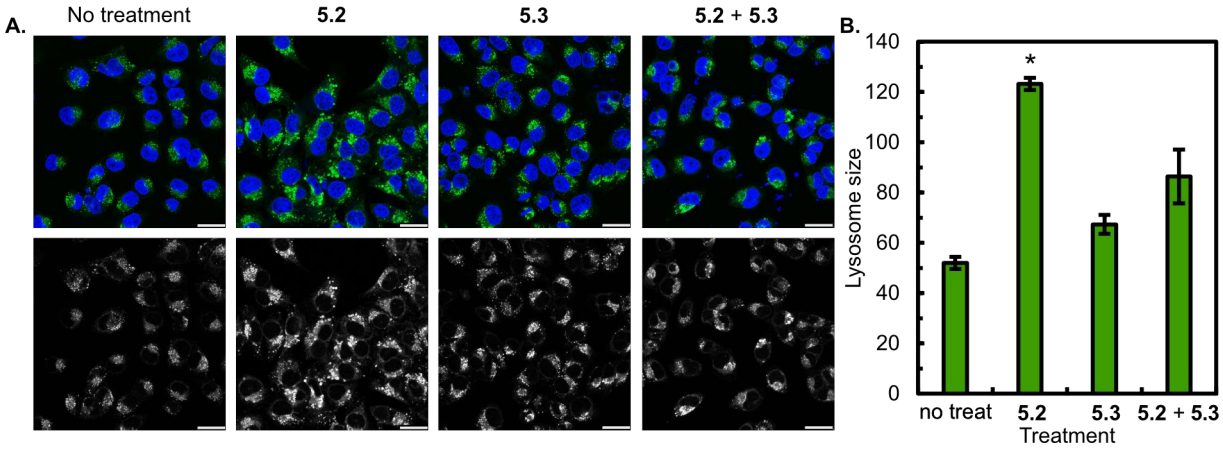

Figure 5.15. Confocal microscopy visualizing endosomal disruption via LysoTracker green staining of A375 cells. (A) Multi channel microscopy of LysoTracker (green, top panel), Hoescht (blue, top panel) and black and white staining of the lysosomes (bottom panel). (B) Quantification of stained lysosomes. Bars represent the average of three representative images and error bars represent the standard deviation of 3 images. Statistical significance is defined by a one-sided Student T-test with unequal variance compared to no treatment control. * $p < 0.05$

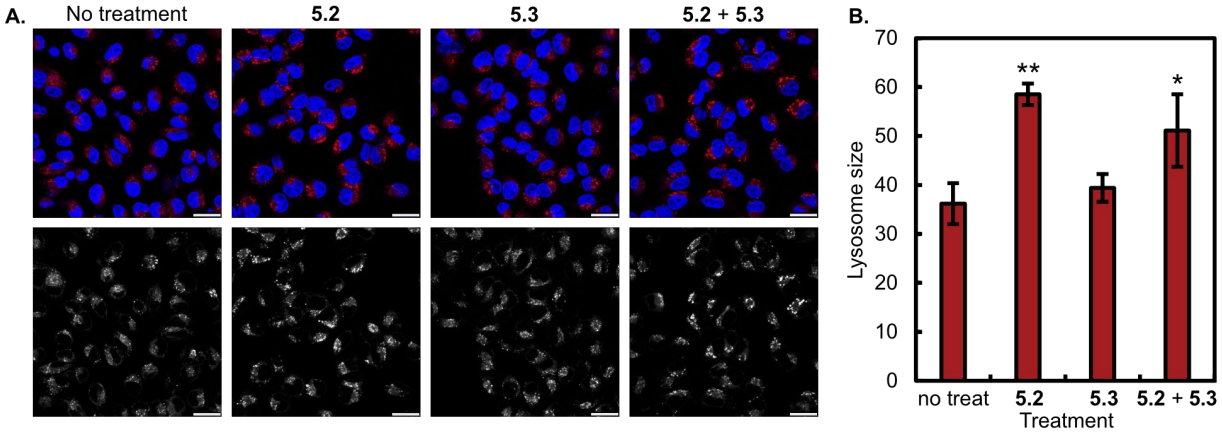

Figure 5.16. Confocal microscopy visualizing endosomal disruption via LysoTracker red staining of A375 cells. (A) Multi channel microscopy of LysoTracker (red, top panel), Hoescht (blue, top panel) and black and white staining of the lysosomes (bottom panel). (B) Quantification of stained lysosomes. Bars represent the average of three representative images and error bars represent the standard deviation of 3 images. Statistical significance is defined by a one-sided Student T-test with unequal variance compared to no treatment control. * $p < 0.05$

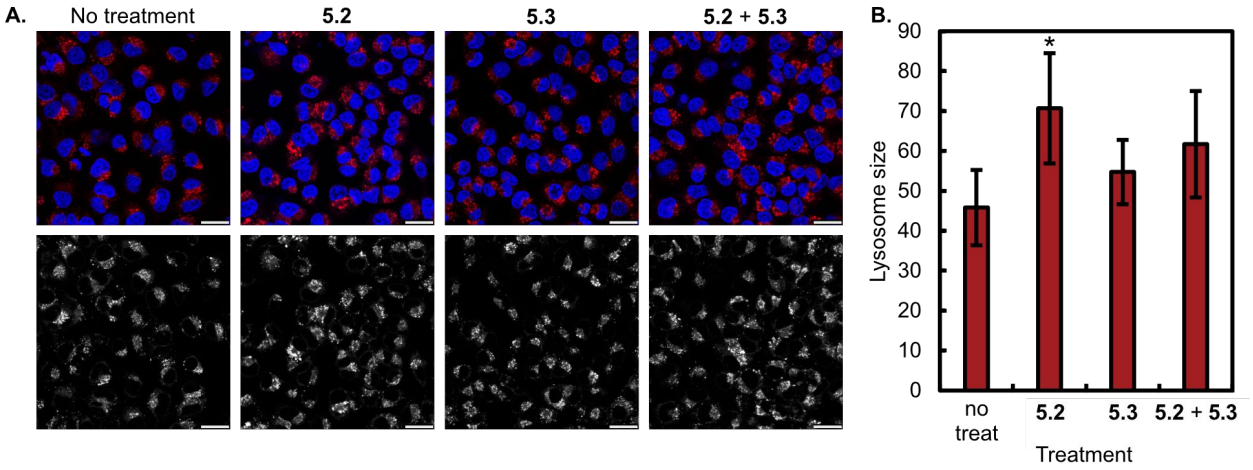

Figure 5.17. Confocal microscopy visualizing endosomal disruption via LysoTracker red staining of A375 cells. (A) Multi channel microscopy of LysoTracker (red, top panel), Hoescht (blue, top panel) and black and white staining of the lysosomes (bottom panel). (B) Quantification of stained lysosomes. Bars represent the average of three representative images and error bars represent the standard deviation of 3 images. Statistical significance is defined by a one-sided Student T-test with unequal variance compared to no treatment control. * $p < 0.05$

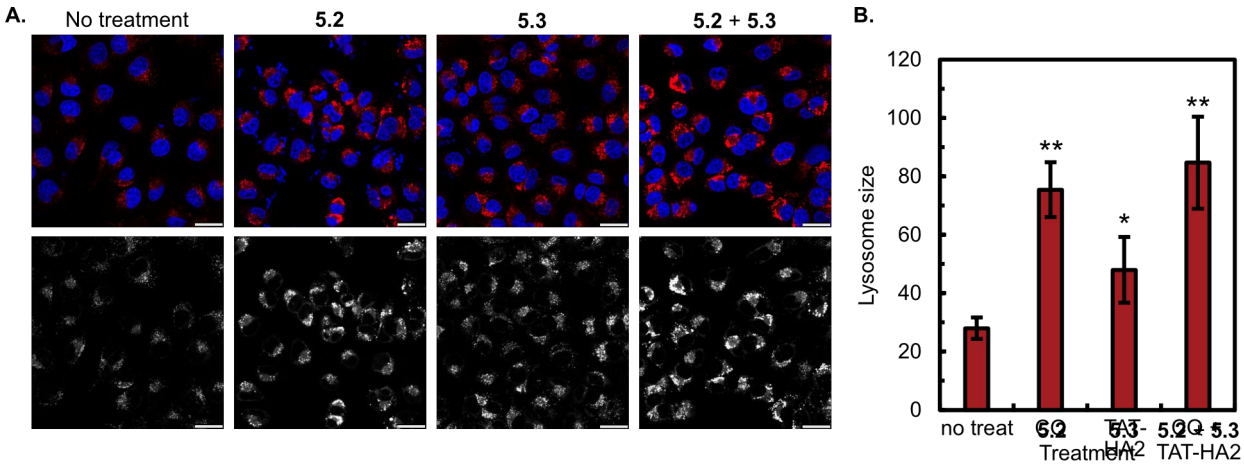

Figure 5.18. Confocal microscopy visualizing endosomal disruption via LysoTracker red staining of A375 cells. (A) Multi channel microscopy of LysoTracker (red, top panel), Hoescht (blue, top panel) and black and white staining of the lysosomes (bottom panel). (B) Quantification of stained lysosomes. Bars represent the average of three representative images and error bars represent the standard deviation of 3 images. Statistical significance is defined by a one-sided Student T-test with unequal variance compared to no treatment control. * $p < 0.05$

We corroborated that we were indeed achieving endosomal rupture upon treatment with **5.2/5.3** by using a genetically engineered human melanoma cell line (MDA-MB-231, Figure 5.2C vii.-viii.). To establish endosomal rupture in the MDA-MB-231 cell line, the number of puncta per cell was quantified by applying a threshold to each image, counting the number of puncta and normalizing by the number of nuclei in each image. More puncta per cell represent greater endosomal disruption. We found that endosomes were significantly disrupted when nanoemulsions and **5.2** were added, regardless of timing (Figure 5.19). Upon treatment with endosomal disruption agents **5.2/5.3** the puncta to nuclear ratio increases ~3-fold compared to untreated controls (Figure 5.2E, gray).

We next looked to multiplex the visualization of lysosome size with the genetically engineered MDA-MB-231 cells and LysoTracker red. Indeed, we observed an ~1.5 fold increase in lysosome size in the MDA-MB-231 cells line (Figure 5.2E, 5.20-5.21), confirming the lysosome size and genetically encoded cell lines were successful at visualizing endosomal disruption with **5.2/5.3**. This is consistent with both RAW264.7 and A375 cells, demonstrating that this assay can easily be applied to a variety of cell lines.

We then moved to compare the calcein, lysosome size, and genetically modified MDA-MB-231 cells to visualize endosomal disruption via PCI (Figure 5.22A).[16,36–39] PCI uses a photosensitizer that produces reactive oxygen species (ROS) when irradiated with light to induce membrane destabilization, and endosomal/lysosomal rupture. PFC nanoemulsions are an ideal nanomaterial for PCI as the fluorous phase boasts 20-fold higher dissolved oxygen concentrations than water, increasing the amount of ROS that can be produced.[40–42] As such, we used a platform previously optimized for photodynamic therapy with PFC nanoemulsions,[43] with shortened irradiation times to disrupt the endosomes/lysosomes without causing cell death (Figure 5.23). As PFC

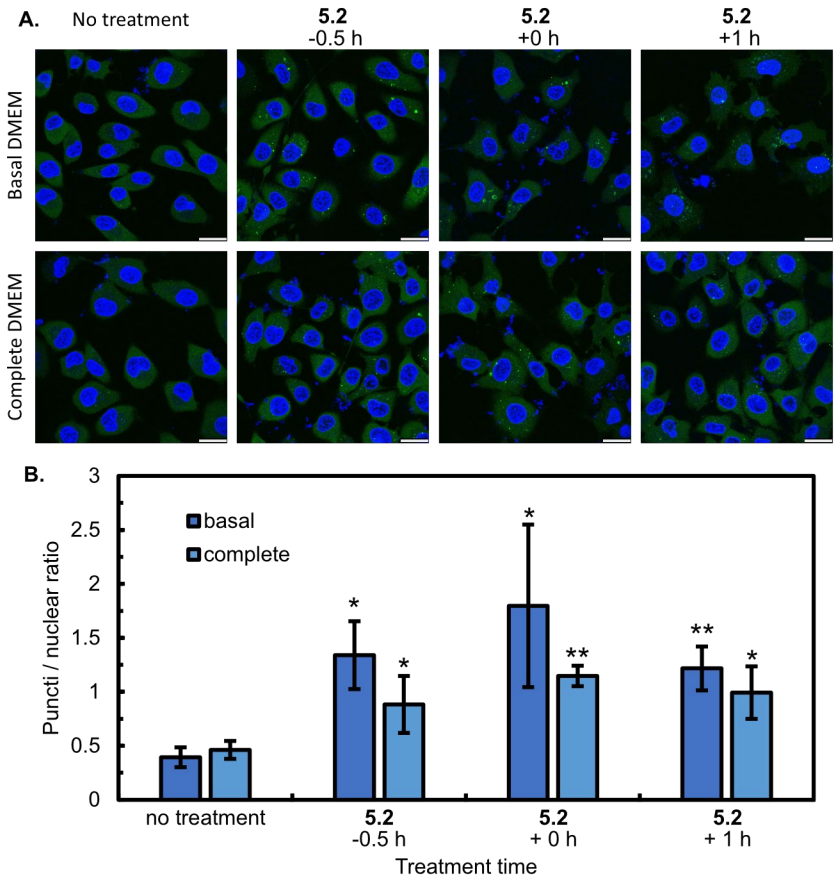

Figure 5.19. Confocal microscopy visualizing endosomal disruption via Lysosome size and Gal8-YFP localization in MDA-MB-231 cells. (A) Multi channel microscopy of Gal8 (green) and Hoescht (blue). Cells were treated with chloroquine (**5.2**, 100 mM) 0.5 h before addition of emulsions (-0.5 h), at the same time as emulsions (+0 h), or one hour after emulsions (+1 h). (B) Quantification of puncta (Gal8) of cells treated in basal media (dark blue) or complete media (light blue). Bars represent the average of three representative images and error bars represent the standard deviation. Statistical significance is defined by a one-sided Student T-test with unequal variance compared to no treatment control. * $p < 0.05$ ** $p < 0.01$

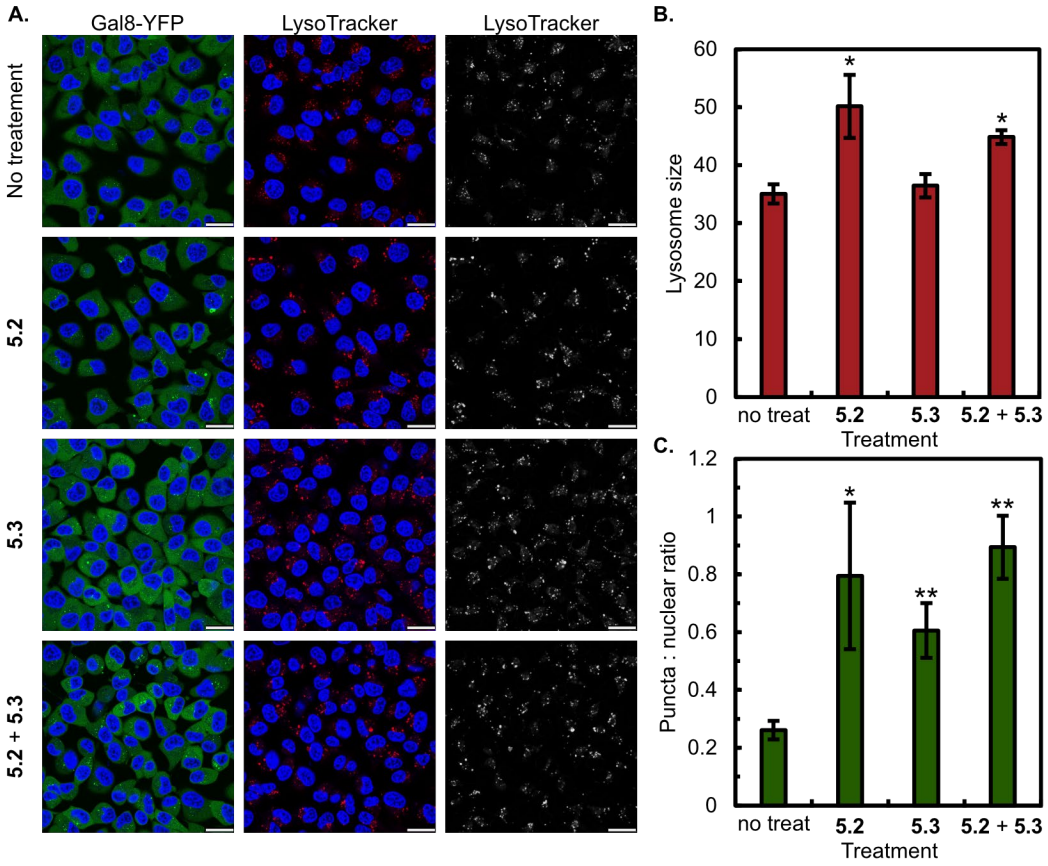

Figure 5.20. Confocal microscopy visualizing endosomal disruption via Lysosome size and Gal8-YFP localization in MDA-MB-231 cells. (A) Multichannel microscopy of Gal8 localization (green, first panel); lysosomes stained with LysoTracker (red, second panel); black and white images of lysosomes stained with LysoTracker (third panel). Nuclei are stained with Hoescht (blue, first and second panel). (B) Quantification of lysosome size of panel 2 images. (C) Quantification of puncta to nuclear ratio of panel 1 images. Bars represent the average of three representative images and error bars represent the standard deviation of 3 images. Statistical significance is defined by a one-sided Student T-test with unequal variance compared to no treatment control. * $p < 0.05$ ** $p < 0.01$

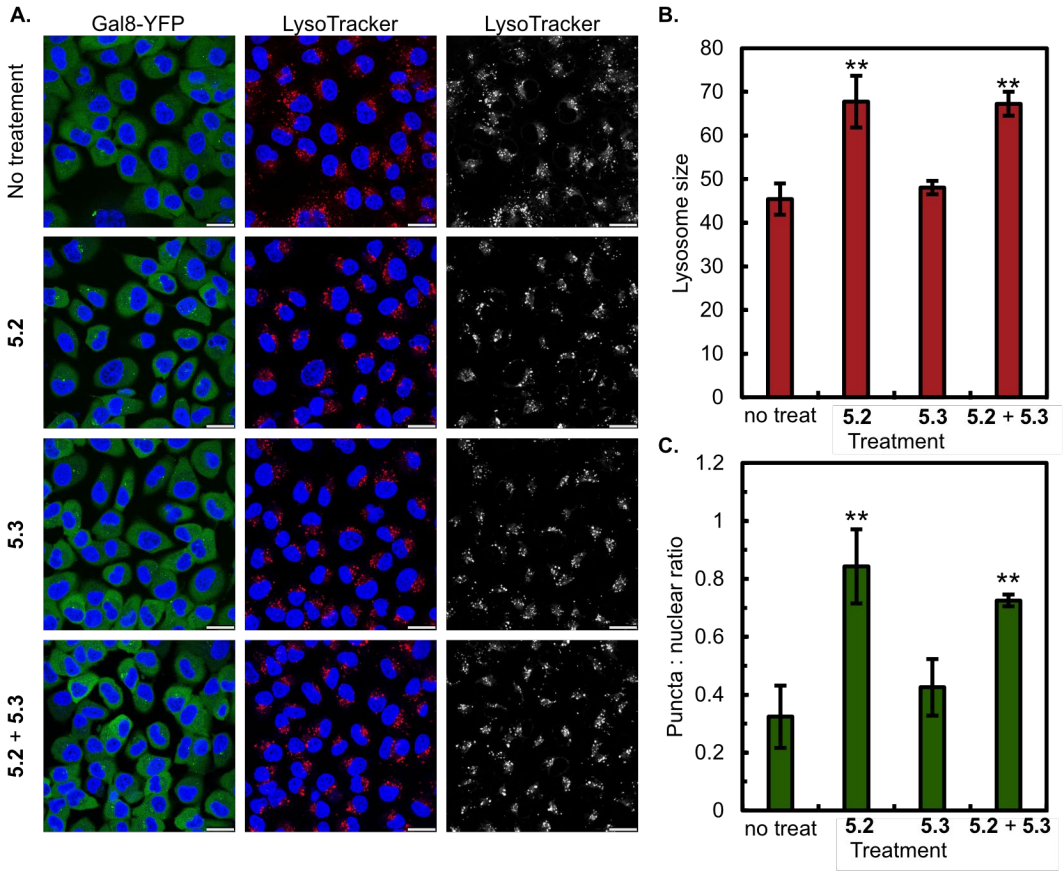

Figure 5.21. Confocal microscopy visualizing endosomal disruption via Lysosome size and Gal8-YFP localization in MDA-MB-231 cells. (A) Multichannel microscopy of Gal8 localization (green, first panel); lysosomes stained with LysoTracker (red, second panel); black and white images of lysosomes stained with LysoTracker (third panel). Nuclei are stained with Hoescht (blue, first and second panel). (B) Quantification of lysosome size of panel 2 images. (C) Quantification of puncta to nuclear ratio of panel 1 images. Bars represent the average of three representative images and error bars represent the standard deviation of 3 images. Statistical significance is defined by a one-sided Student T-test with unequal variance compared to no treatment control. * $p < 0.05$ ** $p < 0.01$

nanoemulsions were a new approach to deliver the photosensitizer necessary for PCI, we first optimized the conditions using the MDA-MB-231 cells. We found hydrophobic photosensitizer (**5.4**, Figure 5.22B), encapsulated in PFC nanoemulsions irradiated for 1 min (420 nm, 8.5 mW/cm^2), produced optimal lysosomal disruption (Figure 5.22C vii., viii.). The puncta : nuclear ratio (Figure 5.22E, Figure 5.24-5.29) increased 5-fold compared to dark controls after 1 minute of irradiation.

Moving to apply PCI to RAW264.7 cells, which readily internalize PFC nanoemulsions,[28] we treated cells with PFC nanoemulsions containing **5.4**, irradiated them with or without light, and stained with calcein (**5.1**). We found that cells that did not undergo light treatment (Figure 5.22C, i.) displayed localized fluorescence indicating calcein was trapped within the lysosomes. However, cells that had undergone irradiation (Figure 5.22C, ii.) did show some weak cytosolic labelling, supporting the results observed with the MDA-MB-231 cells that ROS disrupts the endosomal/lysosomal membrane (Figure 5.22C, Figure 5.30-5.32). Analyzing the calcein that remained in the lysosome after light treatment did not suggest an increase in lysosome size, despite the two other assays supporting endosomal rupture (Figure 5.22D). We reasoned this result was due to the distinct mechanism of PCI which causes endosomal membrane disruption via ROS instead of promoting osmotic imbalance.

To confirm the lysosome size results observed with calcein, we treated RAW264.7 cells with PFC nanoemulsions containing **5.4** in the presence or absence of light. These cells were then stained with either LysoTracker green or red and analyzed lysosomes size. In cells lacking light treatment, lysosomes are ~40 pixels (Figure 5.22C/D, iii., iv.) and do not display statistically significantly increase in size after light treatment (Figure 5.22C/D, v., vi.; Figure 5.33-5.34). We observed a similar result with A375 cells (Figure 5.35-5.36).

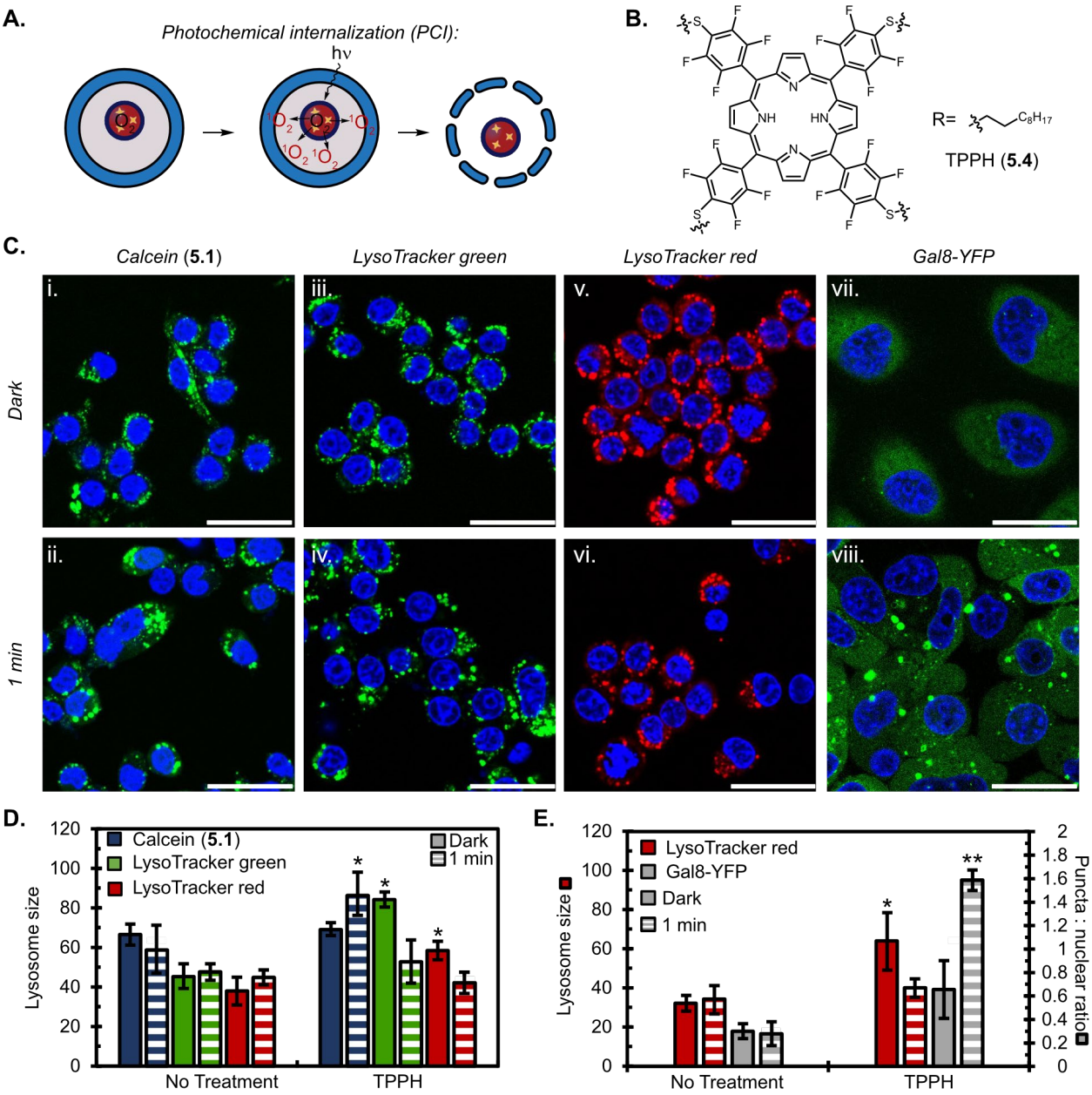

Figure 5.22. PCI disruption of endosomes. (A) Schematic showing the production of ROS upon irradiation disrupting endosomal/lysosomal membranes. (B) Photosensitizer (**5.4**), irradiated with 420 nm light (8.5 mw/cm^2) produces ROS. (C) Confocal scanning laser microscopy of RAW264.7 cells +/- light treatments. Scale bar represents 25 mm. (D) Quantification of lysosome size (calcein, blue; LysoTracker green, green; LysoTracker red, red), dark treatment (solid), 1 min light treatment (striped). (E) Quantification of puncta : nuclear ratio (vii.-viii.) See ImageJ Analysis Section in Supporting Information for description of quantification. Statistical significance is defined by one tailed Student T's test of unequal variance compared to no treatment controls. *p<0.05, **p<0.01.

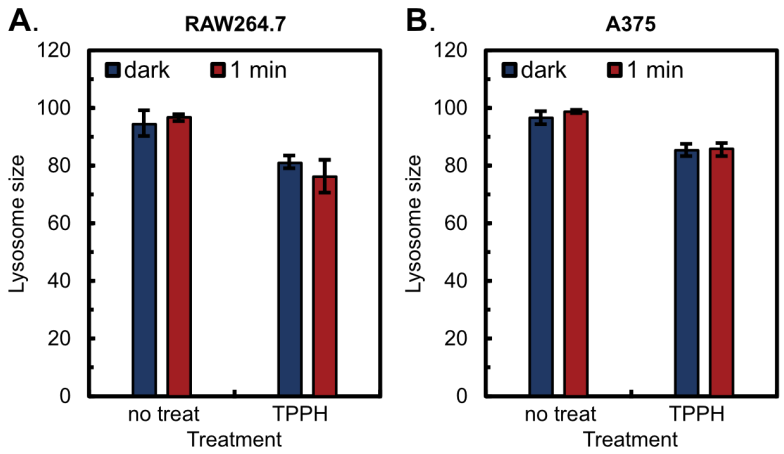

Figure 5.23. Cell viability of (A) RAW and (B) A375 cells after PCI endosomal disruption. Cells were treated with media (no treat) or PFC nanoemulsions containing TPPH (TPPH) in the dark (blue) or after 1 min irradiation (red). Bars represent the average of three wells and error bars represent the standard deviation of 3 wells.

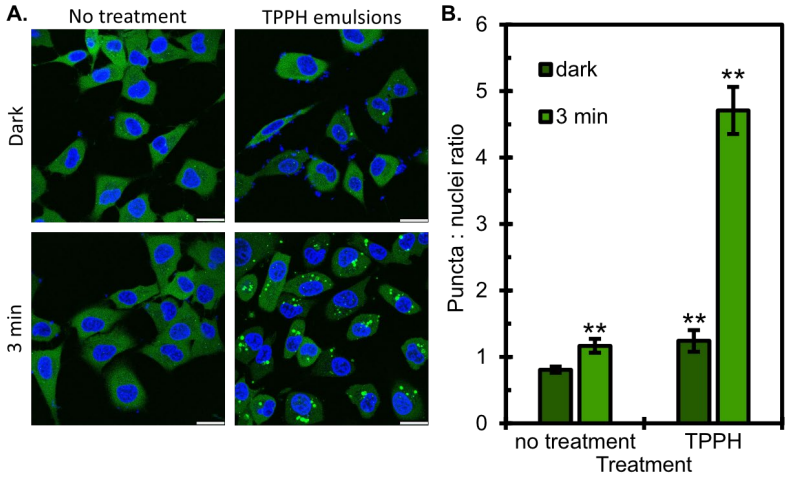

Figure 5.24. Confocal microscopy visualizing endosomal disruption via Gal8-YFP localization in MDA-MB-231 cells. (A) Multichannel microscopy of Gal8 localization (green). Nuclei are stained with Hoescht (blue). (B) Quantification of puncta to nuclear ratio of cells treated with media (no treat) or PFC nanoemulsions containing TPPH (TPPH) in the dark (dark green) or after 1 min irradiation (light green). Bars represent the average of three representative images and error bars represent the standard deviation of 3 images.

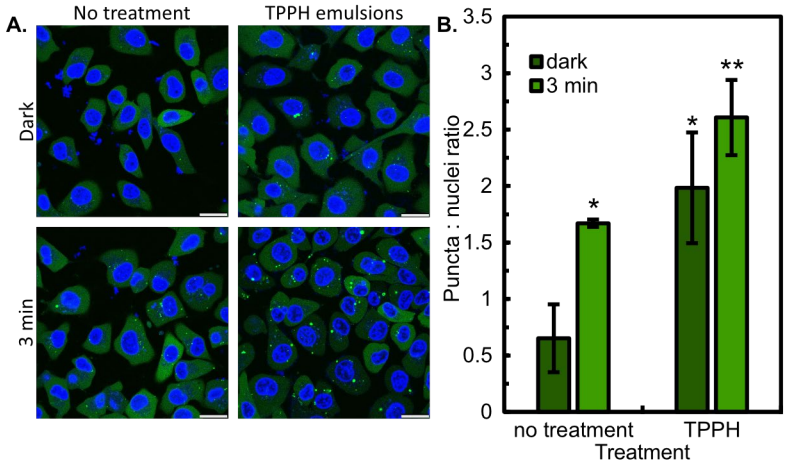

Figure 5.25. Confocal microscopy visualizing endosomal disruption via Gal8-YFP localization in MDA-MB-231 cells. (A) Multichannel microscopy of Gal8 localization (green). Nuclei are stained with Hoescht (blue). (B) Quantification of puncta to nuclear ratio of cells treated with media (no treat) or PFC nanoemulsions containing TPPH (TPPH) in the dark (dark green) or after 1 min irradiation (light green). Bars represent the average of three representative images and error bars represent the standard deviation of 3 images.

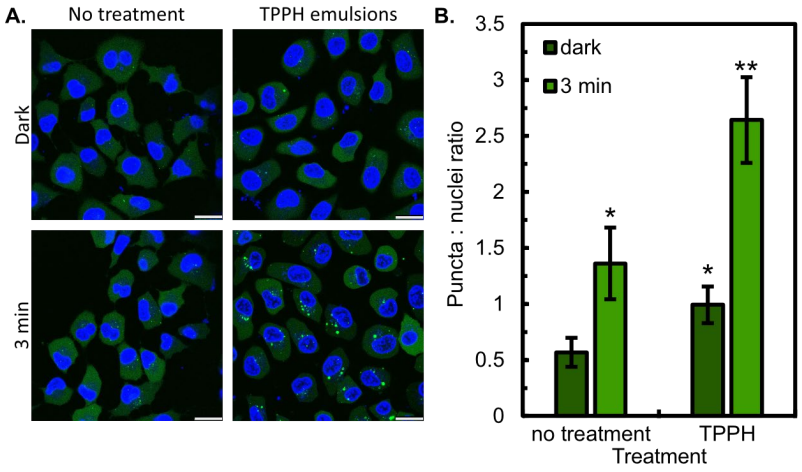

Figure 5.26. Confocal microscopy visualizing endosomal disruption via Gal8-YFP localization in MDA-MB-231 cells. (A) Multichannel microscopy of Gal8 localization (green). Nuclei are stained with Hoescht (blue). (B) Quantification of puncta to nuclear ratio of cells treated with media (no treat) or PFC nanoemulsions containing TPPH (TPPH) in the dark (dark green) or after 1 min irradiation (light green). Bars represent the average of three representative images and error bars represent the standard deviation of 3 images.

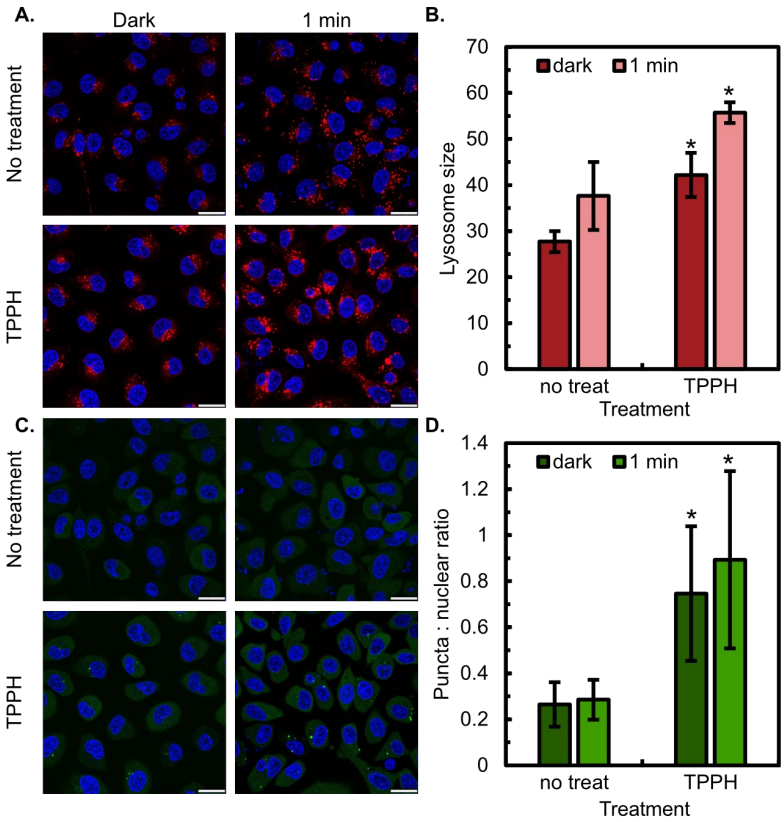

Figure 5.27. Confocal microscopy visualizing endosomal disruption via Lysosome size and Gal8-YFP localization in MDA-MB-231 cells. (A) Multichannel microscopy of lysosome size (red). Nuclei are stained with Hoescht (blue). (B) Quantification of lysosome size of cells treated with media (no treat) or PFC nanoemulsions containing TPPH (TPPH) in the dark (dark red) or after 1 min irradiation (pink). (C) Multichannel microscopy of Gal8 localization (green). Nuclei are stained with Hoescht (blue). (D) Quantification of puncta to nuclear ratio of cells treated with media (no treat) or PFC nanoemulsions containing TPPH (TPPH) in the dark (dark green) or after 1 min irradiation (light green). Bars represent the average of three representative images and error bars represent the standard deviation of 3 images.

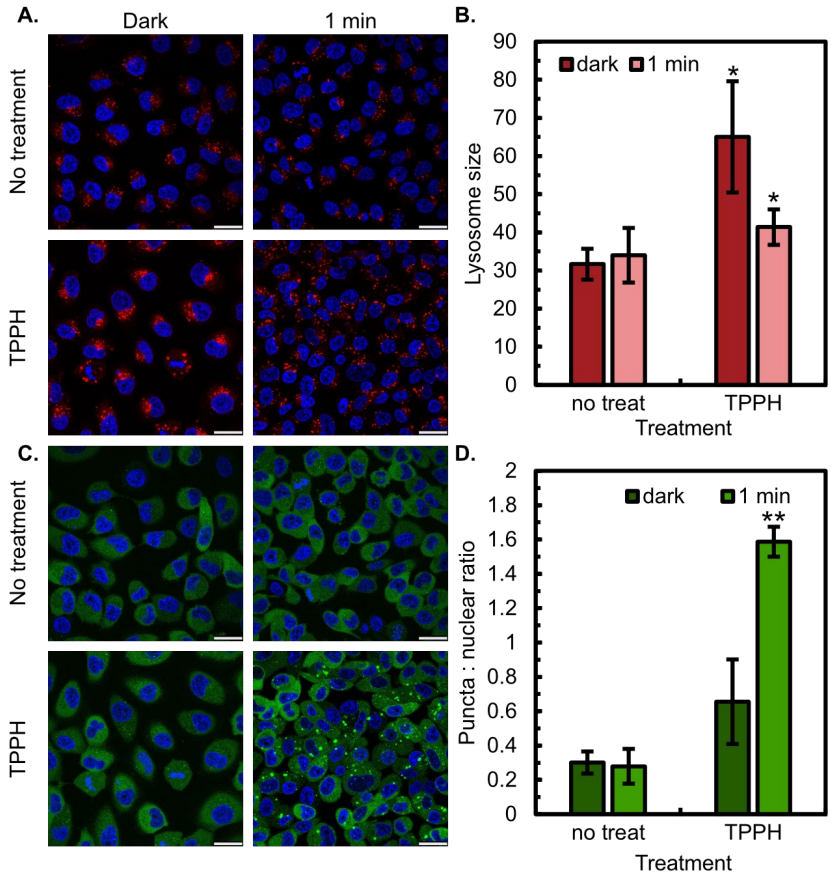

Figure 5.28. Confocal microscopy visualizing endosomal disruption via Lysosome size and Gal8-YFP localization in MDA-MB-231 cells. (A) Multichannel microscopy of lysosome size (red). Nuclei are stained with Hoescht (blue). (B) Quantification of lysosome size of cells treated with media (no treat) or PFC nanoemulsions containing TPPH (TPPH) in the dark (dark red) or after 1 min irradiation (pink). (C) Multichannel microscopy of Gal8 localization (green). Nuclei are stained with Hoescht (blue). (D) Quantification of puncta to nuclear ratio of cells treated with media (no treat) or PFC nanoemulsions containing TPPH (TPPH) in the dark (dark green) or after 1 min irradiation (light green). Bars represent the average of three representative images and error bars represent the standard deviation of 3 images.

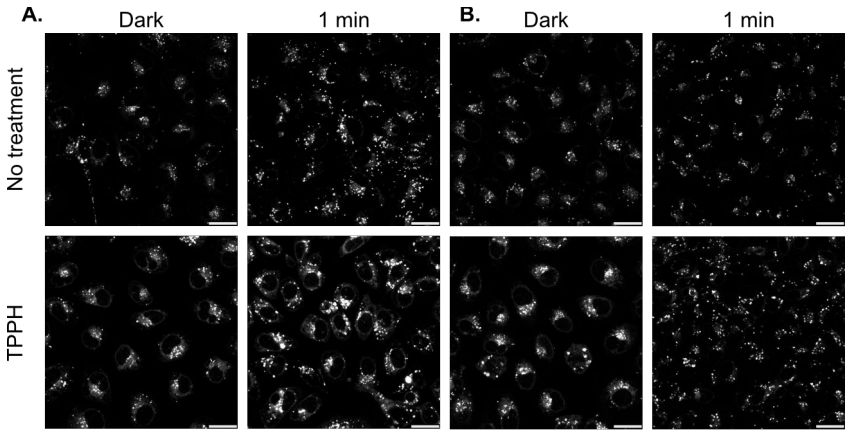

Figure 5.29. Black and white images for LysoTracker red (A) Figure 5.27A and (B) Figure 5.28A.

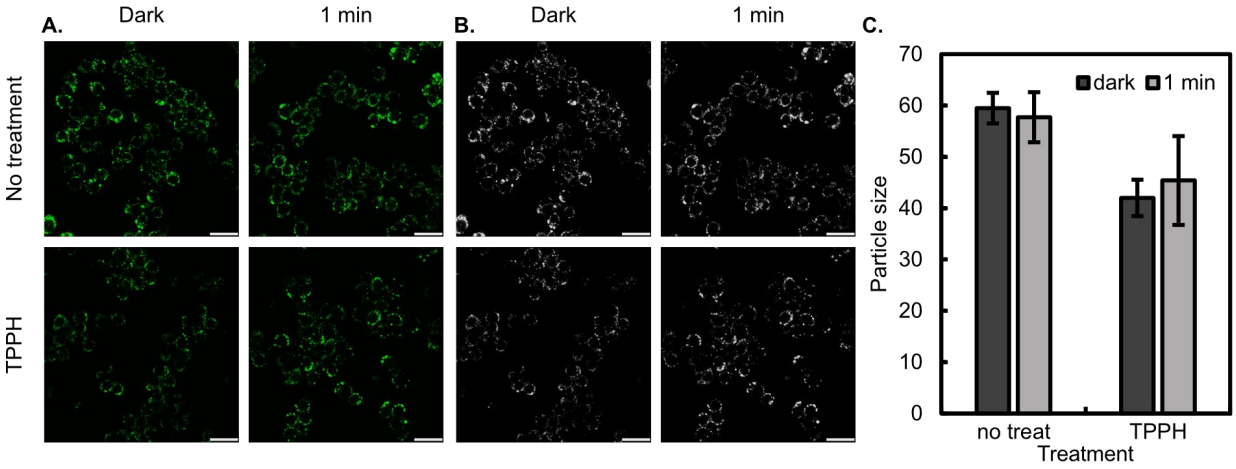

Figure 5.30. Confocal microscopy visualizing endosomal disruption via calcein (**5.1**) staining of RAW cells. (A) Single channel microscopy of calcein stained lysosomes (green). (B) Black and white images of A. (C) Quantification of lysosome size of cells treated with media (no treat) or PFC nanoemulsions containing TPPH (TPPH) in the dark (dark gray) or after 1 min irradiation (light gray). Bars represent the average of three representative images and error bars represent the standard deviation of 3 images.

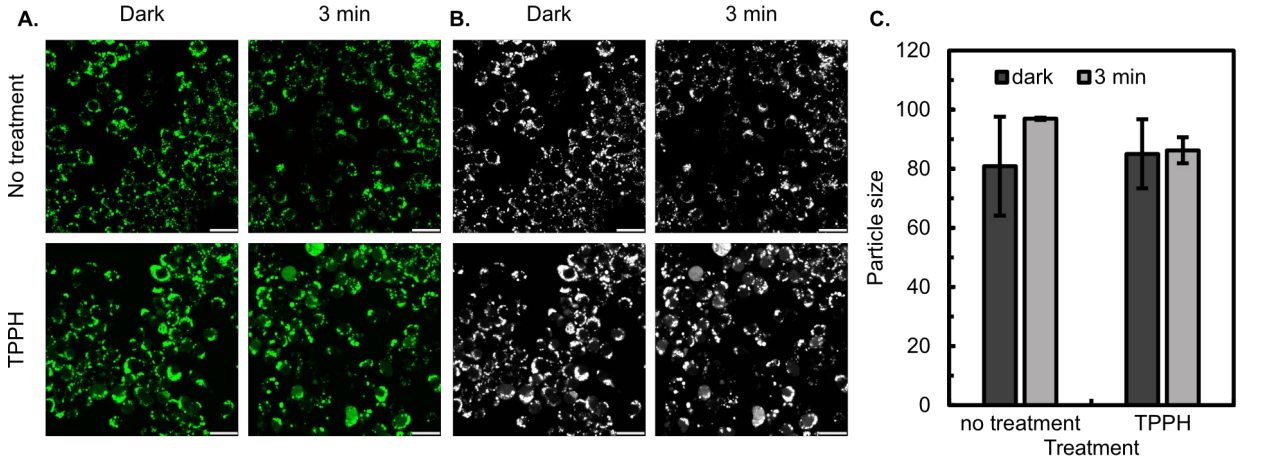

Figure 5.31. Confocal microscopy visualizing endosomal disruption via calcein (**5.1**) staining of RAW cells. (A) Single channel microscopy of calcein stained lysosomes (green). (B) Black and white images of A. (C) Quantification of lysosome size of cells treated with media (no treat) or PFC nanoemulsions containing TPPH (TPPH) in the dark (dark gray) or after 1 min irradiation (light gray). Bars represent the average of three representative images and error bars represent the standard deviation of 3 images.

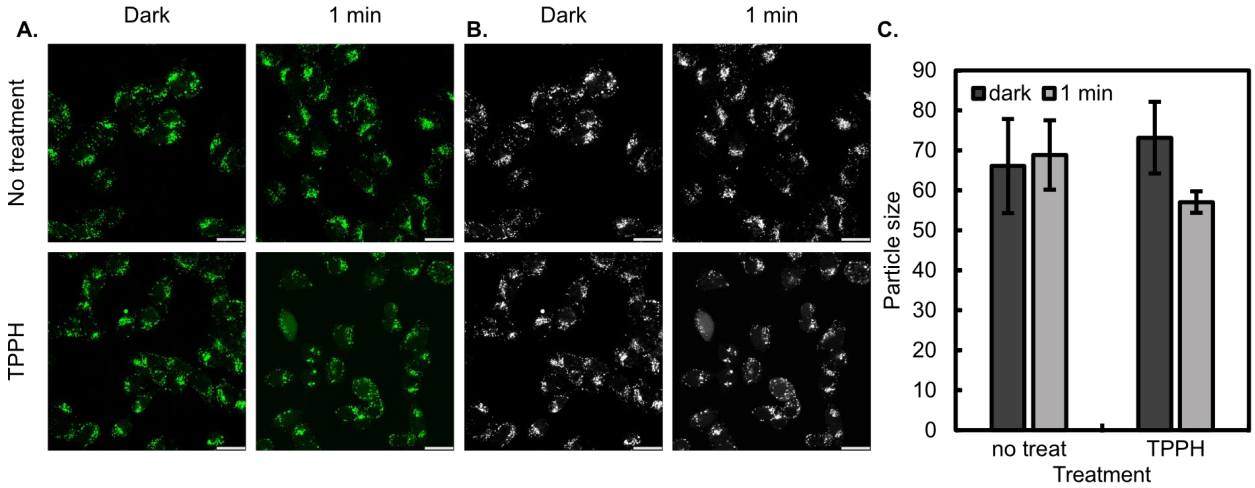

Figure 5.32. Confocal microscopy visualizing endosomal disruption via calcein (**5.1**) staining of A375 cells. (A) Single channel microscopy of calcein stained lysosomes (green). (B) Black and white images of A. (C) Quantification of lysosome size of cells treated with media (no treat) or PFC nanoemulsions containing TPPH (TPPH) in the dark (dark gray) or after 1 min irradiation (light gray). Bars represent the average of three representative images and error bars represent the standard deviation of 3 images.

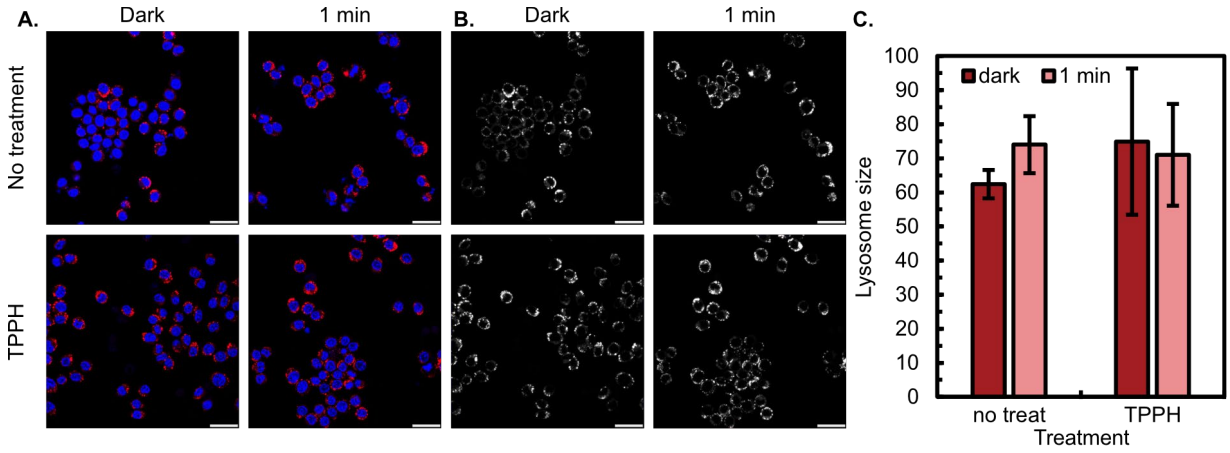

Figure 5.33. Confocal microscopy visualizing endosomal disruption via LysoTracker red staining of RAW cells. (A) Single channel microscopy of LysoTracker stained lysosomes (red), nuclei are stained with Hoescht (blue). (B) Black and white images of lysosomes stained with LysoTracker. (C) Quantification of lysosome size of cells treated with media (no treat) or PFC nanoemulsions containing TPPH (TPPH) in the dark (dark red) or after 1 min irradiation (pink). Bars represent the average of three representative images and error bars represent the standard deviation of 3 images.

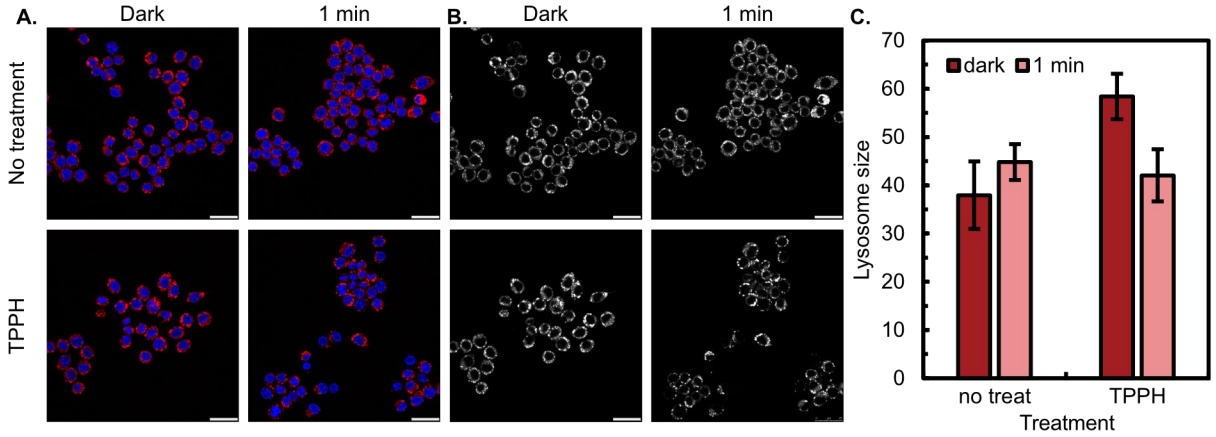

Figure 5.34. Confocal microscopy visualizing endosomal disruption via LysoTracker red staining of RAW cells. (A) Single channel microscopy of LysoTracker stained lysosomes (red), nuclei are stained with Hoescht (blue). (B) Black and white images of lysosomes stained with LysoTracker. (C) Quantification of lysosome size of cells treated with media (no treat) or PFC nanoemulsions containing TPPH (TPPH) in the dark (dark red) or after 1 min irradiation (pink). Bars represent the average of three representative images and error bars represent the standard deviation of 3 images.

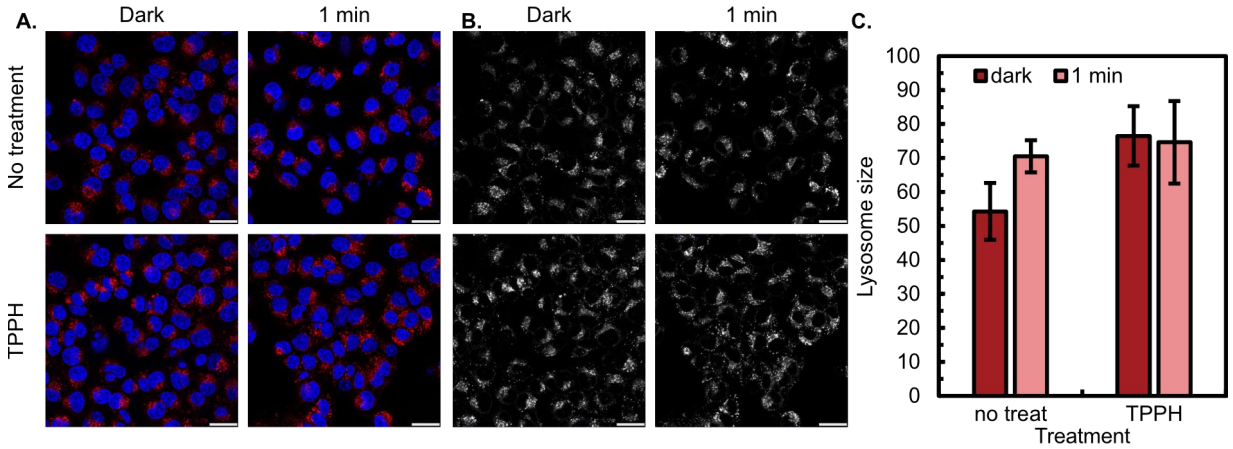

Figure 5.35. Confocal microscopy visualizing endosomal disruption via LysoTracker red staining of A375 cells. (A) Single channel microscopy of LysoTracker stained lysosomes (red), nuclei are stained with Hoescht (blue). (B) Black and white images of lysosomes stained with LysoTracker. (C) Quantification of lysosome size of cells treated with media (no treat) or PFC nanoemulsions containing TPPH (TPPH) in the dark (dark red) or after 1 min irradiation (pink). Bars represent the average of three representative images and error bars represent the standard deviation of 3 images.

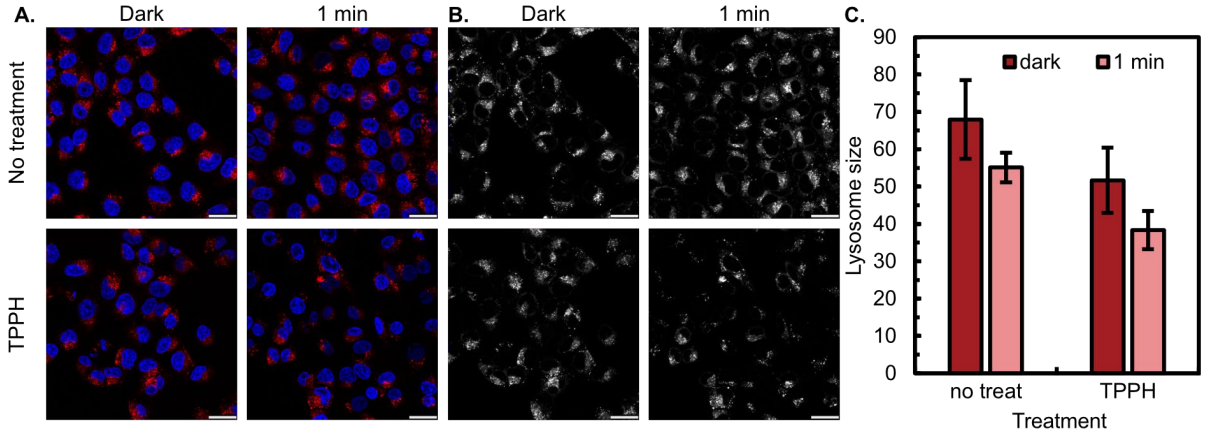

Figure 5.36. Confocal microscopy visualizing endosomal disruption via LysoTracker red staining of A375 cells. (A) Single channel microscopy of LysoTracker stained lysosomes (red), nuclei are stained with Hoescht (blue). (B) Black and white images of lysosomes stained with LysoTracker. (C) Quantification of lysosome size of cells treated with media (no treat) or PFC nanoemulsions containing TPPH (TPPH) in the dark (dark red) or after 1 min irradiation (pink). Bars represent the average of three representative images and error bars represent the standard deviation of 3 images.

5.4 Conclusion

Here, we discuss a variety of methods to visualize endosomal disruption in an effort to decouple endosomal rupture from the release of payload. We use three different assays, calcein dye dilution, lysosome size and direct visualization of endosomal disruption with a genetically engineered cell line. Calcein, although a finicky assay, is still viable to visualize endosomal swelling in osmotic rupture and can be used to visualize loss of endosomal membrane integrity via PCI, though faint cytosolic labeling was observed in our hands. When inducing endosomal escape via osmotic rupture, lysosome size is an easily monitored parameter that can be visualized with various LysoTracker probes. Importantly, this approach is applicable to many different cell types and can be used in combination with standard fluorescent proteins. Genetically engineered cell lines can visualize the endosomal disruption, regardless of method of disruption; however, these experiments are limited to the spectral properties of genetically encoded fluorescent protein. An additional limitation of the genetically engineered cell line is the cell type of relevance to one's experiment may be different from the MDA-MB-231 cell line, meaning endosomal disruption conditions may not translate. Nevertheless, we have found the MDA-MB-231 cells to be an advantageous cell line to begin endosomal escape studies with and highly recommend this cell line developed by Duvall to all struggling to optimize endosomal escape.

5.5 Experimental Procedures

5.5.1 General experimental procedures

Chloroquine diphosphate (**5.2**) was purchased from VWR (Cat # 102624-086), TAT-HA2 (**5.3**) was purchased from VWR (Cat # 103008-568) and used without further purification.

5.5.2 General cell culture procedures

RAW264.7 cells were purchased from ATCC (Cat# TIB-71). A375 cells were purchased from ATCC (Cat# CRL-1619). MDA-MB-231 Gal8-YFP cells were a gift from Craig Duvall's lab at Vanderbilt University.

RAW264.7 and A375 cells were cultured in Dulbecco's Modified Eagle Media (DMEM, Life Technologies, cat# 11995073) supplemented with 10% fetal bovine serum (Corning, lot# 35016109) and 1% penicillin-streptomycin (Life Technologies, cat# 15070063). MDA-MB-231 cells were cultured in Dulbecco's Modified Eagle Media (DMEM, Life Technologies, cat# 11995073) supplemented with 10% fetal bovine serum (Corning, lot# 35016109) and 1% gentamicin (Fisher, cat# 50-983-231). Cells were washed with PBS, or lithium chloride buffer (LiCl: 0.25 M LiCl, 1 mM EDTA, 10 mM Tris-HCl). Cells were incubated at 37 ˚C, 5% CO_2, during treatments and throughout culturing, in HERACell 150i CO2 incubators. Cells were pelleted through use of Sorvall ST 40R centrifuge. All cell work was performed in 1300 Series A2 biosafety cabinets.

Confocal microscopy was performed on a TCS SPE Leica confocal microscope containing 405 nm, 488 nm, 532 nm and 635 nm lasers.

5.5.3 Live cell imaging procedures

Following treatment, washes, and staining, cells were placed in complete DMEM (10% FBS, 1% PenStrep or gentamicin) and transferred to the microscope. Cells were imaged in <1 h to prevent cell death.

All images were acquired with 63x oil objective and 1024 x 1024 resolution.

Confocal microscopy was performed on a TCS SPE Leica confocal microscope containing 405 nm, 488 nm, 532 nm and 635 nm lasers. Confocal settings were as follows: Hoechst (405 laser-50%, 800 gain, offset -0.35, collection 410-470nm), LysoTracker green and calcein (488 laser-50%, 900 gain, offset -0.35, collection 495-525 nm), LysoTracker red (532 laser-50%, 800 gain, offset -0.35, collection 560-700nm), DIC (scan-BF, 450 gain, offset -0.4). Scale bar represents 25 μm.

5.5.4 General nanoemulsion formation procedure

Polymer surfactant (5.6 mg, 2.8 wt%) was dissolved in cosolvent (20 μL, DMF, MeOH or THF) and sonicated in a bath sonicator (~15 minutes) until fully dissolved, at which point 7:3 perfluorodecalin : perfluorotripropylamine (10 vol%, 20 μL) was added, followed by PBS buffer pH 7.4 (200 μL). Sonication was performed by lowering the probe directly at the liquid-liquid interface of the two immiscible solvents (90s, 35% amp). To remove cosolvents, emulsions are washed by centrifugation (5.6 x *g*, 3 min, 2x).

TPPH (**5.4**) was incorporated into nanoemulsions by taking 100 mL of emulsions, adding 2 mL of TPPH stock (1 mg/mL in acetone) and sonicating for a further 90s at 35% amp.

5.5.5 PCI Endosomal Disruption

PFC nanoemulsions were made following the **General nanoemulsion formation procedure** containing TPPH. TPPH (**5.4**) was incorporated into nanoemulsions by taking 100 mL of emulsions, adding 2 mL of TPPH stock (1 mg/mL in acetone) and sonicating for a further 90s at 35% amp.

RAW264.7 or A375 cells were plated 100,000 cells/well on two identical Ibidi m-slide 8 well (IbiTreat, Cat # 80826), and allowed to adhere overnight. The next day, media was removed and replaced with complete media and emulsions containing **5.4** (10 mL) and incubated (3h, 37 °C, 5% CO_2). After incubation, cells were washed gently 3x with LiCl buffer and slight rocking, 1x complete media with slight rocking. Nuclei were stained with Hoescht (3.24 μM, 10 min, 37 ˚C, ThermoFisher Cat# PI62249). Hoescht staining was removed, and one plate was irradiated (THORLabs, 420 nm, 8.5 mW/cm^2, 1 min), while the other was kept in the dark. After irradiation LysoTracker (LysoTracker green (50 nM, Cell Signaling Technologies Cat# 8783S), or LysoTracker red (50 nM, Fisher Cat# L7528)) was added and imaged to prevent excess photobleaching of lysosome stain during imaging.

5.6 ImageJ Analysis

5.6.1 Lysosome size

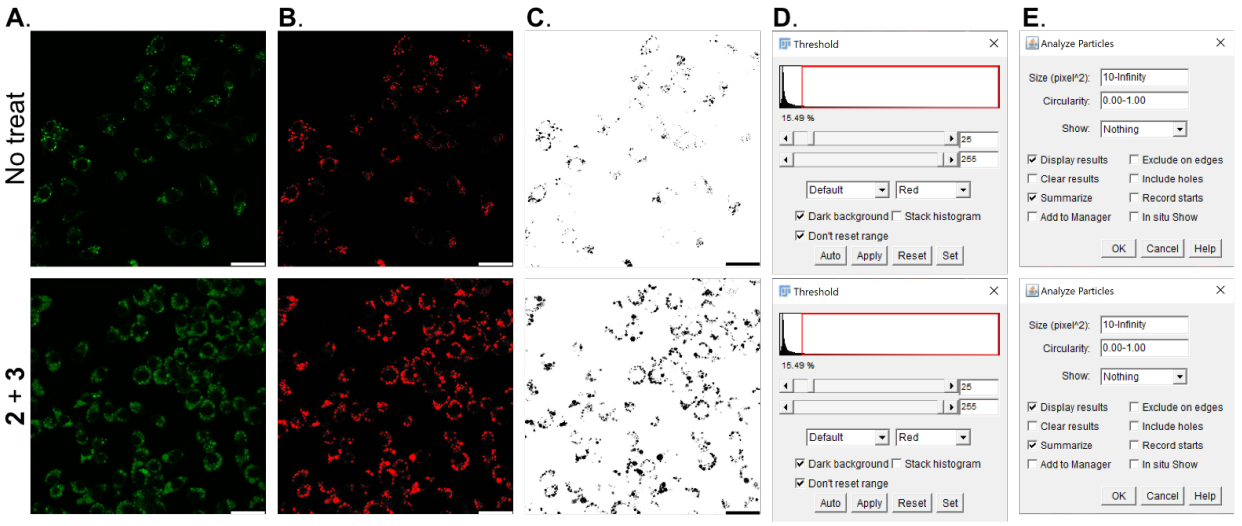

F.

Slice	Count	Total Area	Average Size	%Area	Mean	Perim.	Median
Lyso - no treat - Series009 threshold.jpg	286	12684	44.350	1.210	255	29.774	255
Lyso - CQ+TAT-HA2 - Series014 - imagej example threshold bw.jpg	515	51262	99.538	4.889	255	58.668	255

ImageJ analysis of all confocal images.

A) RGB images of LysoTracker green images seen in Figure 5.2C.

B) Threshold images (settings in D) prior to clicking apply. This is done such that the lysosomes (seen in red) can be counted. Only those particles shown in red are analyzed. The threshold was chosen to reduce the amount of background and then kept constant for each experimental set analyzed.

C) Threshold images (settings in D) after clicking apply.

D) Threshold settings for each image were kept constant.

E) Analysis of particles (on images represented by C). Particles larger than 10 pixel^2 were analyzed.

F) Readout of analysis gives number (count), total area, average size, % area, mean, perimeter, and median of all particles in C. The average size was averaged for 3 representative images for each graph (Figure 5.2/5.3 D and throughout the Supplemental).

Analysis of lysosome size was inspired by Verkman and Braeckmans.[19,22]

To quantify the size of lysosomes, we used ImageJ "Threshold" and "Analyze Particles." All images were treated identically, with all ImageJ settings kept constant in order to compare between treatments and images. The single-color image of the lysosomes (calcein, LysoTracker green as seen above in A, or LysoTracker red) were used as raw data files. This image was then converted from the RGB (A) to an 8-bit image. A constant threshold (D) was applied as seen in B and C. After the black and white thresholded image (C) was produced, we used the "Analyze Particles" plug-in to measure the average size of all particles seen in C. ImageJ produced the data from this plug-in as seen in F. For all graphs displaying the "Particle size" of the lysosomes, the "average size" as seen in F was averaged for three independent images. The error was determined by the standard deviation of the "average size" as seen in F for three independent images.

Scale bar represents 25 μm.

5.6.2 Gal8-YFP puncta : nuclear quantification

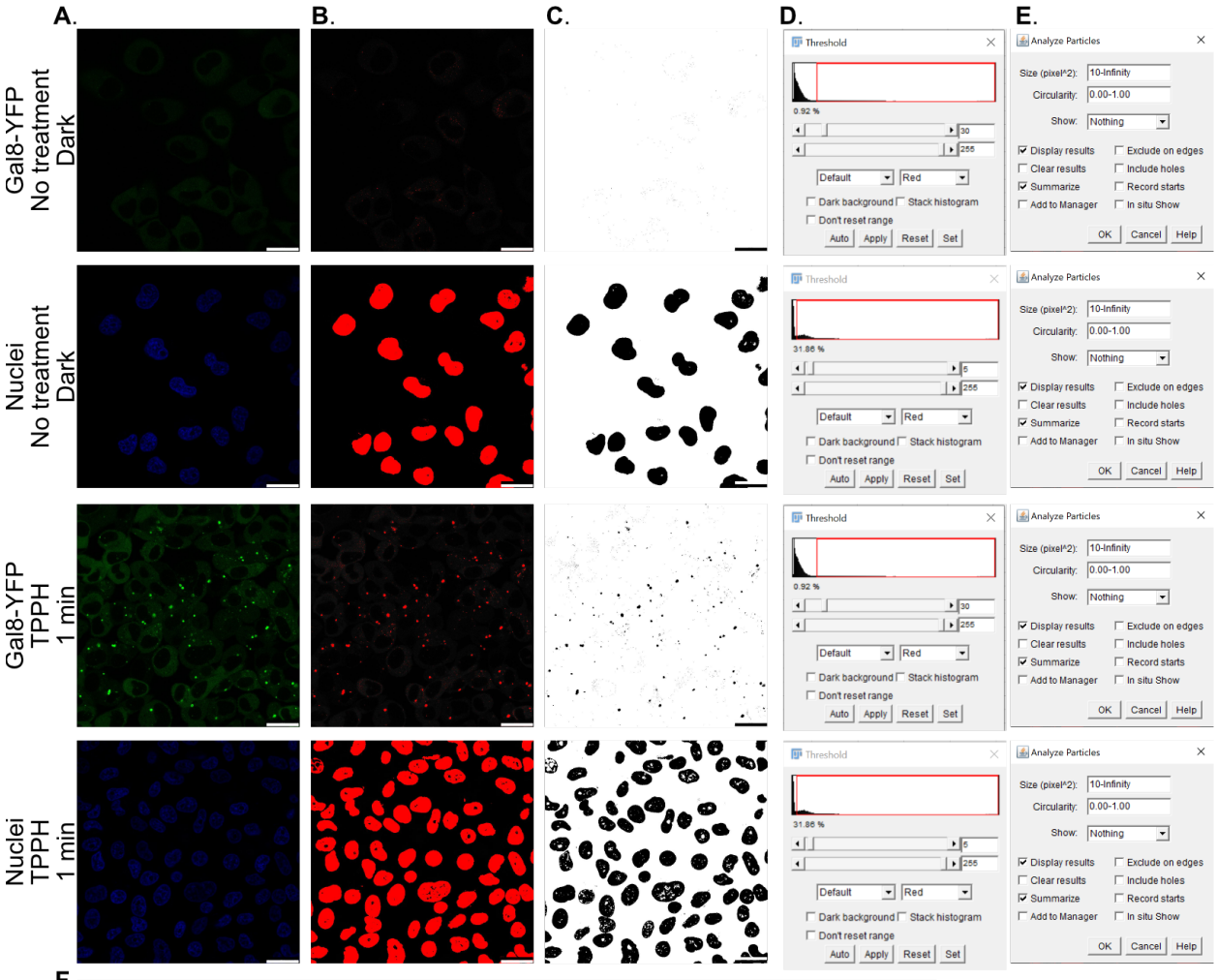

F.

Slice	Count	Total Area	Average Size	%Area	Mean
MDA - no treat - dark - Series005 - RGD.jpg	8	472	59.000	0.045	255
MDA - no treat - dark - Series005 Hoescht - threshold settings.jpg	29	134051	4622.448	12.784	255
MDA - TPPH - 1 min - Series019 - RGD.jpg	133	7486	56.286	0.714	255
MDA - TPPH - 1 min - Series019 nuclei - bw.jpg	92	308417	3352.359	29.413	255

ImageJ analysis of all confocal images.

A) RGB images of Gal8-YFP (green) and nuclei (blue) images seen in Figure 5.22C.

B) Threshold images (settings in D) prior to clicking apply. The threshold settings in D were set such that the diffuse Gal8-YFP staining was below the limit (see first row compared to third row).

C) Threshold images (settings in D) after clicking apply.

D) Threshold settings for each image were kept constant for all Gal8 or nuclear images.

E) Analysis of particles (on images represented by C). Particles larger than 10 pixel^2 were analyzed.

F) Readout of analysis gives number (count), total area, average size, % area, mean, perimeter, and median of all particles in C. The average size was averaged for 3 representative images for each graph (Figure 5.2/5.22 D and throughout the Supplemental).

To quantify the number of puncta, we used ImageJ "Threshold" and "Analyze Particles." All images were treated identically, with all ImageJ settings kept constant in order to compare between treatments and images. The single-color image of Gal8-YFP was used as raw data files. This image was then converted from the RGB (A) to an 8-bit image. A constant threshold (D) was applied as seen in B and C. After the black and white thresholded image (C) was produced, we used the "Analyze Particles" plug-in to count the number of all particles seen in C. ImageJ produced the data from this plug-in as seen in F.

The count for Gal8-YFP puncta was then divided by the count for the number of nuclei. Sample calculation:

$$Puncta : nuclear\ ratio = \frac{8\ (punta\ in\ line\ 1)}{29\ (nuclei\ in\ line\ 2)} = 0.28 \qquad (5.1)$$

This was inspired by a Matlab code written by Duvall and coworkers that identified and counted the number of puncta when endosomes were disrupted.[20]

Scale bar represents 25 μm.

5.7 Figure experimental procedures

Figure 5.2C-E

RAW264.7 cells (ATCC Cat# TIB-71) or MDA-MB-231 Gal8-YFP cells (gift from Duvall lab) were plated on Ibidi m-slide 8 well, IbiTreat (Cat # 80826), and allowed to adhere overnight. The next day, media was removed and replaced with treatment. No treatment wells: 200 μL media; **5.2**+**5.3** wells: 160 mL media, 40 mL Chloroquine (**5.2,** 100 mM; 500 mM stock, made fresh in complete media), 10 mL TAT-HA2 (**5.3,** 14.5 mM), 10 mL emulsions. **5.3** and emulsions were pre-mixed for ~5 min at room temperature before being added to the labelled well. The cells and treatment were incubated for 3 h (37 ˚C, 5% CO_2).

For cells stained with calcein (**5.1**, 150 mM): 60 mL (500 mM stock, made fresh in DI H_2O, Fisher Cat# ICN19508701) was added to the cells at the time of treatment, with a total volume of 200 mL of complete media + treatment).

After incubation, cells were washed gently 3x with LiCl buffer and slight rocking, 1x complete media with slight rocking. Nuclei were stained with Hoescht (3.24 μM, 10 min, 37 ˚C, ThermoFisher Cat# PI62249), LysoTracker green (50 nM, Cell Signaling Technologies Cat# 8783S), or LysoTracker red (50 nM, Fisher Cat# L7528). Hoescht staining was removed and replaced with LysoTracker staining and imaged to prevent excess photobleaching of lysosome stain during imaging.

Confocal microscopy was performed on a TCS SPE Leica confocal microscope containing 405 nm, 488 nm, 532 nm and 635 nm lasers. Confocal settings were as follows: Hoechst (405 laser-

50%, 800 gain, offset -0.35, collection 410-470nm), LysoTracker green and calcein (488 laser-50%, 900 gain, offset -0.35, collection 495-525 nm), LysoTracker red (532 laser-50%, 800 gain, offset -0.35, collection 560-700nm), DIC (scan-BF, 450 gain, offset -0.4). Scale bar represents 25 μm.

Images were processed in ImageJ. To quantify the size of the lysosomes stained by calcein, LysoTracker green or LysoTracker red, a constant threshold of each image was made, then the particles were analyzed for average size (See **ImageJ Analysis**). Each bar is an average of 3 individual images, and the error bars represent the standard deviation of three images. Significance was determined with a one-tailed Student's T test of unequal variance compared to no treatment controls.

Figure 5.3-5.4.

RAW264.7 cells (ATCC Cat# TIB-71) were plated on Ibidi m-slide 8 well (100,000 cells/well), IbiTreat (Cat # 80826), and allowed to adhere overnight. The next day, media was removed and replaced with treatment. RAW cells were treated with media (no treatment), emulsions (Pluronic F-68, 2.8 wt%; 7:3 PFD : PFTPA, 10 vol%) or combination of emulsions, and chloroquine (**5.2**, 100 mM). **2** treatment was added 0.5 h prior to emulsions (-0.5), at the same time as emulsions (+0) or 1 h post emulsions (+1). Calcein (**5.1**, 150 mM, green) was added at the same time as the emulsions / endosomal disruption treatment. Following treatment, cells were washed (3x LiCl buffer, 1x media).

Cells were then imaged in complete media – see **Live cell imaging procedure**. Cells were imaged via excitation at 488 nm to visualize calcein. Scale bars represent 25 μm.

Figure 5.5.

RAW264.7 cells (ATCC Cat# TIB-71) were plated on Ibidi m-slide 8 well (100,000 cells/well), IbiTreat (Cat # 80826), and allowed to adhere overnight. The next day, media was removed and replaced with treatment. RAW cells were treated with emulsions (Pluronic F-68, 2.8 wt%; 7:3 PFD : PFTPA, 10 vol%) or combination of emulsions, chloroquine (**5.2**, 100 mM) and cationic, cell penetrating peptide TAT-HA2 (**5.3**, 14.5 mM) for 3 h (37 ˚C, 5% CO_2). Calcein (**5.1**, 150 mM, green) was added at the same time as the emulsions / endosomal disruption treatment. Following treatment, cells were washed (3x LiCl buffer, 1x media) and stained with Hoescht (blue) in complete media for 10 min.

Cells were then imaged in complete media – see **Live cell imaging procedure**. Cells were imaged via excitation at 405 nm to visualize Hoescht, 488 nm to visualize calcein, and merged. Scale bars represent 25 μm.

Figure 5.6.

RAW264.7 cells (ATCC Cat# TIB-71) were plated on flat bottom 96-well plate (100,000 cells/well) (Fisher Cat # 07-201-94), and allowed to adhere overnight. The next day, media was removed and replaced with treatment. No treatment wells: 200 mL media; **5.2**+**5.3** wells: 160 mL media, 40 mL **5.2** (500 mM stock, made fresh in media), 10 mL TAT-HA2 (**3**, 14.5 mM), 10 mL emulsions (Pluronic F-68, 2.8 wt%; 7:3 PFD : PFTPA, 10 vol%). **5.3** and emulsions were pre-

mixed for ~5 min at room temperature before being added to the labelled well. The cells and treatment were incubated for 3h (37 ˚C).

Cells were then washed with media 3x, LiCl buffer 3x, PBS 1x, then lifted with trypsin and transferred to a v-bottom 96-well plate (Fisher, Cat# 07-200-96). Cells were washed by centrifugation (2x, 526 x *g*, 3 min) and resuspended in FACS buffer (PBS + 1% FBS) to a final volume of 200 μL. Uptake was analyzed by FL2 channel on a FACSCalibur flow cytometer.

Cells were stained with propidium iodide (2 μL, 1 mg/mL, 15 min) on ice. Viability was analyzed by FL2 channel on a FACSCalibur flow cytometer. 15,000 cells were collected per sample. Error bars represent the standard deviation of three replicate experiments.

Figure 5.7-5.10.

RAW264.7 cells (ATCC Cat# TIB-71) were plated on Ibidi m-slide 8 well (100,000 cells/well), IbiTreat (Cat # 80826), and allowed to adhere overnight. The next day, media was removed and replaced with treatment. RAW cells were treated with emulsions (Pluronic F-68 (S6), $Me_{30}Non_{10}$ (S7-S9), 2.8 wt%; 7:3 PFD : PFTPA, 10 vol%) or combination of emulsions, chloroquine (**5.2**, 100 mM) and cationic, cell penetrating peptide TAT-HA2 (**5.3**, 14.5 mM) for 3 h (37 ˚C, 5% CO_2). Following treatment, cells were washed (3x LiCl buffer, 1x media) and stained with Hoescht (blue) in complete media for 10 min followed by LysoTracker green (50 nM) and imaged with the stain on the cells the prevent photobleaching.

Cells were then imaged in complete media – see **Live cell imaging procedure**. Cells were imaged via excitation at 405 nm to visualize Hoescht, 488 nm to visualize LysoTracker green, and merged. Black and white images of LysoTracker green are below the merged images. Scale bars represent 25 μm.

Figure 5.11-5.12.

RAW264.7 cells (ATCC Cat# TIB-71) were plated on Ibidi m-slide 8 well (100,000 cells/well), IbiTreat (Cat # 80826), and allowed to adhere overnight. The next day, media was removed and replaced with treatment. RAW cells were treated with media (no treatment), emulsions ($Me_{30}Non_{10}$, 2.8 wt%; 7:3 PFD : PFTPA, 10 vol%) or combination of emulsions, chloroquine (**5.2**, 100 mM) and cationic, cell penetrating peptide TAT-HA2 (**5.3**, 14.5 mM) for 3 h (37 ˚C, 5% CO_2). Following treatment, cells were washed (3x LiCl buffer, 1x media) and stained with Hoescht (blue) in complete media for 10 min followed by LysoTracker red (50 nM) and imaged with the stain on the cells the prevent photobleaching.

Cells were then imaged in complete media – see **Live cell imaging procedure**. Cells were imaged via excitation at 405 nm to visualize Hoescht, 532 nm to visualize LysoTracker red, and merged. Scale bars represent 25 μm.

Figure 5.13-5.15.

A375 cells (ATCC Cat# CRL-1619) were plated on Ibidi m-slide 8 well (100,000 cells/well), IbiTreat (Cat # 80826), and allowed to adhere overnight. The next day, media was removed and replaced with treatment. A375 cells were treated with media (no treatment), emulsions

($Me_{30}Non_{10}$, 2.8 wt%; 7:3 PFD : PFTPA, 10 vol%) or combination of emulsions, chloroquine (**5.2**, 100 mM) and cationic, cell penetrating peptide TAT-HA2 (**5.3**, 14.5 mM) for 3 h (37 ˚C, 5% CO_2). Following treatment, cells were washed (3x LiCl buffer, 1x media) and stained with Hoescht (blue) in complete media for 10 min followed by LysoTracker green (50 nM) and imaged with the stain on the cells the prevent photobleaching.

Cells were then imaged in complete media – see **Live cell imaging procedure**. Cells were imaged via excitation at 405 nm to visualize Hoescht, 488 nm to visualize LysoTracker green, and merged. Scale bars represent 25 μm.

Figure 5.16-5.18.

A375 cells (ATCC Cat# CRL-1619) were plated on Ibidi m-slide 8 well (100,000 cells/well), IbiTreat (Cat # 80826), and allowed to adhere overnight. The next day, media was removed and replaced with treatment. A375 cells were treated with media (no treatment), emulsions ($Me_{30}Non_{10}$, 2.8 wt%; 7:3 PFD : PFTPA, 10 vol%) or combination of emulsions, chloroquine (**5.2**, 100 mM) and cationic, cell penetrating peptide TAT-HA2 (**5.3**, 14.5 mM) for 3 h (37 ˚C, 5% CO_2). Following treatment, cells were washed (3x LiCl buffer, 1x media) and stained with Hoescht (blue) in complete media for 10 min followed by LysoTracker red (50 nM) and imaged with the stain on the cells to prevent photobleaching.

Cells were then imaged in complete media – see **Live cell imaging procedure**. Cells were imaged via excitation at 405 nm to visualize Hoescht, 532 nm to visualize LysoTracker red, and merged. Scale bars represent 25 μm.

Figure 5.19.

MDA-MB-231 Gal8-YFP (gift from Duvall lab) were plated on Ibidi m-slide 8 well (100,000 cells/well), IbiTreat (Cat # 80826), and allowed to adhere overnight. The next day, media was removed and replaced with treatment. MDA-MB-231 Gal8-YFP cells were treated with media (no treatment), emulsions ($Me_{30}Non_{10}$, 2.8 wt%; 7:3 PFD : PFTPA, 10 vol%) or combination of emulsions, chloroquine (**5.2**, 100 mM) and cationic, cell penetrating peptide TAT-HA2 (**5.3**, 14.5 mM) for 3 h (37 ˚C, 5% CO_2). **2** treatment was added 0.5 h prior to emulsions (-0.5), at the same time as emulsions (+0) or 1 h post emulsions (+1). Following treatment, cells were washed (3x LiCl buffer, 1x media) and stained with Hoescht (blue) in complete media for 10 min followed by LysoTracker red (50 nM) and imaged with the stain on the cells the prevent photobleaching.

Cells were then imaged in complete media – see **Live cell imaging procedure**. Cells were imaged via excitation at 405 nm to visualize Hoescht, 488 nm to visualize Gal8, 532 nm to visualize LysoTracker red, and merged. Scale bars represent 25 μm.

Figure 5.20-5.21.

MDA-MB-231 Gal8-YFP (gift from Duvall lab) were plated on Ibidi m-slide 8 well (100,000 cells/well), IbiTreat (Cat # 80826), and allowed to adhere overnight. The next day, media was removed and replaced with treatment. MDA-MB-231 Gal8-YFP cells were treated with media (no treatment), emulsions ($Me_{30}Non_{10}$, 2.8 wt%; 7:3 PFD : PFTPA, 10 vol%) or combination of emulsions, chloroquine (**5.2**, 100 mM) and cationic, cell penetrating peptide TAT-HA2 (**5.3**, 14.5 mM) for 3 h (37 ˚C, 5% CO_2). Following treatment, cells were washed (3x LiCl buffer, 1x

media) and stained with Hoescht (blue) in complete media for 10 min followed by LysoTracker red (50 nM) and imaged with the stain on the cells the prevent photobleaching.

Cells were then imaged in complete media – see **Live cell imaging procedure**. Cells were imaged via excitation at 405 nm to visualize Hoescht, 488 nm to visualize Gal8, 532 nm to visualize LysoTracker red, and merged. Scale bars represent 25 μm.

Figure 5.22C-E

RAW264.7 cells (ATCC Cat# TIB-71) or MDA-MB-231 Gal8-YFP cells (gift from Duvall lab) were plated on Ibidi m-slide 8 well, IbiTreat (Cat # 80826), and allowed to adhere overnight. The next day, media was removed and replaced with treatment. No treatment wells: 200 mL media; TPPH (**4**) wells: 190 mL media, 10 mL emulsions (described in General nanoemulsion formation procedure). This was repeated on two plates – one for dark images, and one for irradiation.

For cells stained with calcein (**5.1**, 150 mM): 60 mL (500 mM stock, made fresh in DI H_2O, Fisher Cat# ICN19508701) was added to the cells at the time of treatment, with a total volume of 200 mL of complete media + treatment). The cells and treatment were incubated for 3h (37 ˚C).

After incubation, cells were washed gently 3x with LiCl buffer and slight rocking, 1x complete media with slight rocking. Nuclei were stained with Hoescht (3.24 μM, 10 min, 37 ˚C, ThermoFisher Cat# PI62249), LysoTracker green (50 nM, Cell Signaling Technologies Cat# 8783S), or LysoTracker red (50 nM, Fisher Cat# L7528). Hoescht staining was removed, and the plate for irradiation for irradiated (THORLabs, 420 nm, 8.5 mW/cm^2, 1 min). After irradiation LysoTracker staining was added and imaged to prevent excess photobleaching of lysosome stain during imaging.

Confocal microscopy was performed on a TCS SPE Leica confocal microscope containing 405 nm, 488 nm, 532 nm and 635 nm lasers. Confocal settings were as follows: Hoechst (405 laser-50%, 800 gain, offset -0.35, collection 410-470nm), LysoTracker green and calcein (488 laser-50%, 900 gain, offset -0.35, collection 495-525 nm), LysoTracker red (532 laser-50%, 800 gain, offset -0.35, collection 560-700nm), DIC (scan-BF, 450 gain, offset -0.4). Scale bar represents 25 μm.

Images were processed in ImageJ. To quantify the size of the lysosomes stained by calcein, LysoTracker green or LysoTracker red, a constant threshold of each image was made, then the particles were analyzed for average size (See **ImageJ Analysis**). Each bar is an average of 3 individual images, and the error bars represent the standard deviation of three images. Significance was determined with a one-tailed Student's T test of unequal variance compared to no treatment controls.

Figure 5.23.

RAW264.7 cells (ATCC Cat# TIB-71) and A375 cells (ATCC Cat# CRL-1619) were plated 100,000 cells / well in a flat bottom 96-well plate (Fisher Cat # 07-201-94) and allowed to adhere overnight. The next day, media was removed, replaced with complete DMEM (200 mL) and emulsions containing TPPH (10 mL). Cells were incubated for 3 h with treatment (37 °C, 5% CO_2). Following treatment cells were washed 3x with complete media, with rocking. Cells were then lifted via trypsonization and transferred to a 96-well v-bottom (Fisher, Cat # 07-200-96) and washed 1x by centrifugation.

Cells were resuspended in 200 mL FACS buffer (PBS + 1% FBS), and one plate was irradiated (1 min, 420 nm, 8.5 mW / cm^2). Cells were then transferred to FACS tubes, and stained with propidium iodide (VWR Cat # 89139-064) (2 mL, 1 mg/mL stock) and incubated on ice for 15 min. Cells were then analyzed for FL2 fluorescence. Cells were considered alive if they were not fluorescent ($<10^2$), and cells were considered dead if they were fluorescent ($>10^2$).

Figure 5.24-5.26.

MDA-MB-231 Gal8-YFP (gift from Duvall lab) were plated on Ibidi m-slide 8 well (100,000 cells/well), IbiTreat (Cat # 80826), and allowed to adhere overnight. The next day, media was removed and replaced with treatment. No treatment wells: 200 mL media; TPPH wells: 190 mL media, 10 mL emulsions (described in General nanoemulsion formation procedure). This was repeated on two plates – one for dark images, and one for irradiation. Following treatment, cells were washed (3x LiCl buffer, 1x media) and stained with Hoescht (blue) in complete media for 10 min followed by LysoTracker red (50 nM) and imaged with the stain on the cells to prevent photobleaching.

After incubation, cells were washed gently 3x with LiCl buffer and slight rocking, 1x complete media with slight rocking. Nuclei were stained with Hoescht (3.24 μM, 10 min, 37 ˚C, ThermoFisher Cat# PI62249). Hoescht staining was removed, and the plate for irradiation for irradiated (THORLabs, 420 nm, 8.5 mW/cm^2, 1 min).

Cells were then imaged in complete media – see **Live cell imaging procedure**. Cells were imaged via excitation at 405 nm to visualize Hoescht, 488 nm to visualize Gal8 and merged. Scale bars represent 25 μm.

Figure 5.27-5.29.

MDA-MB-231 Gal8-YFP (gift from Duvall lab) were plated on Ibidi m-slide 8 well (100,000 cells/well), IbiTreat (Cat # 80826), and allowed to adhere overnight. The next day, media was removed and replaced with treatment. No treatment wells: 200 mL media; TPPH wells: 190 mL media, 10 mL emulsions (described in General nanoemulsion formation procedure). This was repeated on two plates – one for dark images, and one for irradiation. Following treatment, cells were washed (3x LiCl buffer, 1x media) and stained with Hoescht (blue) in complete media for 10 min followed by LysoTracker red (50 nM) and imaged with the stain on the cells to prevent photobleaching.

Cells were then imaged in complete media – see **Live cell imaging procedure**. Cells were imaged via excitation at 405 nm to visualize Hoescht, 488 nm to visualize Gal8, 532 nm to visualize LysoTracker red, and merged. Scale bars represent 25 μm.

Figure 5.30-5.31.

RAW264.7 cells (ATCC Cat# TIB-71) were plated on Ibidi m-slide 8 well, IbiTreat (Cat # 80826), and allowed to adhere overnight. The next day, media was removed and replaced with treatment. No treatment wells: 200 mL media; TPPH wells: 190 mL media, 10 mL emulsions (described in

General nanoemulsion formation procedure). This was repeated on two plates – one for dark images, and one for irradiation.

Cells were stained with calcein (**5.1**): 60 mL (500 mM stock, made fresh in DI H_2O, Fisher Cat# ICN19508701) was added to the cells at the time of treatment, with a total volume of 200 mL of complete media + treatment). The cells and treatment were incubated for 3h (37 ˚C).

After incubation, cells were washed gently 3x with LiCl buffer and slight rocking, 1x complete media with slight rocking. Nuclei were stained with Hoescht (3.24 μM, 10 min, 37 ˚C, ThermoFisher Cat# PI62249). Hoescht staining was removed, and the plate for irradiation for irradiated (THORLabs, 420 nm, 8.5 mW/cm^2, 1 min).

Figure 5.32.

A375 cells (ATCC Cat# CRL-1619) were plated on Ibidi m-slide 8 well, IbiTreat (Cat # 80826), and allowed to adhere overnight. The next day, media was removed and replaced with treatment. No treatment wells: 200 mL media; TPPH wells: 190 mL media, 10 mL emulsions (described in General nanoemulsion formation procedure). This was repeated on two plates – one for dark images, and one for irradiation.

Cells were stained with calcein (**5.1**): 60 mL (500 mM stock, made fresh in DI H_2O, Fisher Cat# ICN19508701) was added to the cells at the time of treatment, with a total volume of 200 mL of complete media + treatment). The cells and treatment were incubated for 3h (37 ˚C).

After incubation, cells were washed gently 3x with LiCl buffer and slight rocking, 1x complete media with slight rocking. Nuclei were stained with Hoescht (3.24 μM, 10 min, 37 ˚C,

ThermoFisher Cat# PI62249). Hoescht staining was removed, and the plate for irradiation for irradiated (THORLabs, 420 nm, 8.5 mW/cm^2, 1 min).

Figure 5.33-5.34.

RAW264.7 cells (ATCC Cat# TIB-71) were plated on Ibidi m-slide 8 well, IbiTreat (Cat # 80826), and allowed to adhere overnight. The next day, media was removed and replaced with treatment. No treatment wells: 200 mL media; TPPH wells: 190 mL media, 10 mL emulsions (described in General nanoemulsion formation procedure). This was repeated on two plates – one for dark images, and one for irradiation.

After incubation, cells were washed gently 3x with LiCl buffer and slight rocking, 1x complete media with slight rocking. Nuclei were stained with Hoescht (3.24 μM, 10 min, 37 ˚C, ThermoFisher Cat# PI62249). Hoescht staining was removed, and the plate for irradiation for irradiated (THORLabs, 420 nm, 8.5 mW/cm^2, 1 min). After irradiation LysoTracker red (50 nM) was added and imaged to prevent excess photobleaching of lysosome stain during imaging.

Figure 5.35-5.36.

A375 cells (ATCC Cat# CRL-1619) were plated on Ibidi m-slide 8 well, IbiTreat (Cat # 80826), and allowed to adhere overnight. The next day, media was removed and replaced with treatment. No treatment wells: 200 mL media; TPPH wells: 190 mL media, 10 mL emulsions (described in General nanoemulsion formation procedure). This was repeated on two plates – one for dark images, and one for irradiation.

After incubation, cells were washed gently 3x with LiCl buffer and slight rocking, 1x complete media with slight rocking. Nuclei were stained with Hoescht (3.24 μM, 10 min, 37 ˚C, ThermoFisher Cat# PI62249). Hoescht staining was removed, and the plate for irradiation for irradiated (THORLabs, 420 nm, 8.5 mW/cm^2, 1 min). After irradiation LysoTracker red (50 nM) was added and imaged to prevent excess photobleaching of lysosome stain during imaging.

Cells were then imaged in complete media – see **Live cell imaging procedure**. Cells were imaged via excitation at 405 nm to visualize Hoescht, 532 nm to visualize LysoTracker red and merged. Scale bars represent 25 μm.

5.8 Supplemental figures

5.8.1 FACS histograms

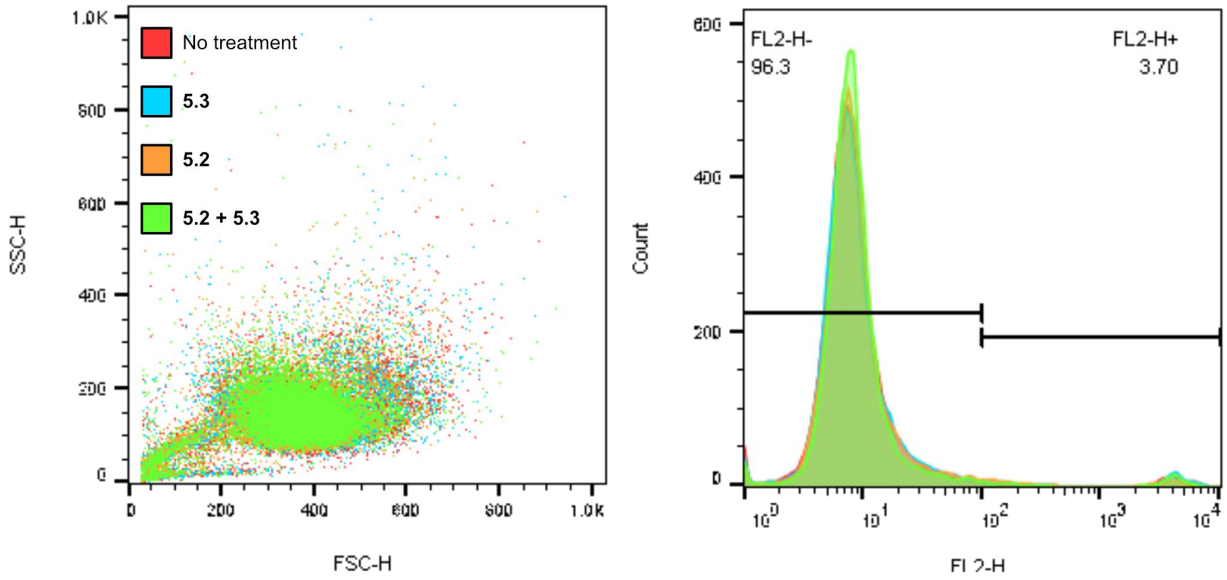

Figure S5.1 Histograms for flow cytometry data in Figure 5.6

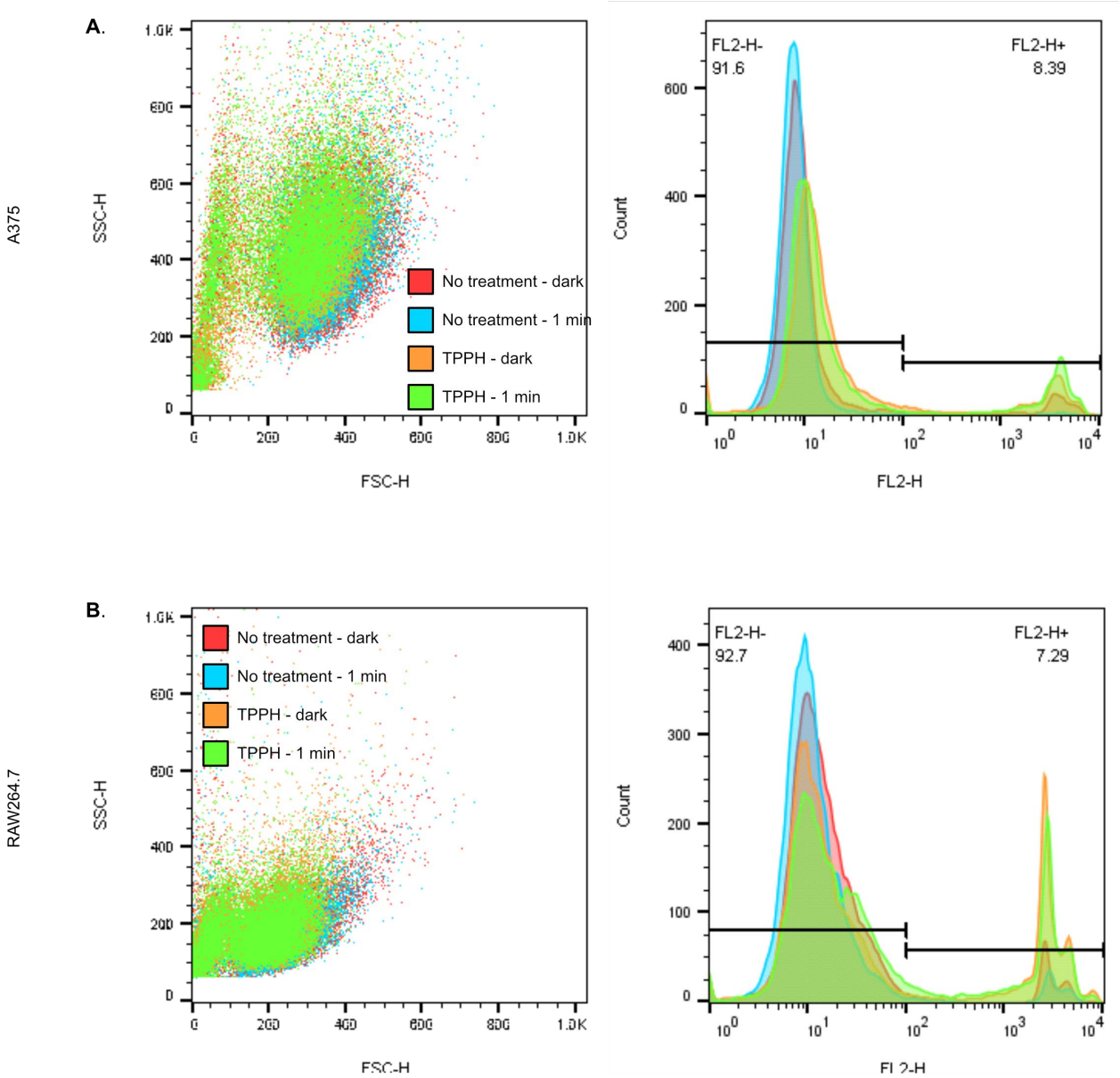

Figure S5.2 Histograms for flow cytometry data in Figure 5.23

5.9 References and Notes

(1) Haute, D. Van; Liu, A. T.; Berlin, J. M. Coating Metal Nanoparticle Surfaces with Small Organic Molecules Can Reduce Nonspecific Cell Uptake. *ACS Nano* **2018**, *12*, 117–127.

(2) Linares, J.; Concepcio, M.; Marques, P. A. A. P.; Portole, M. T. Endocytic Mechanisms of Graphene Oxide Nanosheets in Osteoblasts, Hepatocytes and Macrophages. *ACS Appl. Mater. Interfaces* **2014**, *6*, 13697–13706.

(3) Francia, V.; Yang, K.; Deville, S.; Reker-smit, C.; Nelissen, I.; Salvati, A. Corona Composition Can Affect the Mechanisms Cells Use to Internalize Nanoparticles. *ACS Nano* **2019**, *13*, 11107–11121.

(4) Si, S.; Grant, B. D.; Donaldson, J. G. Pathways and Mechanisms of Endocytic Recycling. *Nat. Rev. Mol. Cell Biol.* **2009**, *10*, 597.

(5) Maxfield, F. R.; Mcgraw, T. E. Endocytic Recycling. *Nat. Rev. Mol. Cell Biol.* **2004**, *5*, 121.

(6) Manganiello, M. J.; Cheng, C.; Convertine, A. J.; Bryers, J. D.; Stayton, P. S. Diblock Copolymers with Tunable PH Transitions for Gene Delivery. *Biomaterials* **2012**, *33*, 2301–2309.

(7) Lakadamyali, M.; Rust, M. J.; Babcock, H. P.; Zhuang, X. Visualizing Infection of Individual Influenza Viruses. *Proc. Natl. Acad. Sci. U. S. A.* **2003**, *100*, 9280–9285.

(8) Martens, T. F.; Remaut, K.; Demeester, J.; De Smedt, S. C.; Braeckmans, K. Intracellular Delivery of Nanomaterials: How to Catch Endosomal Escape in the Act. *Nano Today* **2014**, *9*, 344–364.

(9) Selby, L. I.; Cortez-Jugo, C. M.; Such, G. K.; Johnston, A. P. R. Nanoescapology: Progress toward Understanding the Endosomal Escape of Polymeric Nanoparticles. *Wiley Interdiscip. Rev. Nanomedicine Nanobiotechnology* **2017**, *9*, e1452.

(10) Larochelle, J. R.; Cobb, G. B.; Steinauer, A.; Rhoades, E.; Schepartz, A. Fluorescence Correlation Spectroscopy Reveals Highly Efficient Cytosolic Delivery of Certain Penta-Arg Proteins and Stapled Peptides. *J. Am. Chem. Soc.* **2015**, *137*, 2536–2541.

(11) Wissner, R. F.; Steinauer, A.; Knox, S. L.; Thompson, A. D.; Schepartz, A. Fluorescence Correlation Spectroscopy Reveals Efficient Cytosolic Delivery of Protein Cargo by Cell-Permeant Miniature Proteins. *ACS Cent. Sci.* **2018**, *4*, 1379–1393.

(12) Allen, J.; Najjar, K.; Erazo-Oliveras, A.; Kondow-Mcconaghy, H. M.; Brock, D. J.; Graham, K.; Hager, E. C.; Marschall, A. L. J.; Dübel, S.; Juliano, R. L.; Pellois, J. P. Cytosolic Delivery of Macromolecules in Live Human Cells Using the Combined Endosomal Escape Activities of a Small Molecule and Cell Penetrating Peptides. *ACS Chem. Biol.* **2019**, *14*, 2641–2651.

(13) Wang, T.; Yang, S.; Petrenko, V. A.; Torchilin, V. P. Cytoplasmic Delivery of Liposomes into MCF-7 Breast Cancer Cells Mediated by Cell-Specific Phage Fusion Coat Protein. *Mol. Pharm.* **2010**, *7*, 1149–1158.

(14) Wagner, E.; Plank, C.; Zatloukal, K.; Cotten, M.; Birnstiel, M. A. X. L. Influenza Virus Hemagglutinin HA-2 N-Terminal Fusogenic Peptides Augment Gene Transfer by Transferrin-Polylysine-DNA Complexes : Toward a Synthetic Virus-like Gene-Transfer Vehicle. *PNAS* **1992**, *89*, 7934–7938.

(15) Kongkatigumjorn, N.; Cortez-Jugo, C.; Czuba, E.; Wong, A. S. M.; Hodgetts, R. Y.; Johnston, A. P. R.; Such, G. K. Probing Endosomal Escape Using PHlexi Nanoparticles. *Macromol. Biosci.* **2017**, *17*, 1600248.

(16) Wang, Y.; Xie, Y.; Kilchrist, K. V.; Li, J.; Duvall, C. L.; Oupický, D. Endosomolytic and Tumor-Penetrating Mesoporous Silica Nanoparticles for SiRNA/MiRNA Combination Cancer Therapy. *ACS Appl. Mater. Interfaces* **2020**, *12*, 4308–4322.

(17) Yuhua, H.; Litwin, T.; Nagaraja, A. R.; Kwong, B.; Katz, J.; Watson, N.; Irvine, D. J. Cytosolic Delivery of Membrane-Impermeable Molecules in Dendritic Cells Using PH-Responsive Core-Shell Nanoparticles. *Nano Lett.* **2007**, *7*, 3056–3064.

(18) Smith, S. A.; Selby, L. I.; Johnston, A. P. R.; Such, G. K. The Endosomal Escape of Nanoparticles: Toward More Efficient Cellular Delivery. *Bioconjug. Chem.* **2019**, *30*, 263–272.

(19) Vermeulen, L. M. P.; Brans, T.; Samal, S. K.; Dubruel, P.; Demeester, J.; De Smedt, S. C.; Remaut, K.; Braeckmans, K. Endosomal Size and Membrane Leakiness Influence Proton Sponge-Based Rupture of Endosomal Vesicles. *ACS Nano* **2018**, *12*, 2332–2345.

(20) Kilchrist, K. V; Dimobi, S. C.; Jackson, M. A.; Evans, B. C.; Werfel, T. A.; Dailing, E. A.; Beding, S. K.; Kelly, I. B.; Duvall, C. L. Gal8 Visualization of Endosome Disruption Predicts Carrier-Mediated Biologic Drug Intracellular Bioavailability. *ACS Nano* **2019**, *13*, 1136–1152.

(21) Evans, B. C.; Fletcher, R. B.; Kilchrist, K. V; Dailing, E. A.; Mukalel, A. J.; Colazo, J. M.; Oliver, M.; Cheung-flynn, J.; Brophy, C. M.; Tierney, J. W.; Isenberg, J. S.;

Hankenson, K. D.; Ghimire, K.; Lander, C.; Gersbach, C. A.; Duvall, C. L. An Anionic, Endosome-Escaping Polymer to Potentiate Intracellular Delivery of Cationic Peptides, Biomacromolecules, and Nanoparticles. *Nat. Commun.* **2019**, *10*, 5012.

(22) Sonawane, N. D.; Szoka, F. C.; Verkman, A. S. Chloride Accumulation and Swelling in Endosomes Enhances DNA Transfer by Polyamine-DNA Polyplexes. *J. Biol. Chem.* **2003**, *278*, 44826–44831.

(23) Herrera, M.; Kim, J.; Eygeris, Y.; Jozic, A.; Sahay, G. Illuminating Endosomal Escape of Polymorphic Lipid Nanoparticles That Boost MRNA Delivery. *Biomater. Sci.* **2021**.

(24) Du Rietz, H.; Hedlund, H.; Wilhelmson, S.; Nordenfelt, P.; Wittrup, A. Imaging Small Molecule-Induced Endosomal Escape of SiRNA. *Nat. Commun.* **2020**, *11*, 1809.

(25) Ilchrist, K. A. V. K.; Vans, B. R. C. E.; Rophy, C. O. M. B.; Uvall, C. R. L. D. Mechanism of Enhanced Cellular Uptake and Cytosolic Retention of MK2 Inhibitory Peptide Nano-Polyplexes. *BMES* **2016**, *9*, 368–381.

(26) Munson, M. J.; O'Driscoll, G.; Silva, A. M.; Lázaro-Ibáñez, E.; Gallud, A.; Wilson, J. T.; Collén, A.; Esbjörner, E. K.; Sabirsh, A. A High-Throughput Galectin-9 Imaging Assay for Quantifying Nanoparticle Uptake, Endosomal Escape and Functional RNA Delivery. *Commun. Biol.* **2021**, *4*, 211–225.

(27) Tet Htut Soe, K. W. and T. O. Photoinduced Endosomal Escape Mechanism : A View from Photochemical Internalization Mediated by CPP-Photosensitizer Conjugates. *Molecules* **2021**, *26*, 36.

(28) Estabrook, D. A.; Ennis, A. F.; Day, R. A.; Sletten, E. M. Controlling Nanoemulsion Surface Chemistry with Poly(2-Oxazoline) Amphiphiles. *Chem. Sci.* **2019**, *10*, 3994–4003.

(29) Day, R. A.; Estabrook, D.; Wu, C.; Chapman, J. O.; Togle, A. J.; Sletten, E. M. Systematic Study of Perfluorocarbon Nanoemulsions Stabilized by Polymer Amphiphiles. *ACS Appl. Mater. Interfaces* **2020**, *12*, 38887–38898.

(30) Patrick, M. J.; Janjic, J. M.; Teng, H.; Hear, M. R. O.; Brown, C. W.; Stokum, J. A.; Schmidt, B. F.; Ahrens, E. T.; Waggoner, A. S. Intracellular PH Measurements Using Perfluorocarbon Nanoemulsions. *J. Am. Chem. Soc.* **2013**, *135*, 18445–18457.

(31) Misinzo, G.; Delputte, P. L.; Nauwynck, H. J. Inhibition of Endosome-Lysosome System Acidification Enhances Porcine Circovirus 2 Infection of Porcine Epithelial Cells. *J. Virol.* **2008**, *82*, 1128–1135.

(32) Cervia, L. D.; Chang, C. C.; Wang, L.; Yuan, F. Distinct Effects of Endosomal Escape and Inhibition of Endosomal Trafficking on Gene Delivery via Electrotransfection. *PLoS One* **2017**, *12*, e0171699.

(33) Seglen, P.; Grinde, B.; Solheim, A. E. Inhibition of the Lysosomal Pathway of Protein Degradation in Isolated Rat Hepatocytes by Ammonia , Methylamine , Chloroquine and Leupeptin. *Eur. J. Biochem.* **1979**, *95*, 215–225.

(34) Ye, S.; Kang, N.; Chen, M.; Wang, C.; Wang, T.; Wang, Y.; Liu, Y.; Li, D.; Ren, L. Tat/HA2 Peptides Conjugated AuNR@pNIPAAm as a Photosensitizer Carrier for Near Infrared Triggered Photodynamic Therapy. *Mol. Pharm.* **2015**, *12*, 2444–2458.

(35) Farkhani, S. M.; Valizadeh, A.; Karami, H.; Mohammadi, S.; Sohrabi, N.; Badrzadeh, F. Cell Penetrating Peptides: Efficient Vectors for Delivery of Nanoparticles, Nanocarriers, Therapeutic and Diagnostic Molecules. *Peptides* **2014**, *57*, 78–94.

(36) Bruin, K. G. De; Fella, C.; Ogris, M.; Wagner, E.; Ruthardt, N.; Bräuchle, C. Dynamics of Photoinduced Endosomal Release of Polyplexes. *J. Control. Release* **2008**, *130*, 175–182.

(37) Mellert, K.; Lamla, M.; Scheffzek, K.; Wittig, R.; Kaufmann, D. Enhancing Endosomal Escape of Transduced Proteins by Photochemical Internalisation. *PLoS One* **2012**, *7*, e52473.

(38) Gillmeister, M. P.; Betenbaugh, M. J.; Fishman, P. S. Cellular Trafficking and Photochemical Internalization of Cell Penetrating Peptide Linked Cargo Proteins : A Dual Fluorescent Labeling Study. *Bioconjug. Chem.* **2011**, *22*, 556–566.

(39) Pasparakis, G.; Manouras, T.; Vamvakaki, M.; Argitis, P. Harnessing Photochemical Internalization with Dual Degradable Nanoparticles for Combinatorial Photo – Chemotherapy. *Nat. Commun.* **2014**, *5*, 3623.

(40) Riess, J. G.; Riess, J. G. Oxygen Carriers ("blood Substitutes") - Raison d'etre, Chemistry, and Some Physiology. *Chem. Rev.* **2001**, *101*, 2797–2919.

(41) Fraker, C. A.; Mendez, A. J.; Stabler, C. L. Complementary Methods for the Determination of Dissolved Oxygen Content in Perfluorocarbon Emulsions and Other Solutions. *J. Phys. Chem. B* **2011**, *115*, 10547–10552.

(42) Krafft, M. P. Alleviating Tumor Hypoxia with Perfluorocarbon-Based Oxygen Carriers.

Curr. Opin. Pharmacol. **2020**, *53*, 117–125.

(43) Day, R. A.; Estabrook, D. A.; Logan, J. K.; Sletten, E. M. Fluorous Photosensitizers Enhance Photodynamic Therapy with Perfluorocarbon Nanoemulsions. *Chem. Commun.* **2017**, *53*, 13043–13046.

CHAPTER SIX

Readily synthesized cyclic RGD as a functional targeting agent

6.1 Abstract

One of the main limitations of nanomedicine is the inability to control the biodistribution and uptake of nanomaterials within the body. The enhanced permeability and retention effect has been shown to be effective in mouse models, but does not translate to human disease, and thus very few nanomaterials successfully pass clinical trials. To better control the biodistribution of nanomaterials, the addition of active targeting agents such as antibodies, small molecules, aptamers, and peptides have been used to functionalize nanomaterials. Here we use a dibromo maleimide to simultaneously cyclize and add a functional handle to the small peptide Arg-Gly-Asp (RGD) for its ability to target the $\alpha_v\beta_3$ integrin that is upregulated on the surface of many cancer types. Ultimately, we did not obtain significant targeting with this system, but are working towards adding avidity by functionalizing nanoemulsions with the targeting peptide.

6.2 Introduction

Peptides have been used as targeting agents due to the ease of manipulation, ease of production, and homology to native proteins that interact with cell surface receptors.[1] We are interested in the Arg-Gly-Asp (RGD) peptide, with the goal of targeting PFC nanoemulsions to diseased sites. RGD is the binding sequence of fibronectin, a soluble protein that interacts with integrin $\alpha_v\beta_3$. Integrins are cell surface proteins involved in signalling during morphogenesis, tissue modelling, tissue repair,[2] and have been associated

with the initiation, progression, and metastasis of solid tumors.[3] Integrin $\alpha_v\beta_3$ is expressed at low levels in most healthy tissues, but is highly upregulated in many solid tumors.[4,5] This upregulation led to interest in targeting integrin $\alpha_v\beta_3$ as a way to easily differentiate between healthy and cancerous tissues.[6–8]

Original studies in the 1980s focused on determining the shortest amino acid sequence required for binding to integrin $\alpha_v\beta_3$.[5,9] To do this, short amino acid sequences were mutated systematically, and affinities were measured. The short peptide, GRGDSP was found to have an order of magnitude less binding compared to the native protein, fibronectin. Mutating the glycine to an alanine drops the binding by 400 fold and reversing the consensus sequence to SDGR completely inactivates the peptide binding for the integrin.[5,9] Showing that the short peptide GRDGSP, and later shortening to RGD, although less effective than fibronectin, is the shortest sequence of amino acids necessary for binding to integrin $\alpha_v\beta_3$.

This led to the desire to increase the binding affinities of the RGD peptide to be more similar to that of the native protein. This led to the cyclization of peptides,[7,10–14] resulting in rigid structures that are stable to proteases and similar to the natural confirmation of the native protein. There are four main classes of cyclization: head-to-tail, side chain-to-tail, head-to-side chain and side chain-to-side chain. In each of these methods, sacrificial amino acids, often lysine, are used to conjugate the peptide to nanocarriers, fluorophores, or drugs.[15]

Efforts to find new, selective probes for cysteine bioconjugation,[16] led to the discovery of bromomaleimides. Maleimides are cysteine selective, undergoing a Michael addition to from a thiosuccinimide bond, with the caveat of being reversible and susceptible to thiol

exchange (path 1, Figure 6.1).[16,17] Singly brominated maleimides, react with cysteine, releasing HBr, and can then subsequently react with a new nucleophile, trapping the maleimide reagent and releasing the free cysteine (path 2, Figure 6.1). This was first shown on small molecules,[17,18] then expanded to peptides[19] and larger proteins.[20–22] The next advance came with dibromo maleimides, which are able to react with two cysteines and have been used to staple peptides[19] and proteins (path 3, Figure 6.1).[23–26] Here, we explore side chain-to-side chain cyclizations through the use of bromomaleimide Michael addition chemistry to both permanently cyclize the peptide and provide functionality simultaneously.

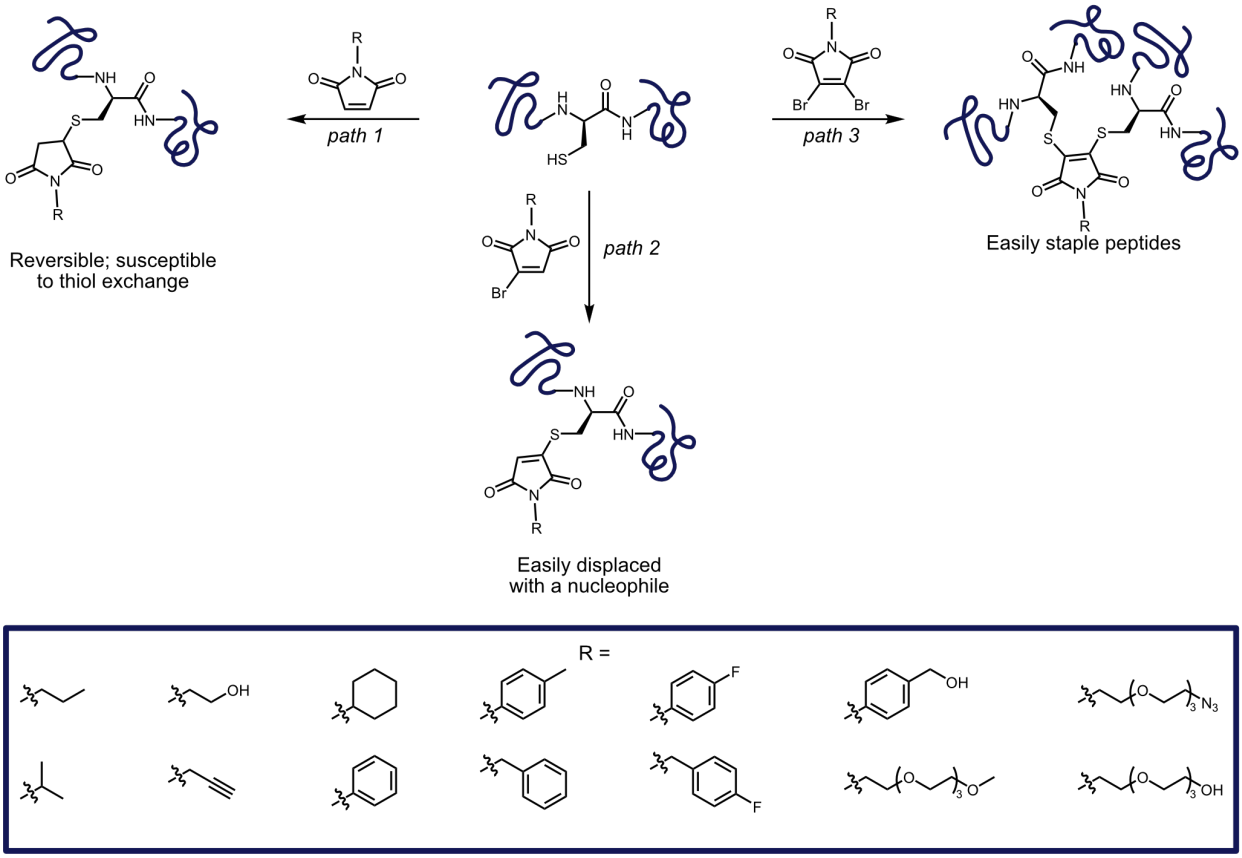

Figure 6.1 Cysteine bioconjugation with three generations of maleimide probes. Maleimide (path 1), bromomaleimide (path 2) and dibromo maleimide (path 3), provide methods to label proteins with various functional groups (blue box).

6.3 Results and Discussion

6.3.1 Rhodamine functionalized bromomaleimides

We looked to bromomaleimides as functional molecules to cyclize RGD peptides due to the non-reversible nature of a thiol adding into the dibromomaleimide.[17,19,20] We synthesized four peptides using solid phase peptide synthesis, cRGD (**6.1**), lRGD (**6.2**), control lKGD (**6.3**), and lRGDSPC (**6.4**) (Figure 6.2). Clean peptides **6.1**-**6.4** were then covalently linked with functionalized maleimides (Scheme 6.1).

Rhodamine was functionalized with piperazine (**6.5**) following Francis and coworkers procedure.[27] This was coupled to dibromo-maleimidohexanoic acid (**6.6**) or 6-maleimidohexanoic acid (**6.7**) to yield functionalized rhodamine **6.8** and **6.9**. The brominated maleimide was then reacted with reduced cRGD (**6.1**) to produce bridged peptide **6.10**. The non-brominated maleimide underwent a Michael addition with either lRGD (**6.2**) or lKGD (**6.3**) to form **6.11** and **6.12** (Scheme 6.1). The cyclization conditions to achieve **6.10** were optimized by changing the solvent, pH of the buffer, and the identity of the buffer, seen in Table 6.1, or the HPLC traces in Supplemental figures 6.8.3.

After an initial screen with the fluorescein linked bromomaleimide (**6.8**) we synthesized a simpler bromomaleimide to screen cyclization conditions. Following Baker and Caddick,[33] we synthesized activated *N*-methoxycarbonylmaleimide (**6.13**). This activated maleimide readily reacts with amine containing molecules at room temperature, therefore we subjected it to propargyl bromide to form (**6.14**). We used **6.14** to screen cyclization conditions, again changing solvent, pH and identity of the buffer (Table 6.1). Helpfully, thiomaleimide compound (**6.15**) absorbs at 400 nm, providing means of easy visualization with HPLC. A representative HPLC trace can be seen in Figure 6.3 (entry 7, Table 6.1).

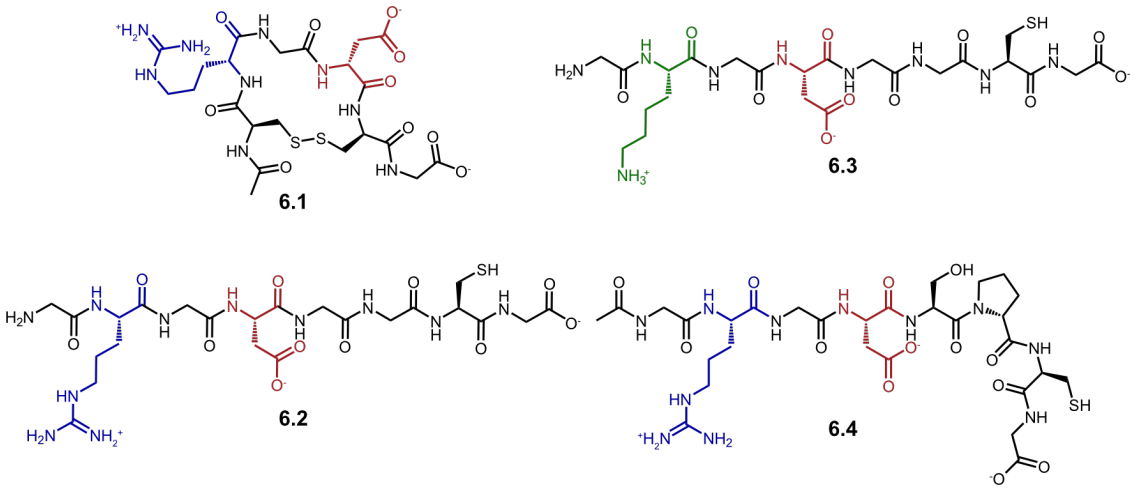

Figure 6.2 Solid phase peptide synthesis of peptides **6.1-6.4**.

Scheme 6.1 Synthetic scheme for peptides **6.10-6.12**.

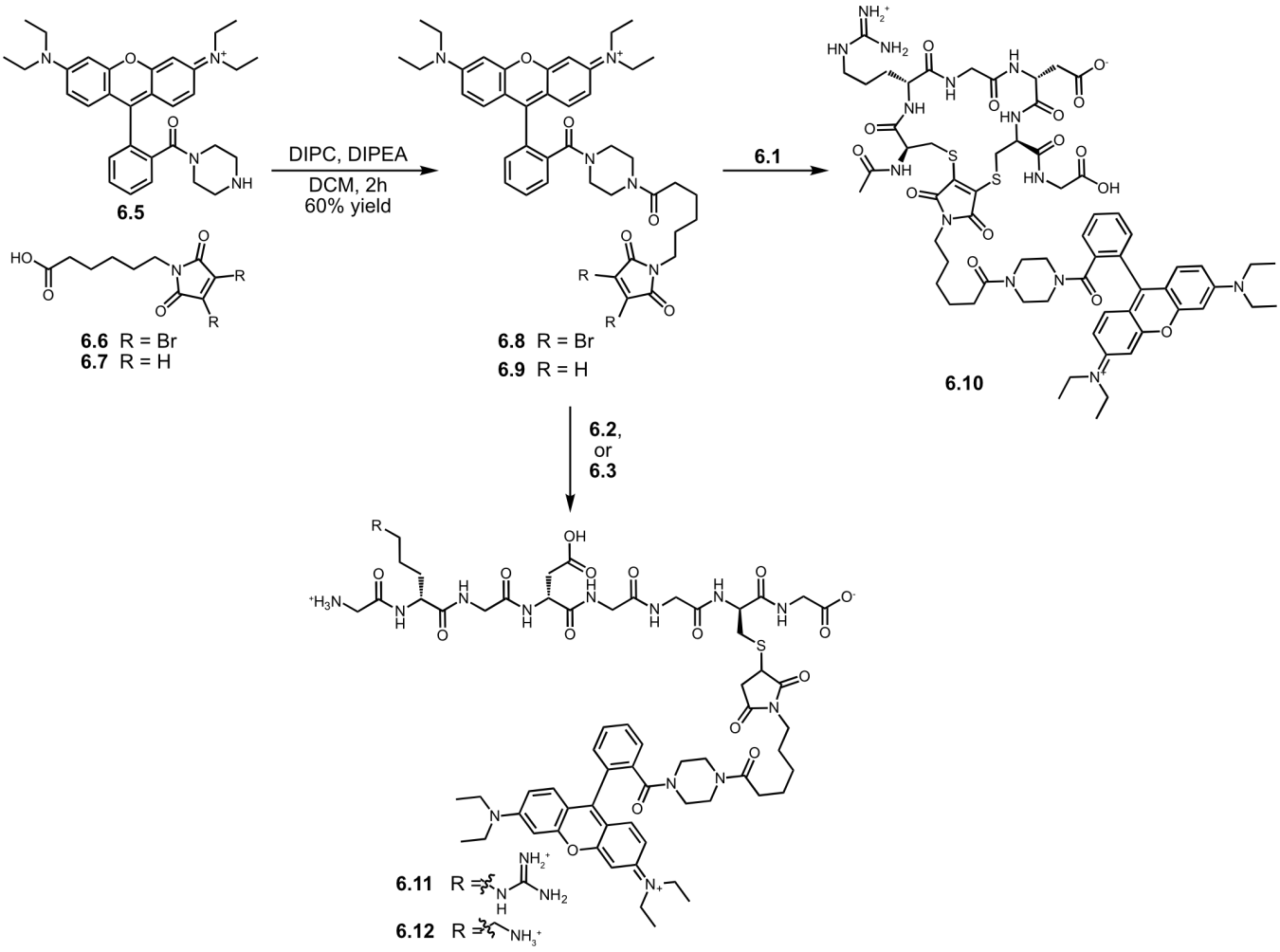

Scheme 6.2 Synthetic scheme for model BrMal (**6.14**) used to optimize bridging conditions.

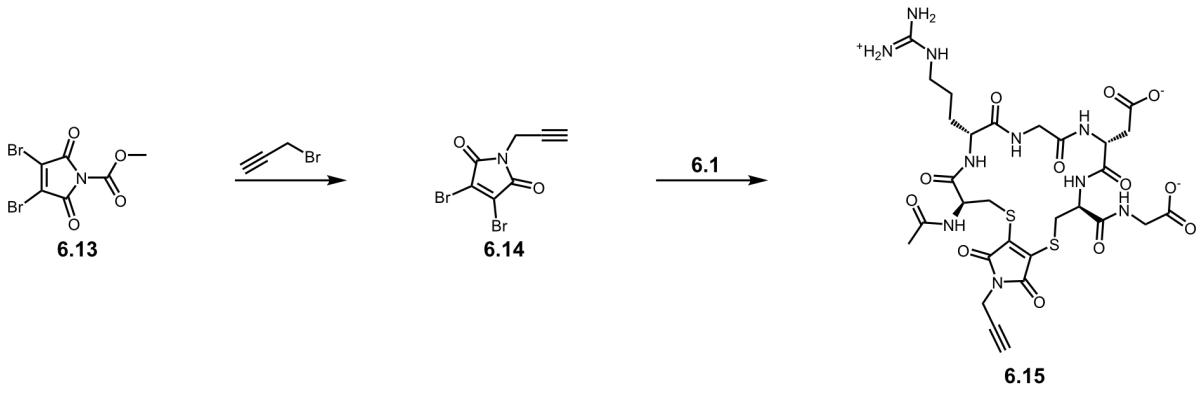

Table 6.1 HPLC cRGD bridging screen.

Entry	Solvent	Reduction agent	Time	Retention time of product (min)	Retention time of side products (min)	Product : side product
1	1:1 MeOH : MilliQ	TCEP	2 h	No product	-	-
2	1:1 MeCN : MilliQ	TCEP	2 h	No product	-	-
3	3:1 DMF PBS	TCEP	2 h	15.4 (**6.10**)	15.8; 16.9	1:2; 1:3
4	PBS + 10% DMF	TCEP	2 h	15.38 (**6.10**)	15.5; 16.8	1:1; 2:1
5	4.5:1.5 H2O DMF	TCEP	2 h	18.2 (**6.15**)	17.8; 18; 19	2:1; 2:1; 1.5:1
6	4:1:0.5 DCM : MeOH : MilliQ water	TCEP	2 h	15.5 (**6.10**)	13.1; 13.5; 16.9	2:1; 2:1; 3:1
7	50 mM NaPO4 pH 5.4; 40% MeCN; 2.5% DMF	TCEP	2 h	18.3 (**6.15**)	19	1.5 : 1
8	50 mM NaPO4 pH 6.2 ; 40% MeCN; 2.5% DMF	TCEP	1 h TCEP, 1 h **6.8**	18.3 (**6.15**)	17.8; 19	2:1; 2:1
9	50 mM NaPO4 pH 6.2 ; 40% MeCN; 2.5% DMF	TCEP	2 h	18.3 (**6.15**)	14.7; 15.8; 17.9; 19	1:1; 1:1; 2:1; 2:1
10	50 mM NaPO4 pH 7.7 ; 40% MeCN; 2.5% DMF	TCEP	2 h	18.3 (**6.15**)	15.3; 19.1	4:1 (400 nm); 1.5:1

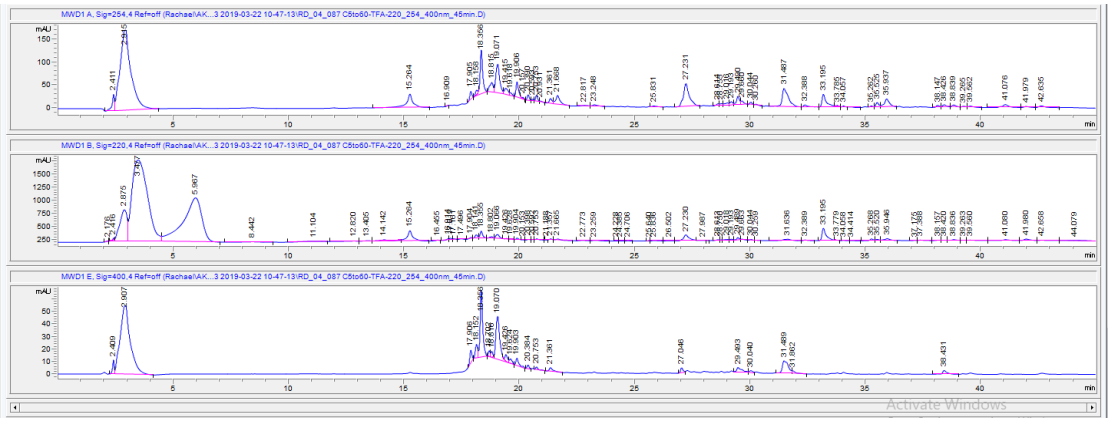

Figure 6.3 HPLC trace of entry 7 (Table 6.1). Elutions are as follows: DMF (0.9 min); **6.15** (18.3 min); major side product (19.07 min). Absorbance at 400 nm is visualizing thio-maleimide formation.

In all conditions tested, side products were observed, but ultimately, we arrived at condition 7 as the least amount of side products were formed. After bridging, peptides were purified by HPLC prior to cell studies. Linear peptides **6.11** and **6.12** were also purified by HPLC prior to cell studies.

We first confirmed the presence of the $\alpha_v\beta_3$ integrin on the surface of A375 cells using a known antibody, LM609 (Figure 6.4A).[28] As this is a cell surface protein with cationic residues present, it is sensitize to trypsinization,[29–31] meaning these cells were kept trypsin free throughout propagation and experiments by lifting the cells through scraping. This was also true for the negative control cell line HEK293 which do not express the $\alpha_v\beta_3$ integrin (Figure 6.4A). We then treated both A375 and HEK293 cells with two doses of **6.10-6.12** (Figure 6.4B) and monitored the cellular uptake via flow cytometry. We expected to see **6.10** > **6.11** > **6.12** in A375 cells, with minimal uptake of all peptides in the HEK293 cells. Unfortunately, the uptake between A375 (red) and HEK293 (blue) cells was similar across both concentrations of peptide used. In addition, cRGD (**6.10**) had less signal than lRGD (**6.11**) and control lKGD (**6.12**) (Figure 6.4B). We hypothesized the cationic rhodamine dye covalently linked to the peptides caused non-specific adhesion of the peptides to the anionic cell surface. To counteract this, we modified the system to use fluorescein as a fluorescent payload instead (Scheme 6.3).

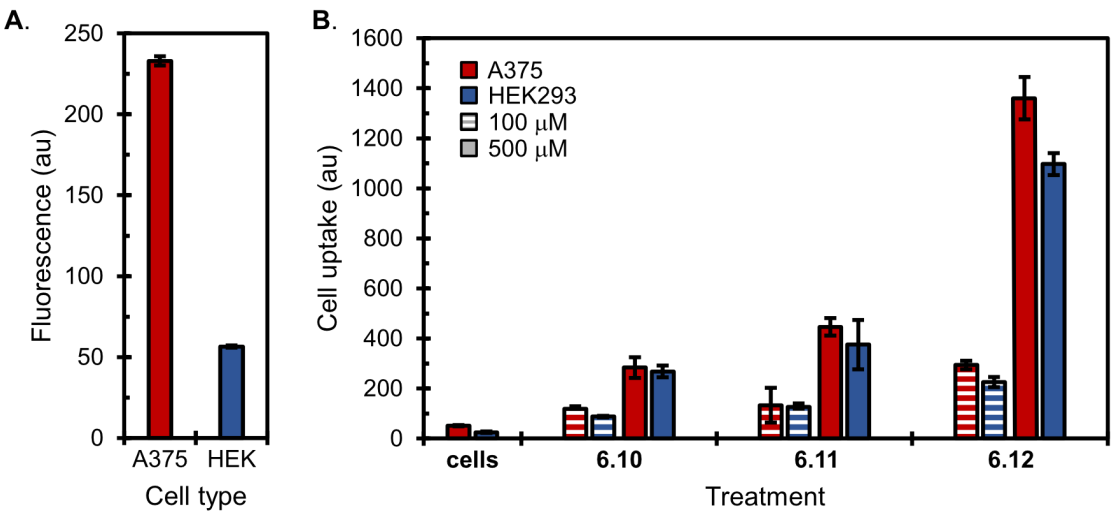

Figure 6.4 FACS Cytometry uptake of peptide (**6.10-6.12**) (A) Control with LM609 antibody showing $\alpha_v\beta_3$ is present on A375 cells (red), but not on HEK cells (blue). (B) Uptake of each cell type with each peptide after 1 h treatment. Cells were then washed and analyzed for rhodamine fluorescence (FL2).

6.3.2 Fluorescein functionalized bromomaleimides

First, we synthesized fluorescein probe **6.18** through a coupling of 6-maleimidohexanoic acid (**6.7**) and 4,7,10-Trioxa-1,13-tridecanediamine (**6.16)** to form **6.17**. Compound **6.17** was reacted with fluorescein isothiocyanate (FITC) under standard conditions to form the functional fluorescein probe. With **6.18** in hand, we reacted peptides **6.2**-**6.4** to form fluorescently labeled peptides **6.19**-**6.21**.

With the linear peptides in hand, both A375 and HEK293 cells were treated (15 μM, **6.19-6.21**) for 15 or 30 minutes to prevent endocytosis and non-specific uptake. The concentration and time were greatly reduced from the previous, rhodamine containing probe (**6.10-6.12**), in the hope that this would help prevent non-specific binding. The amount of the $\alpha_v\beta_3$ integrin was analyzed with a fluorescent antibody, LM609, and isotype antibody to ensure no nonspecific antibody labeling (Figure 6.5A). After washing, we analyzed cell targeting with flow cytometry, looking at the fluorescence of the fluorescein tagged peptides. We expected to see **6.19** ≈ **6.21** > **6.20** in A375 cells, with minimal fluorescence in HEK293 cells. Unfortunately, we saw similar fluorescence across all cells, all peptides, and all times of incubations (Figure 6.5B).

We are currently working to incorporate multiplexing into this system to increase the binding affinities of the RGD containing peptides compared to KGD peptides. To achieve this, we aim to functionalize the surface of perfluorocarbon (PFC) nanoemulsions by covalently attaching RGD containing peptides to the surfactant stabilizing the nanoemulsions. Functional handles can be incorporated into the hydrophilic block of poly(2-oxazoline) polymers through statistical copolymerization (Figure 6.6A). This surface exposed alkyne handle, can undergo Cu(II) mediated click chemistry, to functionalize the surface of the nanoemulsions with fluorophores.[32] We are

Scheme 6.3 Synthetic scheme for peptides **6.19-6.21**.

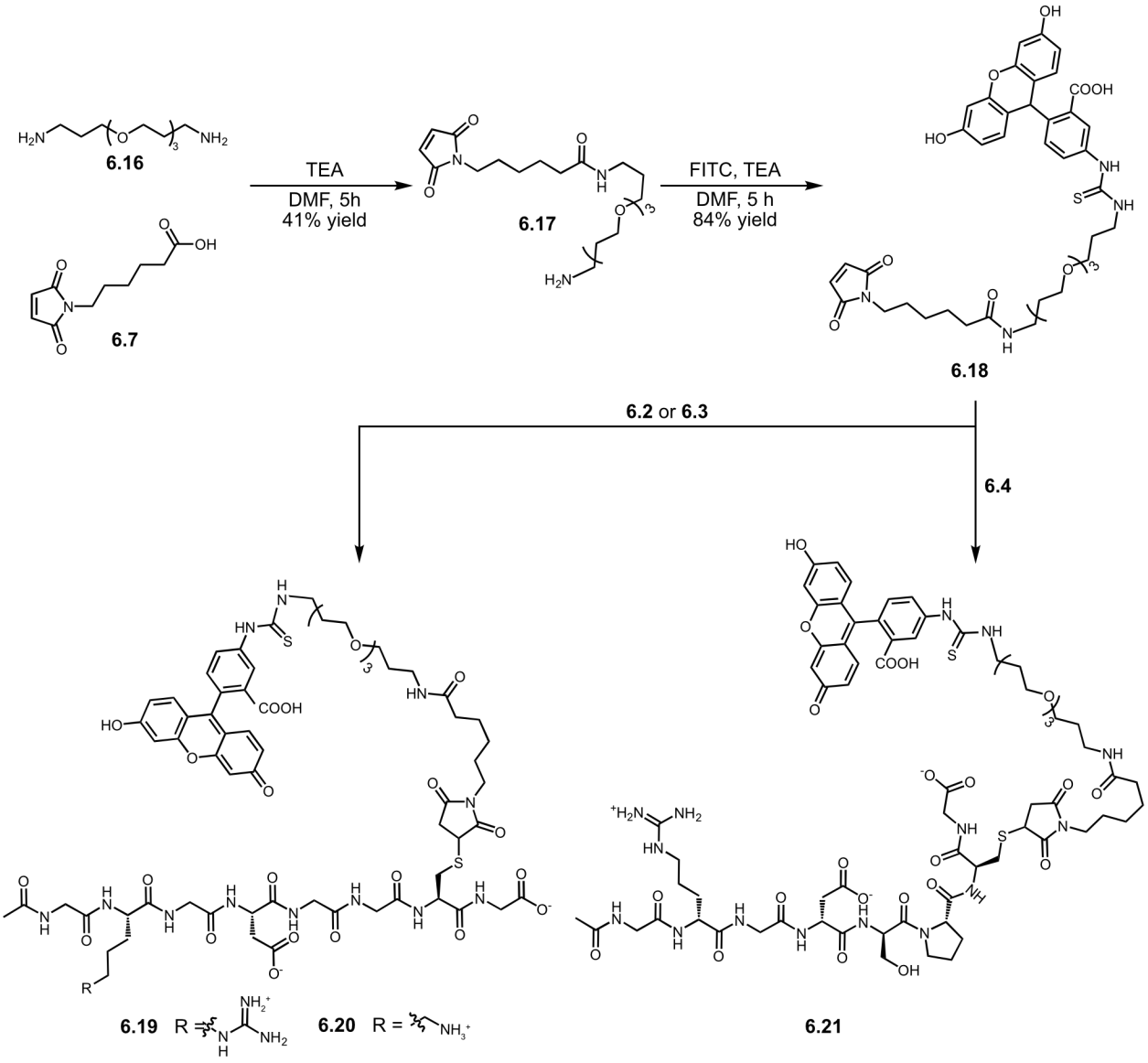

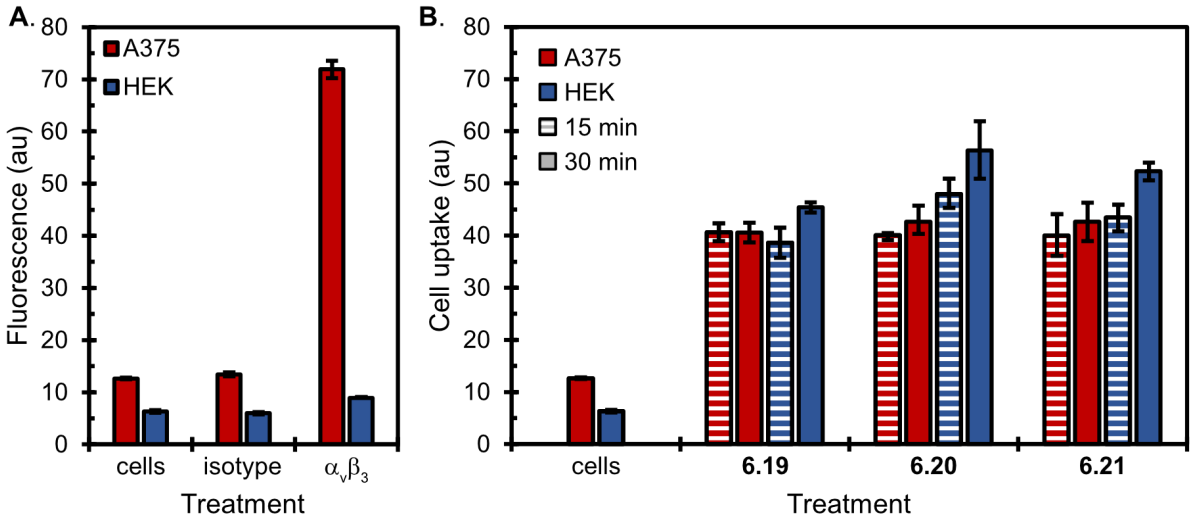

Figure 6.5 FACS Cytometry uptake of linear peptide (**6.19-6.21**) (A) Control with LM609 antibody showing $\alpha_v\beta_3$ is present on A375 cells (red), but not on HEK cells (blue). (B) Uptake of each cell type with each peptide after 15 min (striped) or 30 min (solid) treatment. Cells were then washed and analyzed for fluorescein fluorescence (FL1).

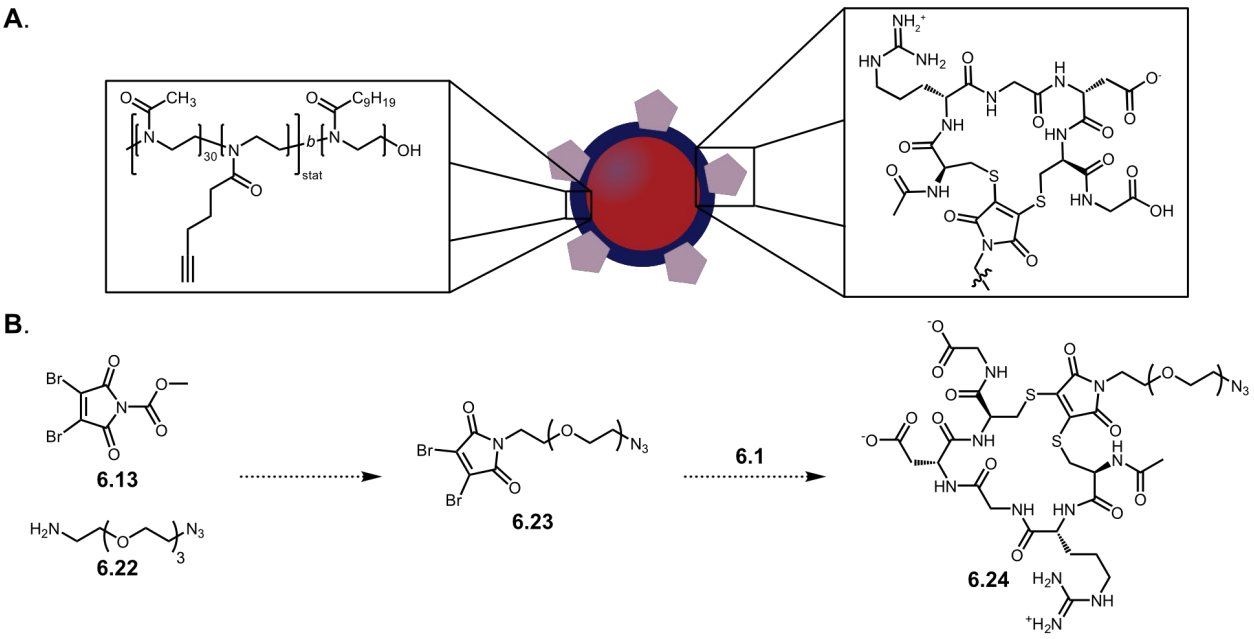

Figure 6.6 (A) Schematic of targeted PFC nanoemulsions using functional polyoxazoline and cyclic RGD peptide. (B) Synthetic scheme resulting in functionalized cyclic peptide **6.24** with a clickable azide handle.

planning to use the same chemistry to covalently link the various peptides (**6.1**-**6.4**) to the surface of the emulsions.

In order to functionalize the surface of nanoemulsions, we need to synthesize a dibromomaleimide with an azide handle. To do this, we again looked to Caddick and Baker[33] to react activated maleimide (**6.13**) with an azide containing PEG (**6.22**) to form the functionalize bromomaleimide (**6.23**) (Figure 6.6B). We are currently working toward these molecules and are hopeful that increasing avidity will help increase the targeting capabilities of these peptides.

6.4 Conclusion

Short peptide Arg-Gly-Asp is a well know ligand for the $\alpha_v\beta_3$ integrin and has been used ubiquitously as a targeting agent. Here, we use bromomaleimide chemistry to simultaneously cyclize and functionalize the peptide. This is done by incorporating strategically placed cysteines around the binding sequence. By covalently functionalizing the control linear peptides, and the cyclic peptides to a variety of fluorophores, we hoped to visualize the increased uptake of cells overexpressing the $\alpha_v\beta_3$ integrin. Unfortunately, that was not observed, leading to next steps of using avidity by covalently linking the peptide to the surface of nanoemulsions, to increase the binding and uptake. We hope that this work will ultimately result in targeted PFC nanoemulsions that can be used *in vivo* to better target diseases.

6.5 Experimental Procedures

6.5.1 General procedures

Chemical reagents were purchased from Sigma-Aldrich, TCI America or Acros Organics and used without purification unless noted otherwise. Anhydrous and deoxygenated dimethylformamide (DMF) was dispensed from a Grubb's-type Phoenix Solvent Drying System. Thin layer chromatography was performed using Silica Gel 60 F_{254} (EMD Millipore) plates. Flash chromatography was performed with technical grade silica gel with 60 Å pores and 40–63 μm mesh particle size (Sorbtech Technologies). Solvent was removed under reduced pressure with a Büchi Rotovapor with a Welch self-cleaning dry vacuum pump and further dried with a Welch DuoSeal pump. Bath sonication was performed using a Branson 3800 ultrasonic cleaner. Emulsions were prepared using a QSonica (Q125) sonicator. Nuclear magnetic resonance (^{1}H NMR and ^{19}F NMR) spectra were taken on Bruker Avance 500 (^{1}H NMR), Bruker Avance 400 (^{1}H NMR, ^{19}F NMR) or Bruker Avance 300 (^{19}F NMR) instruments and processed with TopSpin or MNova software.

6.5.2 Solid phase peptide synthesis

First, swell the resin (Fmoc-glycine 4-alkoxybenzyl alcohol resin; CHEM-IMPEX INT'L INC Cat# 01908) in 20% piperidine in DMF (15 min). A Kaiser test was used to confirm the resin was deprotected completely after swelling. All amino acids (5 eq, CHEM-IMPEX INT'L INC) were dissolved in HCTU (0.4 M, DMF, aapptec Cat# CXZ030) for 5 min prior to coupling, but no longer than 30 min as this diminished coupling capabilities. Prior to adding the next amino acid to the deprotected resin, activate the dissolved amino acid by adding *N*-methylmorpholine (0.4 M, DMF). Shake for 1 min, the solution should become slightly yellow. Add the activated

amino acid to the deprotected resin and couple for 1 hour, using N_2 to stir. After coupling, a Kaiser test was used to confirm the reaction proceeded to completion. After washing with DMF, the amino acid was deprotected for 5 min (20% piperidine, DMF, 5 min). The resin was washed again, and the next activated amino acid was added to the resin. This iterative process is continued until the peptide is complete. Once the peptide is complete, the side chains are cleaved and the peptide is cleaved from the resin: no cysteine present (90% TFA, 5% TIPS, 5% water); with cysteine present (905 TFA, 4% TIPS, 3% water, 3% EDT). The resin was rocked in the cleaving solution for 2.5 hours. The cleaving solution was then drained and evaporated by blowing nitrogen over the peptide solution. Once dried, the peptide is purified by triturating with cooled dry ethyl ether. The peptide is dissolved in water and lyophilized.

6.5.3 General cRGD bridging procedure

Purified cyclic peptide (**6.1**) was dissolved in ~1 mL of solvent (see table 6.1). TCEP and functionalized bromomaleimide (**6.8**) were added and stirred for 1 h. After the reaction was complete, the solvent was blown off, the product was dissolved in acetonitrile and filtered to remove any salts from the buffer the reaction was performed in. HPLC analysis was performed to determine cyclization.

6.5.4 General cell culture procedures

A375 cells were purchased from ATCC (Cat# CRL-1619). HEK293 cells were purchased from ATCC (Cat# CRL-1573).

A375 and HEK293 cells were cultured in Dulbecco's Modified Eagle Media (DMEM, Life Technologies, cat# 11995073) supplemented with 10% fetal bovine serum (Corning, lot# 35016109) and 1% penicillin-streptomycin (Life Technologies, cat# 15070063). Cells were washed with PBS. Cells were incubated at 37 ˚C, 5% CO_2, during treatments and throughout culturing, in HERACell 150i CO2 incubators. Cells were pelleted through use of Sorvall ST 40R centrifuge. All cell work was performed in 1300 Series A2 biosafety cabinets.

6.6 Figure experimental procedures

Figure 6.4

A375 cells (ATCC Cat# CRL-1619) and HEK293 cells (ATCC Cat# CRL-1573) were lifted by scraping to preserve integrin on the surface of the cells. Cells were plated (200,000 cells / well) on a v-bottom 96-well plate (Fisher, Cat# 07-200-96). Cells were incubated in media for two hours. Purified peptide (**6.10-6.12**) was added at either 100 μM or 500 μM concentrations and incubated (1 h, 37 °C, 5% CO_2). Antibody control was 2 μL antibody in 200 μL total of buffer. After treatment, cells were washed via centrifugation (2x, 526 x *g*, 3 min) to remove unbound peptide and resuspended in FACS buffer (1% FBS in PBS). Cells were lifted via pipetting and transferred to FACS tubes to measure the rhodamine (FL2) fluorescence.

Figure 6.5

A375 cells (ATCC Cat# CRL-1619) and HEK293 cells (ATCC Cat# CRL-1573) were lifted with TrypLE express (a gentler Trypsin-EDTA). Cells were plated (100,000 cells/well) on a v-bottom 96-well plate (Fisher, Cat# 07-200-96). Cells were incubated in media for two hours. Purified peptide (**6.19-6.21**) was added (15 μM) and incubated (15 min or 30 min, 37 °C, 5% CO_2). Antibody control was 1 μL antibody (LM609) or 2 μL isotype antibody in 200 μL total of buffer (1 h, 37 °C, 5% CO_2). After treatment, cells were washed via centrifugation (2x, 526 x *g*, 3 min) to remove unbound peptide and resuspended in FACS buffer (1% FBS in PBS). Cells were lifted via pipetting and transferred to FACS tubes to measure the fluorescein (FL1) fluorescence.

6.7 Scheme experimental procedures

Dibromomaleimido hexanoic acid (6.6)

Maleimido hexanoic acid (300 mg, 1.4 mmol, 1 eq) was dissolved in glacial acetic acid (5 mL) and cooled to 0 °C. Liquid bromine (100 μL, 2.1 mmol, 1.5 eq) was added dropwise. The mixture was then heated to 100 °C and refluxed for four hours. After cooling, the mixture was partioned between cold D.I. water and ethyl acetate. The ethyl acetate was washed with a saturated solution of NaS_2O_4 several times to remove excess bromine, dried over $MgSO_4$ and concentrated *in vacuo*. The product was purified by silica gel chromatography, eluting with hexane : ethyl acetate. ^{1}H NMR (400 MHz, $CDCl_3$) δ 11.35 (s, 0H), 3.59 (t, *J* = 7.2 Hz, 1H), 2.33 (t, *J* = 7.4 Hz, 1H), 1.71 – 1.62 (m, 1H), 1.64 – 1.56 (m, 1H), 1.41 – 1.27 (m, 1H).

N-(9-(2-(4-(6-(3,4-dibromo-2,5-dioxo-2,5-dihydro-1H-pyrrol-1-yl)hexanoyl)piperazine-1-carbonyl)phenyl)-6-(diethylamino)-3H-xanthen-3-ylidene)-*N*-ethylethanaminium (6.8)

Dibromomaleimido hexanoic acid (**6.9**) (18 mg, 49 μmol, 2.5 eq) was dissolved in anhydrous DCM (1 mL). Diisopropylcarbodiimide (DIPC, 4.5 μL, 20 μmol, 1 eq) and diisopropylethyl amine (DIPEA, 3.5 μL, 20 μmol, 1 eq) were added and stirred (1 h, 25 °C). Rhodamine piperazine[27] was added and stirred overnight. The crude product was concentrated onto silica and purified by silica gel chromatography, eluting with acetonitrile : water (100:1). ^{1}H NMR (400 MHz, MeOD) δ 7.79 – 7.72 (m, 3H), 7.69 (s, 1H), 7.51 – 7.48 (m, 1H), 7.26 (d, *J* = 9.6 Hz, 2H), 7.05 (d, *J* = 10.4 Hz, 2H), 6.94 (d, *J* = 2.5 Hz, 2H), 3.75 – 3.61 (m, 22H), 3.55 (d, *J* = 7.4 Hz, 4H), 3.36 (s, 9H), 3.32 (d, *J* = 1.5 Hz, 2H), 3.20 (p, *J* = 7.3 Hz, 17H), 2.31 (t, *J* = 7.4 Hz, 3H), 1.56 (dt, *J* = 15.4, 7.7 Hz, 12H), 1.39 – 1.32 (m, 81H), 1.29 (ddd, *J* = 9.8, 5.5, 2.6 Hz, 51H), 0.87 (t, *J* = 6.8 Hz, 7H). LCMS (ESI): *m/z* calcd for $C_{42}H_{48}Br_2N_5O_5^+$ [M+H$^+$]: 860.20 Observed mass [M+H$^+$]: 862

***N*-(6-(diethylamino)-9-(2-(4-(6-(2,5-dioxo-2,5-dihydro-1H-pyrrol-1-yl)hexanoyl)piperazine-1-carbonyl)phenyl)-3H-xanthen-3-ylidene)-*N*-ethylethanaminium (6.9)**

Maleimido hexanoic acid (10 mg, 43 μmol, 1 eq) and HCTU (21 mg, 47 μmol, 1.1 eq) were dissolved in 1 mL anhydrous DCM and stirred (1 h, 25 °C). Separately, rhodamine piperazine[27] (21 mg, 39 μmol, 0.9 eq) and triethylamine (TEA, 6 μL, 43 μmol, 1 eq) were dissolved in 1 mL anhydrous DCM and stirred (1 h, 25 °C). The rhodamine / TEA mixture was transferred to the acid / HCTU mixture and stirred for a further 2 h. The crude product was concentrated onto silica and purified by silica gel chromatography, eluting with acetonitrile : water. (R_f : 0.3 in 10:1 MeCN : H_2O). ^{1}H NMR (300 MHz, MeOD) δ 7.81 – 7.71 (m, 4H), 7.68 – 7.62 (m, 1H), 7.54 (d, *J* = 2.9 Hz, 1H), 7.30 (d, *J* = 9.5 Hz, 2H), 7.10 (d, *J* = 8.8 Hz, 2H), 6.98 (d, *J* = 2.4 Hz, 2H), 6.81 (s, 2H), 4.23 (d, *J* = 5.7 Hz, 1H), 3.71 (q, *J* = 7.1 Hz, 9H), 3.51 – 3.38 (m, 10H), 2.35 (t, *J* = 7.5 Hz, 2H), 2.21 (d, *J* = 5.3 Hz, 2H), 1.58 (h, *J* = 6.8 Hz, 6H), 1.03 – 0.78 (m, 6H). LCMS (ESI): *m/z* calcd for $C_{42}H_{50}N_5O_5^+$ [M+H$^+$]: 704.38 Observed mass [M+H$^+$]: 704.1

N-(9-(2-(4-(6-(15-acetamido-6-(carboxymethyl)-3-((carboxymethyl)carbamoyl)-12-(3-guanidinopropyl)-5,8,11,14,18,20-hexaoxo-3,4,5,6,7,8,9,10,11,12,13,14,15,16,18,20-hexadecahydro-2H,19H-pyrrolo[3,4-b][1,4]dithia[7,10,13,16]tetraazacyclononadecin-19-yl)hexanoyl)piperazine-1-carbonyl)phenyl)-6-(diethylamino)-3H-xanthen-3-ylidene)-N-ethylethanaminium (6.10)

Purified cyclic peptide (**6.1,** 3 mg, 4.6 μmol, 1 eq) was dissolved in ~1 mL of buffer (50 mM NaPO4 pH 5.4; 40% MeCN; 2.5% DMF). TCEP (1.5 mg, 5.1 μmol, 1.1 eq) and functionalized bromomaleimide (**6.8,** 4 mg, 4.6 μmol, 1 eq) were added and stirred for 2 h (25 °C). After the reaction was complete, the solvent was blown off, the product was dissolved in acetonitrile and

filtered to remove any salts from the buffer the reaction was performed in. HPLC analysis was performed to determine cyclization. LCMS (ESI): *m/z* calcd for $C_{64}H_{83}N_{14}O_{15}S_2^+$ [M+H$^+$]: 1350.49 Observed mass [M+Isopropanol+H$^+$]: 1410

***N*-methoxycarbonyl-3,4-dibromomaleimide (6.13)**[33]

To a solution of 3,4-dibromomaleimide (50 mg, 200 μmol, 1 eq) and N-methylmorpholine (22 μL, 22 μmol, 0.1 eq) in anhydrous THF (3 mL), methylchloroformate (30 μL, 200 μmol, 1 eq), was added and the mixture was stirred for 20 min at room temperature. Then DCM (x mL) was added, the organic phase was washed with H_2O dried over $MgSO_4$ and the solvent removed *in vacuo* to yield the product **6.19**. (R_f : 0.8 in DCM). ^{1}H NMR (500 MHz, $CDCl_3$) δ 4.00 (s, 3H), 3.82 (d, *J* = 11.8 Hz, 1H). LCMS (ESI): *m/z* calcd for $C_6H_3Br_2NO_4$ [M+H$^+$]: 310.86 Observed mass [M+2Na$^+$–H$^+$] : 367

***N*-(3-(2-(2-(3-aminopropoxy)ethoxy)ethoxy)propyl)-6-(2,5-dioxo-2,5-dihydro-1H-pyrrol-1-yl)hexanamide (6.17)**

4,7,10-Trioxa-1,13-tridecanediamine was monoboc protected by AKA to form tert-butyl (3-(2-(2-(3-aminopropoxy)ethoxy)ethoxy)propyl)carbamate and passed on to me.

Malemidohexanoic acid (200 mg, 950 μmol, 1 eq), perfluorophenyl 2,2,2-trifluoroacetate (325 μL, 1.9 mmol, 2 eq) and TEA (264 μL, 1.9 mmol, 2 eq) were dissolved in anhydrous DMF and stirred for 5h at 25 °C. The crude was concentrated onto silica and purified by silica gel chromatography, eluting in pentane : ether. Then purified maleimidohexanoic PFP ester (100 mg, 265 μmol, 1 eq) was dissolved in 1 mL anhydrous DMF. The tert-butyl (3-(2-(2-(3-aminopropoxy)ethoxy)ethoxy)propyl)carbamate (86 mg, 265 μmol, 1 eq) synthesized by AKA

and TEA (40 μL, 265 μmol, 1 eq) were dissolved in anhydrous DMF. The PEG / TEA mixture was transferred to the PFP ester dropwise and stirred at 25 °C for 2 h. The crude mixture was concentration onto silica and purified by silica gel chromatography, eluting in DCM : MeOH (R_f : 0.1 in 10:1 DCM : MeOH). The Boc protecting group was removed by stirring in DCM (5 mL): HCl (1 mL) for 3 h. ^{1}H NMR (400 MHz, $CDCl_3$) δ 6.62 (s, 2H), 6.51 (s, 1H), 5.07 (s, 1H), 3.58 – 3.40 (m, 14H), 3.26 (q, *J* = 6.1 Hz, 2H), 3.13 (d, *J* = 6.9 Hz, 2H), 2.08 (t, *J* = 7.6 Hz, 2H), 1.68 (q, *J* = 6.9 Hz, 4H), 1.59 – 1.47 (m, 4H), 1.25 – 1.17 (m, 2H). LCMS (ESI): *m/z* calcd for $C_{20}H_{35}N_3O6$ [M+H$^+$]: 413.25; Observed mass [M+H$^+$]: 413. LCMS (ESI): *m/z* calcd for $C_{25}H_{43}N_3O_8$ [M+H$^+$]: 513.25. Observed mass [M+H$^+$]: 513.

5-(3-(20-(2,5-dioxo-2,5-dihydro-1H-pyrrol-1-yl)-15-oxo-4,7,10-trioxa-14-azaicosyl)thioureido)-2-(6-hydroxy-3-oxo-3H-xanthen-9-yl)benzoic acid (6.18)

tert-butyl (3-(2-(2-(3-aminopropoxy)ethoxy)ethoxy)propyl)carbamate synthesized by AKA (200 mg, 614 μmol, 1 eq) and TEA (85 μL, 610 μmol, 1 eq) were dissolved in anhydrous DMF. FITC (200 mg, 510 μmol, 0.8 eq) was added and stirred (1h, 37 °C). The crude was concentrated onto silica and purified by silica gel chromatography, eluting in DCM : MeOH (R_f : 0.6 in 10:1 DCM : MeOH). ^{1}H NMR (500 MHz, MeOD) δ 8.32 (s, 1H), 7.82 (s, 1H), 7.13 (s, 1H), 6.77 (s, 3H), 6.75 – 6.63 (m, 7H), 6.63 – 6.52 (m, 5H), 3.76 – 3.51 (m, 24H), 3.49 – 3.36 (m, 8H), 3.19 (d, *J* = 6.8 Hz, 101H), 2.14 (d, *J* = 6.9 Hz, 5H), 1.96 (s, 33H), 1.89 (d, *J* = 5.9 Hz, 4H), 1.68 (d, *J* = 6.3 Hz, 4H), 1.55 (d, *J* = 7.4 Hz, 8H), 1.44 – 1.26 (m, 143H).

2-(2-(2-azidoethoxy)ethoxy)ethan-1-amine (6.22)

2-[2-(2-aminoethoxy)ethoxy]ethanol (50 mg, 335 μmol, 1 eq) and boc anhydride (65 mg, 300 μmol, 0.9 eq) were dissolved in anhydrous DMF and stirred for 1.5 h at 25 °C. The crude was concentrated onto silica and purified by silica gel chromatography eluting in DCM : MeOH (R_f : 0.5 in 10 : 1 DCM : MeOH). This was then tosylated by reacting monoboc 2-[2-(2-aminoethoxy)ethoxy]ethanol (70 mg, 280 μmol, 1 eq), Tosyl chloride (84 mg, 420 μmol, 1.5 eq) were dissolved in anhydrous DCM. The reaction was cooled to 0 °C and KOH (20 mg, 420 μmol, 1.5 eq) was added and stirred (2 h). The crude was washed with D.I water twice, washed with cold bring, dried with $MgSO_4$ and concentrated. The product was purified with silica gel chromatography, eluting with hexane : ethyl acetate. Lastly the tosyl/boc protected PEG (46 mg, 115 μmol, 1 eq) was displaced with sodium azide (31 mg, 460 μmol) by dissolving in anhydrous DCM, heating to 65 °C and stirring for 24 h. The crude was cooled to room temperature, diluted with D.I. water and extracted with ethylacetate. This was washed twice with D.I. water, once with brine, dried with $MgSO_4$ and concentrated. The boc group was deprotected in DCM (5 mL) and HCl (1 mL). ^{1}H NMR (500 MHz, MeOD) δ 3.73 – 3.62 (m, 8H), 3.41 – 3.37 (m, 2H), 3.31 – 3.26 (m, 2H), 3.10 (t, J = 4.8 Hz, 2H).

6.8 Supplemental figures

6.8.1 FACS Histograms

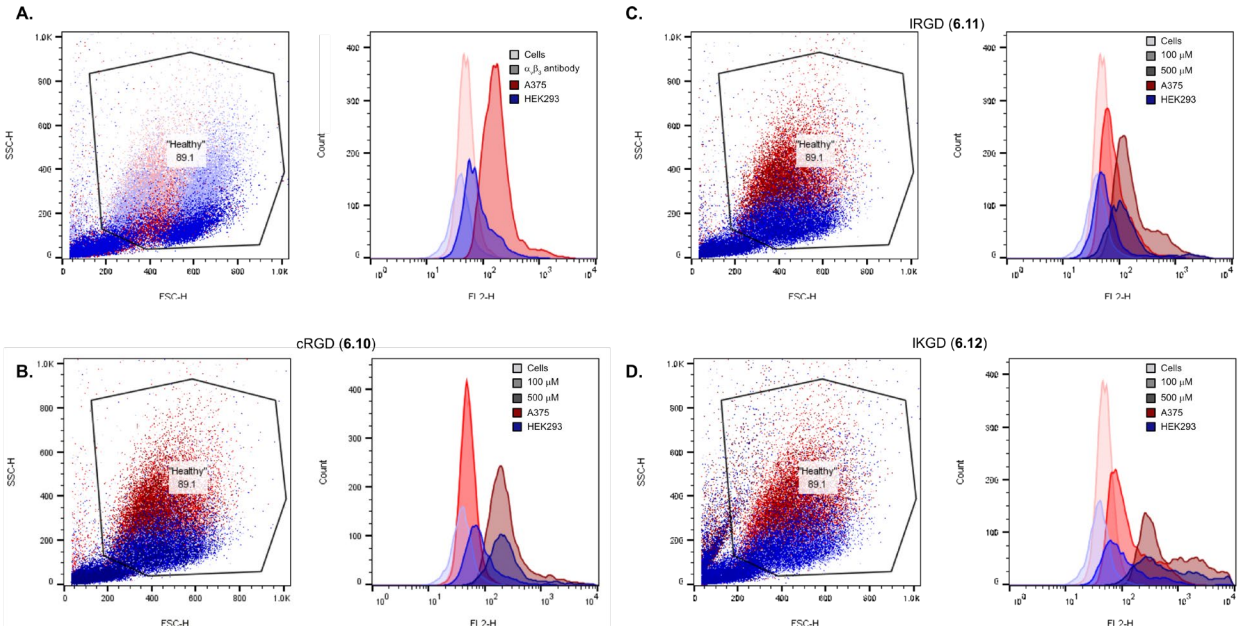

Figure S6.1 Histograms for Figure 6.4

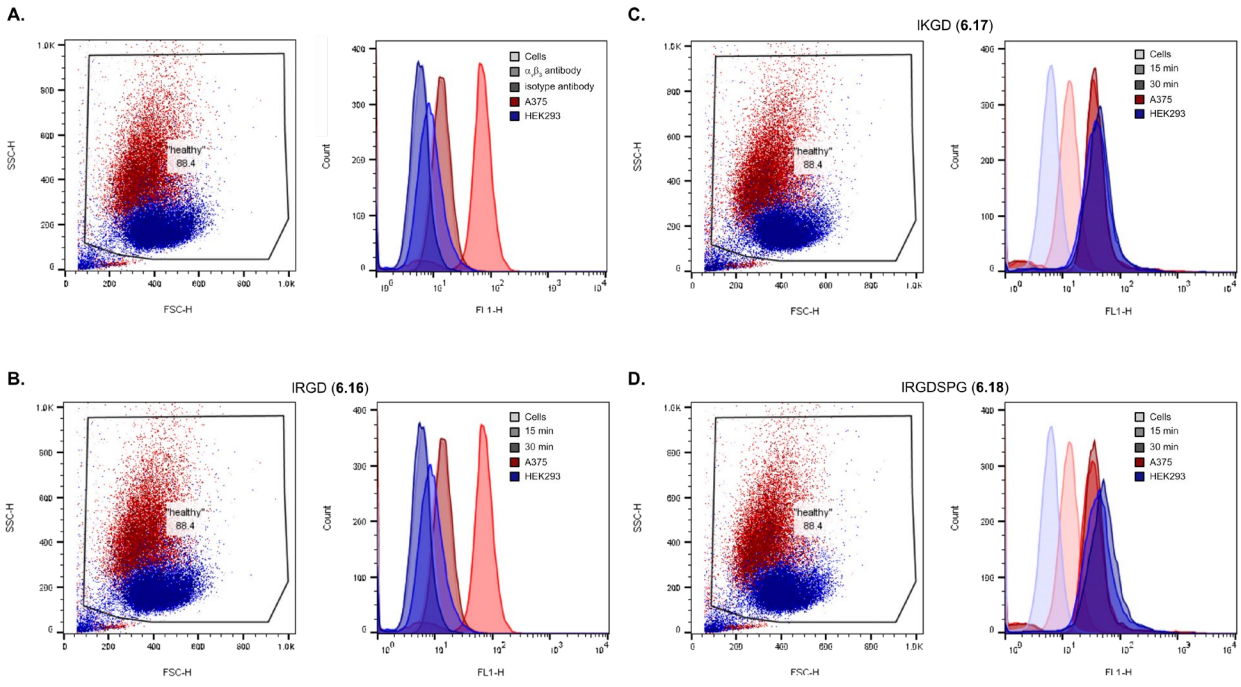

Figure S6.2 Histograms for Figure 6.5

6.8.2 LCMS

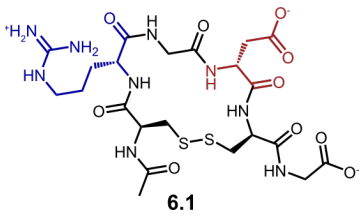

6.1

Calculated mass: 649.10

Found mass (Retention time: 0.9 min): 695 [M+2Na$^+$+H$^+$]; 709 [M+Isopropanol+H$^+$]

Residual plastic (Retention time: 0.3 min): 212

Method: 05 to 50 MeOH : H_2O; mass range 100-1,000 Da; 220 nm visualization

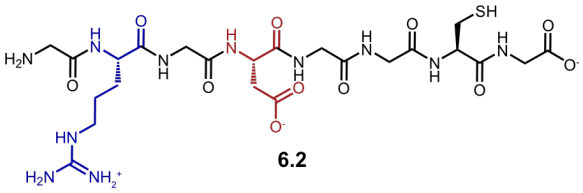

6.2

Calculated mass: 677.26

Found mass (Retention time 0.3 min): 678 [$M+H^+$]

Method: 05 to 40 MeOH : H_2O with 1% formic acid; mass range 100-1,000 Da;

220 nm visualization

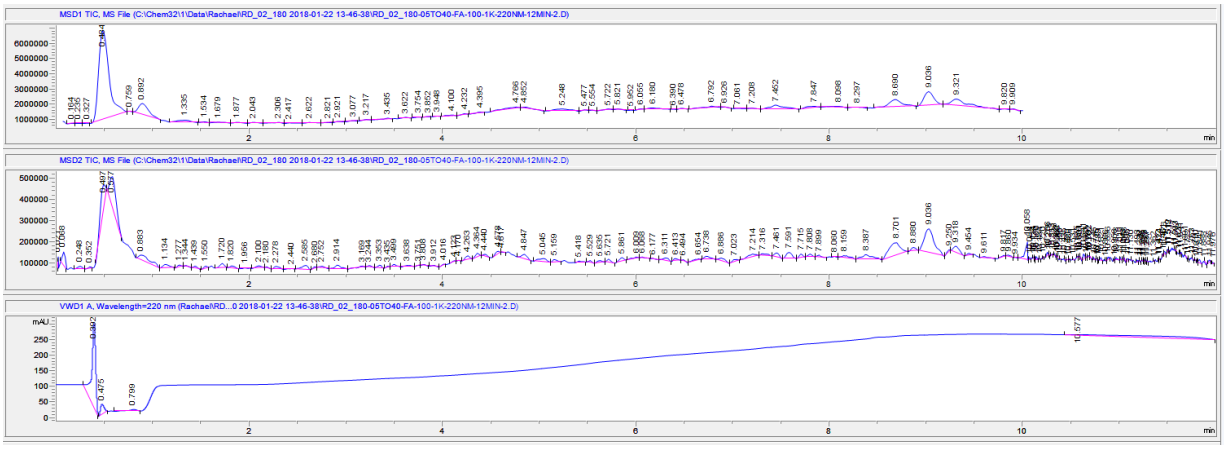

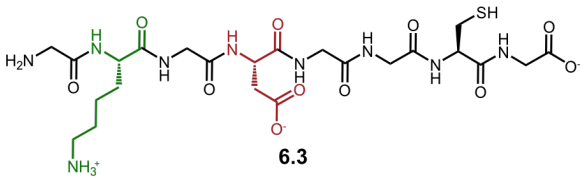

6.3

Calculated mass: 649.25

Found mass (Retention time 0.3 min): 650 [$M+H^+$]

Partially deprotected **6.3** (Retention time 2.0 min and 4.4 min)

Method: 05 to 95 MeOH : H_2O; mass range 100-1,000 Da; 220 nm visualization

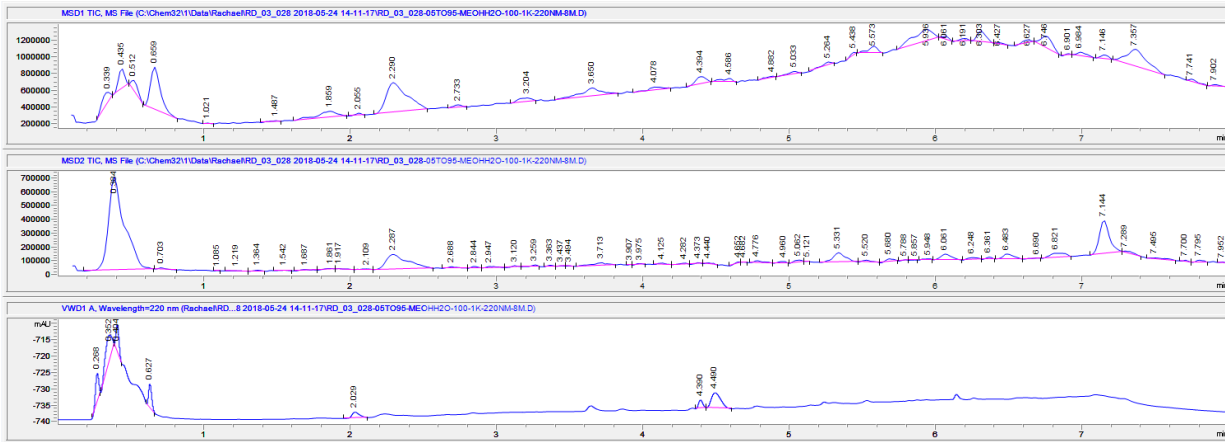

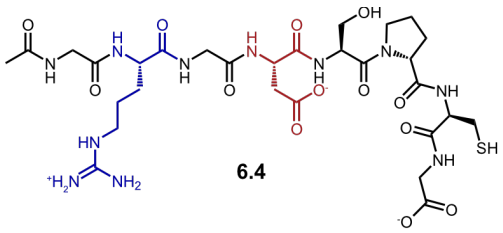

6.4

Calculated mass: 789.31

Found mass (Retention time 3.0 min): 873 [M+Isopropanol+Na^++H^+]; 970 [M+Na^++$2K^+$+H^+]

Method: 05 to 95 MeCN : H_2O with 0.1% formic acid; mass range 100-1,000 Da;

220 nm visualization

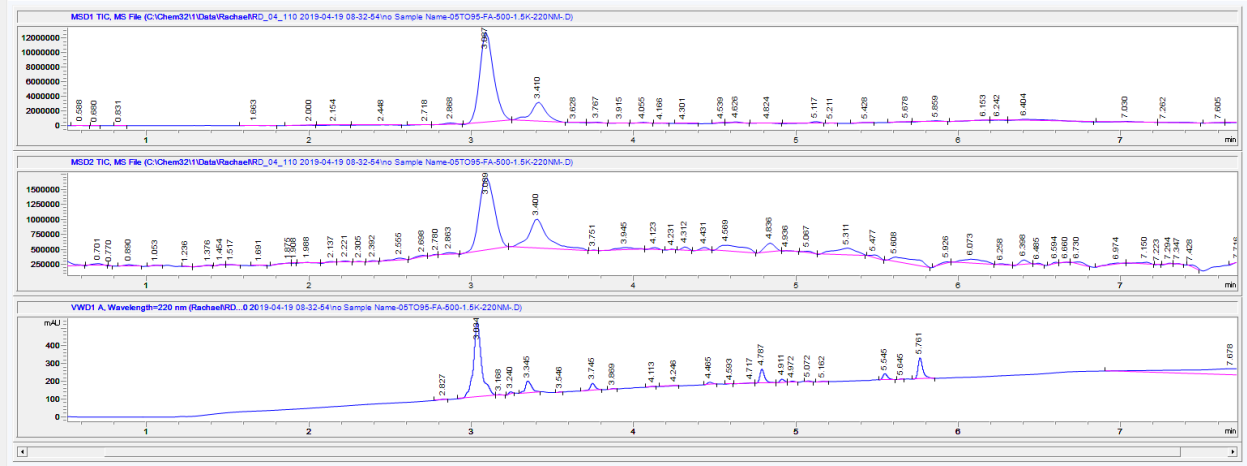

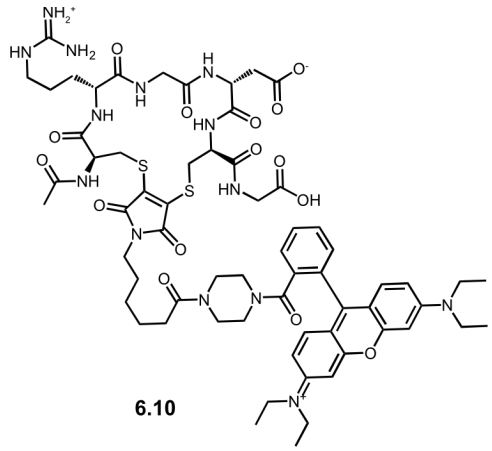

6.10

Calculated mass: 1350.49

Found mass (Retention time 4.6 min): 1410 [M+Isopropanol+H^+]

Partially bridged (Retention time (4.5 min): 1431

Method: 05 to 95 MeCN : H_2O with 0.1% formic acid; mass range 500-1,500 Da;

254 nm visualization

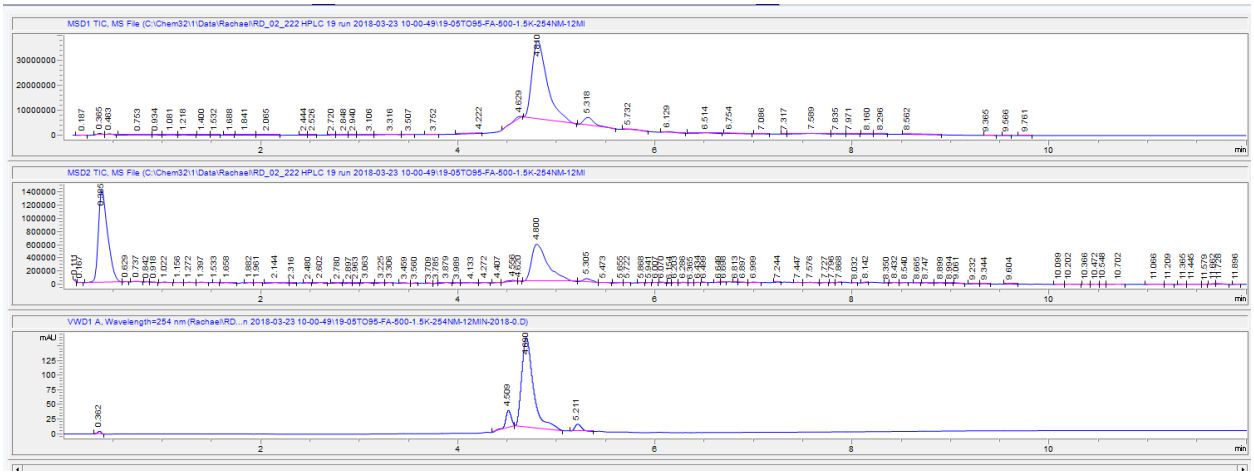

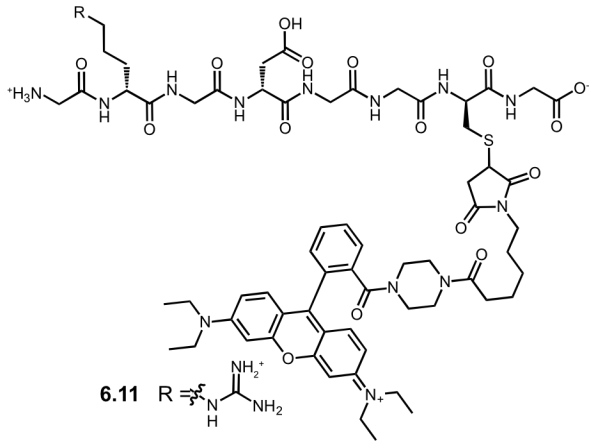

Calculated mass: 1381.64

Found mass (Retention time 4.5 min): 690.8 [M/2^{+}]

Residual plastic (0.4 min): 212

Method: 05 to 95 MeCN : H_2O with 0.1% formic acid; mass range 500-1,500 Da;

254 nm visualization

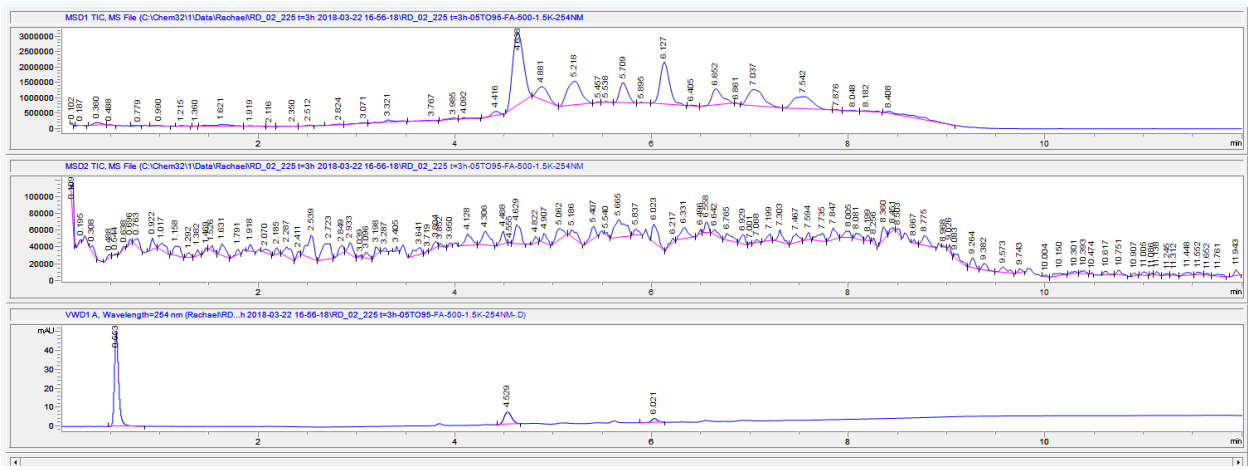

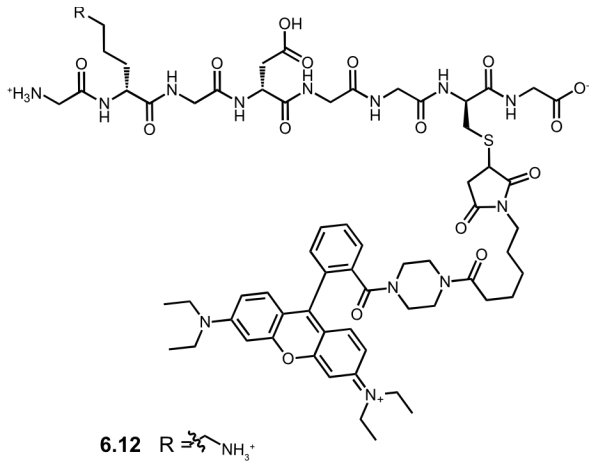

6.12

Calculated mass: 1353.63

Found mass (Retention time 3.27 min): 677.8 [$M/2^+$]

Residual plastic (Retention time 0.7 min): 212

Method: 05 to 95 MeCN : H_2O with 0.1% formic acid; mass range 500-1,500 Da;

254 nm visualization

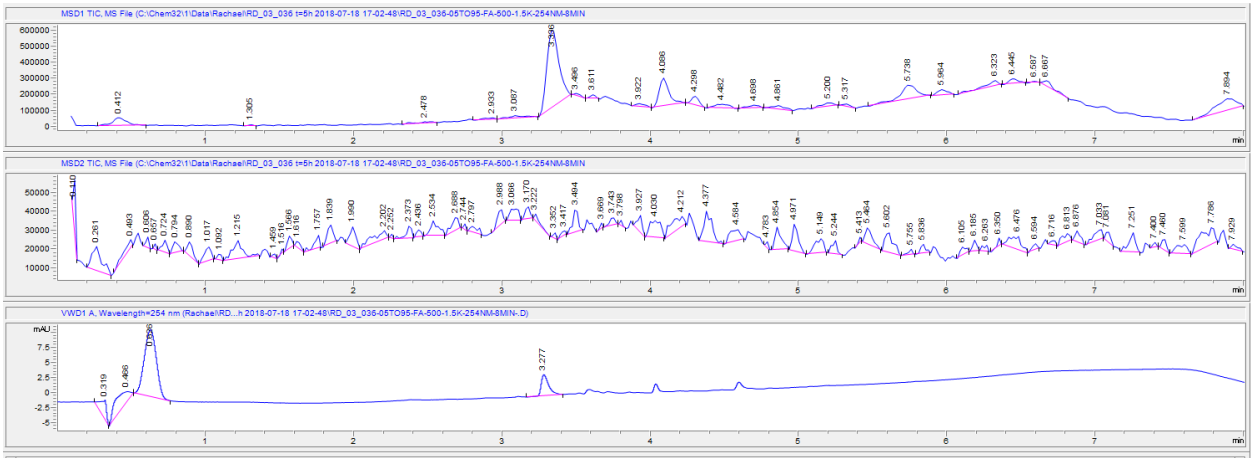

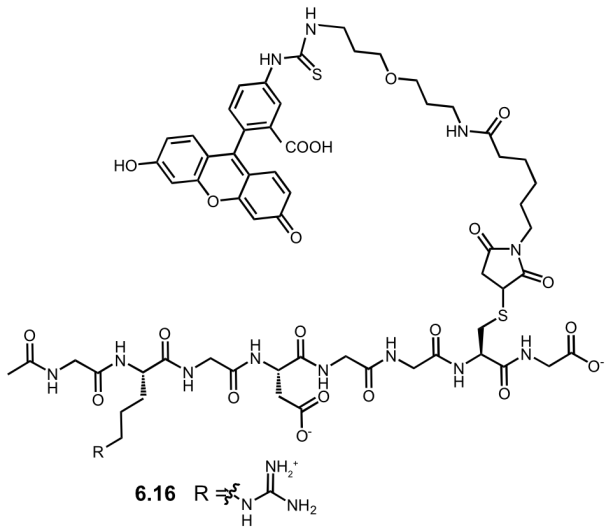

6.16

Calculated mass : 1479.53

Found mass (Retention time 3.7 min): 740 [$M/2^{+}$]

Method: 05 to 95 MeCN : H_2O with 0.1% formic acid; mass range 500-1,500 Da;

254 nm visualization

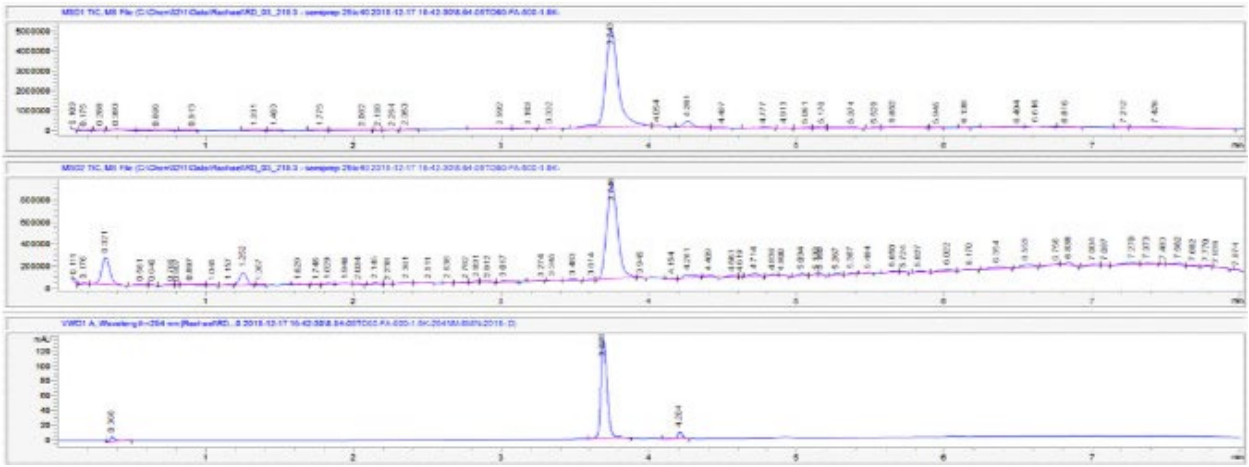

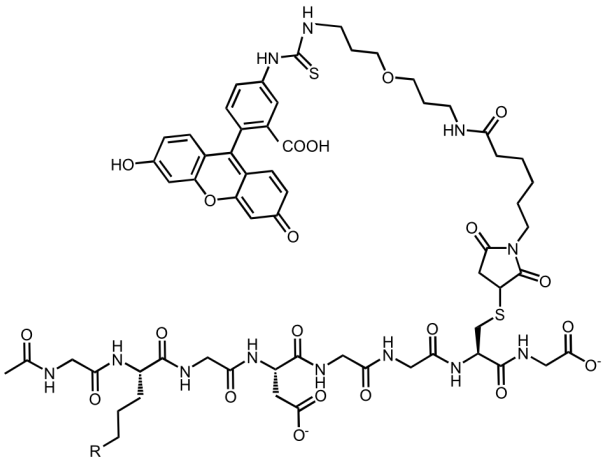

6.17 R = NH_3^+

Calculated mass: 1449.53

Found mass (Retention time 4.0 min): 725 [$M/2^+$]

Method: 05 to 95 MeCN : H_2O with 0.1% formic acid; mass range 500-1,500 Da;

254 nm visualization

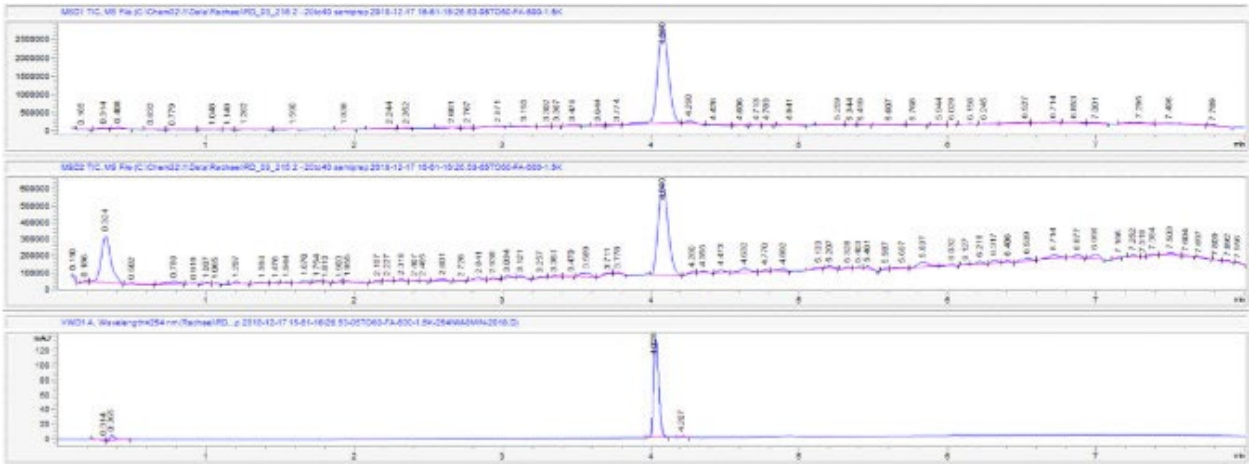

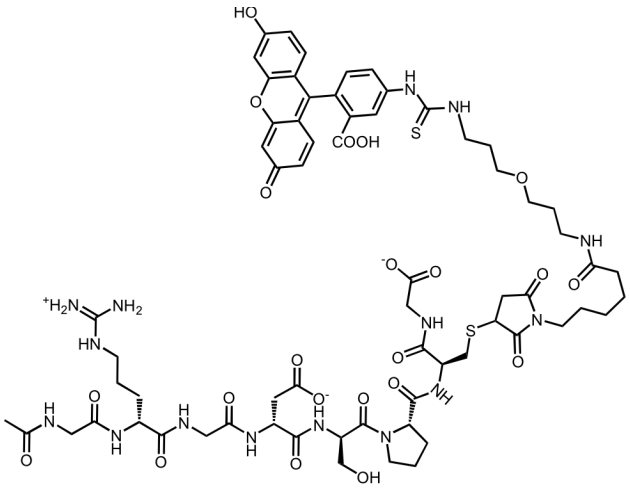

6.18

Calculated mass: 1493.57

Found mass (Retention time 3.8 min): 747 [$M/2^+$]

Method: 05 to 95 MeCN : H_2O with 0.1% formic acid; mass range 500-1,500 Da;

254 nm visualization

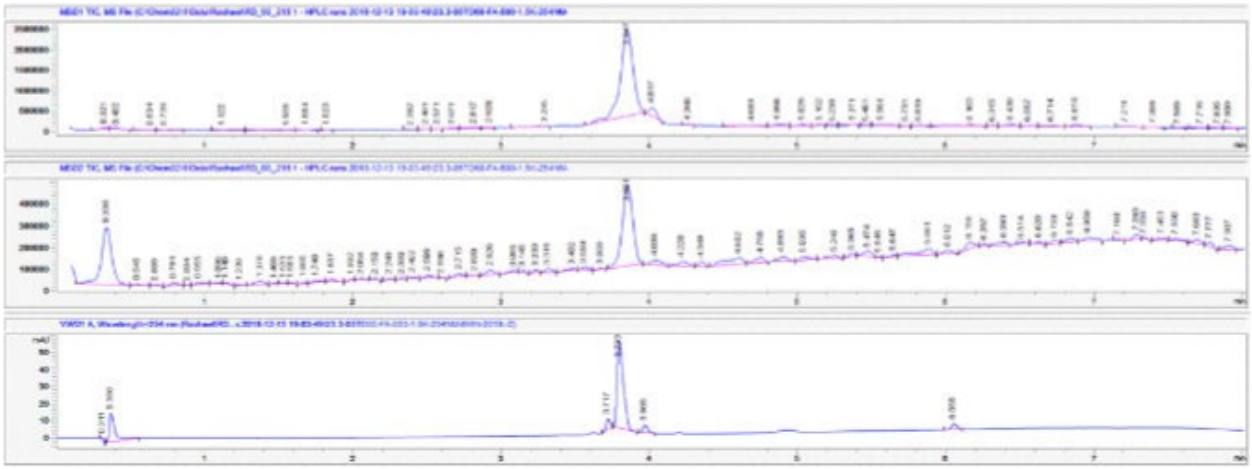

6.8.3 HPLC characterization

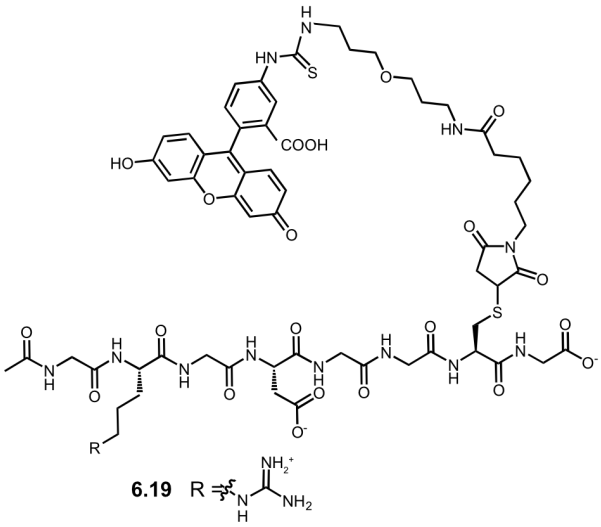

Purification HPLC after coupling with FITC-maleimide (**6.15**). **6.19** elutes at 11.78 min. Unknown products at 7, 7.9, and 9 min. Unreacted peptide elutes at 23.7 min.

Method: 30 to 50 MeCN : H_2O; visualized at 254 (top), 495 (FITC, middle), and 220 (bottom)

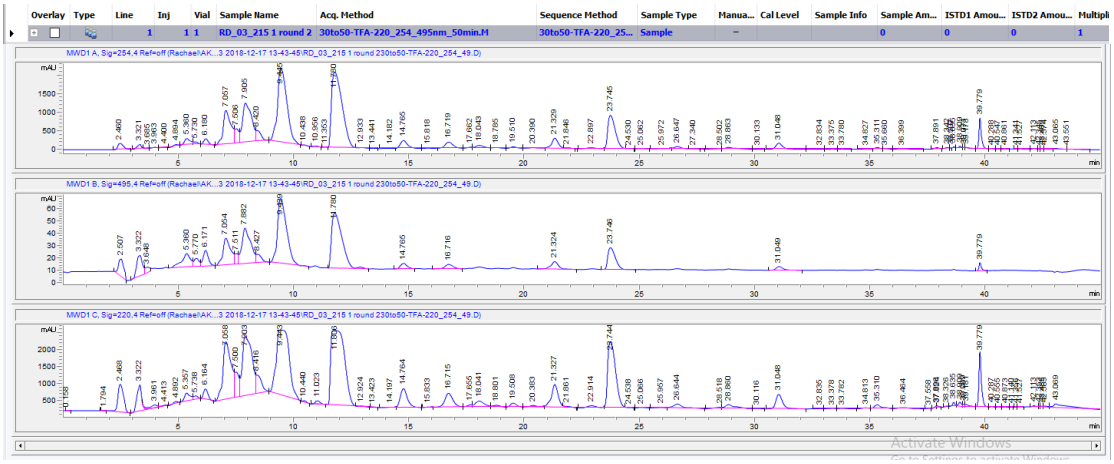

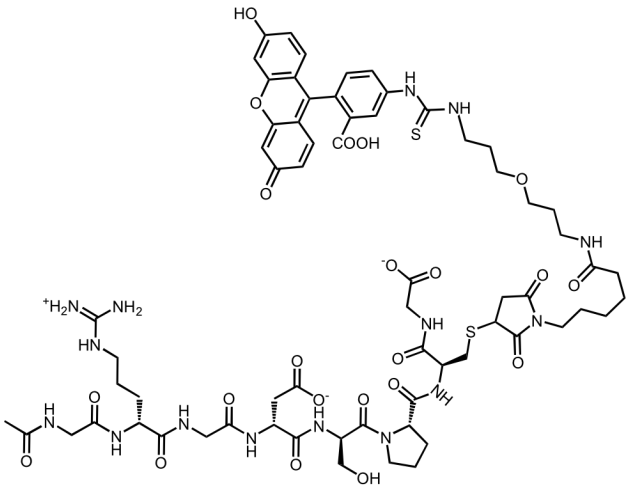

6.21

Purification HPLC after coupling with FITC-maleimide (**6.15**). **6.21** elutes at 11.78 min. DMF elutes at 2 min. Unreacted **6.15** elutes at 14.4 min and unreacted peptide elutes at 19.3 min.

Method: 30 to 60 MeCN : H_2O; visualized at 254 (top), 495 (FITC, middle), and 220 (bottom)

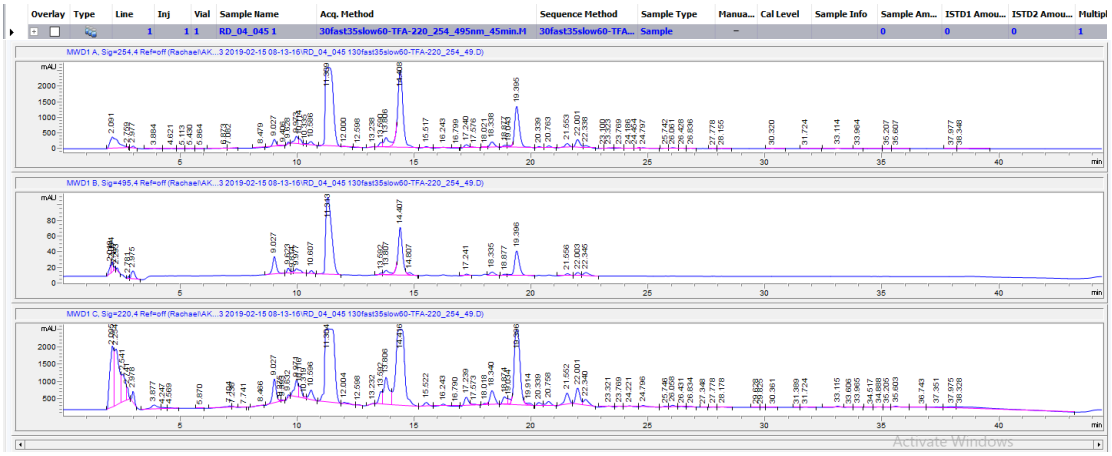

6.1 FMOC protected

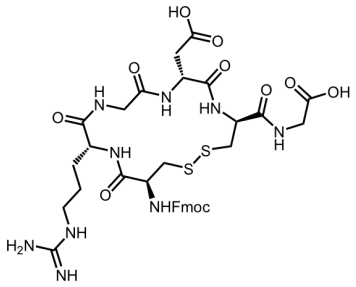

HPLC after SPPS. Product elutes at 25.4 min. DMF elutes at 2 min.

Method: 5 to 60 MeCN : H_2O; visualized at 220 (top), 254 (middle), and 495 (bottom)

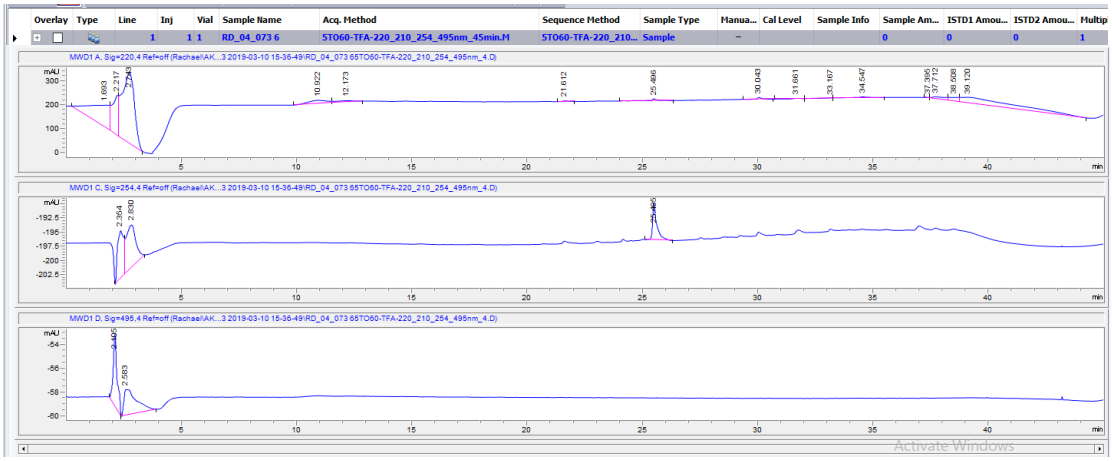

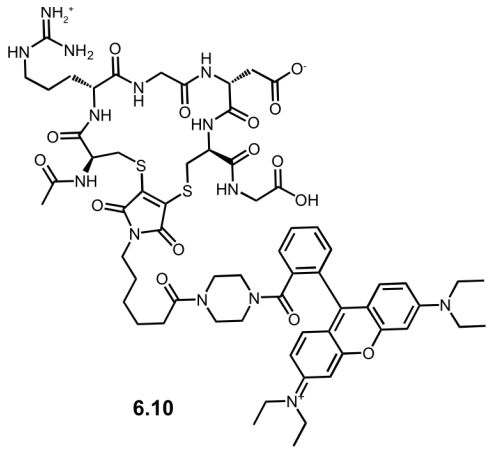

6.10

HPLC after bridging. Product elutes at 22.1 min. DMF elutes at 2 min. Unreacted peptide elutes at 12.3 min.

Method: 30 to 70 MeCN : H_2O; visualized at 254 (top), 400 (middle), and 220 (bottom)

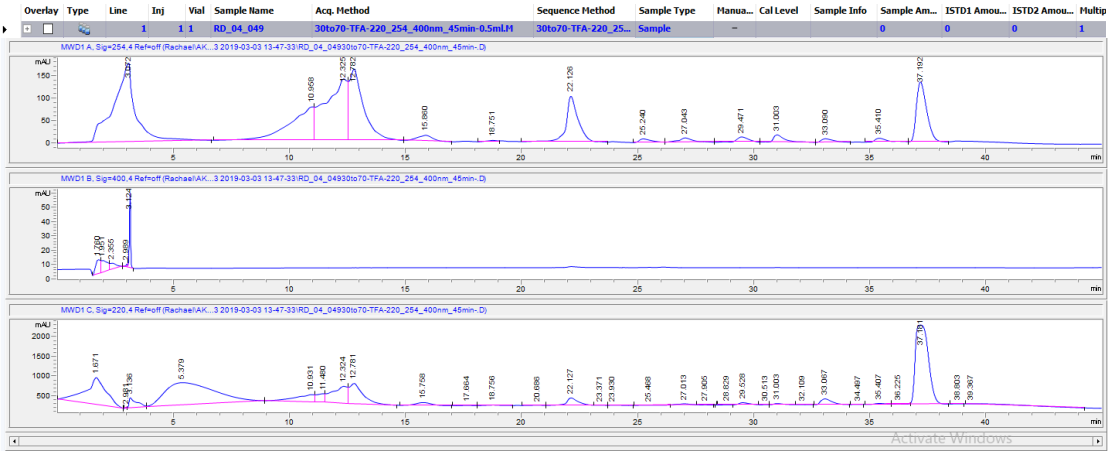

Entry 3, Table 6.1

HPLC after bridging (**6.10**). Product elutes at 15.3 min. DMF elutes at 2 min. Unknown side product elutes at 16.9 min.

Method: 30 to 70 MeCN : H_2O; visualized at 254 (top), 495 (middle), and 220 (bottom)

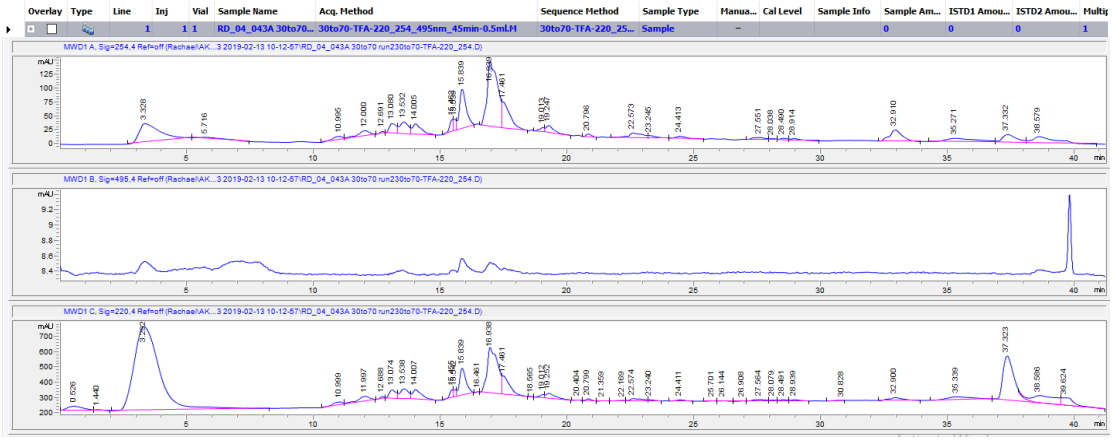

Entry 4, Table 6.1

HPLC after bridging (**6.10**). Product elutes at 15.3 min. DMF elutes at 2 min. Unknown side product elutes at 16.8 min.

Method: 30 to 70 MeCN : H_2O; visualized at 254 (top), 495 (middle), and 220 (bottom)

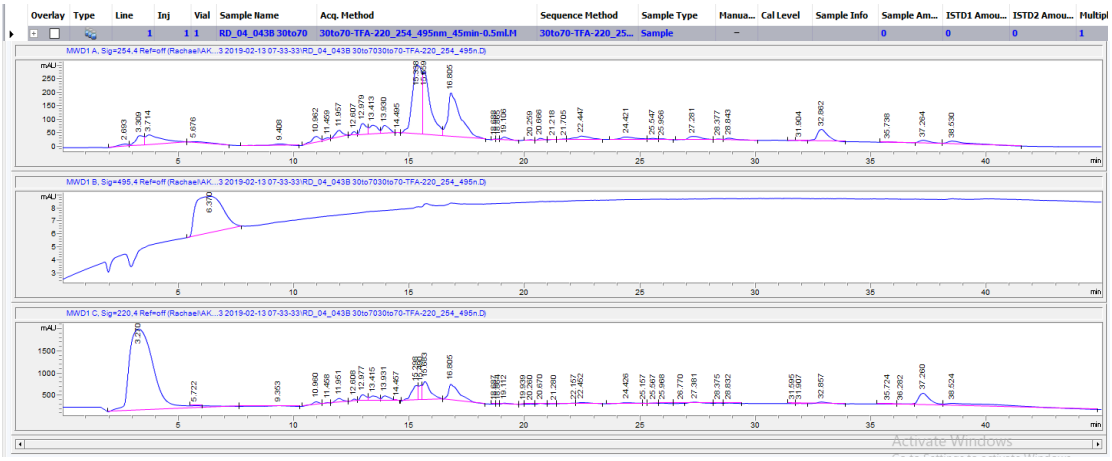

Entry 5, Table 6.1

HPLC after bridging (**6.15**). Product elutes at 18.3 min. DMF elutes at 2 min. Unknown side product elutes at 17-19 min.

Method: 30 to 70 MeCN : H_2O; visualized at 254 (top), 220 (middle), and 400 (bottom)

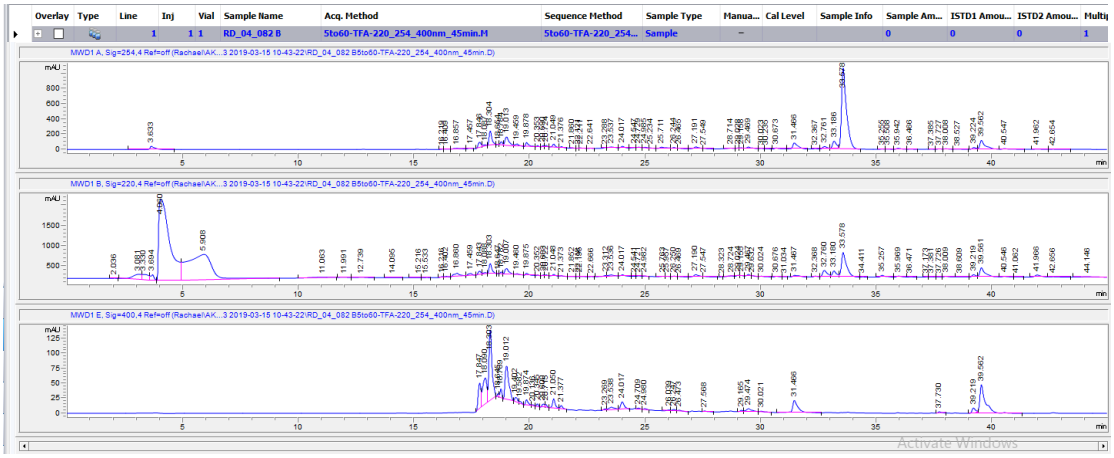

Entry 6, Table 6.1

HPLC after bridging (**6.10**). Product elutes at 15.3 min. DMF elutes at 2 min. Unknown side product elutes at 16.9 min

Method: 30 to 70 MeCN : H_2O; visualized at 254 (top), 495 (middle), and 220 (bottom)

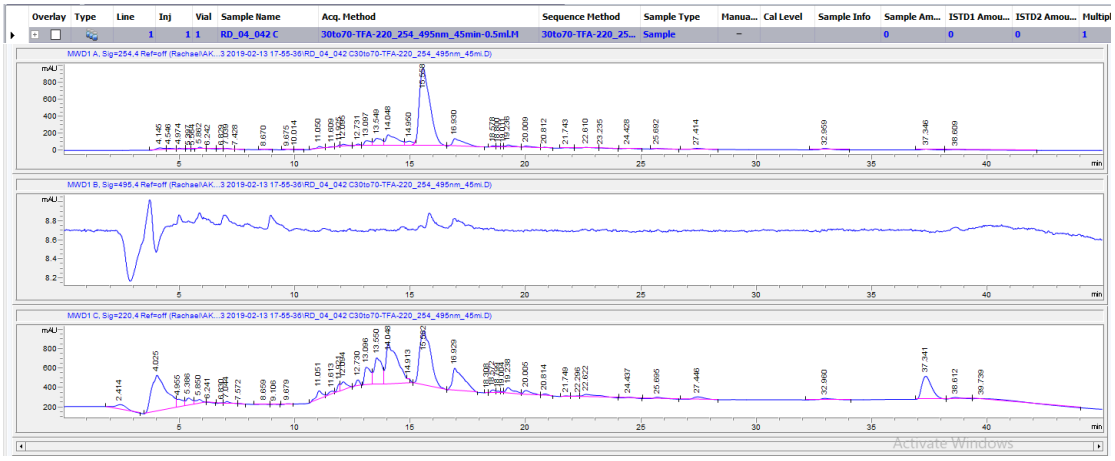

Entry 7, Table 6.1

HPLC after bridging (**6.15**). Product elutes at 15.3 min. DMF elutes at 2 min. Unknown side product elutes at 16.9 min. DMF elutes at 2 min.

Method: 30 to 70 MeCN : H_2O; visualized at 254 (top), 220 (middle), and 400 (bottom)

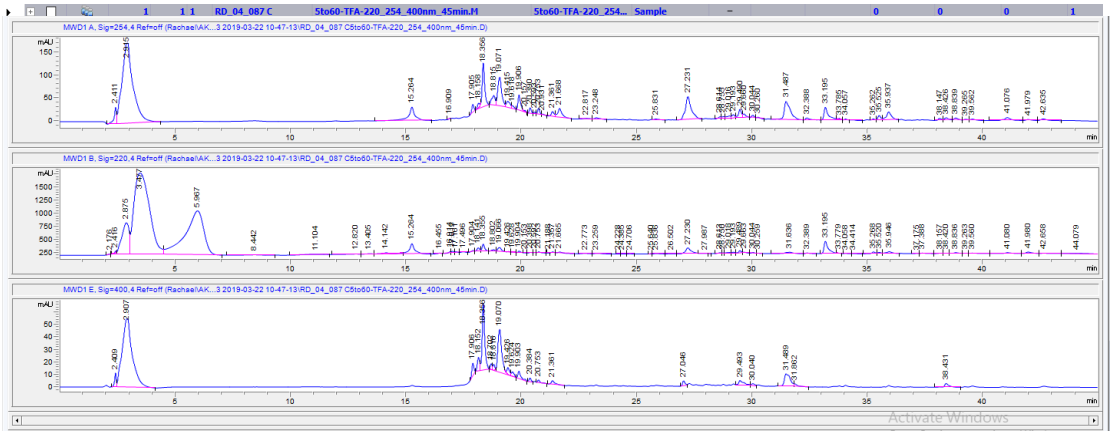

Entry 8, Table 6.1

HPLC after bridging (**6.15**). Product elutes at 15.3 min. DMF elutes at 2 min. Unknown side product elutes at 16.9 min. DMF elutes at 2 min.

Method: 30 to 70 MeCN : H_2O; visualized at 254 (top), 220 (middle), and 400 (bottom)

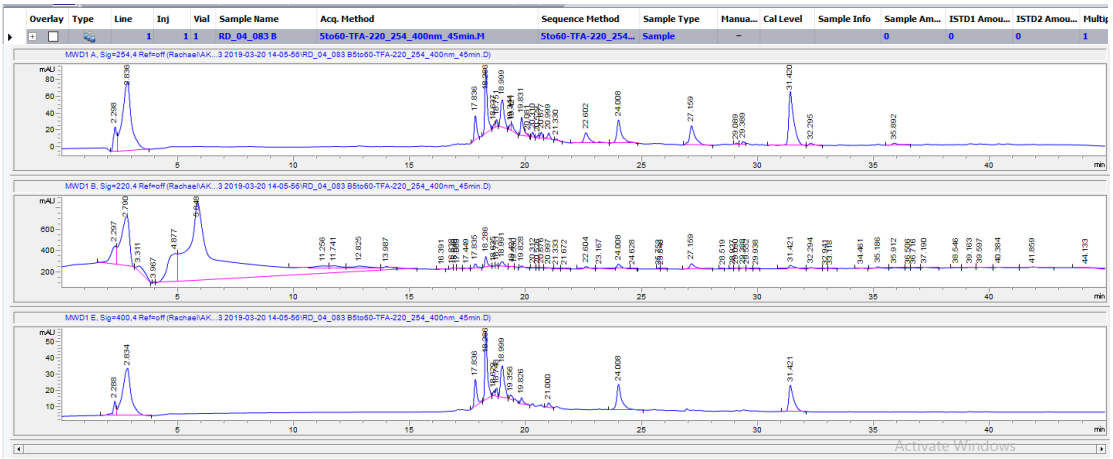

Entry 9, Table 6.1

HPLC after bridging (**6.15**). Product elutes at 15.3 min. DMF elutes at 2 min. Unknown side product elutes at 16.9 min.

Method: 30 to 70 MeCN : H_2O; visualized at 254 (top), 220 (middle), and 400 (bottom)

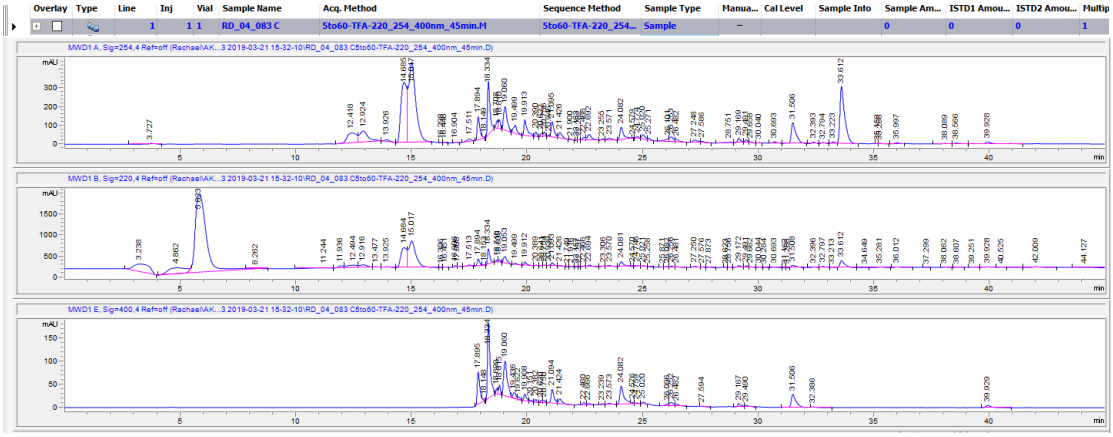

Entry 10, Table 6.1

HPLC after bridging (**6.15**). Product elutes at 15.3 min. DMF elutes at 2 min. Unknown side product elutes at 15.2 min and 19.1 min.

Method: 30 to 70 MeCN : H_2O; visualized at 254 (top), 220 (middle), and 400 (bottom)

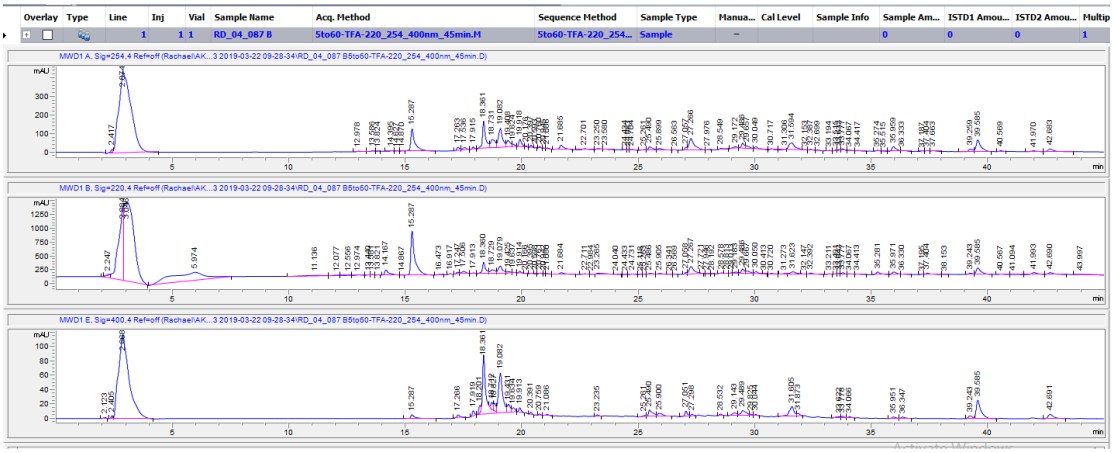

6.9 NMR Characterization

6.9.1 ^{1}H NMR

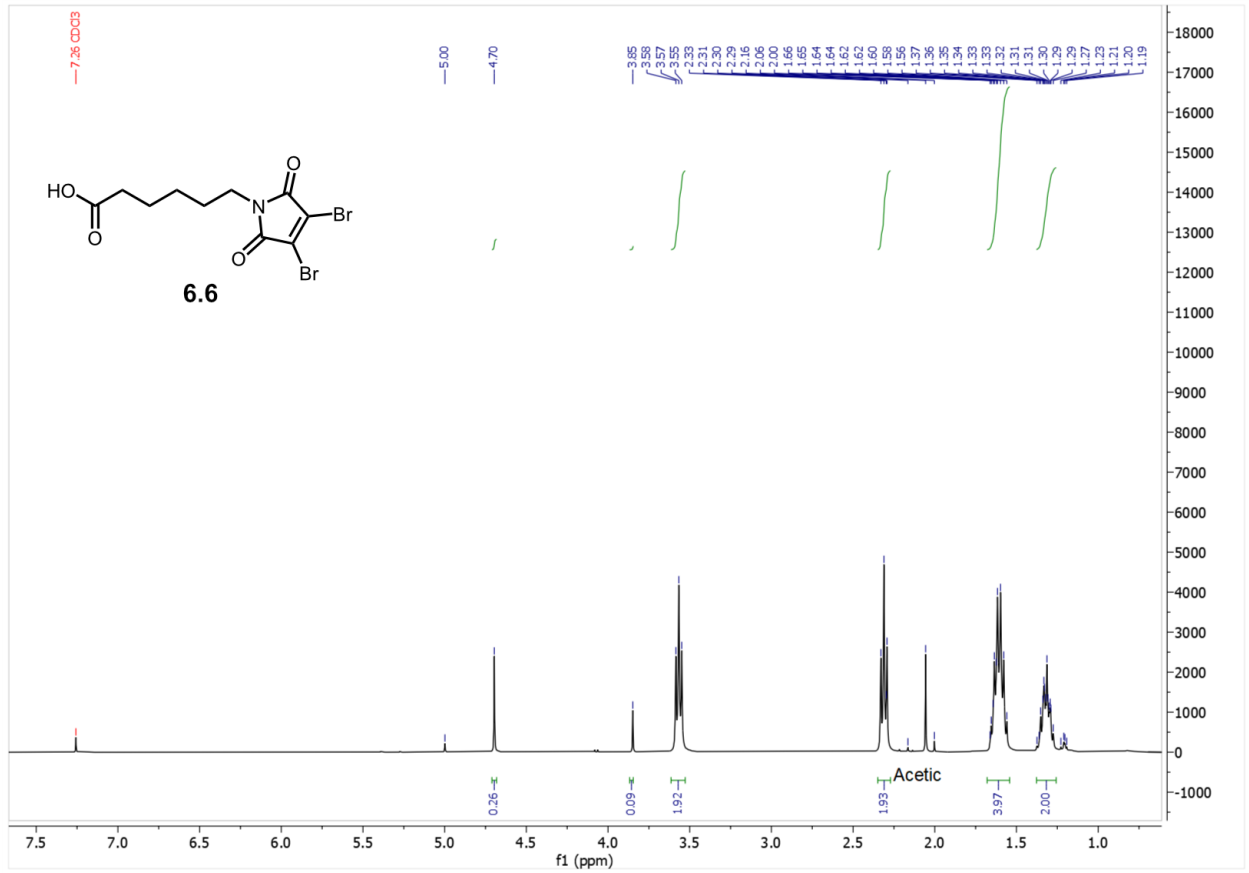

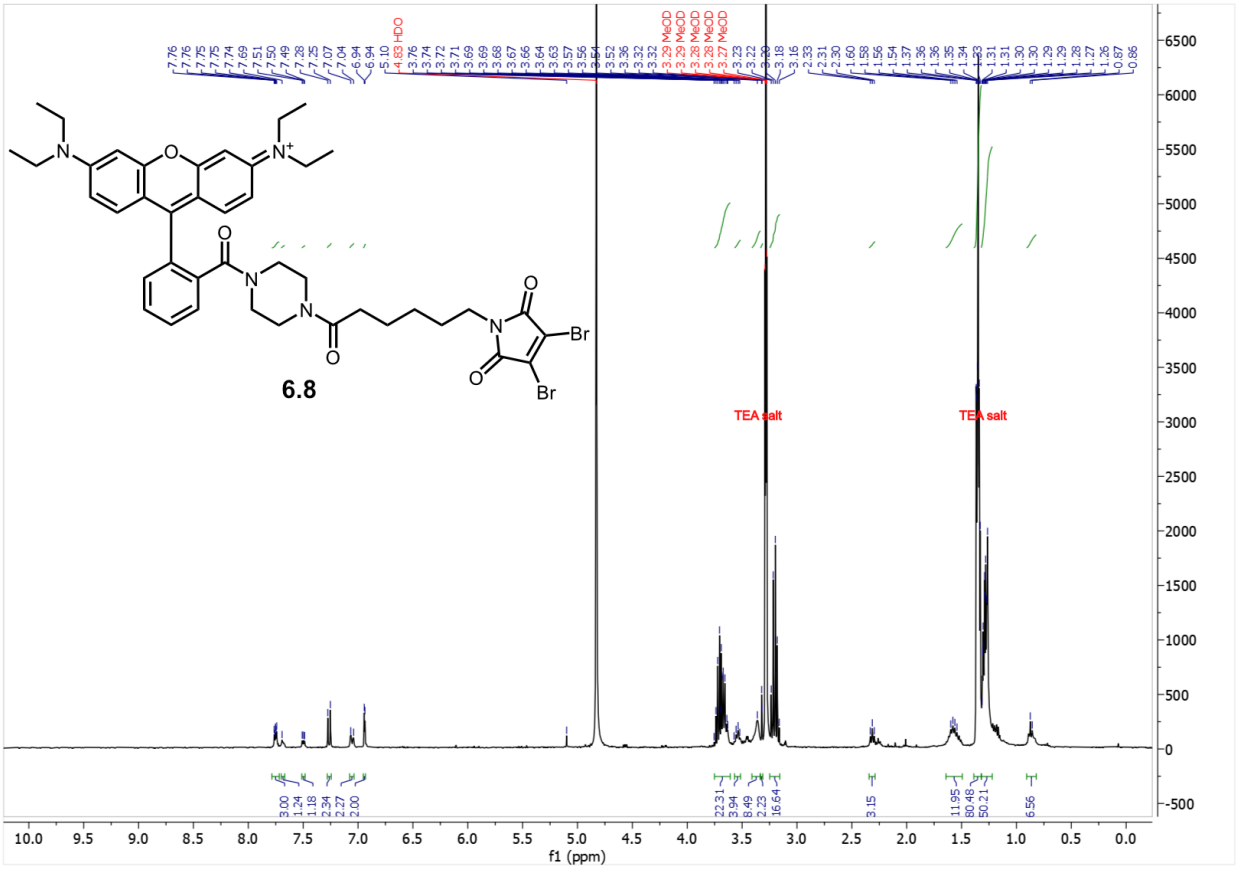
6.8
TEA salt
TEA salt
f1 (ppm)

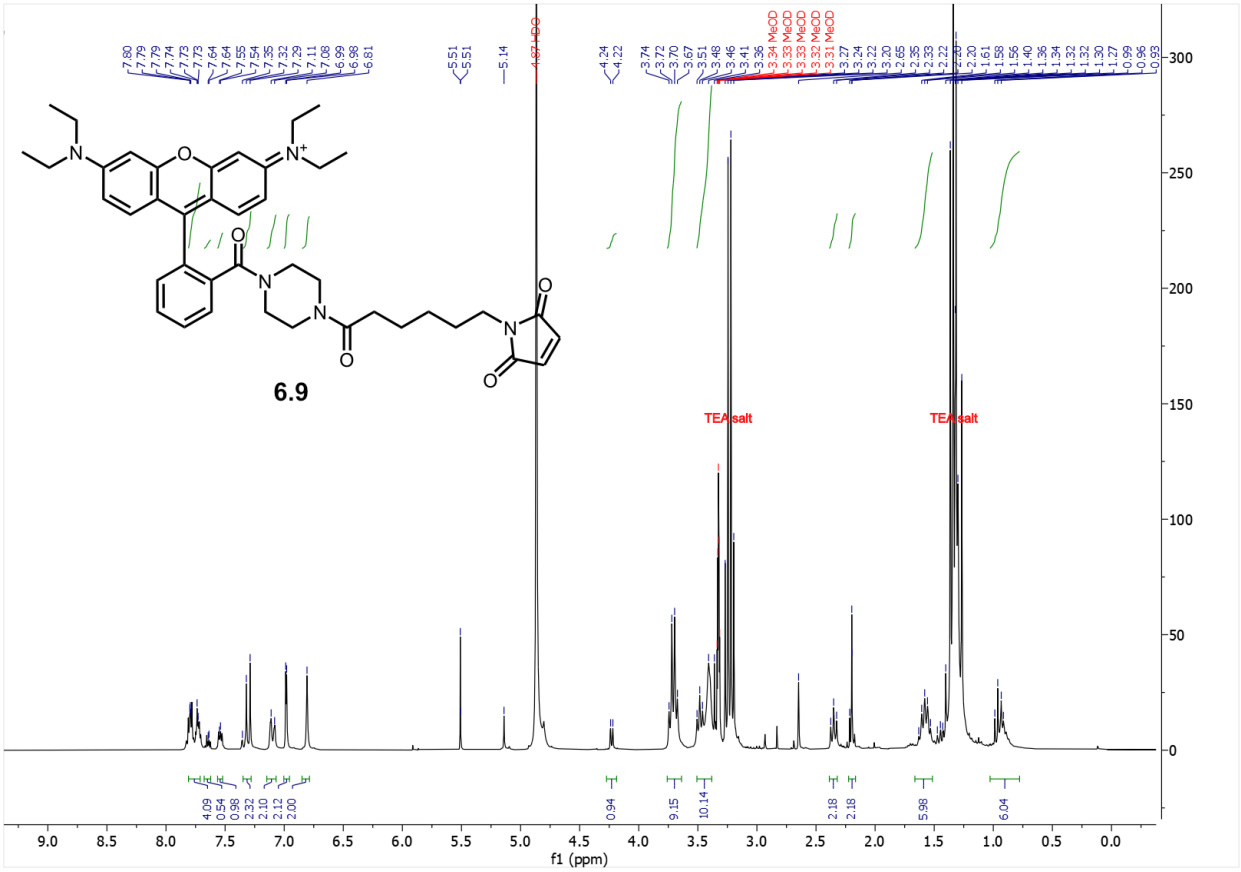
6.9
TEA salt
TEA salt
f1 (ppm)

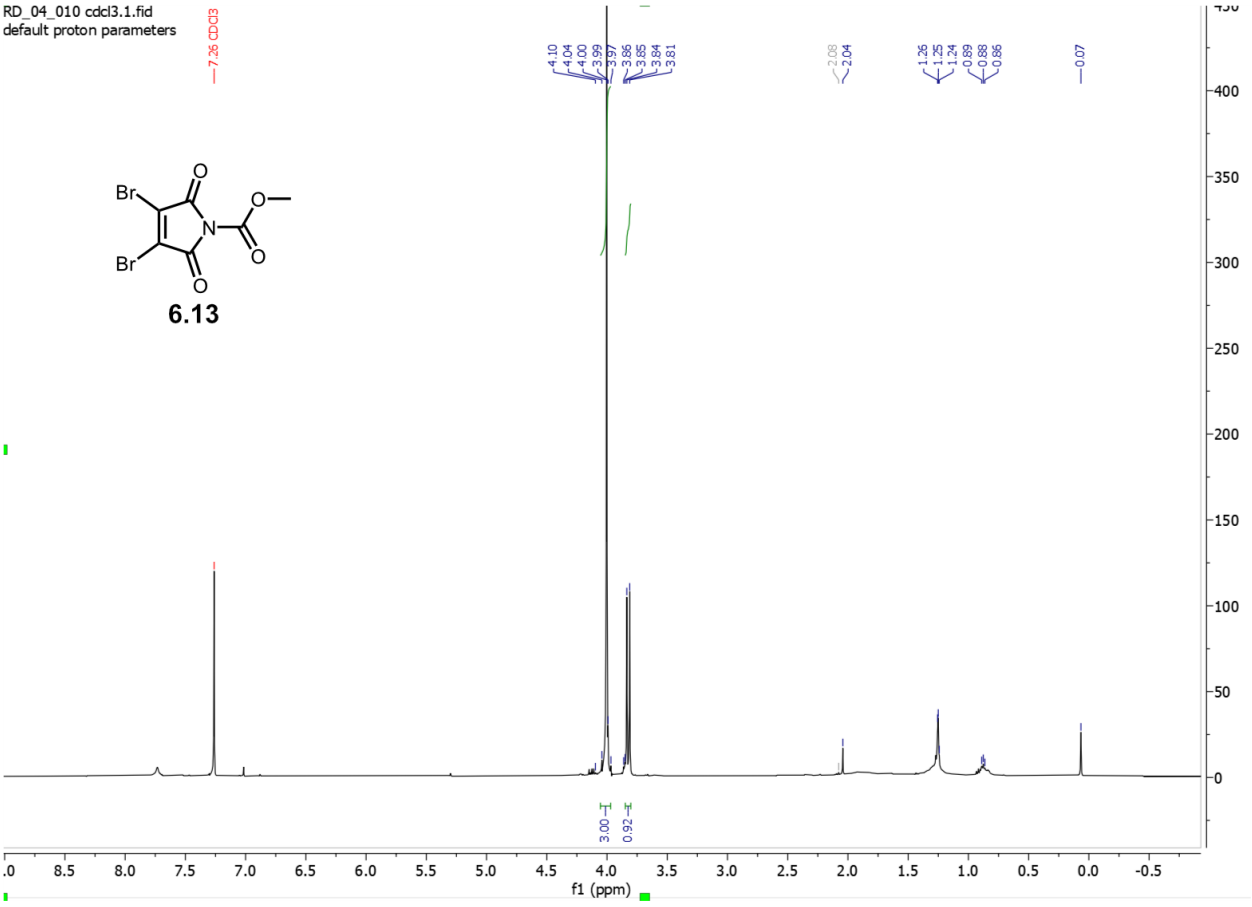
RD_04_010 cdcl3.1.fid
default proton parameters
7.26 CDCl3
4.10
4.04
4.00
3.99
3.97
3.86
3.85
3.84
3.81
2.08
2.04
1.26
1.25
1.24
0.89
0.88
0.86
0.07
Br
Br
O
O
O
N
O
O
6.13
3.00
0.92
f1 (ppm)

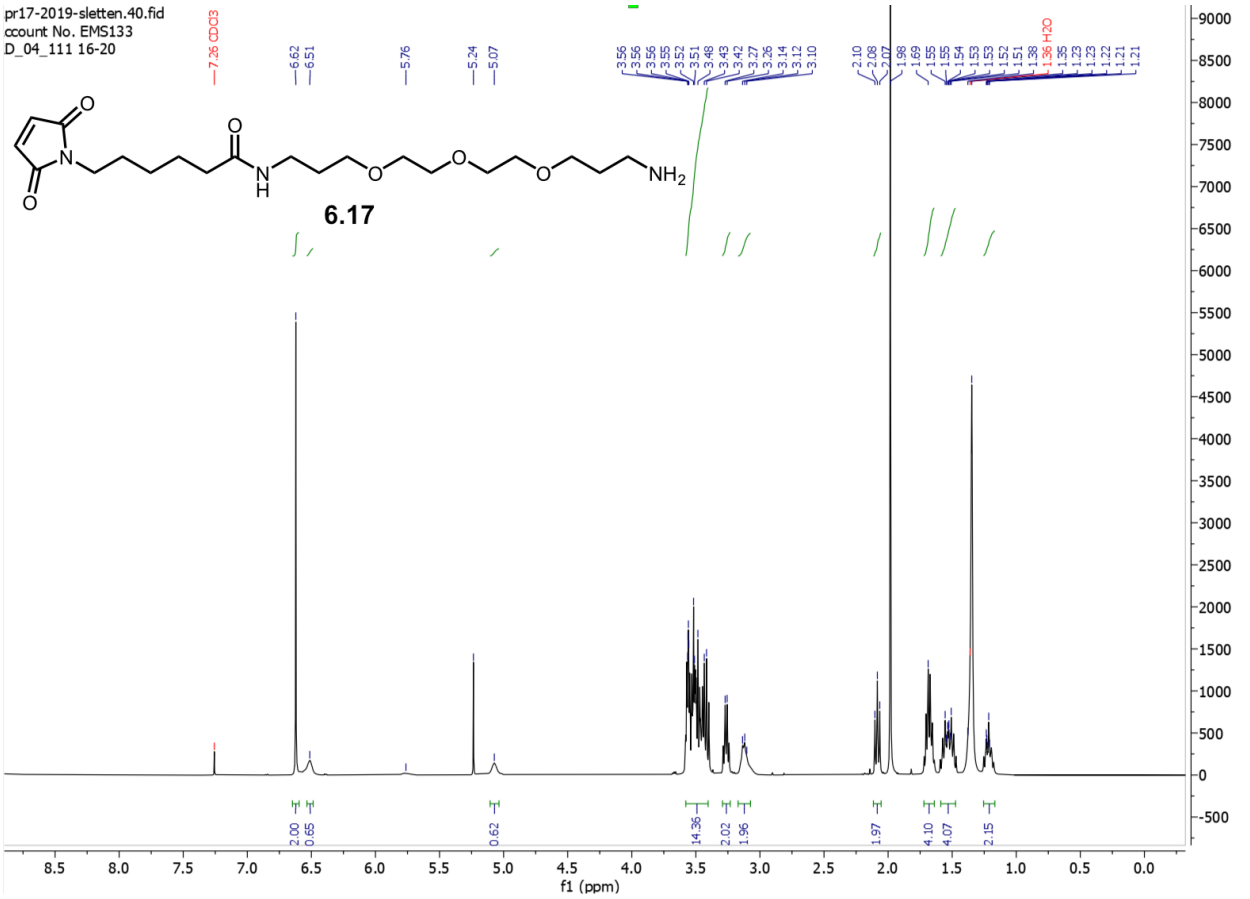
pr17-2019-sletten.40.fid
ccount No. EMS133
D_04_111 16-20
6.17
f1 (ppm)

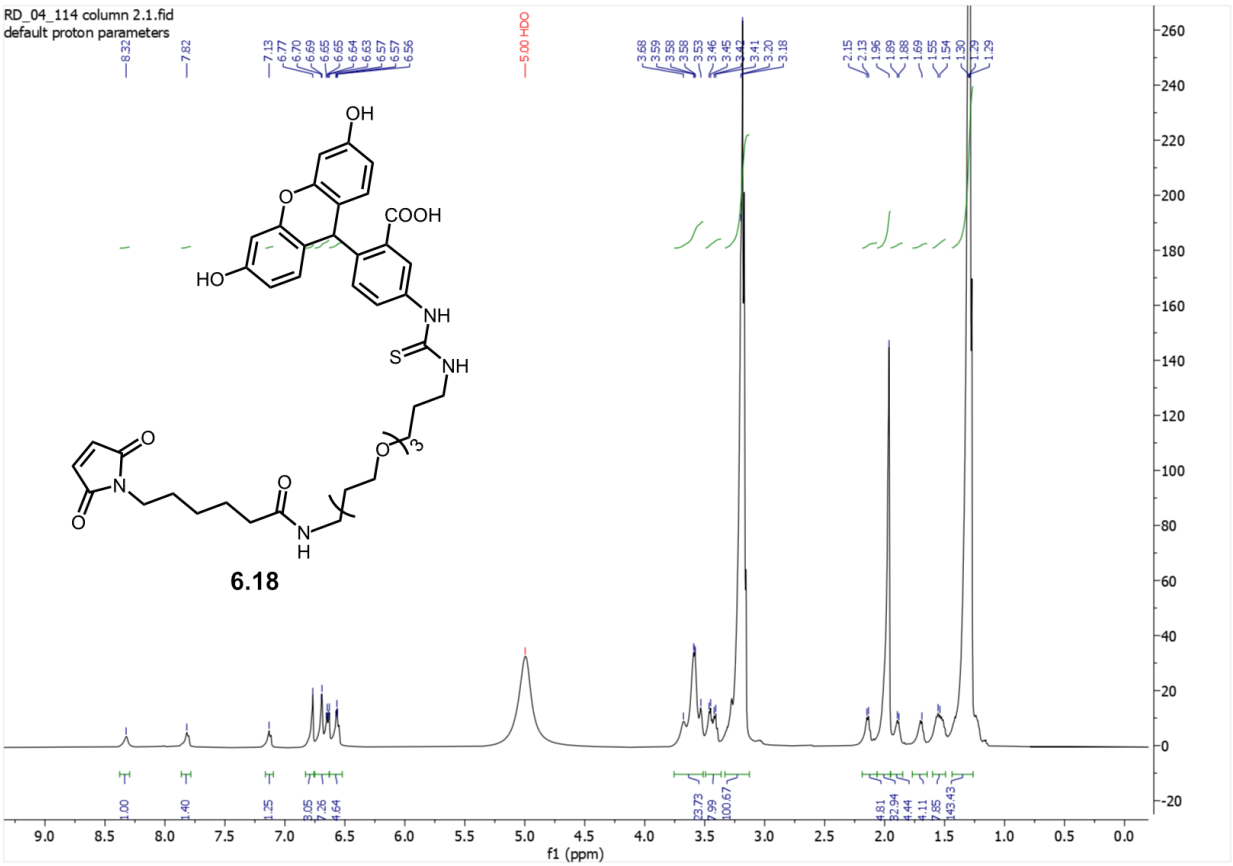
RD_04_114 column 2.1.fid
default proton parameters
OH
O
COOH
HO
NH
S
NH
O
O
N
O
O
N
H
6.18
f1 (ppm)

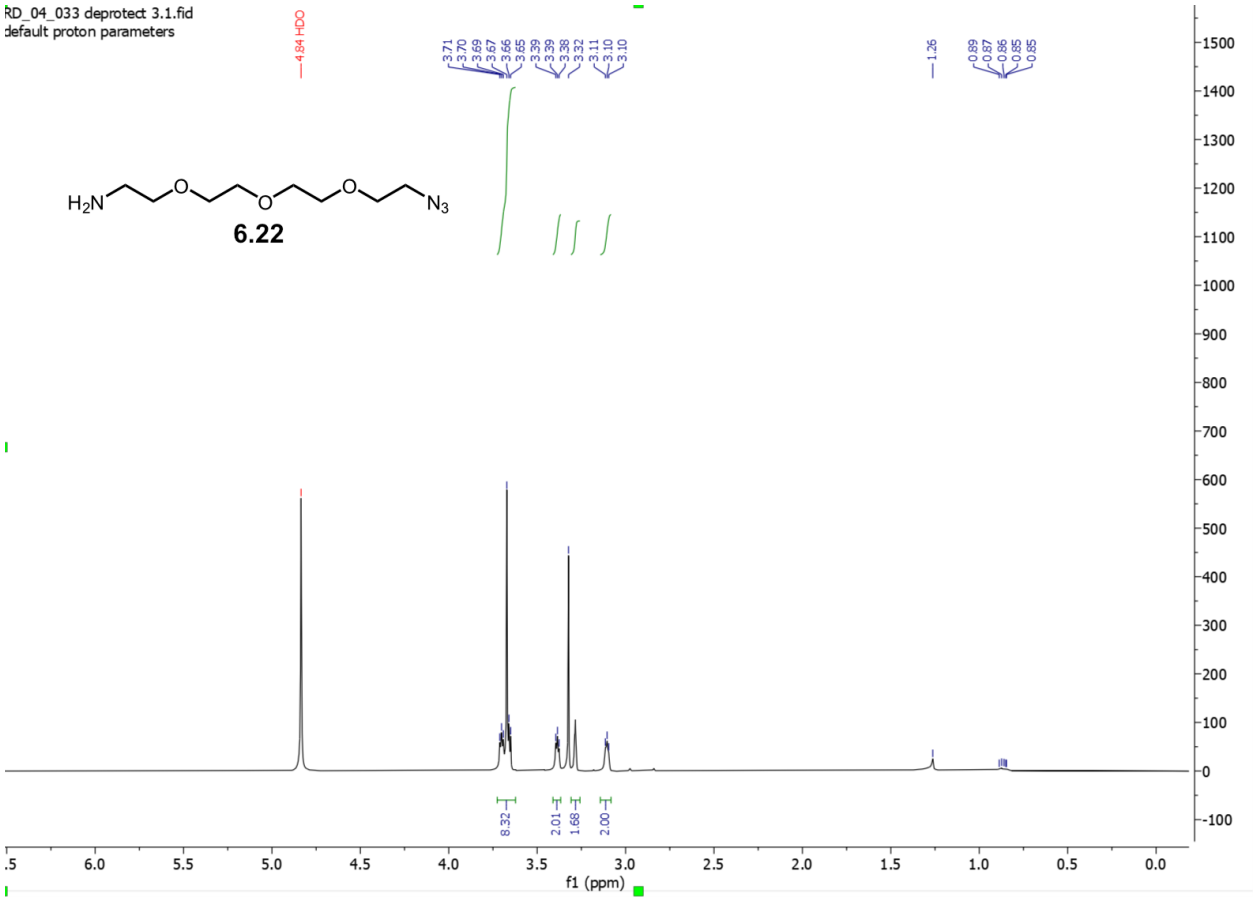
RD_04_033 deprotect 3.1.fid
default proton parameters
4.84 HDO
3.71
3.70
3.69
3.67
3.66
3.65
3.39
3.39
3.38
3.32
3.11
3.10
3.10
1.26
0.89
0.87
0.86
0.85
0.85
H2N
O
O
O
N3
6.22
8.32
2.01
1.68
2.00
f1 (ppm)

6.10 References and Notes

(1) Bazak, R.; Houri, M.; El Achy, S.; Kamel, S.; Refaat, T. Cancer Active Targeting by Nanoparticles: A Comprehensive Review of Literature. *J. Cancer Res. Clin. Oncol.* **2015**, *141*, 769.

(2) Xiong, J. P.; Stehle, T.; Zhang, R.; Joachimiak, A.; Frech, M.; Goodman, S. L.; Arnaout, M. A. Crystal Structure of the Extracellular Segment of Integrin AVβ3 in Complex with an Arg-Gly-Asp Ligand. *Science (80-.).* **2002**, *296*, 151–155.

(3) Desgrosellier, J.; David, C. Integrins in Cancer: Biological Implications in Therapeutic Opportunities. *Nat. Rev. Cancer* **2010**, *10*, 9–22.

(4) Ruoslahti, E. Rgd and Other Recognition Sequences for Integrins. *Annu. Rev. Cell Dev. Biol.* **1996**, *12*, 697.

(5) Pierschbacher, M. D.; Ruoslahti, E. Cell Attachment Activity of Fibronectin Can Be Duplicated by Small Synthetic Fragments of the Molecule. *Nature* **1984**, *309*, 30.

(6) Bloch, S.; Xu, B.; Ye, Y.; Liang, K.; Nikiforovich, G. V.; Achilefu, S. Targeting Beta-3 Integrin Using a Linear Hexapeptide Labeled with a near-Infrared Fluorescent Molecular Probe. *Mol. Pharm.* **2006**, *3*, 539–549.

(7) Hedhli, J.; Czerwinski, A.; Schuelke, M.; P?oska, A.; Sowinski, P.; Hood, L. La; Mamer, S. B.; Cole, J. A.; Czaplewska, P.; Banach, M.; Dobrucki, I. T.; Kalinowski, L.; Imoukhuede, P.; Dobrucki, L. W. Synthesis, Chemical Characterization and Multiscale Biological Evaluation of a Dimeric-CRGD Peptide for Targeted Imaging of AVb3

Integrin Activity. *Sci. Rep.* **2017**, *7*, 3185.

(8) Dechantsreiter, M. A.; Planker, E.; Mathä, B.; Lohof, E.; Hölzemann, G.; Jonczyk, A.; Goodman, S. L.; Kessler, H. N-Methylated Cyclic RGD Peptides as Highly Active and Selective α(v)B3 Integrin Antagonists. *J. Med. Chem.* **1999**, *42*, 3033–3040.

(9) Hautanen, A.; Gailit, J.; Mann, D. M.; Ruoslahti, E. Effects of Modifications of the RGD Sequence and Its Context on Recognition by the Fibronectin Receptor. *J. Biol. Chem.* **1989**, *264*, 1437.

(10) Haubner, R.; Gratias, R.; Diefenbach, B.; Goodman, S. L.; Jonczyk, A.; Kessler, H. Structural and Functional Aspects of RGD-Containing Cyclic Pentapeptides as Highly Potent and Selective Integrin AVB3 Antagonists. *J. Am. Chem. Soc.* **1996**, *118*, 7461.

(11) Danhier, F.; Breton, A. Le; Préat, V. RGD-Based Strategies to Target Alpha(v) Beta(3) Integrin in Cancer Therapy and Diagnosis. *Mol. Pharm.* **2012**, *9*, 2961.

(12) Bogdanowich-Knipp, S. J.; Chakrabarti, S.; Williams, T. D.; Dillman, R. K.; Siahaan, T. J. Solution Stability of Linear vs. Cyclic RGD Peptides. *J. Pept. Res.* **1999**, *53*, 530.

(13) von Wallbrunn, A.; Höltke, C.; Zühlsdorf, M.; Heindel, W.; Schäfers, M.; Bremer, C. In Vivo Imaging of Integrin Avβ3 Expression Using Fluorescence-Mediated Tomography. *Eur. J. Nucl. Med. Mol. Imaging* **2007**, *34*, 745–754.

(14) Cheng, S.; Crain, W. S.; Mullen, D.; Tschopp, J. F.; Dixon, D.; Pierschbacher, M. D. Design and Synthesis of Novel Cyclic RGD-Containing Peptides as Highly Potent and Selective Integren Avb3 Antagonists. *J. Med. Chem.* **1994**, *37*, 1–8.

(15) White, C. J.; Yudin, A. K. Contemporary Strategies for Peptide Macrocylization. *Nat. Chem.* **2011**, *3*, 509–524.

(16) Gunnoo, S. B.; Madder, A. Chemical Protein Modification through Cysteine. *ChemBioChem* **2016**, *17*, 529–553.

(17) Tedaldi, L. M.; Smith, M. E. B.; Nathani, R. I.; Baker, J. R. Bromomaleimides : New Reagents for the Selective and Reversible Modification of Cysteine. *Chem. Commun.* **2009**, 6583–6585.

(18) Caddick, S.; Baker, J. R. Bromo- and Thiomaleimides as a New Class of Thiol-Mediated Fluorescence “turn-on” Reagents. *Org. Biomol. Chem.* **2014**, *12*, 557–560.

(19) Schumacher, F. F.; Nobles, M.; Ryan, C. P.; Smith, M. E. B.; Tinker, A.; Caddick, S.; Baker, J. R. In Situ Maleimide Bridging of Disulfides and a New Approach to Protein PEGylation. *Bioconjug. Chem.* **2011**, *22*, 132–136.

(20) Smith, M. E. B.; Schumacher, F. F.; Ryan, C. P.; Tedaldi, L. M.; Papaioannou, D.; Waksman, G.; Caddick, S.; Baker, J. R. Protein Modification, Bioconjugation, and Disulfide Bridging Using Bromomaleimides. *J. Am. Chem. Soc.* **2010**, *132*, 1960–1965.

(21) Nathani, R. I.; Chudasama, V.; Ryan, C. P.; Moody, P. R.; Morgan, R. E.; Fitzmaurice, R. J.; Smith, M. E. B.; Baker, J. R.; Caddick, S. Reversible Protein Affinity-Labelling Using Bromomaleimide-Based Reagents. *Org. Biomol. Chem.* **2013**, *11*, 2408–2411.

(22) Marculescu, C.; Kossen, H.; Morgan, R. E.; Mayer, P.; Fletcher, S. A.; Tolner, B.; Chester, K. A.; Jones, L. H.; Baker, J. R. Aryloxymaleimides for Cysteine Modification,

Disulfide Bridging and the Dual Functionalization of Disulfide Bonds. *Chem. Commun.* **2014**, *50*, 7139–7142.

(23) Jones, M. W.; Strickland, R. A.; Schumacher, F. F.; Caddick, S.; Baker, J. R.; Gibson, M. I.; Haddleton, D. M. Polymeric Dibromomaleimides As Extremely Efficient Disulfide Bridging Bioconjugation and Pegylation Agents. *J. Am. Chem. Soc.* **2012**, *134*, 1847–1852.

(24) Jones, M. W.; Strickland, R. A.; Schumacher, F. F.; Caddick, S.; Baker, J. R.; Gibson, I.; Haddleton, D. M. Highly Efficient Disulfide Bridging Polymers for Bioconjugates from Radical-Compatible Dithiophenol Maleimides W. *Chem. Commun.* **2012**, *48*, 4064–4066.

(25) Morais, M.; Nunes, J. P. M.; Karu, K.; Forte, N.; Benni, I.; Smith, M. E. B.; Caddick, S.; Chudasama, V.; Baker, J. R. Biomolecular Chemistry Accelerated Post-Conjugation Hydrolysis †. *Org. Biomol. Chem.* **2017**, *15*, 2947–2952.

(26) Bryden, F.; Maruani, A.; Savoie, H.; Chudasama, V.; Smith, M. E. B.; Caddick, S.; Boyle, R. W. Regioselective and Stoichiometrically Controlled Conjugation of Photodynamic Sensitizers to a HER2 Targeting Antibody Fragment. *Bioconjugate* **2014**, *25*, 611–617.

(27) Nguyen, T.; Francis, M. B. Practical Synthetic Route to Functionalized Rhodamine Dyes. *Org. Lett.* **2003**, *5*, 3245.

(28) Borst, A. J.; James, Z. M.; Zagotta, W. N.; Ginsberg, M.; Rey, F. A.; DiMaio, F.; Backovic, M.; Veesler, D. The Therapeutic Antibody LM609 Selectively Inhibits Ligand Binding to Human AVβ3Integrin via Steric Hindrance. *Structure* **2017**, *25*, 1732.

(29) Brown, M. A.; Wallace, C. S.; Anamelechi, C. C.; Clermont, E.; Reichert, W. M.; Truskey, G. A. The Use of Mild Trypsinization Conditions in the Detachment of Endothelial Cells to Promote Subsequent Endothelialization on Synthetic Surfaces. *Biomaterials* **2007**, *28*, 3928–3935.

(30) Kurtis, M. S.; Schmidt, T. A.; Bugbee, W. D.; Loeser, R. F.; Sah, R. L. Integrin-Mediated Adhesion of Human Articular Chondrocytes to Cartilage. *Arthritis Rheum.* **2003**, *48*, 110–118.

(31) Akiyama, S. K.; Yamada, K. M. The Interaction of Plasma Fibronectin with Fibroblastic Cells in Suspension. *J. Biol. Chem.* **1985**, *260*, 4492–4500.

(32) Estabrook, D. A.; Ennis, A. F.; Day, R. A.; Sletten, E. M. Controlling Nanoemulsion Surface Chemistry with Poly(2-Oxazoline) Amphiphiles. *Chem. Sci.* **2019**, *10*, 3994–4003.

(33) Castañeda, L.; Wright, Z. V. F.; Marculescu, C.; Tran, T. M.; Chudasama, V.; Maruani, A.; Hull, E. A.; Nunes, J. P. M.; Fitzmaurice, R. J.; Smith, M. E. B.; Jones, L. H.; Caddick, S.; Baker, J. R. A Mild Synthesis of N-Functionalised Bromomaleimides, Thiomaleimides and Bromopyridazinediones. *Tetrahedron Lett.* **2013**, *54*, 3493–3495.